DESIGN OPTIMIZATION FOR A SUPPORT FOR THE STORAGE RING QUADRUPOLE MAGNET IN A SYNCHROTRON RADIATION FACILITY

A Thesis Submitted to the College of Graduate and Postdoctoral Studies in Partial Fulfillment of the Requirements for the Degree of Master of Science in the Division of Biomedical Engineering, University of Saskatchewan, Saskatoon

By

Sudipto Shekhor Mondol

Permission to Use

In presenting this thesis in partial fulfillment of the requirements for a Postgraduate degree from the University of Saskatchewan, I agree that the Libraries of this University may make it freely available for inspection. I further agree that permission for copying of this thesis in any manner, in whole or in part, for scholarly purposes may be granted by the professor or professors who supervised my thesis work or, in their absence, by the Head of the Department or the Dean of the College in which my thesis work was done. It is understood that any copying or publication or use of this thesis or parts thereof for financial gain shall not be allowed without my written permission. It is also understood that due recognition shall be given to me and to the University of Saskatchewan in any scholarly use which may be made of any material in my thesis.

Requests for permission to copy or to make other use of material in this thesis in whole or part should be addressed to:

Dean

College of Graduate and Postdoctoral Studies

University of Saskatchewan

116 Thorvaldson Building, 110 Science Place

Saskatoon, Saskatchewan S7N 5C9 Canada

and

Chair of Division of Biomedical Engineering

College of Engineering

University of Saskatchewan

57 Campus Drive

Saskatoon, SK

S7N 5A9

Abstract

High brilliance photon beam production requires high gradient magnets. High gradient magnets initiate large magnetic forces to be borne by supports to keep them in position. The objective of this study was to design a support for the CLS 2.0 quadrupole magnet that suppresses vibrations with the goals of the minimal amount of materials and low cost as compared to the existing system. The motivation of this study was associated with upgrading the CLS 2.0's electron beam, specifically the beam size which will be more than a hundred times smaller than that of the current CLS. The optimization goals of the support design were : (1) Maximizing the natural frequency of the whole magnet system (magnet + supports) and (2) Minimizing the weight of the frame, while meeting the constraints: (1) Static deflection less than 10 microns. (2) Stress developed should be less than the yield stress of the frame material (3) Natural frequency of the system should be more than 50Hz. Such a problem, when translated to the optimization problem, is a large problem as too many design parameters are involved, which makes the "All-In-One (AIO)" strategy of optimization infeasible. This study adopted a divide-and-conquer strategy, i.e., to properly decompose the whole problem into a set of small problems and then optimize them separately. By applying this novel design process, the frame was successfully designed, and the verification showed satisfactory results. The contribution of this work lies in the field of computational design, and specifically, it provides a case demonstration of the divide-and-concur strategy usefulness while optimizing the design for large problems.

Acknowledgements

I would first like to thank my thesis supervisors Chris Zhang and Mark Boland for this incredible opportunity. Chris has been very cooperative and understanding throughout the two years. I have learned a lot about written communication and optimization from Chris. Mark is the person I want to be in 20 years. He is the ideal role-model a young professional can have. Mark's way of getting the idea across is what allures me the most. I learned a lot of communication and presentation skills from him. Next, I would like to thank my CLS in-house guides, Madison Adam and Les Dallin. If this work was the Kurukshetra war, Madison played Lord Krishna. His door always open whenever I had trouble or had a question about my work. He continuously steered me in the right direction whenever necessary. Les' contribution was equally important. I learned magnet design from him most of which was not included in the thesis. However, I believe this knowledge was important for this work and might even help me in the future.

I would like to thank my CLS manager Drew Bertwistle for being an amazing mentor. Drew helped me a lot while getting setup at the CLS and continued his support throughout my employment period. Next, I want to thank James Gorin for the help with the storage ring vibration measurements which unfortunately could not find a place in this thesis. The control room would have been way scarier if it was not for Ward Wurtz, Cameron Baribeau, Jignya Patel, Michael Sigrist, Xiaofeng Shen and Bud Fogal. I would also like to thank Adam Janis, John Swirsky, Chris Bodnarchuk and Darwin Taylor for their help with the CAD. Thanks to Kevin Wyatt and Shawn Carriere for their expert engineering guidance. I wish to thank the rest of the Accelerator Operations and Development Department, Engineering Design and other CLS Staff, my Committee Members and Faculty of College of Engineering. A shout-out to all the people I have mentioned above, especially Madison and Les, for being extremely patient with me. I realised what I have put through after I supervised Janmejay. My friend and colleague Jason Gilbert helped me proofread this document.

I want to thank my little sister, Swapnil Mondal, for staying so strong. I would like to thank my friends here in Saskatoon for being there for me when things got tough. Manisha, Rajat, Ketan, Alivia, Rishav, Prachi, Jyoti, Deep, Shrey, Paromita, Pritam, Arindom, Mashrafi, Asif and many more who had a lot to do with here I am today. The members of Advanced Engineering Design Laboratory have also been helpful, especially, Chen, Hasan and Annal.

Dedication

In Loving Memory of my Parents

Mithu Mondal

Swapan Kumar Mondal

Table of Contents

List of Figures

List of Tables

List of Abbreviations

ADT	Axiom Design Theory
AIO	All-In-One
ALS	Advanced Light Source
APS	Advanced Photon Source
AHP	Analytical Hierarchy Process
BOM	Bill of Materials
CAD	Computer-Aided Draft
CLS	Canadian Light Source
CR	Constraint Requirement
CNC	Computer Numeric Control
DID	Decoupled Integrated Design
DOE	Design of Experiments
DOF	Degree of Freedom
DP	Design Parameter
EMA	Experimental Modal Analysis
ESRF	European Synchrotron Radiation Facility
FBD	Free Body Diagram
FCBPSS	Function-Context-Behavior-Principle-State-Structure
FCD	Full Concurrent Design

FE	Finite Element
FFTB	Final Focus Test Beam
FR	Function Requirement
GA	General Assembly
GDO	Goal Driven Optimization
GFRP	Glass Fibre Reinforced Polymer
GTAM	Genesis Topology for ANSYS Mechanical
ID	Insertion Devices
ILSF	Iranian Light Source Facility
ITER	International Thermonuclear Experimental Reactor
LHS	Latin Hypercube Sampling
MADM	Multi-Attribute Decision-Making
MBA	Multi-Bend Achromat
MCDM	Multi-Criteria Decision Making
MMA	Method of Moving Asymptotes
MOO	Multi-Objective Optimization
MODM	Multi-Objective Decision-Making
MOGA	Multi-Objective Genetic Algorithm
MOPCSSO	Multi-Objective Pareto Concurrent Subspace Optimization
NEG	Non-Evaporable Getters

NIS	Negative Ideal Solution
NSGA-II	Non-dominated Sorting Genetic Algorithm
PAES	Pareto Archived Evolution Strategy
PIS	Positive Ideal Solution
PSD	Power-Spectral-Density
PMM	Permanent Magnet Materials
RCS	Restricted Competition Selection
SAW	Simple Additive Weighting
SLAC	Stanford Linear Accelerator Center
SPEA	Strength Pareto Evolutionary Algorithm
SCP	Sequential Convex Programming
SSA	Six-Sigma Analysis
SS	Stainless Steel
TOPSIS	Technique for Order Preference by Similarity to Ideal Solution
VEM	Viscoelastic Materials
VSA	Vector Signal Analyzer

Chapter 1: Introduction

The purpose of this research is to optimize the design of a frame (or support system) for the CLS 2.0 quadrupole magnet (magnet frame for short in later discussions of this thesis), which is expected to minimise the transmission of the floor vibration to the pole tip of the magnet that is producing the fields that control the electron beam and which costs less than the current magnet systems at CLS.

The electron beam size of the Canadian Light Source 2.0 will be more than a hundred times smaller than the electron beam size of the present Canadian Light Source (CLS), and this will increase the probability of particle interaction which corresponds to a hundred times brighter synchrotron radiation. As such, better images are expected. To achieve this goal, the magnets used in CLS 2.0 need to be smaller, stronger, and their frames need to have a better capability of dampening the floor vibrations than those used in CLS. If the floor vibrations propagate through the frame and into the magnet, jitter is created, which will increase the beam size, affecting image quality (Zhang, 1996). To dampen vibrations and withstand the load generated by the magnetic force, a sturdy frame for the magnets is needed. However, little is known about the optimal design of such a frame in the context of synchrotron radiation facility in general and magnets of CLS 2.0 in particular.

1.1 Background and Motivation

The design of the storage ring and the injection system has two stages: physics design and mechanical design. A brief description of the physics design is included in Appendix A. A brief description of CLS is given in Appendix B. Currently, physics design was tentatively completed, and the next phase of design is mechanical design, specifically the mechanical design of the magnet systems (or magnets for short). Realization of the outcome of physics design with a physical system, where every component has a specific location subjected to very tight tolerances, is a challenge to mechanical design. Today, the necessities for alignments of physical components in the storage ring is very complex to meet the requirements of the physics design and to eventually improve the quality of the beam. This high requirement is translated to the complicated requirements for the magnet support system (or magnet frame for short) in this thesis.

1.1.1 Magnet Support

The interface that provides the physical positioning of the magnet parts into precise locations following their adjustment into a 3-D geocentric space can be defined as magnet support (Ruland, 1994). The primary functions of magnet supports are to fix the components close to its required position and to enable the magnet's movement to within the required tolerance of its approximate location via a precise motion system[1]. Ideally, both the magnet and the frame should be designed concurrently.

Magnets are rarely installed on a concrete block or directly on the floor. Girders, tables or individual stands are used to mount the synchrotron components at their required position at a height of 1.4 m above the ground. However, a low centre of mass can reduce both vibrations and thermal deformations (Sharma, 2005). These spacers (girders, tables or individual stands) form the backbone on to which finely machined components with adjustment mechanisms can be installed adjacent to each other at beam height (1.4 m). Unlike tables and individual stands, the girder system allows fine movement of several parts at once as it acts as a common platform. Moreover, girders might amplify floor vibrations and cause thermal deformations which will result in beam instability. Installing damping pads have been reported to be a cost-effective solution to this problem (Mangra et al., 2000).

There are two basic types of girders used in synchrotrons, concrete (Figure 1.1) and stress-relieved structural-steel box (Figure 1.2). The concrete girders are comprised of a rail system formed by I-beams cast into a rectangular cement block which supports the components of the synchrotron. Although concrete girders are difficult to construct with precision they are cheaper compared to steel box girders. On the other hand, steel box girders can easily be manufactured to precision by CNC machines eliminating the need for drilling and tapping holes for mounting components and time-consuming pre-alignment. Figure 1.3 shows a table that supports the LINAC Bunch Compressor at the APS.

[1] This system is not in scope of this work.

In circumstances where the beam components are spread out, individual stands (Figure 1.4) are the preferred solution. The simplest structure of an individual stand is a pipe with plates welded at the two ends. The pipe diameter depends on the required height at which the component is to be placed as well as the weight of the part. Nevertheless, the current project deals with the support structure that holds the magnet to the girder. The girders might be equipped with a fine adjustment system but it is not the focus of this work.

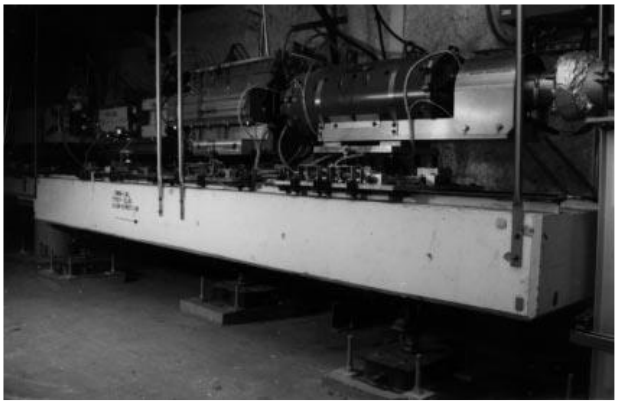

Figure 1.1: SLAC Concrete girder (Ruland, 1994)

Figure 1.2: APS Steel box girders (Sharma, 2005)

Figure 1.3: APS Linac Bunch Compressor Table (Sharma, 2005)

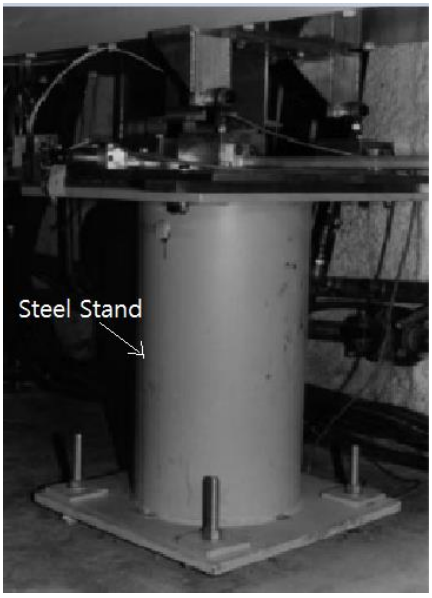

Figure 1.4: Steel Stand (Ruland, 1994)

The function requirements (Suh, 1990) of the magnet frame are twofold. First, it has to be stable and hold the magnet in a precise position (FR1). Second, it has to dampen any floor vibration from being transmitted to the magnet (FR2). Vibration can cause beam instability that degrades the beam quality by altering its intensity and amplifying its size (Masuzawa et al., 2006). The sources of vibration from the floor at the present Canadian Light Source were studied by Li et al (2010). Traffic, mechanical devices, water piping, etc. were reported to be the major sources of vibrations. Moreover, the damping of vibrations also results in the reduction of emittance at the ESRF (Zhang, 1996).

There are three possible methods of vibration elimination: (1) ground vibration reduction, (2) increase of the fundamental frequency of the magnet assembly (magnet and its support), as the ground vibrations are diminished at high-frequency range, and (3) incorporating a damping system. Other than tight vibration tolerances, compactness is another necessity for the next generation synchrotron magnets.

Having a smaller magnet aperture (Figure 1.5) allows having a higher field gradient (Johansson et al., 2014). Magnetic field gradient is the change in magnetic field with respect to position. The magnet aperture is proportional to the increase in storage ring circumference (lattice compactness). The lattice design is explained in Appendix A. The magnet excitation current requirement is lower with a smaller magnet aperture. Subsequently, the coil cross-section also reduces making the magnet more compact.

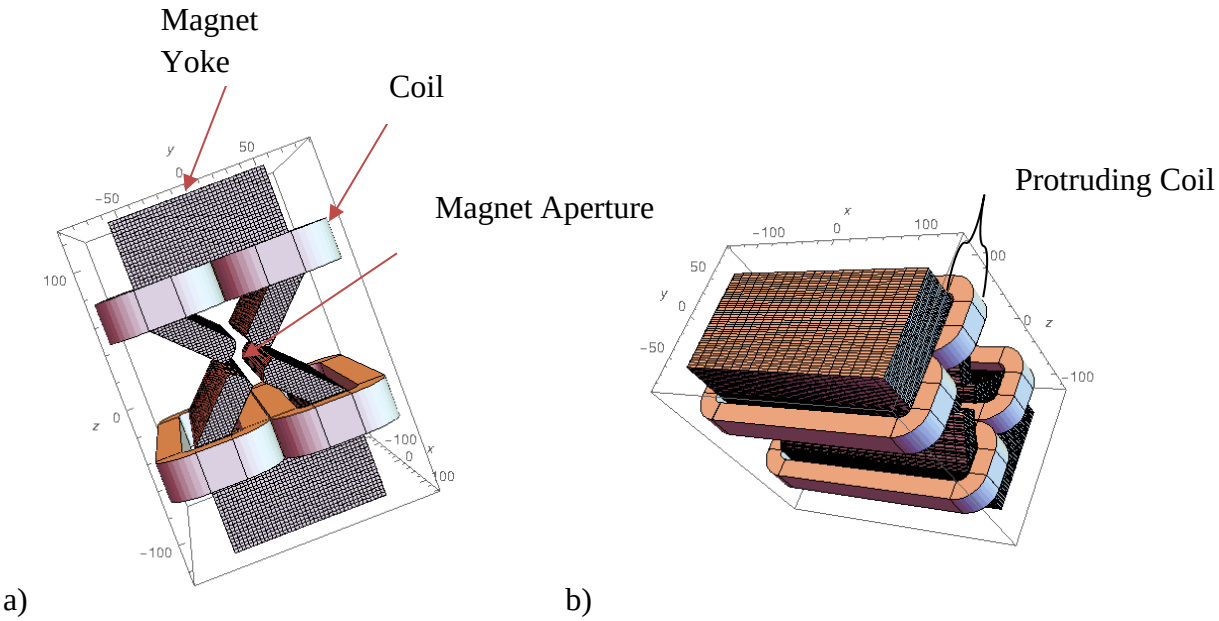

Figure 1.5: Conventional quadrupole. a) The coils are on the magnet poles (also shows magnet aperture) and b) The coils protrude beyond the yoke (Dallin, 2018)

Drift space is the space between two magnets in the lattice in the beam direction (the longitudinal direction). The following schematic diagram in Figure 1.6 shows the side view of two adjacent magnets and clearly explains the idea of drift space. Magnets can be classified into open-sided and closed sided kinds, based on their structural orientation. Open-sided magnets have one (or both) of the sides removed. In a light source this allows access for the photon beam to be taken out (Figure 1.7 a). On the other hand, closed-sided magnets do not allow any such space for beam extraction (Figure 1.7 b).

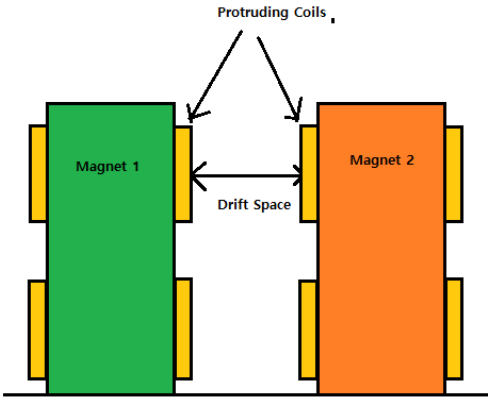

Figure 1.6: Drift Space

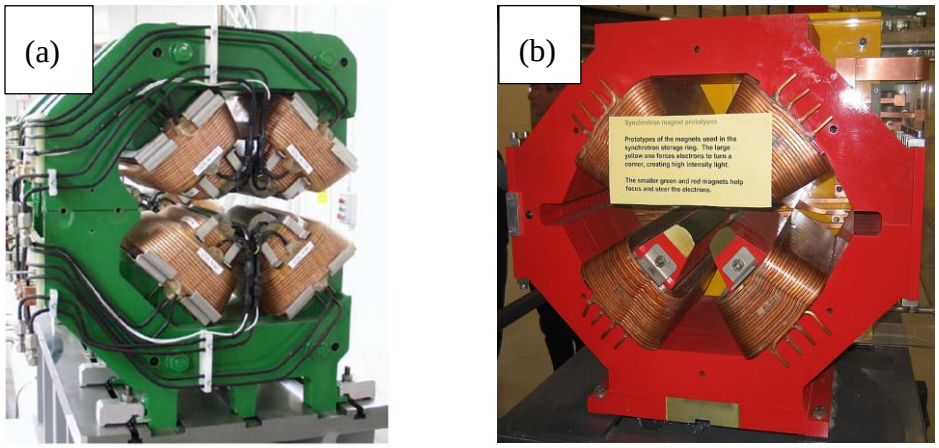

Figure 1.7: Quadrupole Magnet a) Open-Sided (Dallin et al., 2003) b) Closed-sided (Wikimedia Commons contributors, 2019)

1.1.2 CLS 2.0 Compact Quadrupole Magnet

Compact quadrupole magnets with the recessed[2] coils were designed at CLS to meet the space restrictions. The word recess means fitting by setting it back to surface to which it is fixed. So, the coil is attached in such a way that it is set into the magnet surface. A visual difference between a conventional protruding coil magnet and a recessed coil magnet can be observed when Figure 1.8 is compared with Figure 1.5 b. The physics model demonstrates that with the similar field harmonics as the conventional magnets, this magnet can achieve high field gradients and occupies less drift space (Dallin and Bertwistle, 2018). This magnet is further simplified by having only two coils (Figure 1.8).

The magnet geometry was simulated in 3D using RADIA (European Synchrotron Radiation Facility, 1997). There were many design iterations before a final design was reached. The physics design is in its final developmental stage and is being continuously updated and optimized (Dallin, 2016). The latest design modification was a thicker outer yoke. A magnet length of 0.24 m was considered. The recessed coil quadrupole magnet was able to reach the required high field gradients of about 60 T/m. To get an idea of how a quadrupole magnet works, readers are referred to Appendix C. The top-coil placement design is ideal for very tightly packed lattice (Appendix A). Figure 1.8 shows the 3D model of the zero drift quadrupole magnet.

[2] 'Recessed' is the opposite of 'protruded'.

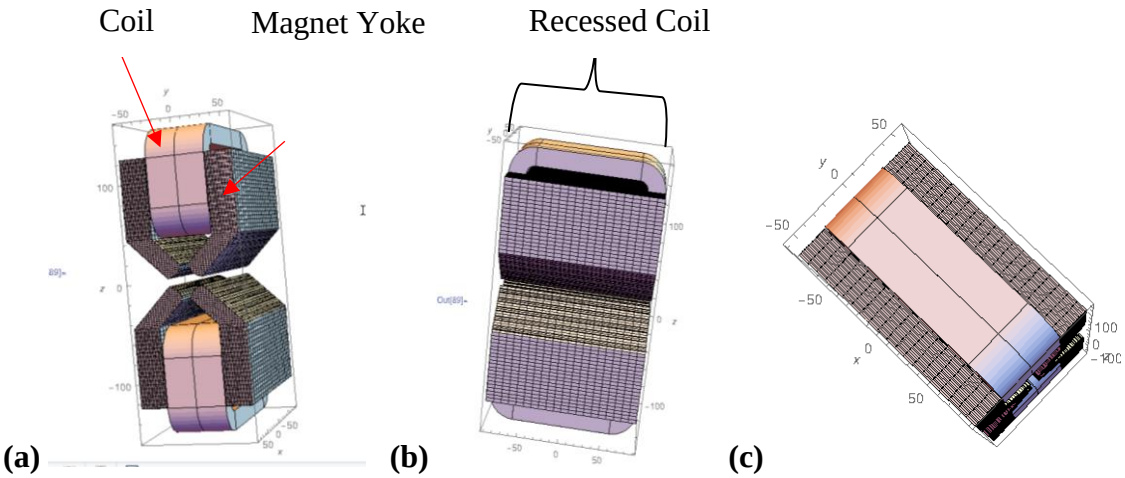

Figure 1.8: Zero Drift Quadrupole: (a) Front View (b) Side View (c) Top View *(Dallin, 2018)*

This magnet configuration showed better magnetic properties compared to those when the coils are placed on the sides. Hence, this magnet design was considered for mechanical design further. An optimal mechanical design of the magnet frame was conducted for this magnet at CLS, which is the work of this thesis.

1.1.3 Optimization

Optimization is the technique by which the best design is found from a set of available alternatives. Optimization is looked at as a time consuming and tedious process and often the engineers are forced to select a non-optimal design to deliver a product in time. This work deals with a multitude of design parameters. The nature of these variables is both discrete and continuous. The design problem is also governed by many restrictions.

A full concurrent design (FCD) has been adopted in many cases to solve such optimization problems (Li et al. 2001, Yan and Yan 2009, Alyaqout et al. 2010). In the FCD approach, all the design variables satisfying all the function requirements are optimized at once. However, this technique is not generalized.

Optimizing such a large number of parameters subjected to multiple constraints can be both challenging and slow. Hence, this work takes a different approach, a divide-and-conquer strategy, i.e., to properly decompose the whole problem into a set of small problems, and then optimize them separately. However, the decomposition of a large optimization problem into small optimization problem needs to be sensible or it may compromise the optimal results. The decomposition of the whole into several pieces is not an ad-hoc process but a rational process. This process is also called decomposition science. This work uses this technique to make the optimization process simpler and efficient.

The major motivation of this work was to stabilize the quadrupole magnet which is unstable by itself. This project came up with a mechanism to hold the magnet in position withstanding the high magnetic force.

1.2 Research Problem

The research problem is how to design an optimal magnet frame for supporting the CLS 2.0 magnet, as described above, for isolating the magnet from the ground, so that the magnet pole can be least affected by the vibration from the ground. The magnet assembly must have a natural frequency above 25 Hz (Tanabe, 2005) and the magnet poles can not deflect beyond 10 microns.

1.3 Research Objective and Scope

The overall objective of this work was to obtain an optimized design of the magnet support system for the CLS 2.0 quadrupole magnet for the best performance in terms of damping and support. The specific research objectives were defined as follows.

Objective 1: *To develop a comprehensive requirement model for the support system. The requirement needs to cover both the functional and constraint aspects.*

The magnet frame not only has to hold the magnet in a precise location and isolate the magnet from ground vibrations but also is subjected to constraints, such as, the material type, space restriction and pole deflection limit.

Objective 2: *To design the magnetic support to best meet the requirement.*

The optimized magnet frame has to be as near to its theoretical position in the storage ring as possible whether it is in a static or dynamic state.

Objective 3: *To conduct a simulation experiment to verify the design.*

Once an optimized model has been built, it has to be tested by subjecting the frame to static dynamic and heat loading similar to what it would experience when in operational conditions inside the storage ring.

The magnet in consideration is with the closed side configuration, which was dictated by the design of the insertion device in CLS 2.0 design. This work was not intended to change any design of the magnet itself. Further, the magnet support is usually clamped on girders. The natural frequency of the whole support system includes the contribution from the girders. The natural frequency of the entire support system should be more than 25 Hz. Thus, for simplicity, it can be assumed that the magnet support may possibly be installed on a machined girder. This girder will rest on concrete pedestals. Moreover, the magnet will be cooled by the hollow copper tubes with water flowing through them. In reality, the cooling system will never be able to remove all the heat generated (i.e. the support have to support some of the magnet/coils & cooling lines at some point) as some contact will allow for heat transfer but this effect can be ignored. The temperature difference of the inlet and outlet water will be assumed to be 8^{o}C, the same as the present CLS quadrupole magnet, for accounting for thermal expansion of the frame. Ambient conditions that will naturally change (air pressure, humidity, cooling water temperature fluctuations) will also allow for small thermal changes. Also, the cooling channels will be treated as a block of copper in the simulations. The base of the frame will be assumed to attain the girder temperature which is assumed to be the same as the ambient temperature of the present storage ring i.e. 23 ^{o}C. Additionally, the material delivered by the vendor may not be perfectly isotropic. Nonmagnetic steel might still react to a magnetic field after machining and in such cases, further heat treatment was recommended. The present work assumed that the material will remain isotropic even after machining.

The design verification will not be possibly conducted on a real system due to the difficulty of building a control or base line for comparison to the simulation on the design, which is possible. This shortcoming can be tolerated for such a large and complex system.

1.4 Research Plan and Methodology

The challenge in this research for achieving the aforementioned objectives is: heterogeneous types of design are involved, such as discrete variable versus continuous variable, topology or shape versus dimension, material type versus material distribution. This challenge is reflected by a list of issues to be addressed.

The first issue is how to find the load on the magnet support. This issue can be addressed by the software called RADIA. RADIA is a 3D magneto-statics computer code, and it is used to solve 3D boundary problems. The field integrals along a line and the magnetic field can be efficiently calculated by this software package. Various linear and nonlinear, isotropic and anisotropic magnetic materials, with distinct shaped current-carrying element problems can be solved in RADIA. The magnetic field calculated in RADIA has been verified experimentally and, hence, its effectiveness is proven. With RADIA, the force that one pole exerts on the rest of the magnet can be found, and then the forces on the remaining poles can be found due to the geometric symmetry and by applying laws of magnetic attraction and repulsion. The second issue is related to the material of the support and allowable deformation. This issue can be addressed by the software called POISSON (Holsinger and Halbach, 2013) along with the methodology called Analytical Hierarchy Process (AHP) (Saaty, 1980). POISSON is a 2D magnet analysis tool that executes the point by point 2D field distribution, which, can help determine changes in the magnetic field gradient due to magnet pole deflections AHP is a systematic method of making complex decisions. Further, when there is a finite pool of choices APH finds an optimal option.

The third issue is the design of the structure of the support. To conduct the conceptual design of the support, Axiom Design Theory can be used to check if the specific principle of the support meets Axiom 1 (Suh, 1990). Moreover, Decoupled Integrated Design (DID) (Sun et al., 2012) can be used to decompose the optimization problem into smaller problems. DID will reduce the number of variables to be dealt with, which is crucial to both design effectiveness and efficiency.

For embodiment design and detailed design of the support, the software called ANSYS can be employed.

Afterward, using machine design concepts, the preliminary dimensions can be found out. However, as deformations can not exceed a certain limit and a thicker frame corresponds to a high natural frequency, the dimensions have to be adjusted economically using Multi-Objective Optimization (MOO) (Deb, 2009). MOO is a decision-making tool, where there are conflicting goals. Furthermore, MOO reduces the number of design points in the vast design space and saves calculation time. The goals in this particular problem are low deformation (less than 10 microns), high natural frequency (more than 25 Hz) and less material usage. When the vibrations from the floor match the natural frequency of the structure it results in resonance and the structure starts to vibrate vigorously. Hence, the natural frequency of above 25 Hz is desirable for the structure as the ground is not sensitive to higher frequencies (Tanabe, 2005). The natural frequency, f_0, of the structure can be calculated by

$$f_0 = \frac{1}{2\pi}\sqrt{\frac{k}{m}} \tag{1.1}$$

where 'm' is the mass and 'k' is the stiffness of the system. Thus, the aim is to keep the mass to be minimum and the stiffness to be maximum. As the mass of the magnet can not be easily changed as it is defined by the physics design, hence, the support system's mass has to be adjusted. On the other hand, the low deformation corresponds to a large frame thickness. A very thick frame will have more material requirements, which will increase the cost. Hence, the goals are in a clash and an optimal thickness has to be chosen using MOO. As assumptions will be involved throughout the design process, the final optimal design must be evaluated. The best way to achieve this is to build a prototype, which is expensive and time-consuming. Therefore, the simulation software can be used to evaluate the optimal design by creating a mathematical model (Preissner et al., 2016).

1.5 Thesis Organization

The thesis is sub-divided into six chapters from now on. **Chapter 2** contains a literature review on Synchrotron Quadrupole Magnets, Magnet Support System incorporated around the world and Optimization techniques; especially, Multi-Objective Optimization has been reviewed thoroughly.

Chapter 3 describes how the design constraints, i.e. magnetic forces, allowable deformation and frame material's magnetic nature were determined. **Chapter 4** deals with the conceptual design or logical design of the magnet frame and introduces the stages in the embodiment design. **Chapter 5** describes how the number of fasteners and the material were selected, the frame plate thickness was optimized by Multi-Objective Genetic Algorithm, and the hole location in the magnet yoke was determined from a parametric study and the optimized design was checked for robustness. **Chapter 6** deals with the mathematical modelling of the developed optimized frame design. The optimized frame design is tested with static loading conditions to calculate the deformation and the stresses. The final design was subjected to relevant random and harmonic vibrations and the stresses and deformation were also found in this chapter. **Chapter 7** contains the conclusion, an overview of the optimized model and recommendations.

Chapter 2: Literature Review

This chapter is divided into three main parts which describe magnet designs, magnet support system designs and optimization processes. An assessment of the already existing synchrotron magnets is necessary as the present work also involves adjusting the dimensions of the design to calculate the allowable deformation. It is also important to keep up with the technology upgrades that all the synchrotrons around the world are making. This project involves defining the design constraints such as magnetic force, material requirements, allowable deformation, and so on, and the scrutiny of fourth generation magnets will help to compare and to verify results. It can also be observed that many of the magnet designs described below have integrated supports systems that are in-built in the magnet themselves and hence these concepts are important to review.

Section 2.1 deals with reviewing existing synchrotron quadrupole magnets. Section 2.2 discusses various support structures that hold the magnets in a predetermined location. Various techniques to determine the natural frequency and support structure's response to vibrations have been reviewed. Section 2.3 deals with the optimization of magnet support structures and design methodology. Optimized design involves concurrent design or 'All-In-One (AIO)' approach. However, the present optimization problem deals with a large number of design variables thus rendering the AIO technique invalid. Topology optimization is an important segment of this research, hence an audit of the optimization techniques used to modify synchrotron support structure to minimize static deformation and reduce vibration response is necessary. Section 2.4 gives a conclusion along with a summary of the rationale of this thesis research.

2.1 Synchrotron Quadrupole Magnets

Quadrupole magnets are used to focus the beam size. At the center of the aperture of a quadrupole magnet, the field strength is zero (Figure 2.1). The field strength linearly increases in the transverse direction. For a horizontally focusing quadrupole, this can be interpreted as the spring force, $F = -kx$, thus, forcing particles to be bent towards the magnet center. In the vertical plane, $F = +ky$ and the particles are bent away from the center of the magnet (where 'F' is the force, 'k' is the spring constant, 'x' and 'y' are the displacements in the horizontal and vertical direction, respectively). This along with the schematic of a quadrupole magnet is illustrated in Figure 2.1.

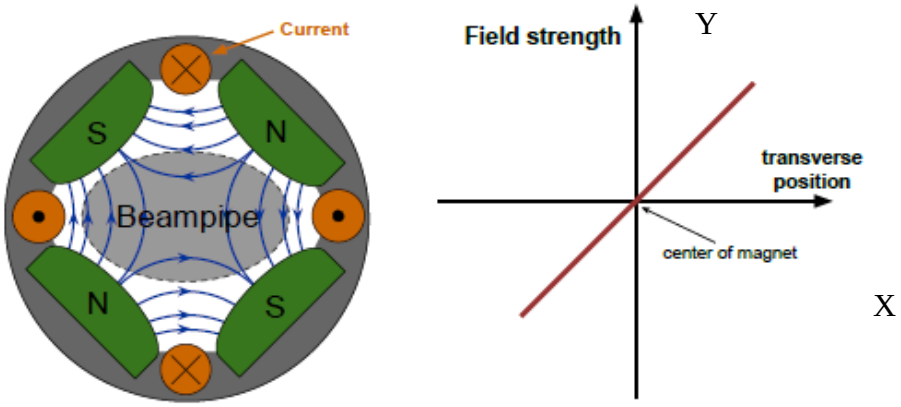

Figure 2.1: Magnetic Field and Transverse Field Dependency of a Quadrupole Magnet

(Accelerator Division — Fermilab Operations Department, 2013)

Thus, quadrupoles can focus a particle by deflecting it by a force proportional to its displacement from the center. However, it can only focus particles in one transverse plane while defocusing in the other. Hence, magnets must be arranged in lattices in order to achieve complete focusing of the beam. Quadrupole magnets are arranged in an alternating repeating pattern with a distance of less than or equal to twice the focal length to ensure overall focusing (Figure 2.2).

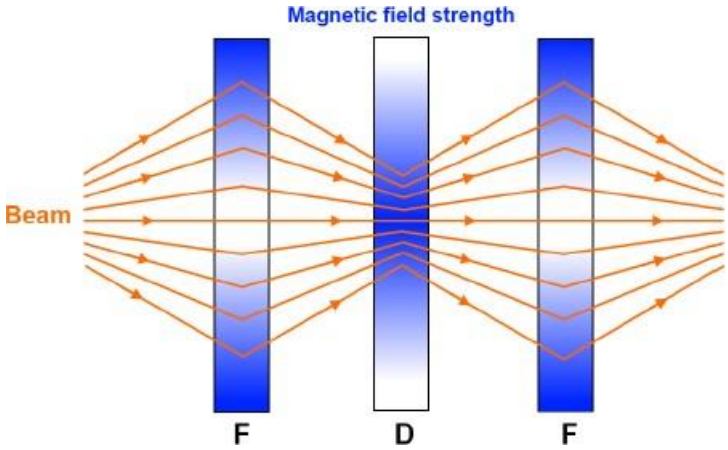

Figure 2.2: Overall Focusing with an Array of Quadrupole Magnets

(Accelerator Division — Fermilab Operations Department, 2013)

Magnets in a synchrotron are used to alter the particle trajectory direction. All magnets produce some magnetic field ($\vec{B}$) that act on the electron beam via the Lorentz force ($\vec{F}$). The Lorentz force is also the mechanism by which an electric field ($\vec{E}$)–accelerates the beam. The Lorentz force (Figure 2.3) really is central to understanding dipoles, quadrupoles, sextupoles – any kind of magnets used at CLS (Fermilab Operations Department, 2013).

$$\vec{F} = q\,(\vec{E} + \vec{v} \times \vec{B}) \qquad (2.1)$$

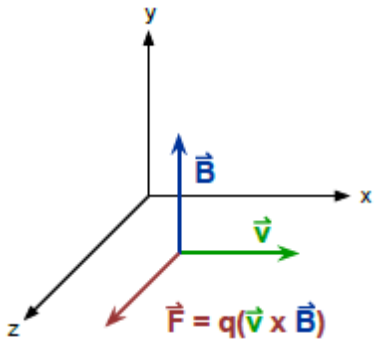

Figure 2.3: Magnetic Force Direction (Accelerator Division — Fermilab Operations Department, 2013)

The cross product in the B-term is important for how magnets are used in a storage ring. As a basic example, consider a dipole magnet that produces a uniform vertical B-field. As the beam passes through the dipole, the cross product term dictates that the beam experiences a Lorentz force perpendicular to both the beam's direction of travel ($\vec{v}$) and the dipole field ($\vec{B}$). The q is the charge of the electron. In other words, a vertical magnetic field exerts a force along the horizontal direction. In this way, dipole magnets are used to steer the beam.

2.1.1 Canadian Light Source

AISI 1010 steel was used in the 2-Dimensional simulations for the CLS magnets (Dallin, 2001). In order to get the light out from the Insertion Devices (IDs), the magnets in the storage ring had to be open sided in CLS. Hence, the bend magnets, the quadrupoles and the sextupoles were

designed to have a C-shape. Chamfering is cutting the pole ends at an angle on the z-axis (longitudinal axis). The end chamfers of the CLS prototype dipole magnets were designed to be removable to accommodate for the error between the simulation-based design and physical set up. Once the chamfer was verified, the production magnets did not have removable chamfers. The chamfers influence the magnetic length and also control the higher order harmonics (Dallin, 2018). As shown in Figure 2.3 through 2.7, the quadrupoles have a top yoke and a bottom yoke. The quadrupoles tips were hyperbolic but as they were not extending infinitely there are two to three bumps that help shape the good field region (Dallin, 2018).

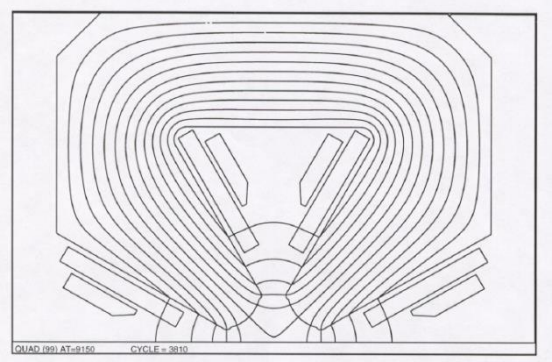

Figure 2.4: CLS Quadrupole Magnet POISSON 2D Model (Dallin, 2001)

The field gradient for these magnets could be excited to have a field gradient of 22.22 T/m with 9500 Amp-turns. The magnetic aperture was 32.5 mm. The RADIA[3] simulation of the above quadrupole was done by Pywell (1999). From the investigation, it was concluded that there was a 4% reduction in the quadrupole field strength when compared to the POISSON[4] simulation results. An effective length of 277 mm from a chamfer of 20^{o} was inferred from the study of the effect of the pole chamfer angles on the magnetic length.

[3] RADIA is 3D magneto-statics code (European Synchrotron Radiation Facility, 1997)

[4] POISSON is 2D analysis tool (Holsinger,and Halbach, 2013)

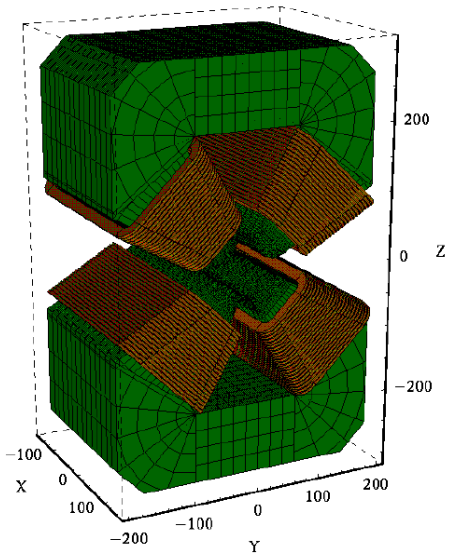

Figure 2.5: Quadrupole RADIA Simulation (Pywell, 1999)

In a quadrupole magnet, other than the quadrupole field gradient there is always some percentage of higher order field gradients like sextupole, octopole, etc present. In this case, only the quadrupole field is useful and the higher order fields can be considered undesirable. The higher order fields also deteriorate the magnetic field quality of the quadrupole and hinders the quadrupole's ability to perform effectively to some extent. The end chamfers were optimized to minimise the effect of the higher order harmonics. The quadrupoles have two sets of coils connected in series. The end plates are nonmagnetic (Pywell, 1999).

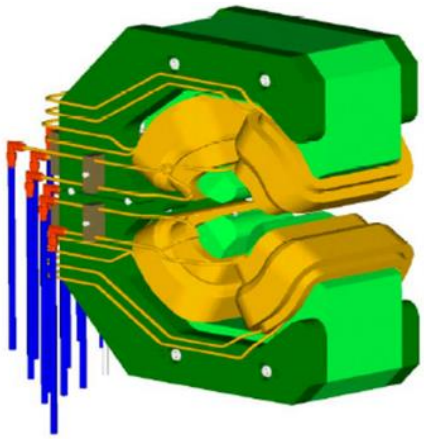

Figure 2.6: Quadrupole 3D Model (Dallin et al., 2003)

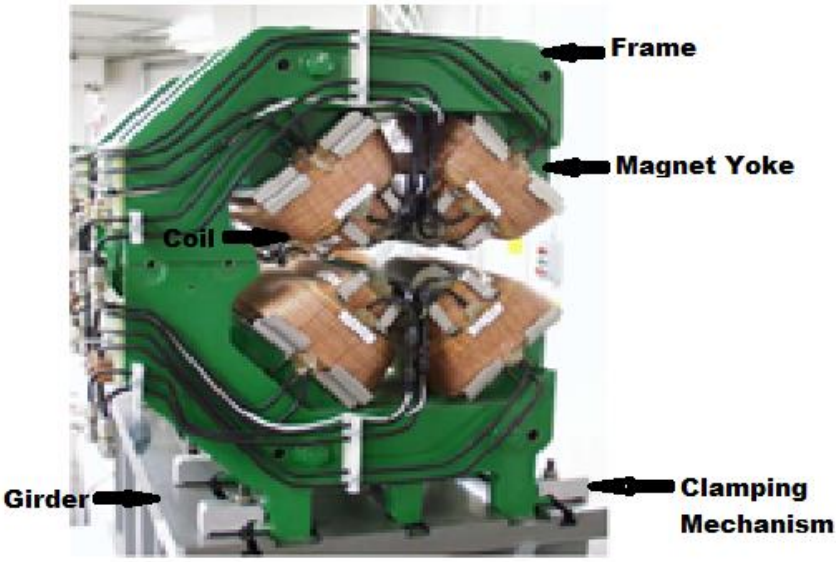

Figure 2.7: Manufactured Quadrupole Magnet (Dallin et al., 2003)

2.1.2 ELETTRA 2.0

Operating at 2 GeV, the compact S6BA (symmetric six bend achromat) magnetic lattice of ELETTRA 2.0 will bring down the horizontal emittance to 0.24-0.28 nm-rad. The next generation

synchrotron, which will replace ELETTRA, has realized the need for a short longitudinal space between magnets to ensure more available space for the insertion devices. Moreover, the magnets were designed such that their magnetic length is almost equal to the physical length, allowing for the 'drift spaces' of only 50-70 mm. The bore diameter of the quadrupole is 28 mm, has a physical length of 0.22 m and a gradient of 18 T/m (Karantzoulis, 2018). ELETTRA 2.0 magnets will be air cooled and thus saving energy considerably. The optics design also involves the use of permanent magnets in conjunction with electroma Coils are recessed vs the quadrupole profile, where it can be observed that the coils do not stick out of the magnet and thus conserving 'drift space'. All the magnets are being prototyped.

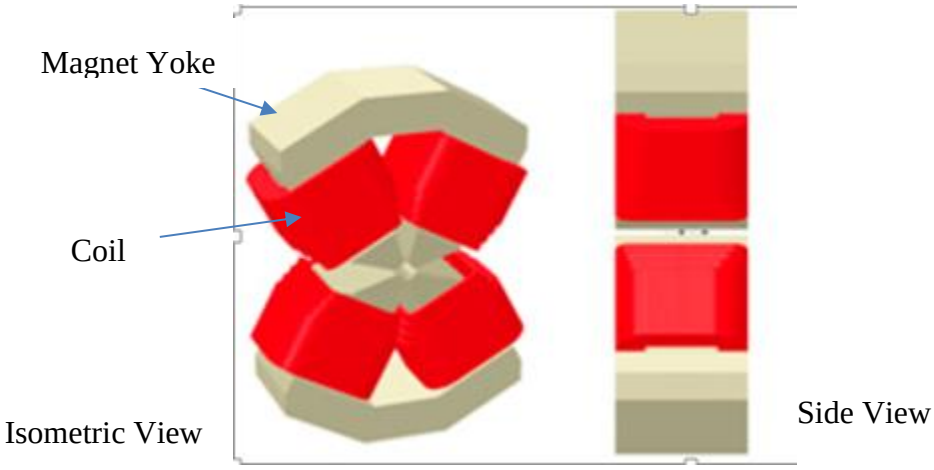

Figure 2.8: ELETTRA 2.0 Quadrupole Magnet (Karantzoulis, 2018)

2.1.3 ALS-U

The Advanced Light Source (ALS) Upgrade will reduce the horizontal emittance down to 50 pm which will consequently increase the soft x-ray brightness by two to three times compared to the present ALS (Steier et al., 2018). It will operate at 2 GeV with a beam current of 500mA. The vacuum chambers will have non-evaporable getters (NEG) coating and have been designed to have a diameter of 13-20 mm in the arcs and 6 mm in the straights. Similar to CLS 2.0, low beam emittance is achieved by using strong focusing magnets and a large number of bend magnets which can be realized by using the MBA (Multi-Bend Achromat) lattice concept. Methodical evaluations

indicated the use of eight or nine bends every arc and quadrupoles having 100 T/m field gradients to attain the above-mentioned requirements. Furthermore, ALS-U will also be using 46 T/m radially off-set geometric quadrupoles combined function bending magnets that have an asymmetric pole-design. This particular magnet will have a C-type frame and is predicted to produce good field quality at low power and mass (Figure 2.9).

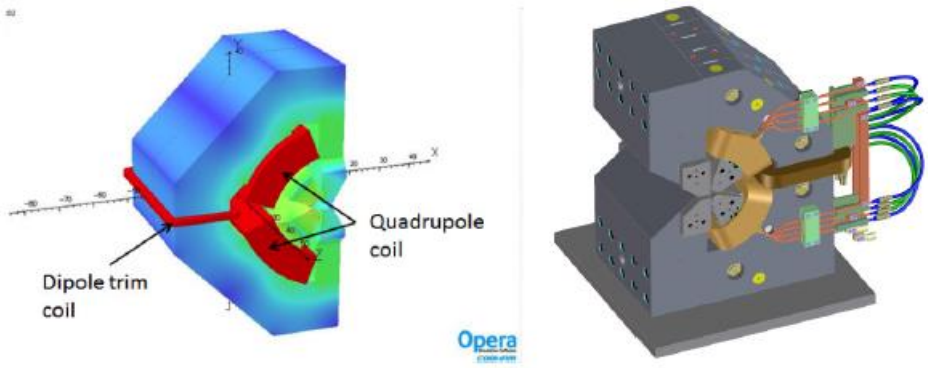

Figure 2.9: Transverse Gradient Dipole Field Simulation (Left) and CAD Model (Right) *(Steier et al., 2018)*

To ensure compactness of the magnet, pole noses were introduced. The pole face to pole face length is equal to the magnet physical length. The yoke and the base of the pole are recessed from the pole tip. Similar to CLS 2.0 quadrupole design, this magnet design also aims to minimize the protrusion of the coil into the "drift space". The transverse gradient dipole employs asymmetric quadrupole bending geometry and the beam trajectory is followed by the curve geometry of the pole.

The magnetic forces deform the magnet poles which results in undesirable changes in the magnetic properties (Jung et al., 2018). Thus, the deformation has to be minimized and evaluated in the design stage to avoid surprises while testing the magnet. Moreover, the magnetic force depends on the field gradient and an increase in gradient may result in an increase of the magnetic force. To

calculate the deformation, the magnetic forces were exerted on the face of the pole and the return yoke. An estimated total deformation of 21.63 microns was observed on the whole body (Figure 2.10). The static structural analysis was used to determine the thickness of the yoke to minimize the deformation caused by the magnetic force.

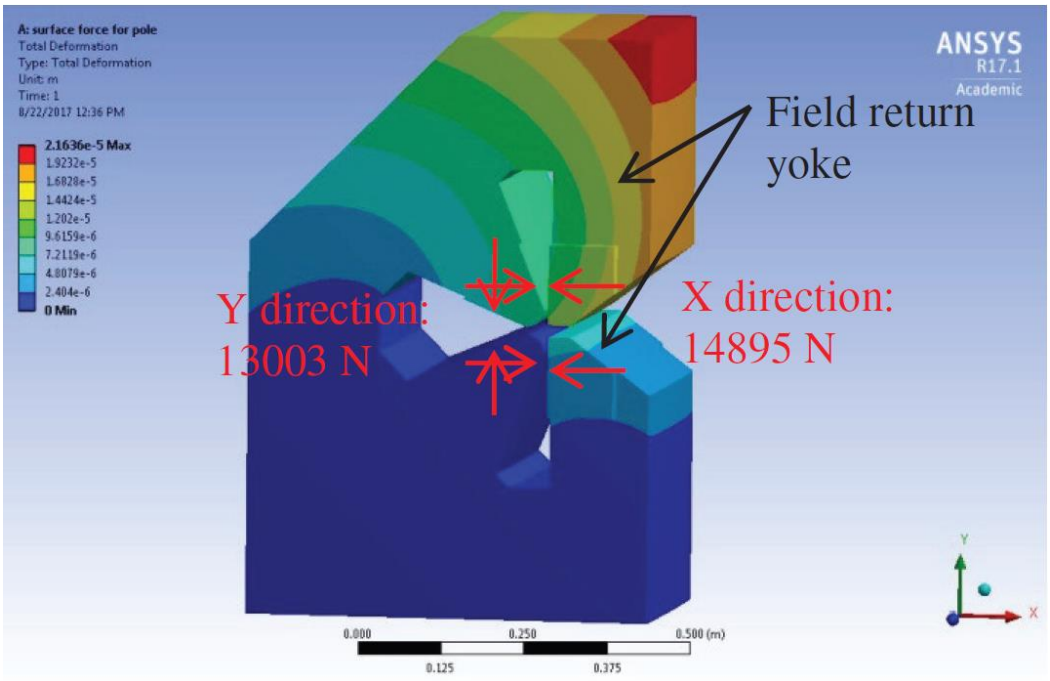

Figure 2.10: Deformation of the Transverse Gradient Dipole (Jung et al., 2018)

Additionally, reverse bend quadrupoles will also be incorporated to lower the natural emittance (Figure 2.11). The lattice, thus, consists of nine bending magnets and ten quadrupoles per arc that are offset which yields a reverse bending of about 10%.

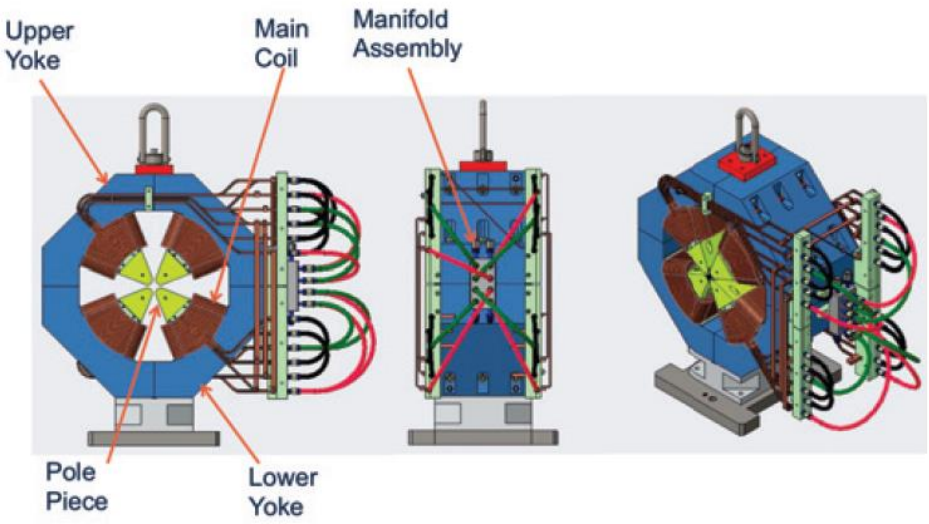

Figure 2.11: Reverse Bend Quadrupole (Steier et al., 2018)

Furthermore, the ALS-U magnets will be designed such that alignment is dependent on the machining precision and a modular approach has been incorporated by keeping the same vertical height for all the magnets (Figure 2.12). The magnets were designed to be as small as possible and to have fewer parts while keeping the center of all the magnets at the same height (Wallen, 2018).

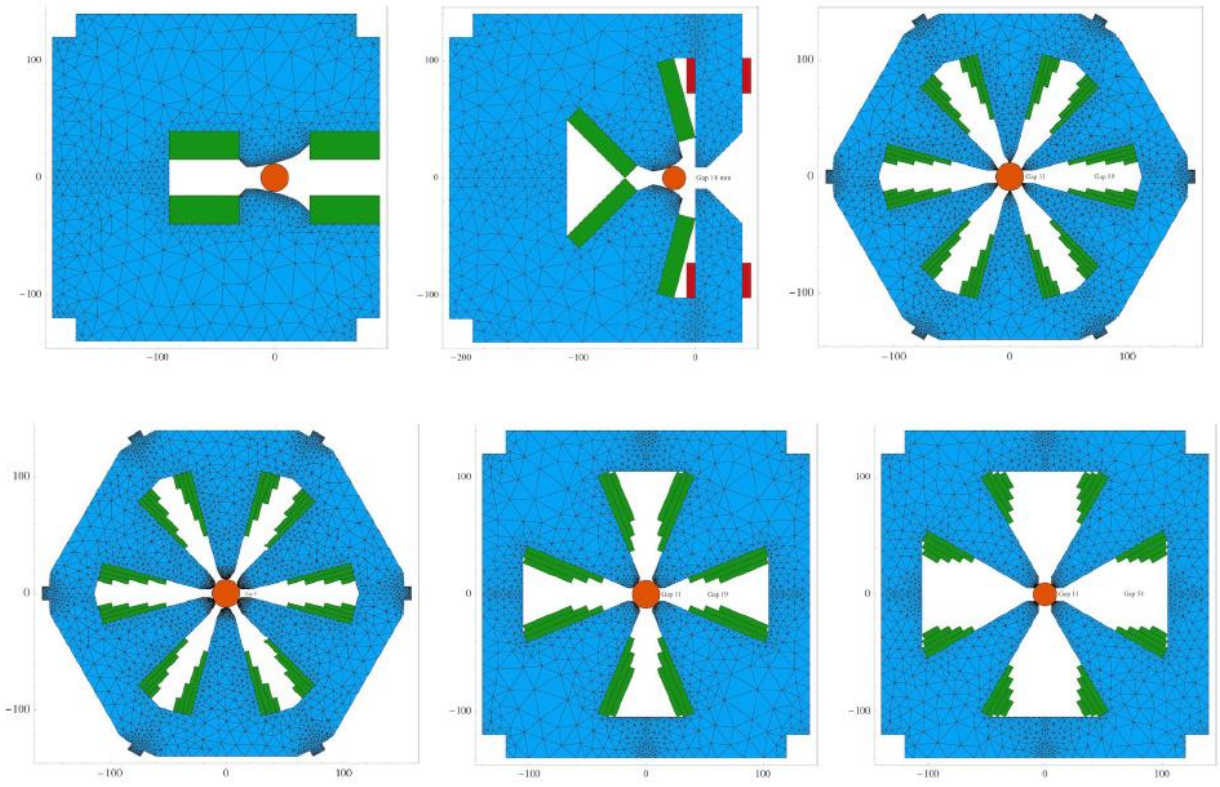

Figure 2.12: ALS-U Magnets (Wallen, 2018)

2.1.4 SIRIUS

Brazilian Synchrotron Light Source is designed to operate at 3GeV 20TBA third-generation electron accelerator and have a beam emittance of 1 nm rad (Tosin et al., 2010). A distinct characteristic of this synchrotron is that it uses permanent magnet materials (PMM) in the lattice. Thus, reducing expenses related to manufacturing, electricity and cooling. As they do not have coils they are more compact than electromagnets and do not experience failure in power and control systems. Moreover, the possibility of producing 70% of the field from permanent magnets and the remaining 30% from electromagnets for flexibility was explored. These quadrupoles have a maximum field gradient of 30T/m and a bore diameter of 55 mm, which means that the magnet aperture is 55 mm. The magnetic simulation and the mechanical design of the SIRIUS quadrupole magnets are shown in Figure 2.13.

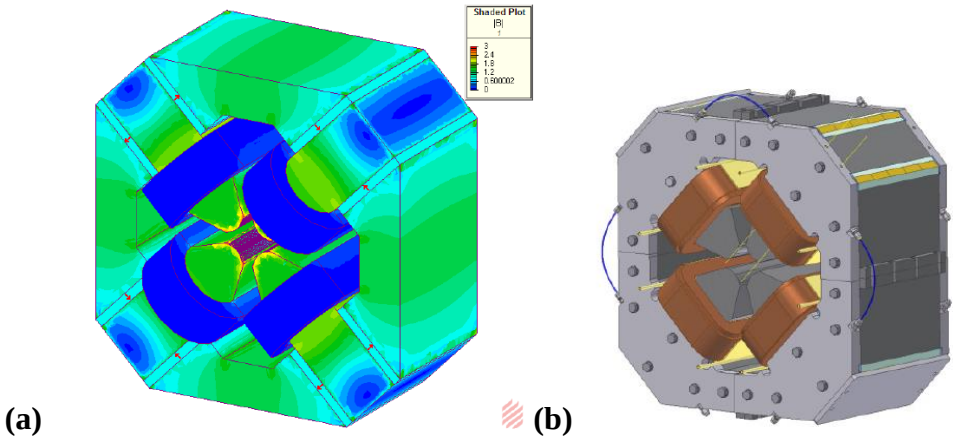

Figure 2.13: Quadrupole: (a) Magnetic Simulation (b) Mechanical Design *(Tosin et al., 2010)*

CLS 2.0 is avoiding the use of hybrid magnets as they have never been used before so it is risky. Furthermore, the properties of PMM might deteriorate in the presence of radiation.

2.1.5 MAX IV

Just like CLS 2.0, MAX IV also has a 3 GeV storage ring. It also has a second 1.5 GeV storage ring, the 3 GeV ring uses the MBA lattice structure to minimise beam emittance (Johansson et al., 2014). However, CLS 2.0 is designed to have a smaller aperture (24mm) compared to MAX IV (25mm). Another aspect of MAX IV magnets is that it uses the magnet block concept where multiple magnets were machined out of a single iron block of iron. Using a block magnet increases the stiffness of the system and increases the natural frequency to about 100Hz. This technique also reduces alignment errors and minimises installation time. They use NEG-coated copper vacuum chambers thus avoiding the pumping limitations and space requirements of conventional pumps. With the quadrupole configuration shown in Figure 2.14, a field strength of 43.55T/m (CLS 2.0 quadrupole strength is 50.96 T/m) was achieved.

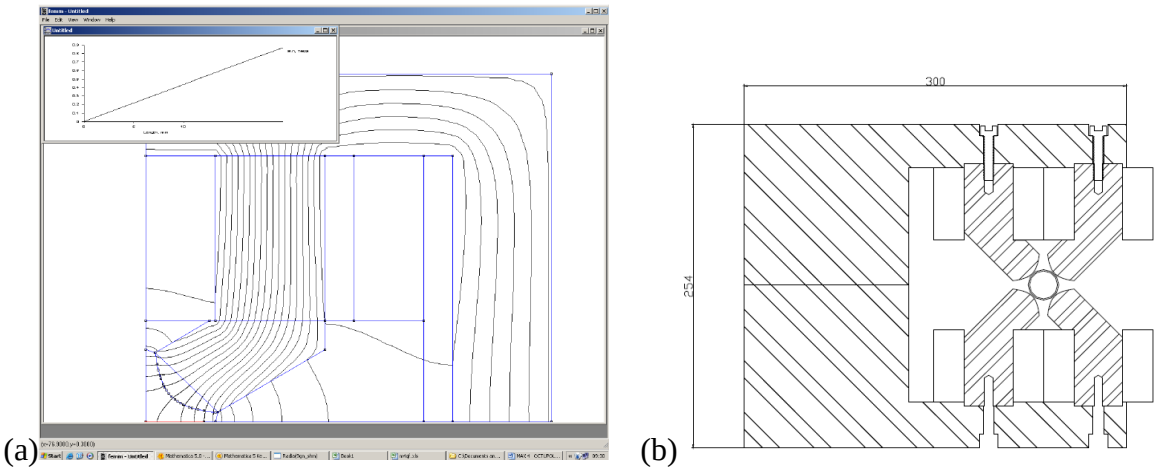

Figure 2.14: MAX IV Quadrupole (a) Quarter-quadrupole (b) Transverse Cut *(MAX IV DDR, 2010)*

2.1.6 Iranian Light Source Facility (ILSF)

Iranian Light Source Facility (ILSF) is a 5BA with a 3GeV storage ring. In the bare lattice, a beam emittance of 0.48 nm rad can be obtained (Saeidi et al., 2016). ILSF quadrupoles have a maximum field gradient of 24.78 T/m and an aperture diameter of 52mm. The Figures 2.15 and 2.16 show the magnetic field and the 2D mechanical layout of the quadrupole magnet respectively.

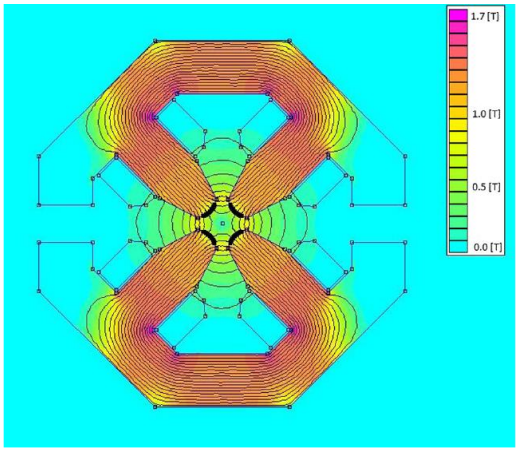

Figure 2.15: Magnetic Field inside the Quadrupole (Saeidi et al., 2016)

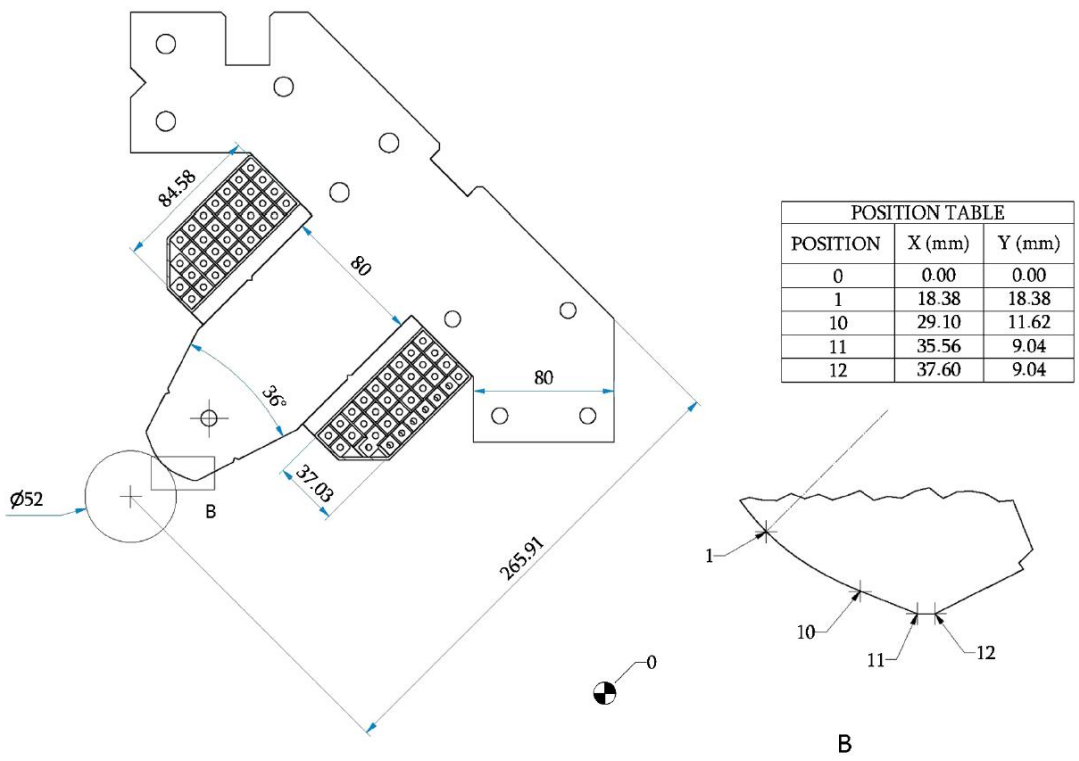

POSITION TABLE		
POSITION	X (mm)	Y (mm)
0	0.00	0.00
1	18.38	18.38
10	29.10	11.62
11	35.56	9.04
12	37.60	9.04

Figure 2.16: Storage Ring Quadrupole Magnet Lamination and Coil Dimension *(Saeidi et al., 2016)*

Yoke deflection was observed for the quadrupole magnet. The weight and the magnetic fields of the poles can be the held responsible for the deflection. This spatial deviation can cause changes in the field quality and can also initiate multipole components. From the static structural analysis, it was concluded that using endplates reduced maximum deflection to 0.02 mm from 0.1 mm. This is illustrated in Figure 2.17.

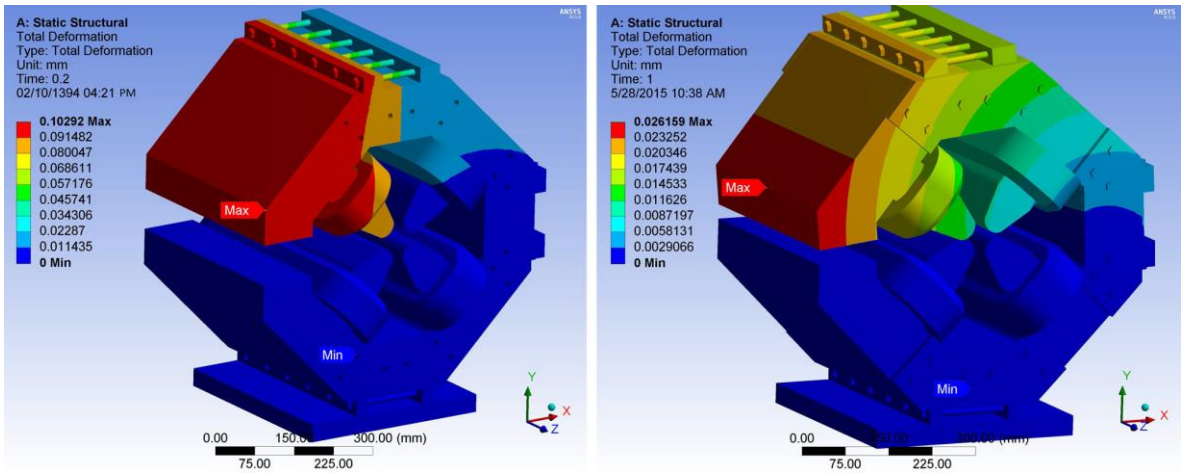

Figure 2.17: Storage Ring Quadrupole with End Plate Analysis on the left and Without End Plate Analysis on the Right (Saeidi et al., 2016)

The end chamfers and shims improved the field quality. Low carbon steel ST52 was used as endplates which were similar (on the basis of hysteresis curve) to magnet steel. Figure 2.18 shows the probable mechanical design of the ISLF quadrupole.

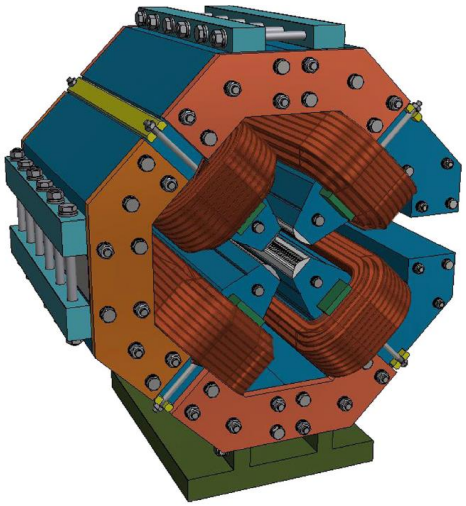

Figure 2.18: Storage Ring Quadrupole Mechanical Design (Saeidi et al., 2016)

2.1.7 Indus-2

Two Families of open type quadrupoles (Q3 and Q4) with 16 T/m maximum gradient in C-configuration were used in the 2.5 GeV Indus-2 to extract the synchrotron radiation (Sreeramulu et al., 2017). Similar to other synchrotrons, ANSYS[5] was used to analyse the mechanical structure aiming to resist deformation at the highest excitation current. The magnetic force between the top and the bottom poles was found to be 39315 N/m from the initial 2D electromagnetic static analysis. Moreover, the structural assembly components are chosen to be AISI 316 grade stainless steel plates which are nonmagnetic in nature. A C-clamp was used to reduce deformation for the Q4 magnet and the vertical magnetic force was found to be 15340 N from 3-D magneto-structural analysis. On the hand, a clamping spacer was used for the Q3 magnet (Figure 2.19). A static structural analysis was done to compare the displacement of the poles caused by the magnetic force with and without the C-clamp. Consequently, the C-clamp was able to reduce the displacement of the poles for the Q4 magnet in the vertical direction from 0.1mm to a range of 0.020-0.025mm while the horizontal displacement was negligible (Figure 2.20).

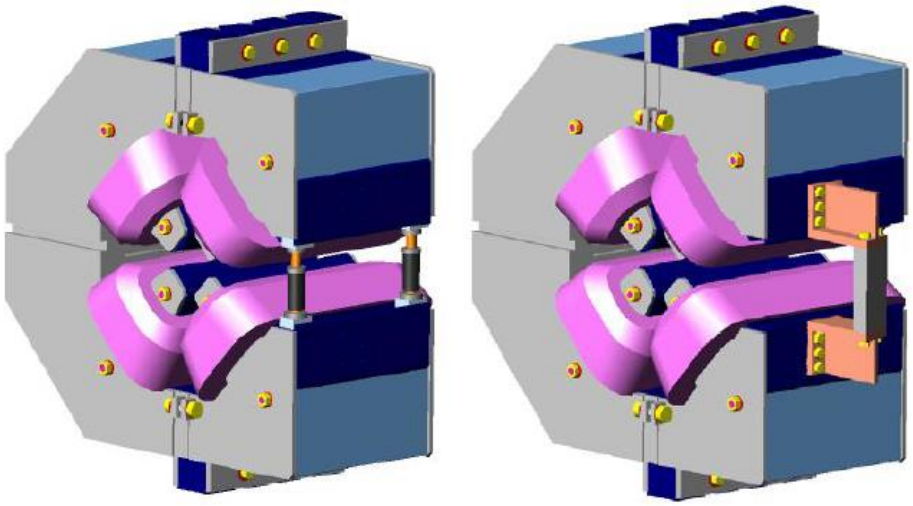

Figure 2.19: CAD Model of Q3 (Left) and Q4 (Right) Quadrupole Magnet *(Sreeramulu et al., 2017)*

[5] It is a finite element analysis software.

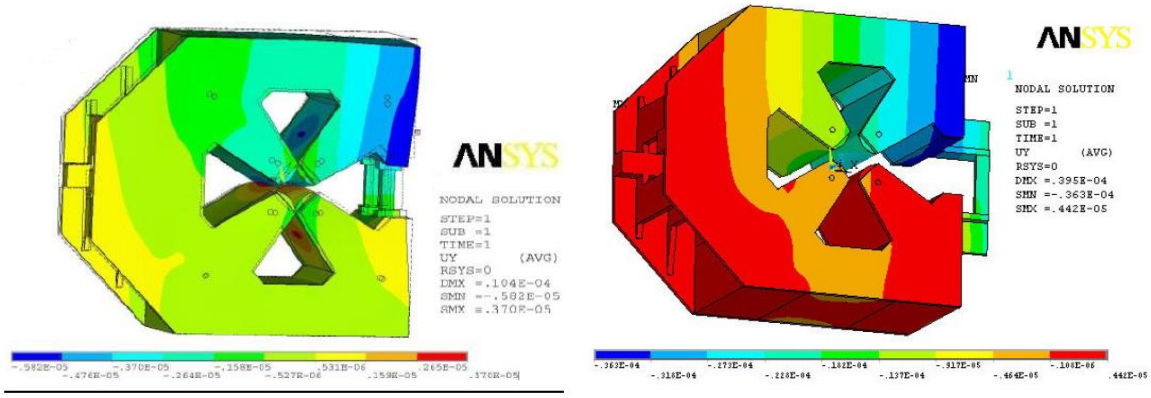

Figure 2. 20: Q3 Quadrupole (Left) and Q4 Quadrupole (Right) Vertical Displacement *(Sreeramulu et al., 2017)*

It was observed from the analysis that the Q4 magnet deformed more than the Q3 magnet. The displacement of the poles for the Q4 magnet in the vertical was found to be 0.04mm from the prototypes and was in agreement with the ANSYS analysis. The magnets were deemed to be of acceptable performance. The assembly was positioned together by dowelling. This idea of using dowel pins was also incorporated in the present work. Figure 2.21 shows the experimental set-up for determining the static deflection of the actual magnet. A similar concept of clamping support might be adopted for CLS 2.0 magnets in the event that open type magnet frames are made necessary.

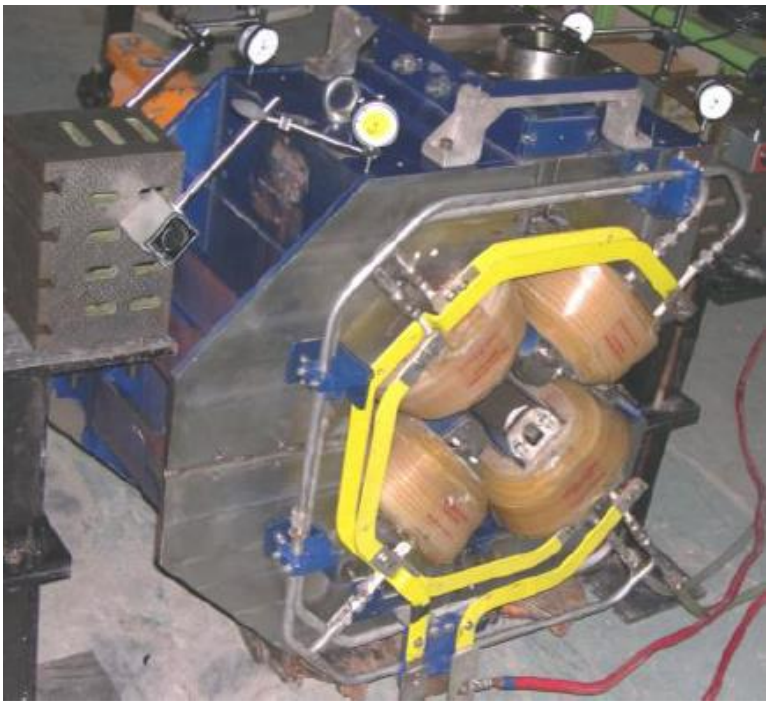

Figure 2. 21: Evaluating Displacement after Energizing with Dial Gauges

(Sreeramulu et al., 2017)

2.1.8 SLS-2

The Swiss Light Source facility aims to minimize the beam emittance by using a 7-bend achromat with 5 magnets in the middle of nominal length and 2 magnets at the ends of half length (Streun, 2017). Additionally, reverse bend combined function magnets combine a dipole field (0.4 T) with a quadrupole (30 T/m) part (Figure 2.22). These reverse bend magnets focus the beam horizontally and have a bore diameter of 24mm. This magnet was designed not have a return yoke just as the magnet in the present project in order to accommodate the ante-chamber. Moreover, asymmetric poles were designed as the beam is offset from the magnet centre. Similar to CLS 2.0 quadrupole, this magnet is water cooled with the largest increase in temperature of 10^{o} C. The effective length of the magnet was found to be 302 mm. Besides, chamfers were cut to reduce dodecapole components. The pole shape is hyperbolic and not optimized.

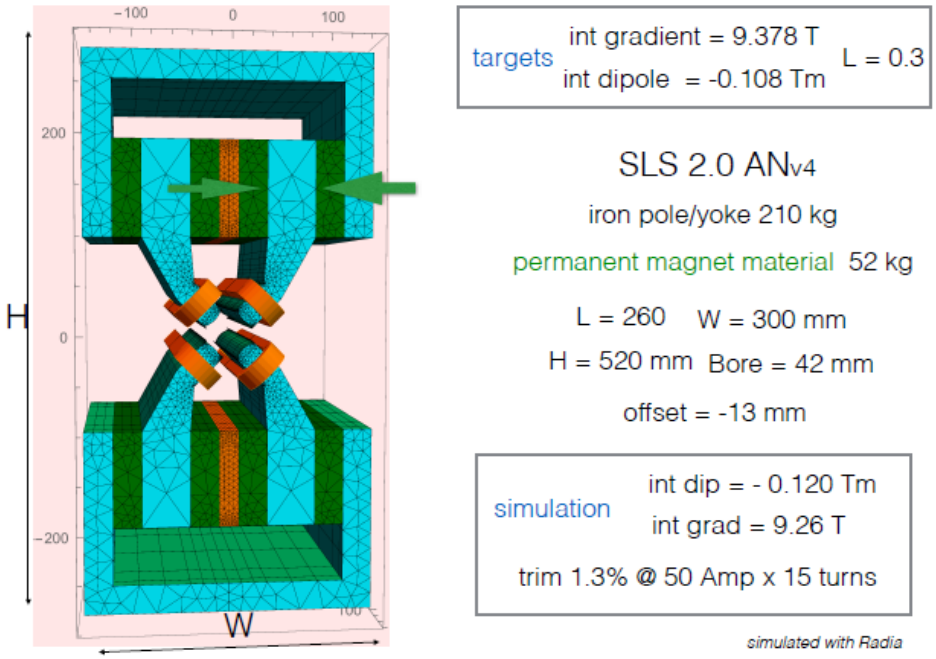

Figure 2. 22: Combined Function Reverse Bend Magnet (Streun, 2017)

INDUS -2 and ILSF quadrupoles are partially supported by mechanical structures and partially by the magnet itself. These two quadrupole designs are less unstable than the magnet in the present work. Hence, partial mechanical support will not work for the CLS 2.0 quadrupole. ALS-U Transverse Gradient Dipole, SIRIUS and MAX IV quadrupoles are instances where the support system is fused with the magnet. The magnet can be considered to be stable by itself. Thus, the function of the magnet is not only to generate the magnetic field but also hold the poles in a constant position over time. This design is a coupled design if the dimensions of the magnet and the excitation current are the two design parameters (Suh, 1990). According to Axiom Design Theory, coupled design do not satisfy the independence axiom. Conversely, ELETTRA 2.0 and the present CLS quadrupoles have a dedicated magnet frame for holding the yokes in position. This thesis had, therefore, adopted the standalone frame concept.

2.2 Magnet Support System

The purpose of a magnet support system is to secure the magnet as close as possible to its theoretical position in the lattice. In this section, the mechanical support that secures the magnet or other components of the synchrotron in position are reviewed. Most of the support systems reviewed here are girders. Besides, the girder design process can also be extended to the magnet frame design.

2.2.1 SLAC QC3 Magnet Support in FFTB

The quadrupoles QM1B and QC3 were installed on anocast steel blocks (Figure 2.23). Moreover, the anocast steel block is placed on a concrete block. As QC3 is a larger magnet, it requires more cooling so a long pier that extends 10 feet down into sandstone supports it. This is an attempt to attain more stable flooring as its location is prone to vibrations (Fenn et al., 2004). QM1B has comparatively more stable flooring as it is located further upstream in the Final Focus Test Beam (FFTB) tunnel.

Figure 2. 23: FFTB Tunnel QC3 Magnet Quadrupole Anocast Stand (Fenn et al., 2004)

Anocast is a granite epoxy which has a granite block look. Granite-epoxy composites were reported to have approximately three times higher logarithmic decrement values compared to grey

cast iron (Piratelli-Filho et al., 2010). Moreover, when necessary the anocast stand can be designed as a hybrid of girder and stand. In the FFTB tunnel, anocast stands can be seen to support both individual magnets and also a group of magnets while keeping up the same cross-section. Not only do these stands dampen vibrations more effectively than steel but they also reduce thermal expansion due to temperature variations owing to their thermal mass. Anocast stands and steel stands have a similar cost. An anocast support could possibly be used for supporting the magnet along with the frame. However, it seems impractical to make the frame out of anocast.

2.2.2 APS-U Support and Alignment Systems

As a part of the APS – Upgrade project the entire storage ring will be replaced with a MBA lattice. The nine magnet module of the APS-U is to be supported by five concrete plinths as shown below (Penicka, 2018). Additionally, pre-aligned and pre-assembled magnet units will be installed due to shortage of time. Furthermore, magnet alignment will depend on the machining tolerances of the mating parts supporting them (Figure 2.24).

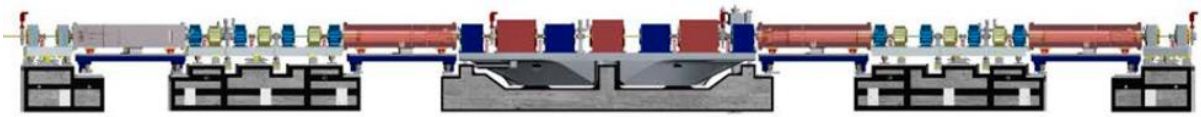

Figure 2. 24: APS-U Storage Ring Layout (Penicka, 2018)

Tolerances, as tight as 100 micron, are targeted to be achieved by adjustments in machining tolerances and mechanical design. Moreover, to ensure proper operation, vibration tolerance of 9 nm RMS will be met on the magnet-to magnet vertical motion by keeping the magnet modules' first mode frequency greater than 50 Hz (Collins et al., 2016). Furthermore, thick Steel plates are being used for supporting the magnets in the Demonstration Multiplet Module. Between the concrete plinths the L-Bend magnets are reinforced by bridges (Figure 2.25).

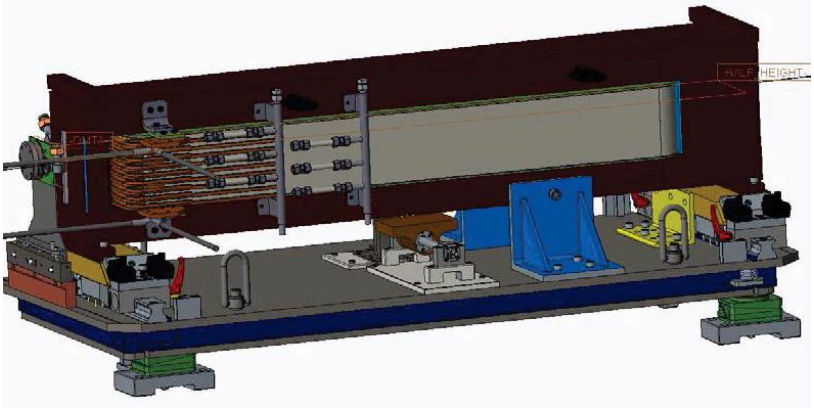

Figure 2. 25: L-Bend Module (Collins et al., 2016)

The vertical support is given by the wedge jacks which comprises of two wedges such that the two inclined planes are sliding over one another. Moreover, the present ALS storage ring girder support uses a turnbuckle-type horizontal adjustment and wedge jack adjuster combination (Figure 2.26). The vertical motion of the wedge jacks is generated when the upper wedge moves in the vertical direction by the virtue of a horizontal motion. The turnbuckle's end is fixed to a rail and can produce two-dimensional push and pull adjustments (Winic, 1994).

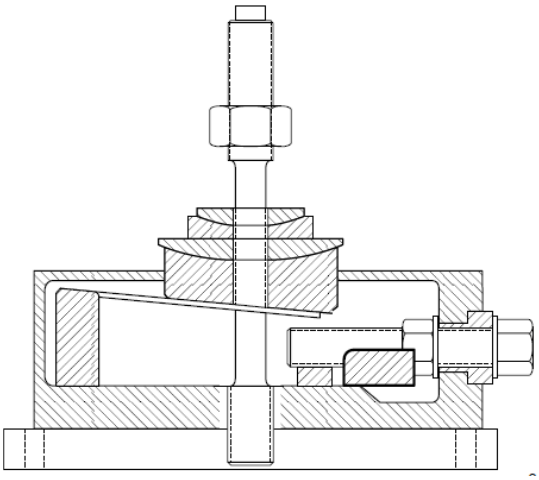

Figure 2. 26: ALS Wedge Jack Adjuster (Winic, 1994)

Furthermore, the wedge jacks in the ALS-U are made of slip plates and spherical bearings in order to disengage translation and rotation from vertical motion. Subsequently, alignment and constraint in the yaw and lateral and longitudinal direction are given by the two lateral pushers and the longitudinal pusher, respectively. Moreover, the girders bear the magnets which are in turn reinforced by concrete plinths using a three-point, semi-kinematic alignment system (Figure 2.27). Before grouting, the girders impart six degrees of freedom via three temporary outriggers, two of which are located on one of the sides of the concrete plinth and the one on the opposite side. Besides, the outriggers are removed once the grout is cured.

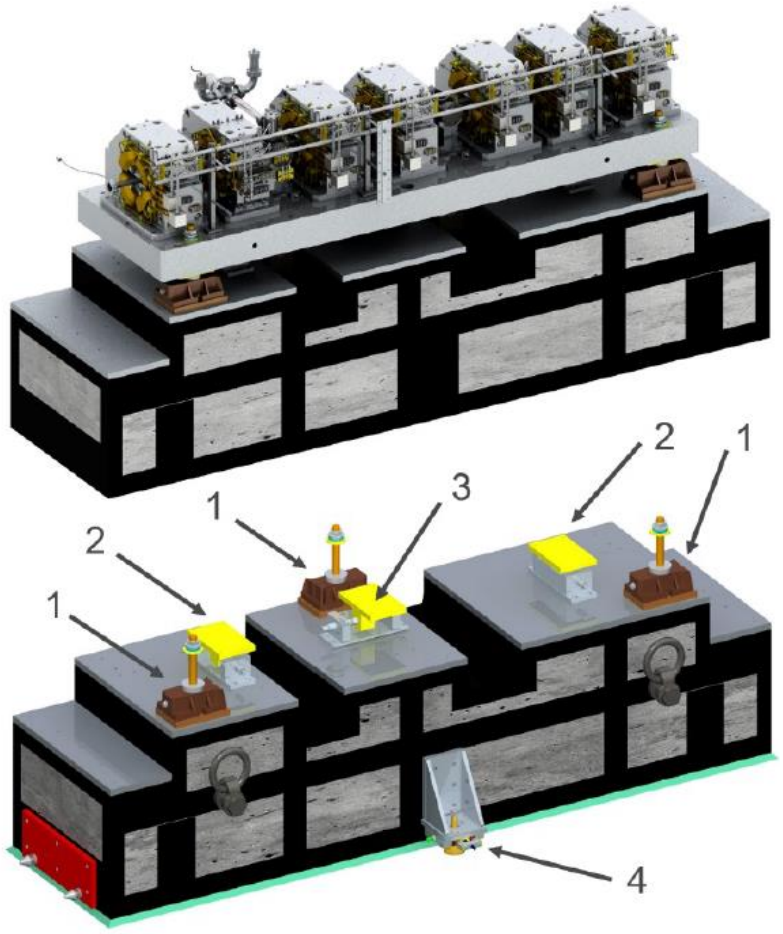

Figure 2. 27: Concrete Plinth Support (1) Wedge-Jack Support (2) Lateral Pushers

(3) Longitudinal Pusher (4) Support Outriggers

(Collins et al., 2016)

Analysis and comparison of many concrete and graphite plinths prototypes concluded with the selection of a hybrid steel and concrete structure plinth. In order to reduce the long term shrinkage issues, a concrete mixture with low- shrinkage and low- moisture, all plates and channels welded to large headed anchor studs, a continuous welded steel frame and steel reinforcing bar is proposed to be used. Consequently, distortion and shrinkage of the concrete plinths prototypes were monitored and shrinkage of less than 20 microns was recorded for the change prone first two months. The experimental setup for shrinkage surveillance is shown in Figure 2.28.

Figure 2. 28: Shrinkage Monitoring of Concrete Plinth Support (Collins et al., 2016)

Concrete plinth supports are also a feasible option to be explored to replace girders. However, the magnet frame itself can not be manufactured from concrete as it may give rise to disassembly problems, and, thus, hindering maintenance.

Over-predictions may result if the full magnet support structure CAD model is used for the vibration or the modal response analysis. The modal analysis of the only magnet assembly and the girders CAD model was performed and rational results were obtained. However, when the modal analysis is performed on the complete magnet support structure i.e. including the magnet support and alignment mechanism (as shown in the Figure 2.29) then an over-prediction of about 100% was observed on the natural frequency (Preissner et al., 2016). In fact, more inaccurate results were observed when a random vibration analysis was performed on the whole test article.

Figure 2. 29: Magnet Support Structure Test Article (Preissner et al., 2016)

It was concluded that these errors are caused as the random vibration and modal response of the system heavily relies on the support mechanism stiffness and damping. However, the overestimation of the system stiffness can also be a result of not accounting for interfaces, loads and friction. Furthermore, the modal analysis results can be tuned and matched with the experiment in a post hoc way by changing the support structure elastic modulus. Nevertheless, it is hard to establish the material damping and modulus changes because of load and direction. As this technique is post hoc in nature, it is hard to use this method in other designs. The magnets support system can be generalized and described by Figure 2.30.

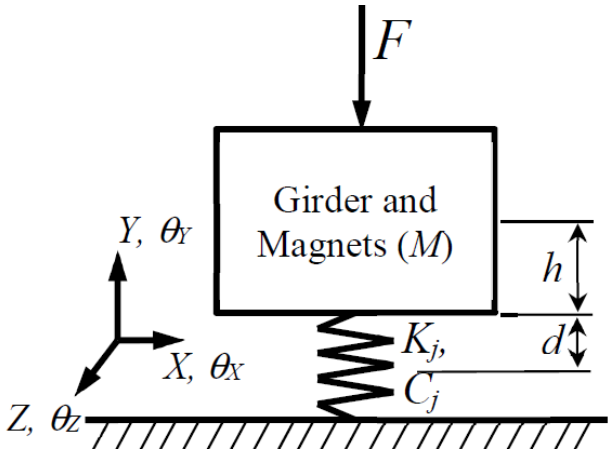

Figure 2.30: Magnet Support System Schematic (Preissner et al., 2016)

In Figure 2.30, K_J is the stiffness, C_J is the damping of the magnet support alignment mechanism, applied forces are represented by F, 'h' is the center of mass and 'd' is the half-height of the support. Assuming no coupling effect, the stiffness matrix would be:

$$K = \begin{bmatrix} K_{XX} & 0 & 0 & 0 & 0 & (h+d)K_{XX} \\ 0 & K_{YY} & 0 & 0 & 0 & 0 \\ 0 & 0 & K_{ZZ} & -(h+d)K_{ZZ} & 0 & 0 \\ 0 & 0 & -(h+d)K_{ZZ} & K_{\theta X} + (h+d)^2 K_{ZZ} & 0 & 0 \\ 0 & 0 & 0 & 0 & K_{\theta y} & 0 \\ (h+d)K_{XX} & 0 & 0 & 0 & 0 & K_{\theta Z} + (h+d)^2 \end{bmatrix} \quad (2.2)$$

Three ways of calculating the stiffness and the damping described by Preissner (2016) are - Finite element modeling, static and dynamic testing. Moreover, the support structure stiffness can be approximated by FE Model Virtual Single-Axis Testing. The model was assembled by defining all the interfaces. A MAX IV support post is shown in Figure 2.31.

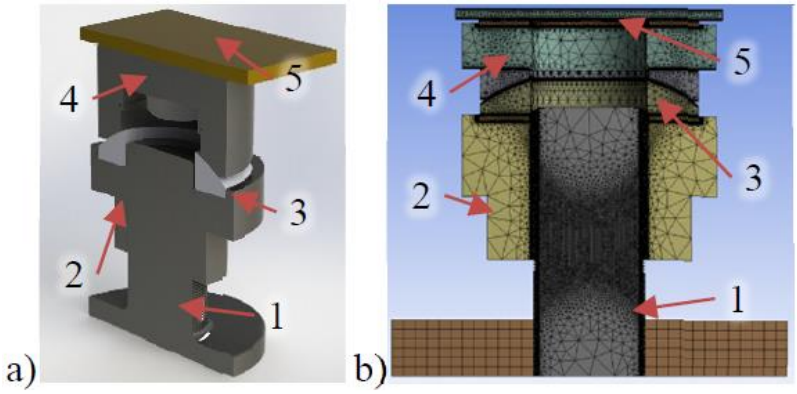

Figure 2.31: MAX IV Support Post (a) Sectional View (b) FE Model (1-Support System Post, 2-Alignment Adjusting Nut, 3-Sperical Washer, 4- Support Spacer, and 5- Support Sliding Plate) (Preissner et al., 2016)

Furthermore, a force equal to the weight of the magnet was applied to the support system in the vertical direction to calculate the directional stiffness. It was concluded that when the interfaces are not defined the stiffness is overestimated. Consequently, when the interfaces are defined and the friction is taken into consideration the stiffness changes. The system stiffness was found to be inversely proportional to the number of interfaces. Moreover, the static testing stiffness data when used in the FE Model dynamics did not match the experiment. However, when the data from the dynamic testing was using in the FE Modelling modal analysis the results matched the experiment. The CAD model can catch the mass and inertia properties of the magnet but not the support and alignment mechanisms as they show non-linear damping and stiffness because of their interfaces (Preissner et al., 2018). Subsequently, the modal response and vibration response of these CAD models are over-predicted and under-predicted, respectively, because their behavior changes with the change in load which is not captured by the CAD model. In order to account for the non-linearity of these mechanisms, discrete stiffnesses are incorporated in the Finite Element model. Additionally, girder and plinth prototypes of the FODO module underwent Experimental Modal Analysis (EMA) and the results proved that the material properties and the geometry assumptions were accurate. Thus, if the EMA and the FE results match then the random vibration response, static and thermal deflection will be precise when the measured damping values are integrated.

For natural frequency and system stiffness analysis of compliant mechanisms, Huang et al. (2012) developed a modeling technique via the use of ANSYS. ANSYS uses many solvers to evaluate the systems' natural frequency. Huang et al (2012) used the block Lanczos method which uses the global stiffness analysis in order to consider for the stiffness of materials and actuators as well.

2.2.3 Elettra 2.0 Magnet Positioning and Support

The design requirements for the support systems for the new Elettra were high stiffness, insensitive to vibrations, nonmagnetic and one common structure that can carry all the magnets and other sub-components (Elettra, 2017). Additionally, the frame will be designed to have two parts such that all the magnets open at the same time so as to allow maintenance, bake-out and easy installation of the vacuum chamber. Moreover, the top part of the support is designed to be lifted by a crane. Similar to the present work, to ensure high repositioning accuracy, dowel pins will be used. Furthermore, the designed supports are confirmed to fit the old girders and the components of the magnet are planned to be assembled beforehand installation. Also, the possibility of using dynamic positioning and alignment system is being studied. Figure 2.32 illustrates the new girder design.

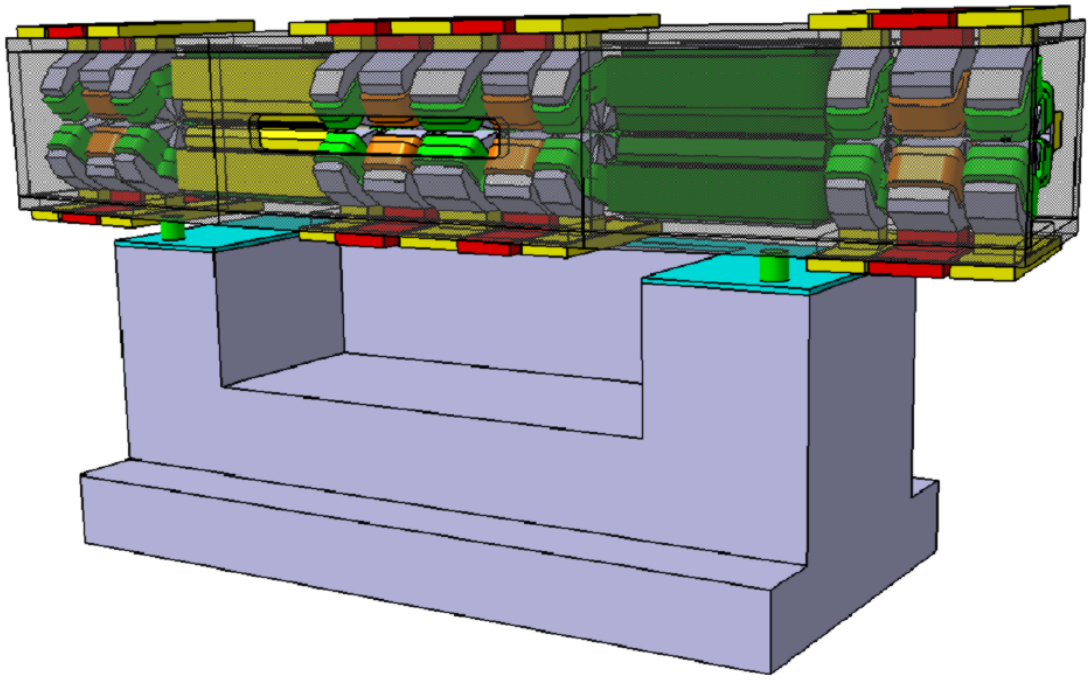

Figure 2.32: Elettra 2.0 Girder Design (Elettra, 2017)

Grouted pillars will be used to bear the light exit chambers and undulators to illuminate the possibility of vibration transmission to magnets. Subsequently, a modal analysis was performed to study the dynamic characteristics of the structure (Figure 2.33). Moreover, the steel plate girder consisting of the adjustment systems is anchored to the concrete pedestals.

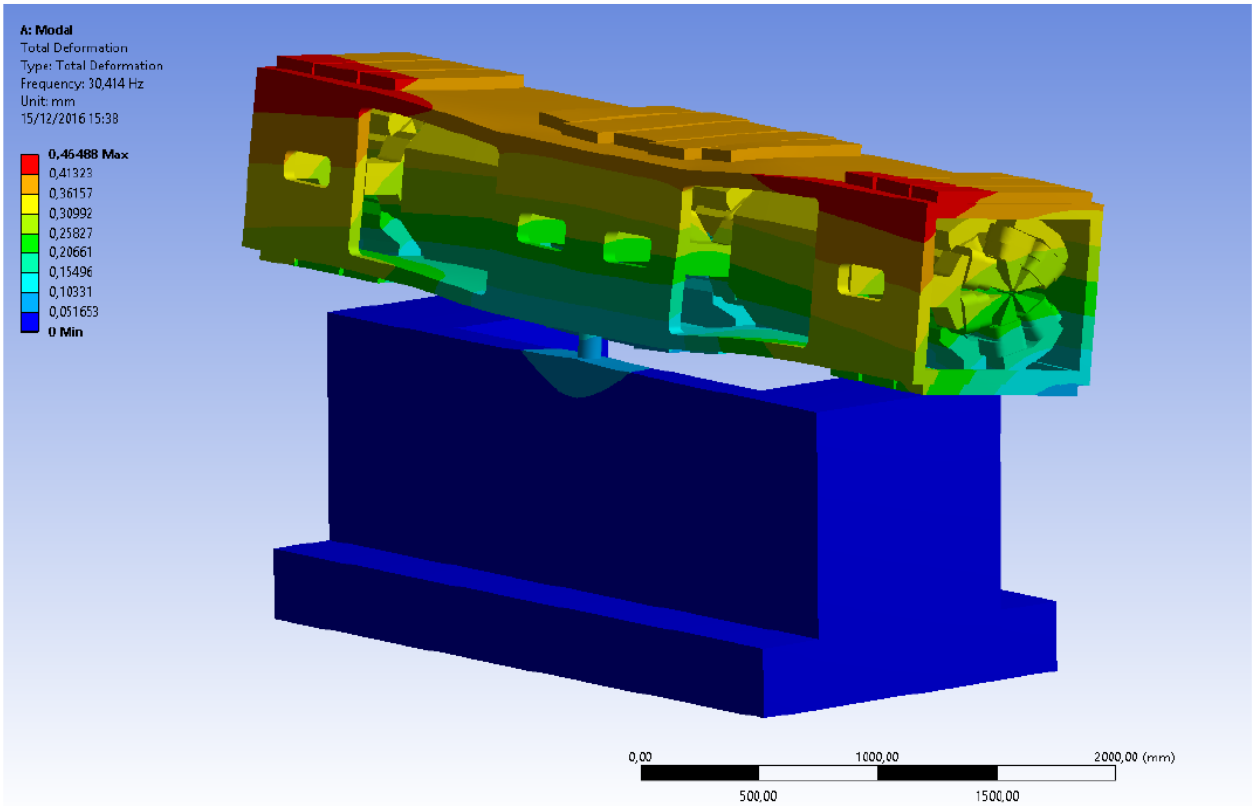

Figure 2.33: Elettra 2.0 Girder First natural Frequency (Elettra, 2017)

The above analysis uses a model with only three supporting points to the base and an increase in the number of support points could possibly increase the natural frequency was concluded. Furthermore, the use of damping pads is being studied so that vibration amplification can be prevented.

All these studies suggest that using FEA is a cost-effective and efficient way of studying the dynamic and static behavior of any mechanical structure. Hence, FEA has been extensively used in this project.

2.3 Optimization

Multi-Criteria Decision-Making is a technique that evaluates conflicting criteria subjected to predetermined constraints. Multi-Criteria Decision Making can be subdivided into two types: Multi-Objective Decision-Making (MODM) and Multi-Attribute Decision-Making (MADM). Multi-Objective Decision-Making is used when the number of solutions is infinite while Multi-Attribute Decision Making deals with a finite number of alternatives (Goswami et al., 2014). As MADM deals with criterions which are non-commensurable, i.e. their criterions have different units of measurement, hence, the process considers the normalization method. Furthermore, in MADM, the criterions are implicit in nature, i.e. no mathematical relations between two criterions. Consequently, MADM is used in situations which involve selection or evaluation whereas MODM is used to control a parameter in the design problem. In the current work, both Multi-Objective Decision-Making and Multi-Attribute Decision-Making Problems have been encountered. A nonmagnetic material with a high elastic modulus has to be selected within an acceptable cost. As the materials pool is finite, this can be termed as a Multi-Attribute Decision-Making Problem. An optimum thickness has to be selected such that the resultant deflection is of the order of microns. This is a Multi-Objective Decision-Making Problem as the number of thicknesses to be chosen from is infinite.

2.3.1 Material Selection

- *Analytical Hierarchy Process (APH):* APH is used when information about the alternatives, the constraints and criteria rank are well known (Saaty, 1980). The four stages of a decision making problem are information collection, information quantification, modelling and optimization. Furthermore, the information collection stage involves identifying the criteria, sub-criteria and alternative hierarchy. Then, the normalization is done by diving each element by the column sum and calculating the overall row average in order to determine the priority ranking. The decision matrix is formed by putting the weights of the different criteria. Moreover, the priority vector from the decision matrix can

be used to obtain the Eigenvector. The consistency ratio can be found out from the Eigenvector. The alternatives are then ranked according to the global priority vector which can be found from the product of weights of the sub-criterions and criterions. Finally, the decision is made according to the benefit percentage which is analogous to the global priority vector.

- *Technique for Order Preference by Similarity to Ideal Solution (TOPSIS):* TOPSIS developed by Ching-Lai Hwang and Yoon, involves the selection of the alternative whose geometric distance is maximum from the negative ideal solution (NIS) and the minimum from the positive ideal solution (PIS) (Assari et al., 2012). The weight of each criterion is recognized and compared with other alternatives using the compensatory aggregation method. Moreover, for each criterion, the normalized and the geometric distance between every alternative and the ideal alternative is calculated. Finally, the worst condition similarity is calculated and the alternatives are ranked.

Simple Additive Weighting method (SAW) is also another method of solving Multi-Attribute Decision-Making. However, out of the three above mentioned techniques, ADH has been extensively used for material selection in literature. Hence, ADH was the chosen method to solve the MADM problem at hand.

Material defects can cause product failure. At the conceptual design phase, material selection has to be done such that it meets the desired product performance at the lowest cost. As a large number of criteria affect material selection, it is a fast growing MCDM problem. Expert Choice™ software was used to perform AHP to select a suitable material for a product (Dweiri et al., 2006). As the consistency of the decision maker is checked, the confidence in the result is high. To grow the confidence in the result, a sensitivity analysis was also conducted. Moreover, the decision maker perceives the problem better as the problem is broken down into smaller sections by the hierarchy framework. Consequently, the alternative pair-wise comparison lowers the designer's inconsistencies. Materials are selected by inflating one or more 'performance indices' which are controlled by design objectives (Ashby et al., 1997). Furthermore, engineers select materials from catalogues and data books however in order to ensure maximum productivity at the lowest cost identification of a strategic method to select the best material. Thus, using APH gives the decision maker the confident judgment by performing the sensitivity analysis.

Moreover, the conventional chart method or the cost-based approach are ineffective because they can only take into account two or three criteria only (Jahan et al., 2010). Jahan et al also proved that incorporating MCDM for selecting material greatly enhances the decision.

Furthermore, Analytic Hierarchy Process was used to select a material for screw production that caused minimum environmental impact while having maximum performance (Kiong, 2013). The screw material and the manufacturing process are the parameters considered. The two manufacturing techniques taken into consideration are forging and machining. Aluminium alloy, stainless steel, cast iron, titanium alloy and low carbon steel are the materials under evaluation. Carbon footprint, air acidification, water eutrophication and energy consumption are the environmental impacts that were taken into account. SolidWorks life cycle assessment (LCA) was used to generate the environmental impact data. The AHP matrices for pair-wise comparison was generated from the sustainability tool. Finally, the screw material for chosen production process was selected based on the ranks generated from the global priorities. The least environmental impact was observed in aluminum when forged and cast iron when casting. On the other hand, Titanium was reported to have the highest impacts on the environment.

The above mentioned studies suggest that using APH for material selection is an efficient way to select an optimal material. Thus, the APH technique has been chosen to select a cost-effective material which has a high Young's modulus.

2.3.2 Optimizing Dimensions

To manage the increasing complexity in manufacturing systems, scientists are researching new design solutions to tackle this complexity. Moreover, many algorithms have been developed to tackle Multi-Objective Optimization problems. In the present project, the Deflection Vs Thickness trade-off can be looked at as a Multi-Objective Optimization problem as the number of solutions can be infinite. This problem can be solved by: non-dominated sorting genetic algorithm (NSGA-II) (Deb, 2009), Pareto Archived Evolution Strategy (PAES) (Knowles et al., 1999) and Strength Pareto Evolutionary Algorithm (SPEA) (Zitzler et al., 1998). NSGA-II is an evolutionary algorithm which will be used to solve this Multi-Objective Optimization problem. The flowchart of the NSGA-II algorithm is included in Figure 2.34. Exploring the use of other optimization techniques is out of scope of this work.

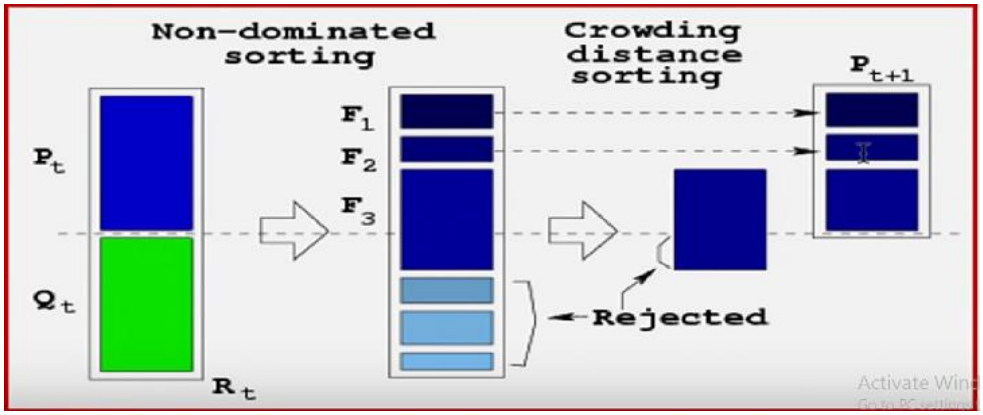

Figure 2.34: NSGA-II Algorithm Flowchart (Deb, 2009)

Elitist Non-dominated Sorting Genetic Algorithm (NSGA-II) can be used to solve the multi-objective optimization problem. It differs from other algorithms as it uses the elitist solution in the iteration that follows. The above flowchart shows one iteration of the NSGA-II algorithm. P_t is the current population from which P_{t+1} is to be determined. An offspring population of the same size as P_t is generated using genetic algorithm techniques (selection, crossover and mutation). R_t is the collective population of P_t and Q_t which is two times the original population. This is followed by non-dominating sorting of the population based on the superiority of fronts. F_1 is the best front and may contain elements from both P_t and Q_t. F2 is the second level of non-domination elements. The P_{t+1} population ca not exceed the parent population and hence some elements from the F3 front have to be rejected. This rejection is based on the crowding distance of the elements. The crowding distance is an estimate of density solution surrounding a particular solution.

Moreover, the non-domination sorting does not have to be done for the entire R_t population but only for a few fronts. As the number of iterations increases the F_1 front becomes very large. Eventually, the fronts converge and an optimum solution can be found out based on information content.

NSGA-II was successfully used to optimally schedule patients to hospitals such that the waiting time and transportation distance is minimum (Dai, 2015). The NSGA-II algorithm computed the optimal solution within a reasonable time and its validity was demonstrated.

Deb et al. dimensionally optimized a cantilever beam under two different loading conditions with the aim to reduce stored strain energy and weight (Deb et al., 2015). This problem is quite similar to the thickness optimization problem encountered in the present work. The cantilever is subjected to two loads: end load (F) and torque (T) as shown in Figure 2.35.

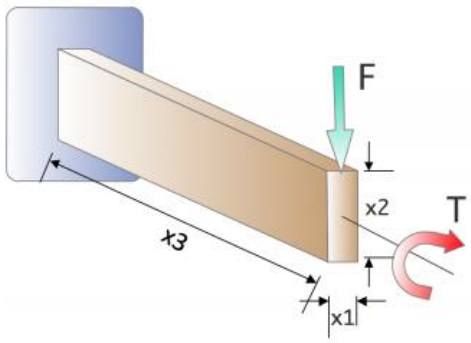

Figure 2.35: Cantilever to be Optimized (Deb et al., 2015)

A bending stress will be induced by the end force F and the beam end will experience shear stress resulting from the torque T. Using NSGA-II, it was concluded that both the two load cases were not too predominant over one another and the optimized solution does not change drastically with the two different scenarios. The optimized solutions had one common property, i.e., x_3 is equal to its lower bound. However, the x_1-x_2 combinations converge at different for different trials. The NSGA-II algorithm could successfully identify the compromised optimal solutions for both the loading cases.

The above studies prove that optimization algorithms are an effective way of calculating an optimal dimension. Hence, an NSGA-II based algorithm will be used to evaluate an optimal thickness.

2.3.3 Topology Optimization

Structural optimization design aims to reduce material usage, cost, while improving the product quality. Topology optimization evaluates the best distribution of material while meeting the design constraints. Furthermore, there are two basic types of topology optimization: rod type and

continuous body structure. In rod-type structure topology optimization, unneeded bar elements are excluded from the matrix structure and the residual bars form the optimized structure (Li et al., 2008). However, continuous body bases the optimization on boundary conditions, loading, calculates non-entity location and number in order to meet the target function and constraints. Moreover, homogenization and Variable Density methods are the most popular techniques used for Continuum topology optimization. A fixed grid finite element was used to design a small cell structure and Bendsoe & Kikuchi used homogenization to calculate the effective material properties. Nevertheless, the homogenization method is only limited to theoretical structural optimization because of its disadvantages. On the contrary, the density method assigns an imaginary material whose relative density varies from 0 to 1. Evolutionary Structural Optimization eliminates all the unnecessary elements and leaves behind the optimized structure. An equal strength based optimization technique is used by ANSYS. ANSYS aims to evaluate the best distribution of material while maintaining the highest possible stiffness. A variable density method is used by ANSYS to perform the topology optimization.

$$E_i(x) = \eta(x)\, q\, E_0 \qquad q \geq 1,\ 0 \leq \eta(x) 1.0 \tag{2.3}$$

$$\int_\Omega \eta(x)\, d\Omega \leq V \tag{2.4}$$

where E_0 is the selected material Young's modulus, E_i material Young's modulus, Ω is the continuum, V is the volume of the continuum, $\eta(x)$ is a variable that is continuous and q is the factor of punitivity.

Further, the topology optimization module of ANSYS Workbench aims to achieve the minimum structural deformation energy by using design variables (η_i) in order to assign every element of the FE model an internal pseudo-density.

Using topology optimization (TO) in magnet support structures is a recent trend. This section deals with topology optimization of magnet support systems for the APS-U and PETRA IV.

FODO is the longest section of the APS-U storage ring consisting of four quadrupoles, three transverse gradient dipole magnets and a wiggler. Furthermore, a single structure supports all the magnets in the FODO module to control alignment tolerances. And a three-point semi-kinematic

mount supports the girder on a concrete plinth. The location of the three-point semi-kinematic vertical mount was optimized to reduce strain energy. Owing to its high vibration damping properties, design versatility and low cost, cast iron was chosen the girder material. Moreover, the model to be optimized had a plate thickness of 160 mm and the three support points are located one along the centre on one side and the other two were symmetrically toward two ends on the other side. The supports were of 200 mm length and a diameter of 100mm. And the supports were positioned at a span of 4 m for the initial study. Figure 2.36 shows the results of the Static Structural Analysis.

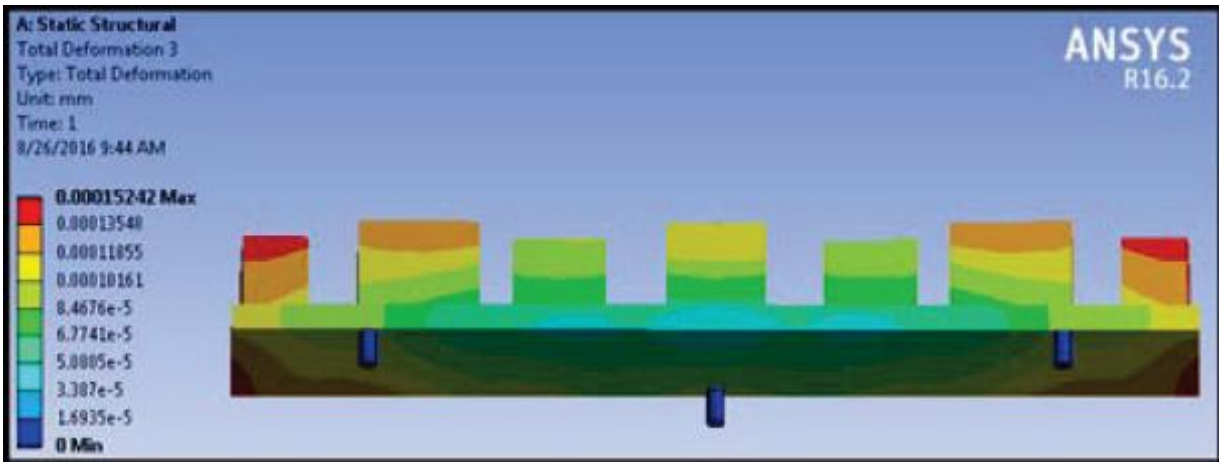

Figure 2.36: Un-optimized FODO Girder (Liu et al., 2016)

From the initial static structural analysis, it was concluded that the horizontal displacements had a high contribution to the total deformation of the system. Also, the span length was chosen to be the design parameter for the optimization. Thereafter, the minimum displacement was observed at span lengths of 4 or 2.6 meters. Additionally, Genesis Topology for ANSYS Mechanical (GTAM) was used to study the use of cast ductile iron as girder material with an objective to minimize the

static deflection and maximize the fundamental frequency of the girder structure (Liu et al., 2016). The first topology optimization results are shown in Figure 2.37.

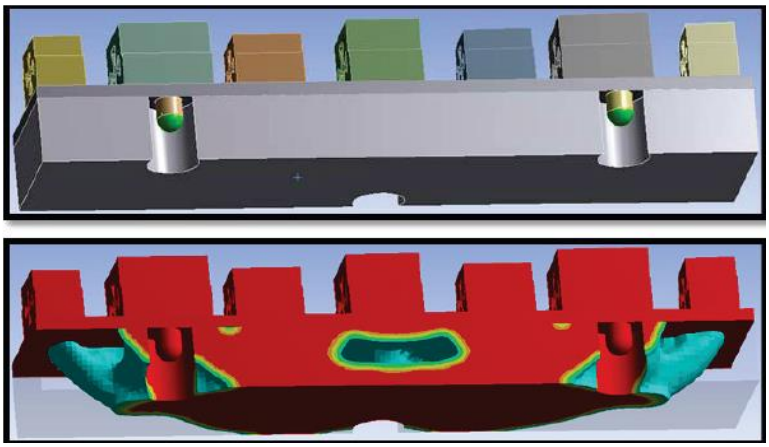

Figure 2.37: 1st FODO Support Topology Optimization (Liu et al., 2016)

Further, a parametric study was performed on the top plate thickness varying it from 20 mm to 100 mm, a bottom plate from 0 mm to 800mm (Figure 2.38). The support pan length of 3.5 m was chosen. From the parametric study, it was inferred that the plate thickness of 50 mm and the girder thickness of 850 mm corresponds to the highest first mode frequency of the system.

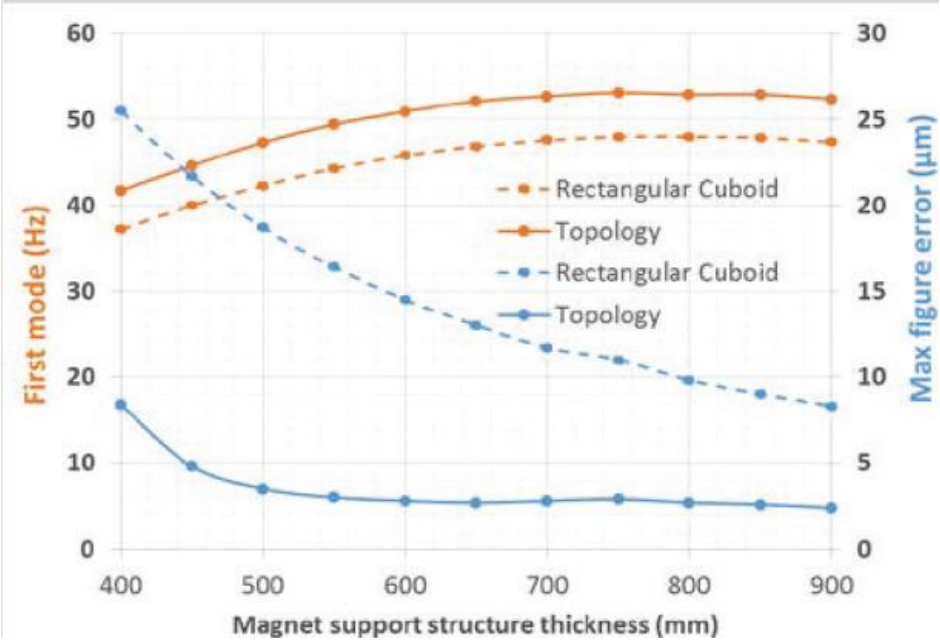

Figure 2.38: Girder Thickness VS First Mode Frequency and Max Error Figure *(Liu et al., 2016)*

The second order topology optimization yielded a top girder thickness of 150 mm and a vertical support span of 3 m (Figure 2.40). Subsequently, A536, GR-60/40/18, ductile cast iron was chosen as the girder material. Moreover, Airloc 414-KSKC wedge jacks were used as the three-point semi-kinematic mount. The first mode frequency of 39 Hz was calculated for the design. If the prototype does not fulfil the design requirements, the design will be further optimized. Consequently, the selected geometry was modified based on the foundry inputs so that the optimized design could be changed to a manufactural casting design (Figure 2.39). Figure 2.41 shows the assembled FODO module.

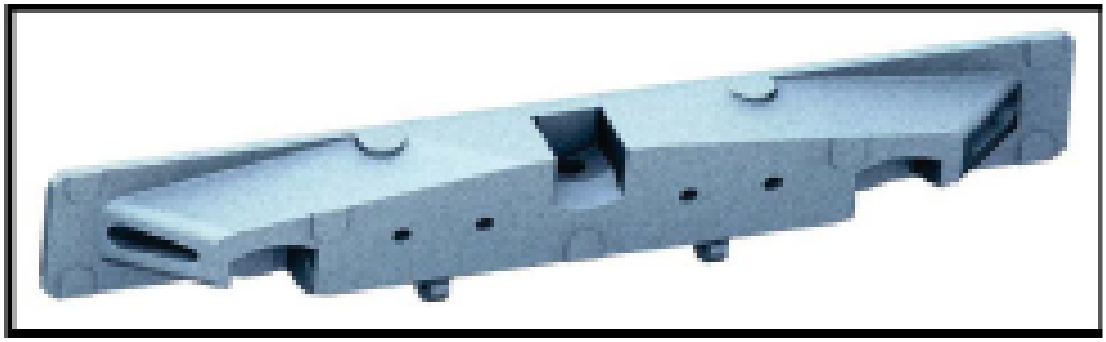

Figure 2.39: Foundry Manufactural Geometry (Liu et al., 2016)

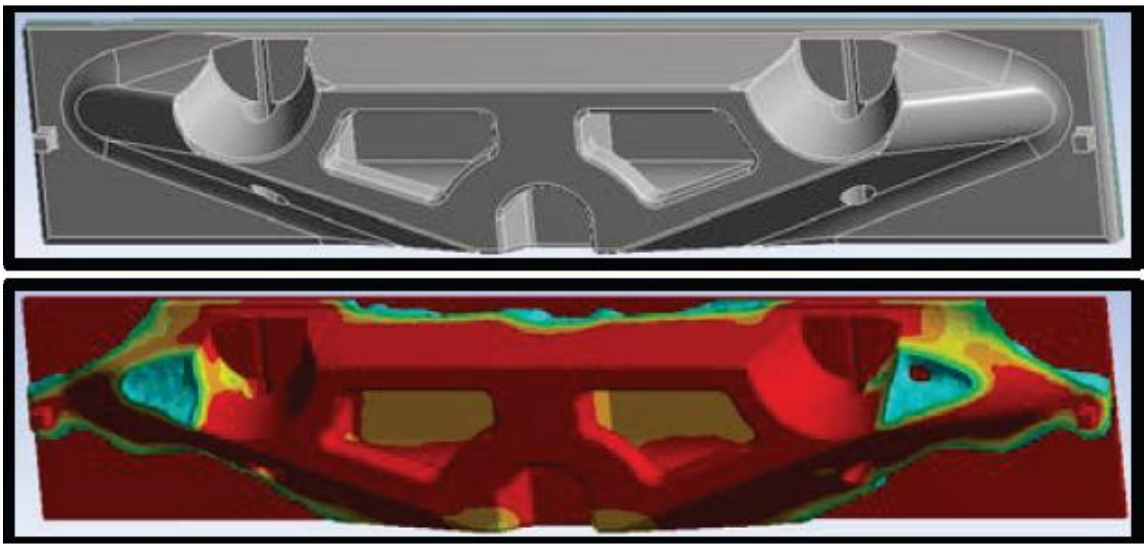

Figure 2.40: 2nd Topology Optimization (Liu et al., 2016)

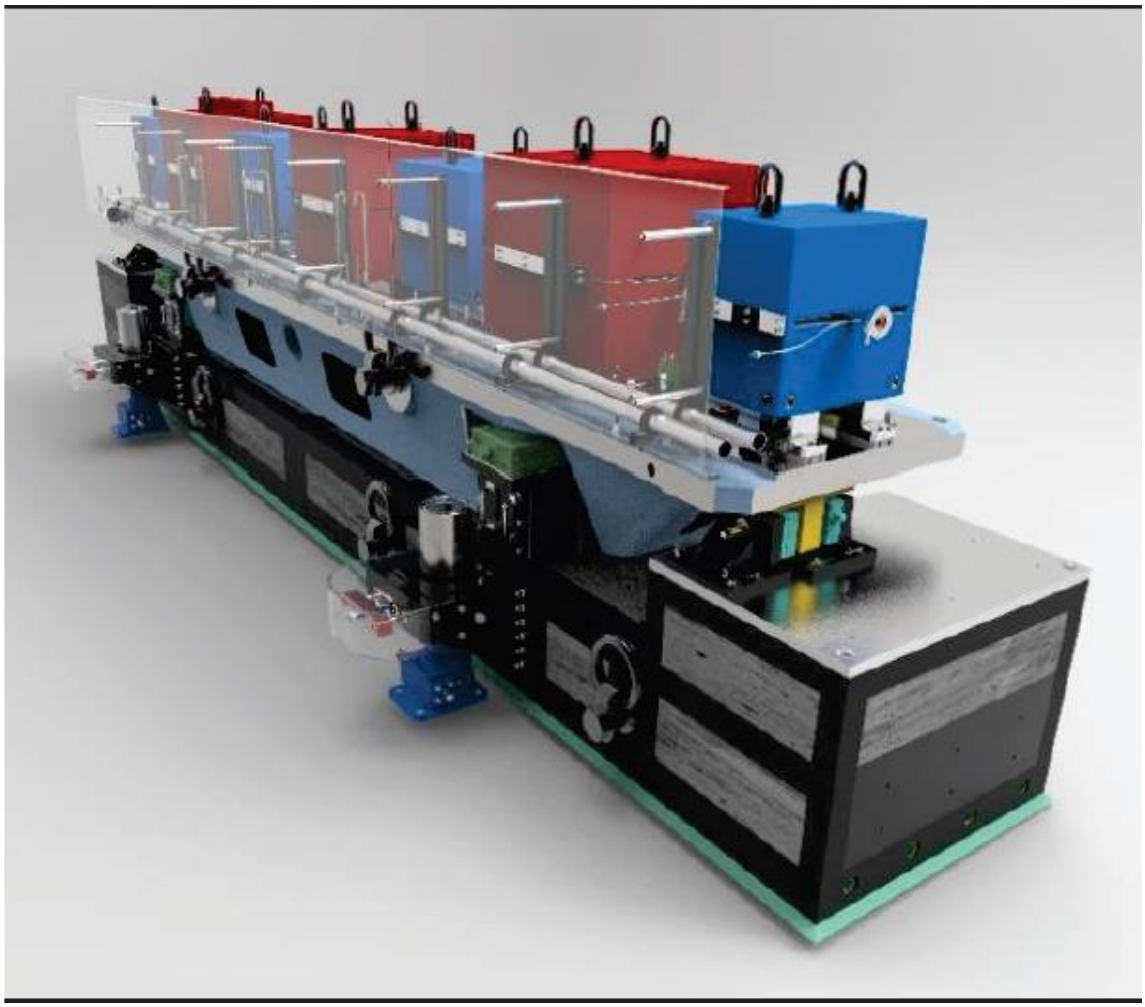

Figure 2.41: Assembled FODO Prototype (Liu et al., 2016)

The lateral and vertical support components underwent dynamic stiffness testing to evaluate the FODO module modal response more precisely. Additionally, rigid body modes were determined experimentally and the system dynamic equations were used to calculate the stiffness matrix and the coefficient of damping. Then, ANSYS modal analysis made use of this stiffness matrix to determine the first mode was at 38.8 Hz (Figure 2.42). When the modal analyses included the floor compliance, the first mode was observed at 35.4 Hz (Nudell et al., 2017).

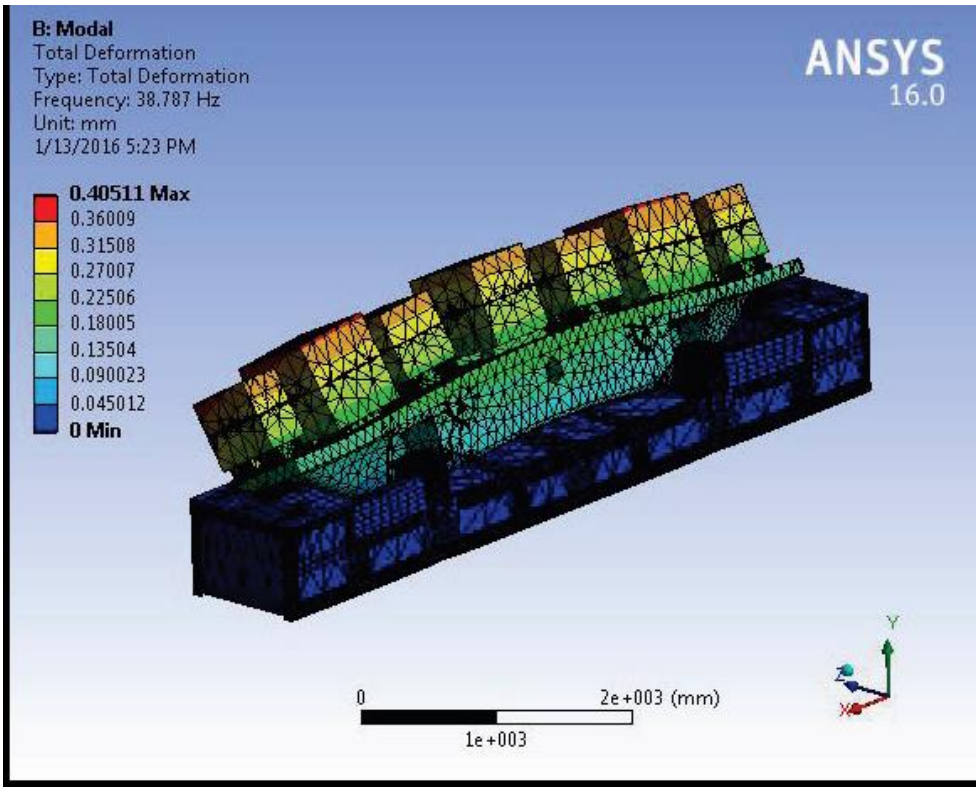

Figure 2.42: FODO First mode (Nudell et al., 2017)

ANSYS random vibration analysis was performed by taking the floor motion data over the frequency range of 1-100 Hz and the damping set to 2%. From this analysis, it was concluded that low-frequency vibrations are not amplified by the system dynamics. Moreover, the fluctuation in the temperature of the storage ring was taken into consideration while calculating the deformation. Consequently, the temperature fluctuation induced misalignment was well within the tolerances.

It can be concluded that modal and random vibration analysis are proven techniques for checking the dynamic behavior of any mechanical structure. In the present work, similar analyses will be used to test the dynamics of the magnet frame.

Bio-inspired PETRA IV girder

Biological shell structures are observed to be light in weight, possess high structural stiffness and high resistivity to vibrations. Accordingly, the PETRA IV girders were systematically designed to

mimic biological structures. Subsequently, a maximum girder mass of 2500 kg, a maximum linear static deflection of 0.5mm and the first mode of natural frequency of 52Hz were set as the optimization goals (Andresen, 2018). The initial topology of the PETRA III which is a steel hollow cuboid was considered for optimization. For the parametric study, 3 point masses representing 3 magnets and shell elements were used, the number of support and their locations were the design parameters. The number of supports was varied from 3 to 6 with their locations at upper girder edges and lower girder surface while considering the constraint: $X=Y=Z=R_x=R_y=R_z=0$. Consequently, the optimal number of support points came out to be six located at upper girder edges near the magnets. Furthermore, Grasshopper's Rhinoceros and Altair's Solver OptiStruct were used to perform this parametric study to evaluate the optimal girder support points (Figure 2.43).

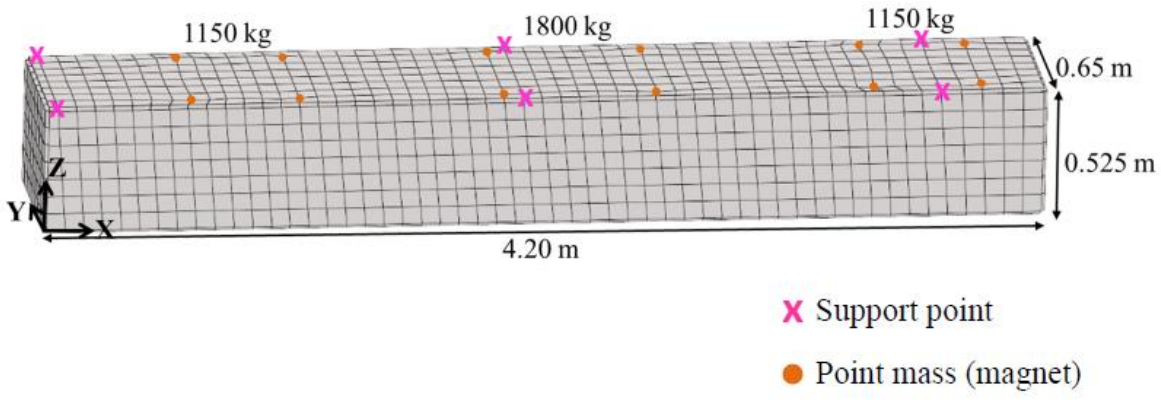

Figure 2.43: Optimized Girder Support Points (Andresen, 2018)

After the support points were evaluated, the girder underwent topology optimization with the constraints that the natural frequency of the structure will be more than 100Hz and only 10 % of design space volume will be retained. Further, Altair's HyperWorks was used to perform this topology optimization. Moreover, the locations where the magnets were supposed to be placed were assigned as non-design space and the rest of the structure was considered for optimization, i.e., design space.

After the topology optimization, the first natural mode frequency was observed at 91Hz with a total mass of 863 kg and maximum static deflection of 0.03 mm. The optimized geometry with element density greater than 0.3 is shown in Figure 2.44.

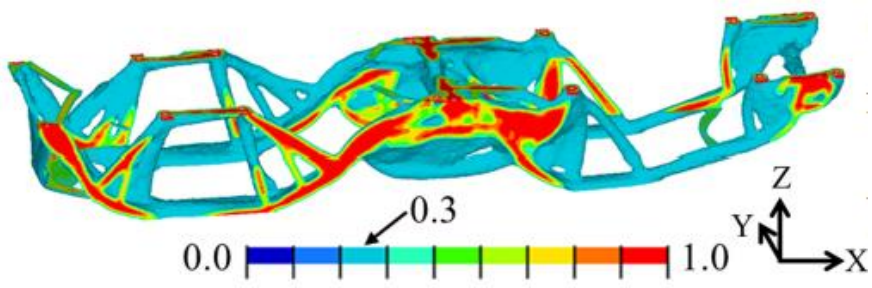

Figure 2.44: Topology Optimized Girder Structure (Andresen, 2018)

The optimized topology thus obtained was smoothened and a more manufacturable structure was obtained. Furthermore, curves were derived and projected on girder walls which formed ribs. The rib thicknesses were also parametrically studied and the following bionic structure was obtained (Figure 2.45).

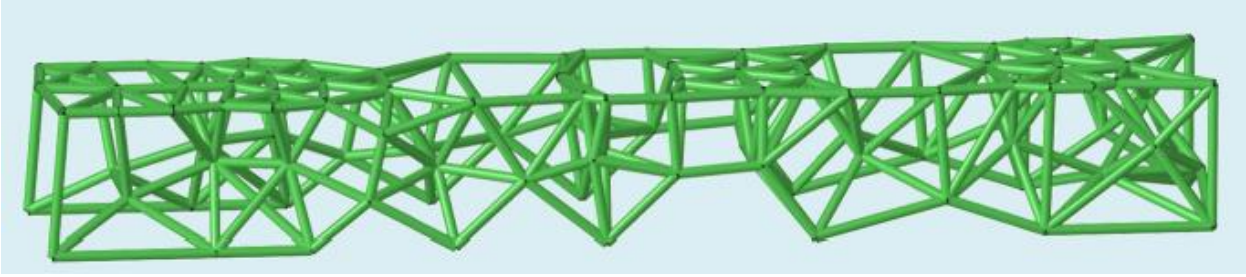

Figure 2.45: Manufacturable Optimized Girder Structure (Andresen, 2018)

Keeping the materials properties, boundary and loading conditions same, a parametric study of the lattice parameters was performed to create various structures. Moreover, the neighboring points were joined to develop lattice structures influenced by attractors. It was found that at a constant mass and/or stiffness the first mode natural frequency can be increased by using bionic lattice structures. Consequently, an optimized girder structure of 2489 kg mass, 70 Hz first mode of natural frequency and a maximum linear static deflection of 0.02 was achieved (Figure 2.46).

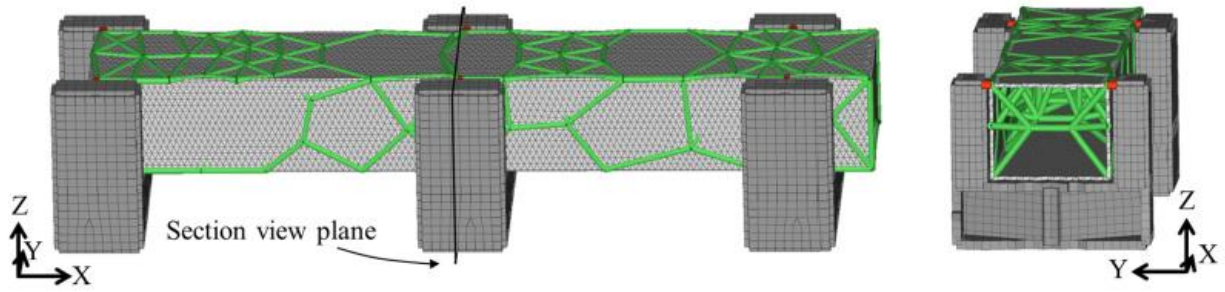

Figure 2.46: Optimized Bio-inspired Girder (Andresen, 2018)

Thus, it is evident that topology optimization is a proven technique to maximize natural frequency and minimize static deflection. Topology optimization will be used in the present work for attaining similar goals.

2.3.4 Optimization Methodology

The popular optimization techniques are described in this section. All of them aim to obtain an optimized design by concurrent design approach. In concurrent design, all the design parameters that fulfils all the design requirements are calculated in a single step.

A niching genetic algorithm has been used to explore the large design space as a result of concurrent and integrated design approach and to optimize the mechatronic design quotient (MDQ) by Behbahani and de Silva (2014). This method was demonstrated on Iron Butcher, a machine that cuts fish, a multi-domain electromechanical system. The optimized design

methodology provides a concurrent, integrated and system-based point of view for designing mechatronic systems. Two steps were involved in the optimization technique. First, a niching genetic algorithm which ensured the elites configurations are presented in the final competition was incorporated. Then, restricted competition selection (RCS) was used so that all the configurations can be available for the final competition while preserving each subpopulation's best solution. By combining several design characteristics, along with intuitive aggregation technique incorporation to demonstrate dynamic interaction between criteria and the use of an evolutionary niching genetic algorithm has given a mechatronic design tool that provides the best design while giving them the highest sense of contentment of the end product.

Another algorithm for novel multimodal evolutionary optimization was developed by the same group to solve concurrent and integrated design problems with various priorities in the field of mechatronics while considering the best topology and best parameters from a multi-criteria perspective (Behbahani et al., 2014). Furthermore, the search space for the problem is complex and huge owing to the existence of several configurations classes, prospective topologies and elements parameter values. The algorithm developed logically investigates the design space for set preferences to realize various configurations that are elite while using the experts' domain knowledge to ensure comprehensive competition and also taking into account few criteria that are not covered by the regular evolutionary optimization. This optimization process takes place in two loops. Among the possible topologies, the elitist specimen is found by using genetic algorithm-based optimization. Moreover, the best design is found by competing the elites. A stipulated competition selection strategy aimed at finding substitute elites that meet customer requirements is used in topology competitions. Thus, a high level of competition between elites can be employed to reach the global optimum. This algorithm can be considered as an improved algorithm because the competition between topologies is more practical and effective as a result of each trial topology being represented by its elite. This tool, hence, can develop multiple optimum structures which satisfy the subjective criteria.

A multidisciplinary design multi-objective optimization framework called the multi-objective Pareto concurrent subspace optimization (MOPCSSO) was developed by Huang et al. In this technique, the concurrent subspace optimization method ability was extended to manage multidisciplinary design multi-objective optimization problems. The major drawback of

conventional concurrent subspace optimization is that the Pareto points on any Pareto frontier's nonconvex section can not be captured by the weighted sum approach. The proposed multi-objective Pareto concurrent subspace optimization technique is in the design processes where each discipline has considerable dominance over its own objective function, while still making sure that the constraints are satisfied in coupled subspaces. Moreover, Pareto frontier endpoints can be effortlessly pinpointed by this optimization method, together with the capability to produce Pareto points within given limits to guarantee a rationally even distribution across the complete frontier. Further, MOPCSSO uses the initial design to generate the Pareto optimum while the objective function values are less than or equal to the beginning design. Thus, MOPCSSO can simultaneously tackle discrete objectives eliminating the need for formulating aggregate objective function.

It can be concluded that all these techniques advocate the optimization of all the design variable together. However, this approach can not handle a problem which involves the optimization of a large number of design parameters. Therefore, a decoupled integrated design (DID) approach (Sun, 2012) has to be undertaken for the present work. Based on axiomatic design theory (ADT) (Suh, 1990), which is the structure design problem analysis, the decoupled integrated design approach was formulated. Moreover, the full concurrent design does not take into account the nature of the design problem. AitShalia et al. (1995) have also pointed out the limitations of the concurrent design process. Hence, for this work, as a large number of parameters need to be dealt with, the decoupled integrated design approach is the plausible decision.

2.4 Conclusion

This literature review has been divided into three main sections: Synchrotron Magnets, Magnet Support Systems and Optimization. The aim of this literature review was to demonstrate the methodology selected for this study. Moreover, it also points out the fact that magnet frames have not been studied in detail and more emphasis has been laid on magnet and girder design. However, the design principle that the girder design is based on also holds true for the magnet frame design. For instance, both the girder and the magnet support must have a high first mode of natural frequency and have minimum static deflection. Moreover, the decoupled integrated design approach is a rational way to decompose a complicated design into smaller optimization problems.

Further, the use of POISSON and RADIA to calculate the magnetic field properties has been done before while designing CLS and other synchrotron magnets. Additionally, the analytical hierarchy process is a proven method for material selection. Also, calculating optimal dimensions using NSGA-II has also been discussed. Finally, Topology optimization of magnet girders have been reviewed and its use in the present work is justified.

Thus, frame design has not been given much emphasis in the literature while designing a synchrotron magnet. There is not much research on how a large optimization problem can be solved. This thesis was aimed to bridge this knowledge gap by adopting a divide-and-conquer (DID) strategy. There is not much literature available on DID apart from Sun's contribution. The contribution of this project is that it gives a demonstration of the usefulness of the decomposition technique in large optimization problems. This work also advances the DID concept to simplify design problems.

Chapter 3: Design Constraints

According to (Dai, 2018), constraints can be defined as a context or condition under which the device has to perform its functions. Moreover, the constraint requirement (CR) can be subdivided into Local Constraint Requirement and Global Constraint Requirement (Dai, 2018). Local CR is applicable to a particular function requirement (FR), whereas, Global CR applies to all the FRs of the design (Dai, 2018). Dai (2018) also defined the rules to distinguish the FRs from the CRs. The rule states that if the requirement is concerned about the usefulness of the product, it is classified as a function requirement. If the requirement concerns an aspect that limits the versatility of the product, it can be deemed as a design constraint. In this chapter, the global design constraints for the magnet frame will be defined, which includes (1) magnetic force, (2) frame material, and (3) allowable deformation.

It is noted that the purpose of finding the magnetic force is that this force will be used as a FEA boundary condition for calculating the deformation and the stresses developed in the magnet. The purpose of studying the frame material is to determine whether using a magnetic frame will have an effect on the magnetic field properties of a magnet. The purpose of studying the allowable deformation is find out to what extent does the magnet poles can deflect before the deflection starts deteriorating the magnetic field.

3.1 Magnetic Force as a Load on the Magnet Frame

The 3D magneto-statics computer code, RADIA, defines the geometry of the magnet in order to find the magnetic forces. Further, it can be observed that from the Offset Length (in m) vs Magnetic field (in T) graph that the designed magnet indeed behaves like a quadrupole. The magnet code developed by Dallin and Bertwistle (2018) was the base of this code. However, a finer mesh was used while calculating the forces. In the x-axis, the number of subdivisions was increased from 22 to 30 and from 15 to 20 subdivisions in the y and z-axes. The descriptions of all functions can be found on the ESRF website (https://www.esrf.eu/). The RADIA code and the variables used in the code are included in Appendix D.

3.1.1 Results with Discussion

The force ‘fr1’, i.e., the magnetic force acting on pole1, has been computed to be -32.27N in the x-direction, -8811.72N in the y-direction and -4729.94N in the z-direction. However, the force in the x-direction should be zero. Hence, the result shown here indicates an error in the analysis, which could be reduced by using a smaller mesh size. In principle, the poles exert a force that is equal and opposite. Thus, an estimate of the forces exerted by all the poles is listed in Table 3.1.

Table 3.1: Magnetic Force on Each Pole

	Fx	**Fy**	**Fz**
pole1	-32.2659	-8811.72	-4729.94
pole2	-32.2659	8811.72	-4729.94
pole3	32.2659	-8811.72	4729.94
pole4	32.2659	8811.72	4729.94

There are forces in both the y and z-direction i.e. horizontal and vertical direction. Consequently, it can be observed that there is a net force that is trying to bring the top yoke and the bottom yoke closer. Owing to the force component in the z-direction, the magnet will also try to twist the frame when the flanges are introduced. This can be illustrated by the schematic diagram in Figure 4.1, where $\overrightarrow{|F1|}$ =$\overrightarrow{|F2|}$ = $\overrightarrow{|F3|}$ = $\overrightarrow{|F4|}$ = 10000.9891 N.

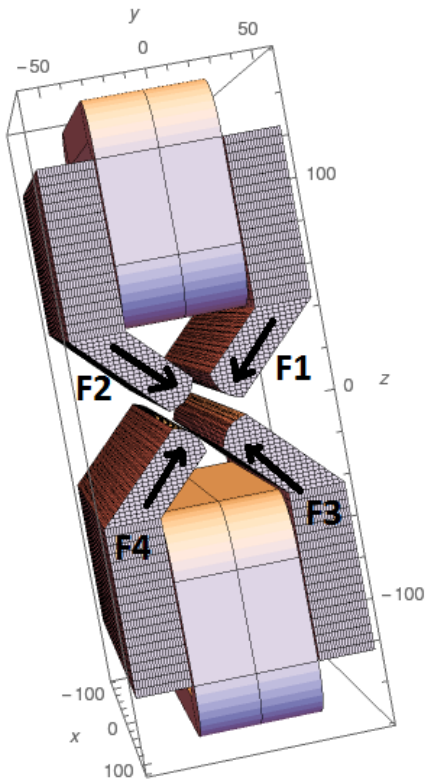

Figure 3.1: Magnetic Forces on Poles

3.1.2 Variation of Magnetic Forces

The quadrupole gradient might need to be changed according to the requirements of the optics code. As such, the magnetic forces can change if the gradient is varied. The gradient was changed by decreasing the current in the coils while keeping the length of the magnet (240 mm) and coil (30 mm x 20 mm) constant in order to study its effect on the magnetic forces.

The gradient was calculated using the equation below:

Gradient (T/m) = Integrated field (T) / Magnet Length (m) (3.1)

The current density was calculated from the dimensions of the coils and the current from the equation below:

Current (Amp-turns) = Area of coil (mm^2) x Current Density (Amp-turns /mm^2) (3.2)

The gradient was changed by changing the current density and the following results were obtained for pole1 (Table 3.2 & Figure 3.2):

Table 3.2: Change in Magnetic force with Gradient

Current Density (Amp-turns /mm^2)	**Integrated field (T)**	**Gradient (T/cm)**	**Current (Amp-turns)**	**F_x (N)**	**F_y (N)**	**F_z (N)**
3	64.784	26.99	1800	63.619	-3241.66	-1865.78
6	118.27	49.28	3600	-19.19	-7794.51	-4227.87
6.15	120.082	50.034	3690	-25.022	-8018.65	-4332.88
6.7	125.95	52.48	4020	-32.2659	-8811.72	-4729.94
8.1	136	56.67	4860	-16.2363	-10590.7	-5440.67
10.05	143.985	59.99	6030	-12.3544	-12669.7	-5969.48
13.4	151.027	62.93	8040	6.92467	-15812.8	-6338.3

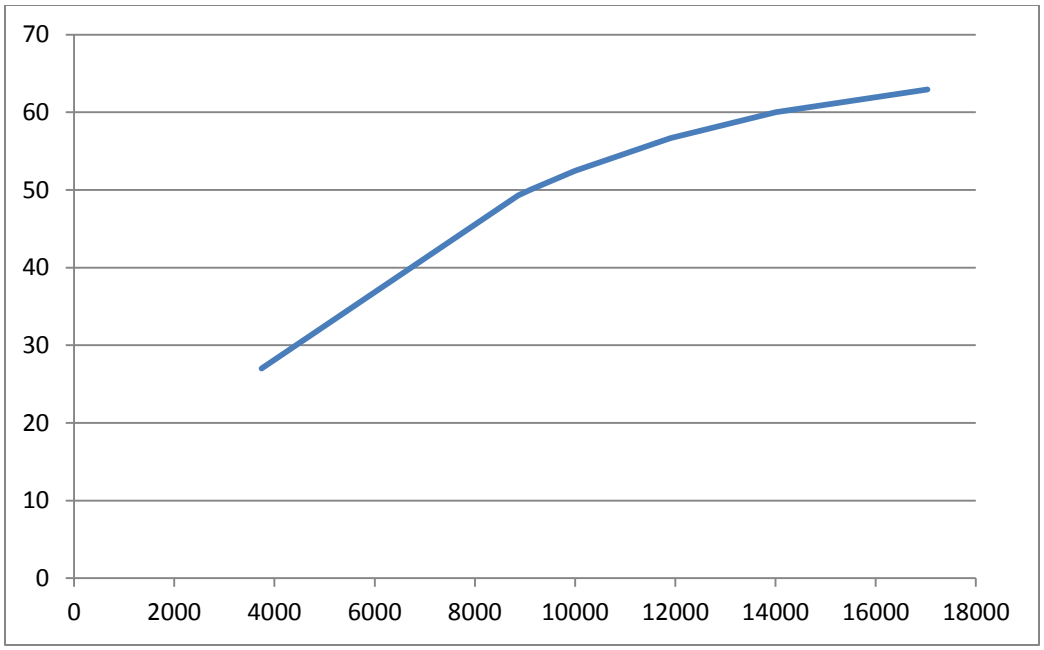

Figure 3.2: Resultant Force vs Gradient

The quadrupole gradient required for the present lattice is 50T/m approximately (Dallin, 2018). If there are no saturation effects, the gradient should be linear with the Amp-turns. However, the forces at 6.7 Amp-turns /mm^2 were considered for the magnet frame design in this thesis.

3.2 Material Property of the Frame

Poisson is a 2D analysis tool that executes the point by point 2D field distribution calculation by solving the following equation:

$$\frac{\partial^2 F}{\partial x^2} + \frac{\partial^2 F}{\partial y^2} = -\mu\mu_0 J_z. \tag{3.3}$$

F is a complex variable function which satisfies Laplace equation.

$$F = \overrightarrow{A} + iV \tag{3.4}$$

where $\overrightarrow{A}$ is the real vector potential and V is the imaginary scalar potential.

'J' is the current density, 'μ' is the relative permeability and 'μ_0' is the permeability of vacuum.

An iterative under-relaxation technique is used by Poisson for matrix inversion and for solving an array of nonlinear equations. This magnet orientation has a 54.06 T/m quadrupole gradient for 4020 Amp-turns. The Poisson code is put in Appendix E. Further, this design aims to study the magnetic properties when the frame is nonmagnetic in nature (Figure 3.3).

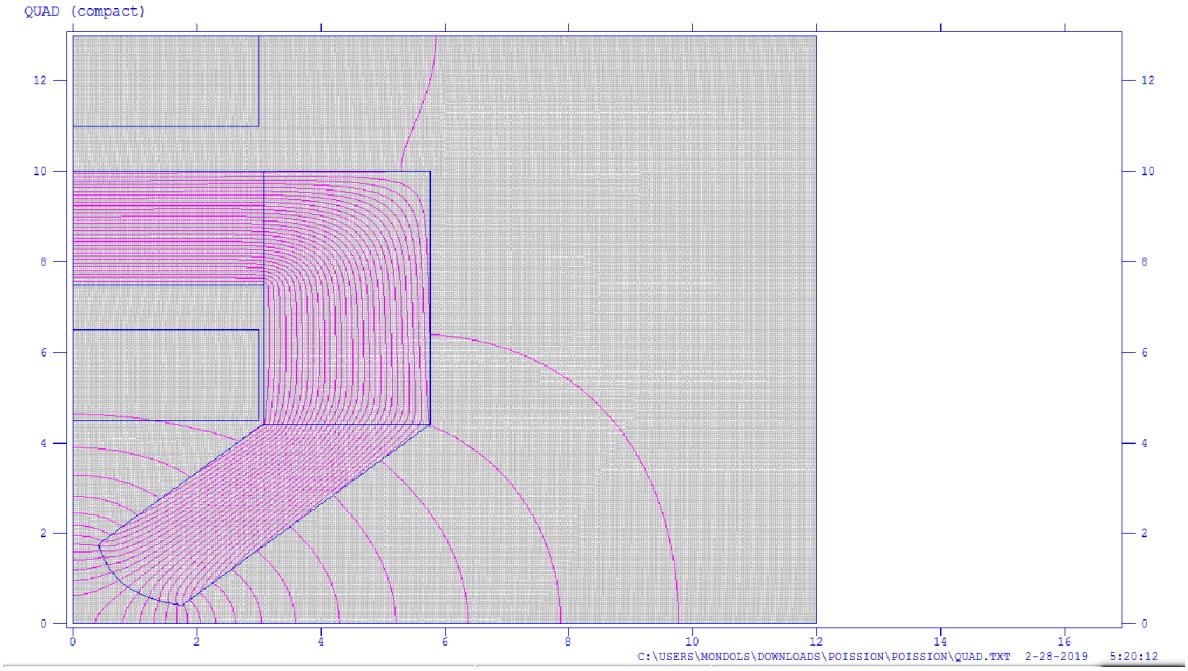

Figure 3.3: Quadrupole Design without a Frame

A frame thickness of 2.4 cm was assumed for this simulation. On the other hand, if the magnet has a frame which is also magnetic then magnetic field lines will have a different path as shown in Figure 3.4.

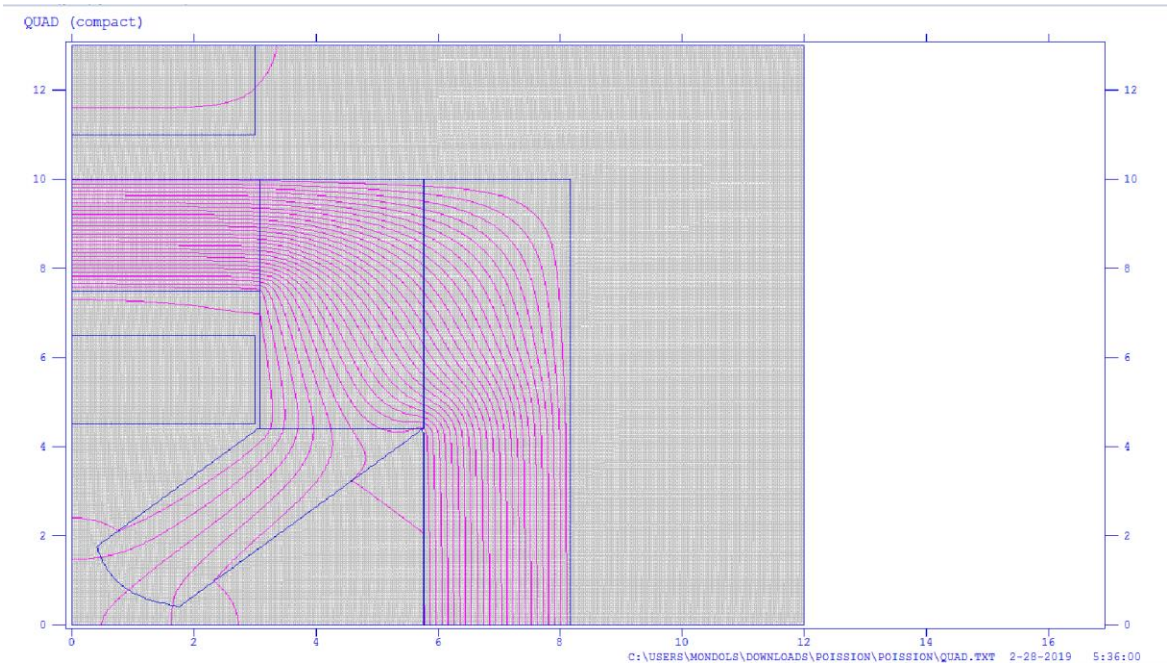

Figure 3.4: Quadrupole Design with a Magnetic Material Frame

This magnet orientation has a quadrupole gradient of 7.9 T/m. Thus, it can be concluded that the magnet frame material has to be a nonmagnetic material or the flux will escape through the frame and reduce the quadrupole gradient drastically. Hence, an optimal material needs to be selected based on the available nonmagnetic materials.

3.3 Allowable Deformation

In order to calculate the allowable deformation for the magnet, the magnet was distorted in the POISSON code to study its effects on the magnetic field. In the POISSON coordinate system, the x and y-axis are the horizontal and vertical direction, respectively. The magnet was displaced from its original position in the y-axis to evaluate the allowable deformation in the vertical direction. Similarly, the allowable deformations were found for the horizontal direction. The POISSON code in Appendix E was edited to calculate the effects of distortion. Subsequently, Table 3.3 lists the harmonic analysis results from the POISSON code for a deformation of 100 micron along the y-

axis. The order column indicates the multipole order denoted by 2 = quadrupole, 3 = sextupole, etc.

Table 3.3: Field Harmonics for 100 micron Deformation along the y-axis

N	Field	Units
2	5.43E+03	G/cm
6	2.85E+00	G/cm^5
10	1.07E+00	G/cm^9
14	-1.17E+00	G/cm^{13}
18	2.56E-01	G/cm^{17}
22	6.90E-02	G/cm^{21}
26	5.21E-01	G/cm^{25}

The harmonic analysis results for a deformation of 50micron along the y-axis shown in Table 3.4.

Table 3.4: Field Harmonics for 50 micron Deformation along the y-axis

N	Field	Units
2	5.41E+03	G/cm
6	1.19E+00	G/cm^5
10	9.80E-01	G/cm^9
14	-1.04E+00	G/cm^{13}
18	1.38E-01	G/cm^{17}
22	9.88E-02	G/cm^{21}
26	4.72E-01	G/cm^{25}

The harmonic analysis results for a deformation of 50micron along both the axes shown in Table 3.5.

Table 3.5: Field Harmonics for 50 micron Deformation along the both axes

N	**Field**	**Units**
2	5.43E+03	G/cm
6	2.73E+00	G/cm^5
10	9.97E-01	G/cm^9
14	-1.05E+00	G/cm^{13}
18	1.40E-01	G/cm^{17}
22	6.21E-02	G/cm^{21}
26	4.88E-01	G/cm^{25}

Table 3.6 shows the harmonic analysis results for a deformation of 10micron on the y-axis.

Table 3.6: Field Harmonics for 10 micron Deformation along the y-axis

n	Field	Units
2	5.39E+03	G/cm
6	2.15E-01	G/cm^5
10	1.10E+00	G/cm^9
14	-8.12E-01	G/cm^{13}
18	-6.33E-02	G/cm^{17}
22	2.09E-01	G/cm^{21}
26	3.49E-01	G/cm^{25}

The percentage error is calculated by the formula:

$$\Delta B/B = \Sigma C_n X^{n-1}/C_2 x \qquad (3.5)$$

where n is 6 to 26.

From the harmonic analysis, the Percentage Deviation from the Ideal Quadrupole Field was calculated using the Equation 3.5. Consequently, the Percentage Deviation from the Ideal Quadrupole for deformation in the vertical direction of 10, 50 and 100 microns is illustrated in the graph shown in Figure 3.5. The raw data for the Relative Deviation from Ideal Field as a result of the deformations are included in Appendix F. Also, it should be noted that the multipole errors

caused by deflection in one direction (say y-axis) were assumed to be the same in the other direction (x-axis).

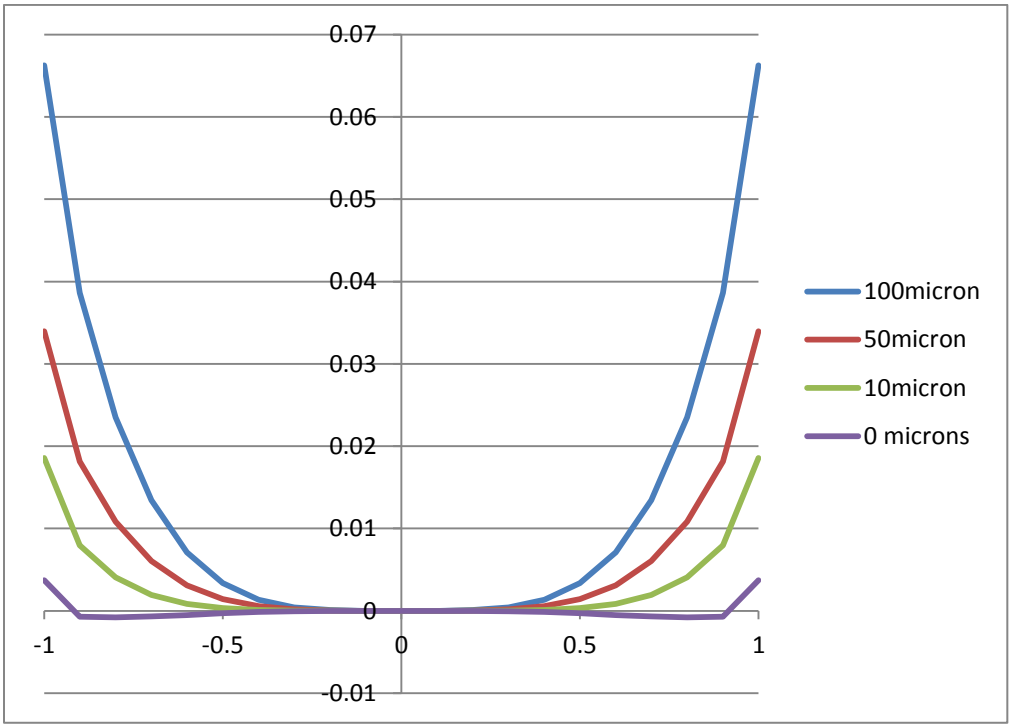

Figure 3.5: Relative Deviation from Ideal Field vs Offset length in cm

The effect of these systematic multipoles on the performance of the storage ring was studied. The evaluation of particle trajectories in an accelerator is called tracking. In a circular accelerator, the phase space stability region is called the dynamic aperture. The presence of multipoles reduces the dynamic aperture of the machine. The dynamic aperture is determined by tracking the particles at larger and larger amplitudes until they are lost. However, at larger amplitudes these higher order harmonics get stronger and either kick the beam out of a stable orbit or change the tune which can also cause beam instability. This decrease in dynamic aperture can be gauged by comparing the ideal machine dynamic aperture with that of a machine with multipole errors. As the CLS 2.0 magnet prototypes have not been developed, the relative value of harmonics which gave satisfactory results in the dynamic aperture studies will be used as reference (Table 3.7). The

relative value of harmonics is found by dividing the multipole component with the quadrupole component (Table 3.8, Table 3.9 and Table 3.10)

Table 3.7: Relative Value of Harmonics at 1 cm from beam axis in x-direction

Harmonic	**Relative Value of Harmonics**
6	$5.e^{-4}$
10	$1.8e^{-4}$
14	$-1.9e^{-4}$
18	$2.5e^{-5}$

The relative values of harmonics shown in Table 3.7 are acceptable as they are obtained for zero misalignment and will be used as reference to compare with harmonic values that include misalignments.

Table 3.8: Relative Value Harmonics for 100 micron misalignments at x = 1cm

Harmonic	**Field**	**Relative Value**
2	5430 G/cm	
6	2.85 G/cm^5	$5.2e^{-4}$
10	1.07 G/cm^9	$1.97e^{-4}$
14	1.17 G/cm^{13}	$2.15e^{-4}$
18	0.26 G/cm^{17}	$0.47e^{-4}$

Comparing Tables 3.7 and 3.8, it was concluded that 100 micron misalignments are unacceptable because the relative values are higher compared to machine with no misalignment (Table 3.7).

Table 3.9: Relative Value Harmonics for 50 micron misalignments at x = 1cm

Harmonic	Field	Relative Value
2	5410 G/cm	
6	1.19 G/cm^5	$2.2e^{-4}$
10	0.98 G/cm^9	$1.8e^{-4}$
14	1.04 G/cm^{13}	$1.9e^{-4}$
18	0.138 G/cm^{17}	$0.26e^{-4}$

Comparing Tables 3.7 and 3.9, it was concluded that 50-micron misalignments are acceptable because the relative values for 50-microns misalignment are less than that in Table 3.7. This means that all misalignments below 50 micron are acceptable and above 50 micron are unacceptable. Therefore, the misalignments should be less than 50 microns or it will negatively affect the dynamic aperture of the machine. However, this design will aim at keeping the total deformation to less than 10 microns so that a higher tolerance can be allowed on the critical surfaces. A higher allowable tolerance corresponds to a lower cost.

3.4 Conclusion

The magnet frame will be designed by taking it into consideration a magnetic force -8811.72N in the horizontal direction and -4729.94N in the vertical direction. Moreover, the magnet frame material has to be nonmagnetic in nature. Also, the magnet can tolerate a deformation of 50 microns in the vertical direction. The deformation in the horizontal direction was predicted to be negligible and this will be later validated in Chapter 6. However, the design was considered to have an allowable deformation of less than 10 microns to avoid unnecessary manufacturing costs. The less than 10-micron allowable deformation makes room for higher allowable tolerances. For instance, a 5 microns deformation from the magnetic force permits the use of higher tolerance values (± 45 microns), which is cheaper.

Chapter 4: Conceptual Design

In order to identify the commonalities of any product to be designed, it must be assumed to be a system. A system can be subdivided into its components. Further, the components of a system form the structure. Also, a generic model of any product can be deemed as a system. In other words, a system or a model is just an abstract of the product but it does not contain all the details.

FCBPSS is the general knowledge of a system and can be used to clearly understand a system (Zhang et al., 2005). This architecture classifies information or parameters of the system into Function, Content, Behavior, Principle, State and System (FCBPSS). Thus, a clear definition of the system parameters can be obtained from FCBPSS architecture. Moreover, FCBPSS can identify which parameters can be optimized and also recognize the design constraints.

Based on FCBPSS, the magnet support system will comprise of the frame and the threaded fasteners which form its structure (Figure 4.1). The states of the magnet system design are the thickness and the length of the plates, the dimensions and the type of the threaded fastener. The constraints imposed are the width of the frame which can not extend into the drift space and the force that might cause a deflection if the thickness is not enough. Moreover, when the magnet is mounted on the frame, the frame does not deform and stays in a stable position and when the magnet is energized, the frame does the same thing. Further, if there are floor vibrations, the frame does not allow the vibrations to propagate to the magnet. This is the behavior of the system. The principle on which the frame works is the 3D-Hooke's Law and principles of vibration isolation. The function of the frame is to position the magnet in a precise location in the lattice and minimize transmission of floor vibrations to the magnet pole. The magnet support system will be placed inside the storage ring (context). The preconditioning of the frame is when the coolant water pump is turned on and the post-conditioning is the magnet being energized.

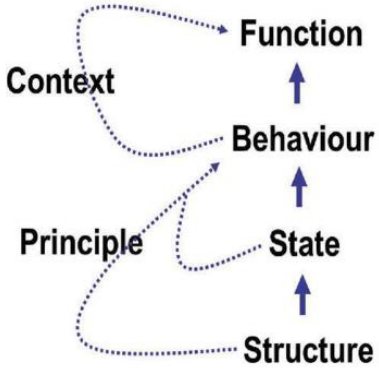

Figure 4.1: FCBPSS-Based Design Process (Zhang et al., 2005)

Science-Based Design is a design decision technique that involves a thorough study of the existing designs while considering the specific needs of the project-specific design goals and restrictions (Zhang, 2018). The aim of this technique is to produce better design solutions. Design Science can be divided into three phases:

- General Design Phase theory
- Design Theory and Methodology
- Design Modeling and Optimization

The phase theory states that the design should be divided into several phases. Design Theory and Methodology is the design at the logical (conceptual) and physical (concrete existence) level. At this stage, the design is expressed as conceptual Design Parameters (DP). Design Modeling involves defining the design in mathematical equations. Moreover, expressing design in equations enables the selection of the best design which is called Design Optimization. Each stage in the Science-Based Design process can be further subdivided.

The design phase theory divides the design phase into four logical phases as shown in Figure 4.2.

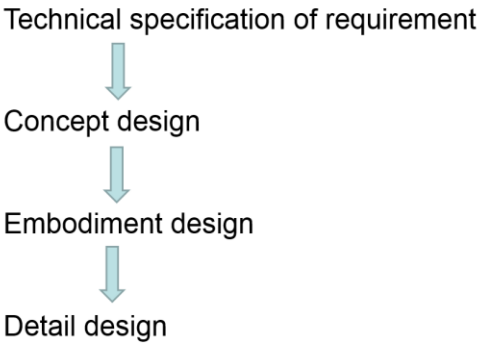

Figure 4.2: Phase Theory (Zhang, 2019)

4.1 Technical Specifications

The translation of the customer requirements into technical specification is the first step in the design phase theory. The technical specifications of the present magnet frame design are listed in Table 4.1.

Table 4.1: Technical Specifications

Customer Requirements	**Technical Specifications**
Low-cost	Cost less than 10,000 CAD
Should not protrude into the drift space	Frame width less than or equal to 240 mm
Should not get sucked-in by the magnetic force	• Deformation & Tolerance less than 10 microns. • Nonmagnetic Material • Able to bear 10000 N
Easy Vacuum Chamber Installment	Easy disassembly mechanism

4.2 Frame Structure Conceptual Design

The orientation and the suitable locations for drilling holes for screws can be found out by ANSYS simulations. As a thumb rule, the thickness of the material surrounding of the bolt must be twice the diameter of the bolt. The stand must be thick enough so that it does not get sucked in and deformed by the magnetic field. Moreover, the iron core will be bolted to the stand which in turn will be clamped to the main magnet girder. The support structure should not interfere with the magnetic field so a nonmagnetic material has to be chosen. Additionally, welds should be avoided as far as applicable as it can deform the structure. Rough ideas of how the support structure might look like are shown in Figure 4.3.

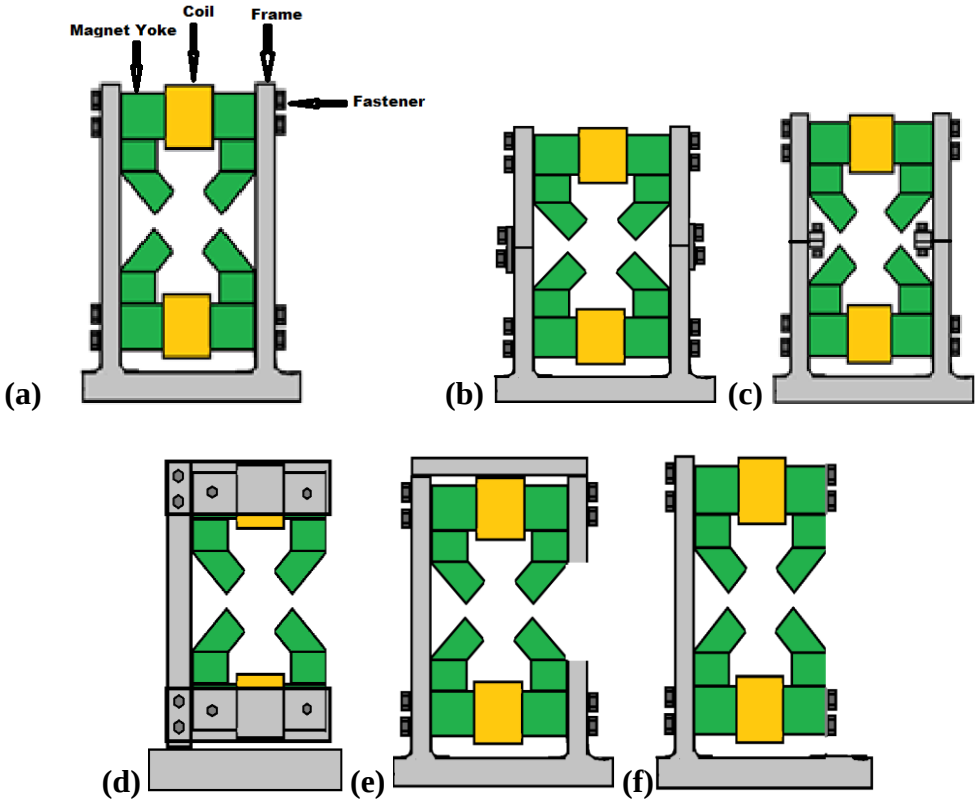

Figure 4.3: (a-c) H-Frame (d-e) C-Frame (f) L-Frame

The schematics above are not to scale. Moreover, if the H-Frame is used the magnet will be closed-sided. According to CLS 2.0 present design, insertion devices will be used to extract the

synchrotron radiation, hence, open-sided magnets are not necessary. However, there are other perks of having an open-sided magnet. For example, the ease of installing the vacuum tube. The C-Frame and the L-Frame are open-sided designs. Also, magnets immediately downstream for the IDs may possibly have to be open-sided. The frame in Figure 4.3 (d) can not be used as it takes up drift space. Further, after topology optimization, the frame shape may not be rectangular in shape.

The current CLS uses stud, nut and washer assembly to attach the yokes to the magnet frame (Swirsky, 2018). The use of stud and other threaded fasteners such as nut and bolt joint can be explored and the joint that imparts minimum stress and causes minimum static deflection on the magnet frame has to be selected. This also has to be evaluated scientifically. Further, the top and the bottom halves of the frame need to be joined. Also, the minimum clearance between the base of the coil and the girder underneath has to be at least 1mm (Dallin, 2018). The pitch and the number of threaded fasteners also have to be evaluated. Once this frame is developed, it can be used as a reference for the sextupoles and dipole frames.

Axiom Design Theory (ADT) is a design framework that applies to all designs (Suh, 1990). Furthermore, ADT comprises of two axioms: Independence Axiom and Information Axiom. A good design will fulfill both the axioms. The Function Requirement (FR) and Design Parameters (DP) is defined and the independence of FR–DP is established. According to Axiom 1, a particular DP can be modified to fulfill its corresponding function requirement without influencing the rest of the function requirement. On the other hand, Axiom 2 states that a design with minimum information content is the best design. From Axiom 1, a number of designs can be selected. Thus, Information Axiom can be used to pick the best design.

Axiom 1 states that every FR has to be satisfied by a DP. The relationship can be articulated in the form of a mathematical expression:

$$FR = A\ DP \tag{4.1}$$

where FR and DP are the function requirement(s) and design parameter(s) vector notation. A is the design matrix. The design matrix's features dictate whether the Independence Axiom (Axiom 1) is met or not. Then, a design which is uncoupled or decoupled has to be chosen.

FR1 = Hold the magnet in a precise position

FR2 = Damping vibrations

DP1 = Support Concept

The support concept that can meet the above two function requirements can be the schemes described pictorially in the figures 4.3 (a-f). Thus, DP1a=Figure 4.3a, DP1b=Figure 4.3b, DP1c=Figure 4.3c and so on. If DP1a is used then the vacuum chambers will be hard to install. Thus, DP1a can be eliminated. DP1d takes up drift space. One of the major requirements for this design is to take up as less drift space as possible. Hence, DP1d will not be used. DP1e and DP1f are prone to deformation. As the magnet exerts a very high magnetic force, the deformation caused can be given by the equation below:

$$\delta = 4PL^3/Ebh^3 \qquad (4.2)$$

where 'δ' is the deformation, 'P' is the force, 'L' is the length, 'E' is the modulus of elasticity, 'b' is the width and 'h' is the height of any beam. 'b' and 'h' correspond to the area perpendicular to the force. From this equation, it can be observed that deformation is dictated by the L term in the formula. The free body diagram for the design concept DP1e is illustrated in Figure 4.4.

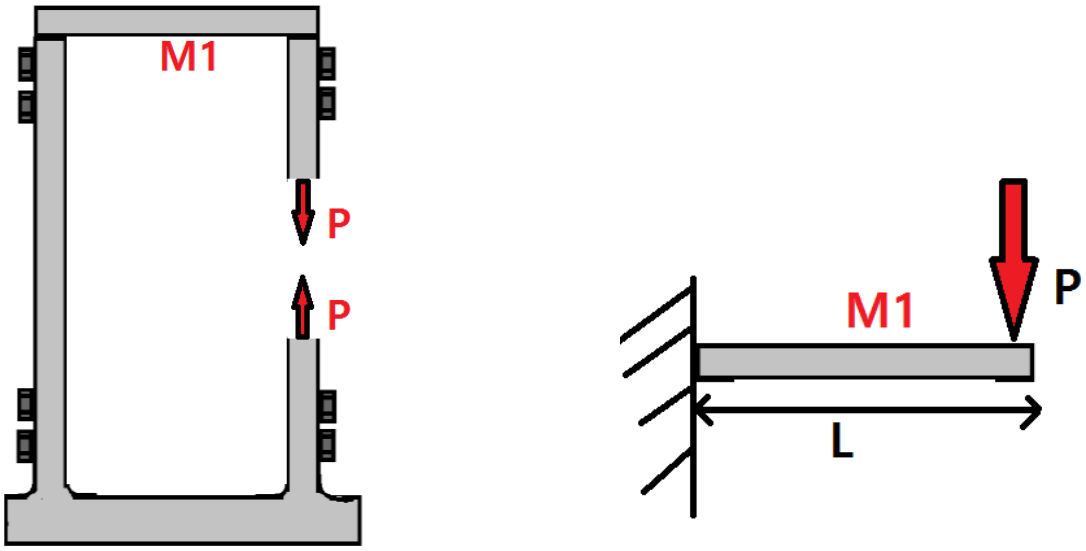

Figure 4.4: Free Body Diagram of C-Frame

Now, if the members of the C-frame are further decomposed and the free body diagram for member M1 is also shown above. Thus, the free body diagram for the H-Frame has been shown in Figure 4.5 for comparison.

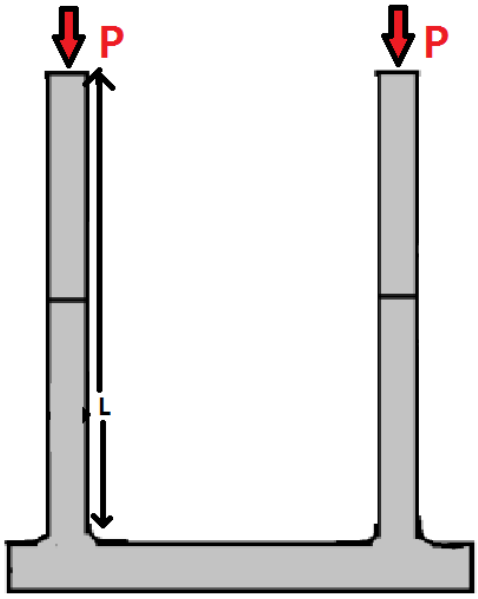

Figure 4.5: Free Body Diagram of H-Frame

The deformation can be given by

$$\delta = \mathrm{PL/AE} \qquad (4.3)$$

'A' is the area perpendicular to the applied force. Thus, it can be concluded that when the beam is under compression the deflection will be lesser. Since, the allowable deformation is in the order of a few microns so these two concepts can be excluded.

DP 2a = Passive Damping

DP 2b = Active Damping

DP 2c = Increase Stiffness

Passive damping systems have been reported to be effective in successfully diminishing vibrations (Nashif, 1992 & Marsh et al., 1996). Viscoelastic materials (VEM) embedded in the structure have

been extensively used in these studies. The damping system material should be chosen such that it has very high loss modulus at operational conditions i.e. temperature, frequency, etc. The large internal friction of the polymer chain molecules imparts these materials their high damping capacity. The geometry of the VEM will be designed by evaluating the appropriate stiffness that corresponds to the maximum strain energy ratio between the VEM and the entire structure (Zhang et al., 2001). However, using VEM in the magnet support structure is impractical as these materials are not mechanically stable. VEMs can be installed in between the girder mounting fixture and the floor mounting fixture as in the ESRF. Using tuned vibration absorbers is another way of dissipating vibrations but it seems to be less practical to use it for a magnet frame and can be expensive at the same time. Hence, DP2a can be eliminated.

Using DP2b can be expensive. As cost is also a design constraint, DP2b can also be excluded. Thus, the design matrix is as follows:

$$\begin{bmatrix} FR1 \\ FR2 \end{bmatrix} = \begin{bmatrix} A11 & A12 & 0 \\ 0 & 0 & A33 \end{bmatrix} \begin{bmatrix} DP1b \\ DP1c \\ DP2c \end{bmatrix} \quad (4.4)$$

$$FR1 = (A11 \times DP1b) + (A12 \times DP1c) \quad (4.5)$$

$$FR2 = A33 \times DP2c \quad (4.6)$$

FR1 is supporting the magnet which will depend on the structure of the frame (DP1b and DP1c). Similarly, FR2 is damping vibrations which only depend on one design parameter i.e. increasing the stiffness of the system. From the design matrix, it can be concluded that the design is decoupled. Furthermore, a decoupled design is more robust than coupled design as it is easier to reduce the design information content which will satisfy Axiom II (Park, 2010).

Thus, using Axiom 1 two conceptual designs has been found. Information axiom can be used to pick the better of the two design concepts. A recent study by Preissner, C (2018) concluded that the higher the number of frictional contacts the lower will be the value of the first mode of natural frequency. In DP1c there will be four additional metal plates at four corners that will correspond to the addition of four more frictional contacts to the system. Additionally, the magnetic property and the suface finish of the extra metal piece also had to be determined. Hence, based on Preissner's work and Axiom 2, it can be inferred that DP1c will have a lower natural frequency that DP1b and hence the DP1c conceptual design is being disregarded.

4.3 Frame Structure Embodiment Design

The next step in the design is developing the embodiment design. This step can also be classified as the Design Theory and Methodology stage of the Science-Based Design. In order to reduce computation time and effort, the optimization problem has to be divided into several parts. However, an optimal solution might not be obtained from sub-diving the optimization problem. For instance, in optimization 1 there are two design parameters P11 & P12, and in optimization two the design parameters are P21& P22. Optimization 1 was set to fulfil objective O1 subjected to a constraint C1. Similarly, in Optimization 2 was set to fulfil objective O2 subjected to a constraint C2. The design problem will have two steps:

Step 1: Optimize P11 & P12 in Optimization 1 for O1 under C1.

Step 2: Optimize P21 & P22 in Optimization 2 for O2 under C2.

Now, while optimizing P21 & P22, P21 & P22 will have to be assumed, say P210 & P220, and different values of them may affect C1 and O1. Thus, the optimal result for Optimization 1, say P11a and P12a, is under the condition of P210 & P220.

In other words, while solving Optimization 2, the optimal result say P21a, P22a will compromise O1 and C1. With the same reason, the optimal result in step 2 is under the condition of the result at Step 1, i.e. P11a & P12a. Hence, the design result for this procedure, P11a, P12a, P21a & P22a are not the optimal result for the system that fulfils objectives O1 and O2 subjected to constraints C1, and C2.

The solution to this problem is concurrent design, i.e., to take all the objective functions and the constraint functions together to determine all the parameters together:

Objective Functions: O1 & O2

Constrain Functions: C1 & C2

Calculate: P11, P12, P21 & P22.

Let the result from this concurrent design process is P11b, P12b, P21b and P22b. Then,

$$P11b \neq P11a \tag{4.6}$$

$P12b \neq P12a$ (4.7)

$P21b \neq P21a$ (4.8)

$P22b \neq P22a$ (4.9)

Thus, a different approach has to be taken. The optimization problem has to be broken down sensibly to obtain the optimized solution.

There are many parameters that affect the functional and constraint requirement. If the parameters are denoted as 'P' and the requirements or objectives as 'O', then, the whole design can be the formulation of the P-O relationship (Zhang et al., 2005). The Ps were identified as follows:

- Number of Threaded Fasteners = P1
- Material = P2
- Plate Thickness = P3
- Flange Location = P4
- Shape = P5

As the design should be an optimized one, the functional requirements also are represented as optimization objectives:

- Hold the magnet in a precise position = O1
- Damping vibrations = O2
- Minimize cost = O3

The number of threaded fasteners will have an effect on the stiffness of the system. The more the number of connection points between the magnet and the frame the more will be the system stiffness. However, the aim is to keep the number of threaded fasteners to a minimum to decrease machining and additional parts expenses. Hence, the holding function of the fasteners is the dominant function and the damping function can be ignored. As long as the material does not exceed its yield stress it will not have a significant effect on the holding function. Hence, the yield stress will be considered as the failure criterion while designing and the holding function can be assumed to be insignificant. On the other hand, the Young's modulus will dictate the stiffness of the frame. The location of the flanges should not have any effect on the system damping properties

or the cost. Plate thickness and the shape of the frame will have an effect on first two objectives functions. The matrix representation of the P-O relationship can be given by:

$$\begin{bmatrix} O1 \\ O2 \\ O3 \end{bmatrix} = \begin{bmatrix} A11 & 0 & A13 & A14 & A15 \\ 0 & A22 & A23 & 0 & A25 \\ A31 & A32 & A33 & 0 & A35 \end{bmatrix} \begin{bmatrix} P1 \\ P2 \\ P3 \\ P4 \\ P5 \end{bmatrix} \tag{4.10}$$

From the matrix representation of the P-O relationship, it is evident that the design problem is a decoupled one. The P-O relationship can be illustrated in Figure 4.6 that follows:

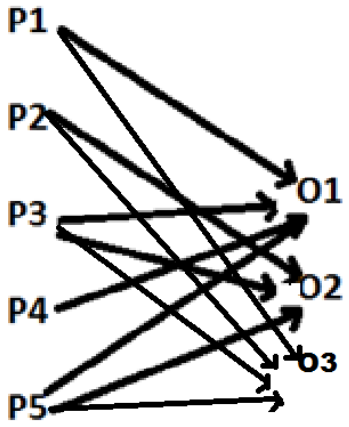

Figure 4.6: P-O relationship

The next step to work out this design problem is to determine whether to solve P1 for O1 and then P2 for O2 and so on or all Ps for all Os simultaneously. Solving all Ps for all Os concomitantly is a methodology coined by Alyaqout et al. as "All-In-One". A full concurrent design (FCD) approach was adopted by Yan and Yan (2009) to optimize a four-bar linkage by taking into consideration all design variables simultaneously. FCD has the ability to calculate design variables more accurately than any other design approach. However, the huge computational overhead is associated with FCD which limits its uses in complex design problems like the one encountered in the present work. Moreover, the integrated design process is another technique to solve design problems that consider all Os together but not necessarily as FCD does.

A decoupled integrated design (DID) process was proposed by Sun et al. (2012) that considered tackling a decoupled design problem with a decoupled design technique. Further, DID is a variant

of the sequential design process whose sequence is determined by the P-O relationship matrix. If the following decoupled design problem is considered:

$$\begin{bmatrix} O1 \\ O2 \end{bmatrix} = \begin{bmatrix} A11 & 0 \\ 0 & A33 \end{bmatrix} \begin{bmatrix} P1 \\ P2 \end{bmatrix} \quad (4.11)$$

Then, the optimization can be performed in the following two stages:

Stage 1: Optimize P2 for O2 following the equation O2 =f_{22} (P2).

Stage 2: Optimize P1 for O1 following the equation O1=f_{11}* (P1, P2*).

P2* is the optimized P2 from stage 1 and is not changed in stage 2.

A decoupled integrated design approach was used to solve the design problem in the present work. The function requirement holding the magnet in a precise position in the lattice can be translated to the optimization goal minimum deformation of less than 10 microns. Similarly, damping floor vibrations can be interpreted as maximizing structural stiffness. Firstly, the number of threaded fasteners has to be determined as it will disclose where in the frame the magnetic forces will act. In the second design phase, Young's modulus was used as a representative of the stiffness of the system and was be optimized using AHP. The material which was found from the AHP analysis was used in the design phase from here on. Then, the thickness of the plate was then optimized using the Multi-Objective Genetic Algorithm (MOGA). The number of threaded fasteners obtained from the manual optimization was used for the calculation of the optimal thickness. This step assumed that the shape of the plate was rectangular. While determining the flange location and the number of bolts to be used static deformation was targeted to be kept below 10 microns. The optimized thickness was then used to generate an optimized frame shape and a parametric study produced the final design. Similar to the technique adopted by Su (2012), the thickness was not changed at the topology optimization step. Thus, the stages in embodiment design for the magnet frame can be subdivided into five phases listed in Table 4.2.

Table 4.2: Embodiment Design Phases

Phase	Parameter	Technique	Goal	Assumptions
1	Number of Threaded Fasteners	Brute Force Optimization	Minimize Deformation and Cost	Thickness = 25mm and 36mm Shape Material= Steel
2	Material	Analytic Hierarchy Process	Maximize Stiffness Minimize Cost	Elastic Modulus is the surrogate for Stiffness
3	Thickness	Multi-Objective Genetic Algorithm	Minimize Deformation and Cost Maximize Stiffness	Shape
4	Flange Location	Mathematical Modelling	Minimized Deformation	Shape
5	Shape	Topology Optimization	Minimized Deformation and Cost, Maximize Stiffness	

4.4 Conclusion

At the conceptual design phase, the frame design is still in the abstract idea level. Embodiment design was the phase where the frame had a concrete existence. This chapter deals with how the customer requirements evolve to technical specifications and how these technical specifications form the conceptual design. The various steps in the embodiment design were determined.

Chapter 5: Optimization for Embodiment Design

This chapter deals with the embodiment design of the frame. This design stage can also be identified as the Design Modeling and Optimization step of the Science-Based Design. The five phases in the optimization defined in the previous chapter will be dealt with in this chapter. Further, ANSYS DesignXplorer module was used to perform the optimization of the frame. Design optimization is a popular problem in engineering. In many cases, the parameters that need to be optimized are not obvious. Design optimization formalizes the process. Based on the objective mathematical modelling, the logical progression for parameter consideration, evaluation and elimination take place. Moreover, ANSYS also bundles the design points into a user-friendly format. Design optimization also saves computation times by reducing the number of plausible design points. Thus, ANSYS DesignXplorer has tools that can drive design decisions. Figure 5.1 shows the steps in the optimization process (Thakker, 2015).

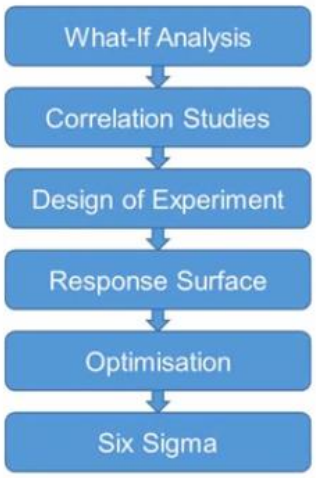

Figure 5.1: Optimization Steps (Thakker, 2015)

The first step is the best guess or manual optimization. Next, the correlation studies determine which variables actually affect the output. Then, the Design of Experiments (DOE) study binds the important variables within a design space. Followed by response surfaces which are the visual presentation of how the input and the output variables are related. After that, the optimization is performed based on a particular goal. Finally, the six-sigma or robust design is done to ensure that

the design will also work in the real-world where the design will be subjected to uncertainties, e.g., material properties, manufacturing, etc.

5.1 Type and Number of Threaded Fastener

Type and number of threaded fastener were determined using manual optimization. The number and the size of the fasteners were varied to find the configuration with the minimum deformation and the minimum number of fasteners was selected. However, ANSYS Workbench can not differentiate between bolt-nut connections and threaded rod-nut connections. Thus, to make the design more robust, threaded rods were used in the real design. Moreover, the present CLS uses threaded rods and nuts to bond the magnets to their frames. Hence, threaded rods and nuts appeared to be a plausible choice.

The next step was to decide whether to have a fully threaded rod with the magnet also having internal threads or to have a rod with the threaded ends only. If a fully threaded fastener design (magnet yoke having internal threads) was chosen then the bolt pretension would not be set up efficiently as some of the magnetic force needs to be borne by the pretension. Therefore, a rod with the threaded ends and nuts was used to fasten the magnet to its frame. For the ease of analysis, the rod was assumed to be formed by three cylinders: one long cylinder equal to the horizontal length of the frame and two short cylinders equal to the width of the nuts. Further, ANSYS can not decode threads from the CAD model. In order to simulate a nut-threaded rod connection, the contact between the two bodies (short cylinder & nut) was assigned as bonded contact. Additionally, the diameter of the through holes in the magnet and the frame for the rod to go through was kept slightly larger than the diameter of the rod to enable thermal expansion. Also, washers were also be incorporated to reduce stress concentration. A pictorial representation of the ANSYS model of the rod and the nut is shown in Figure 5.2.

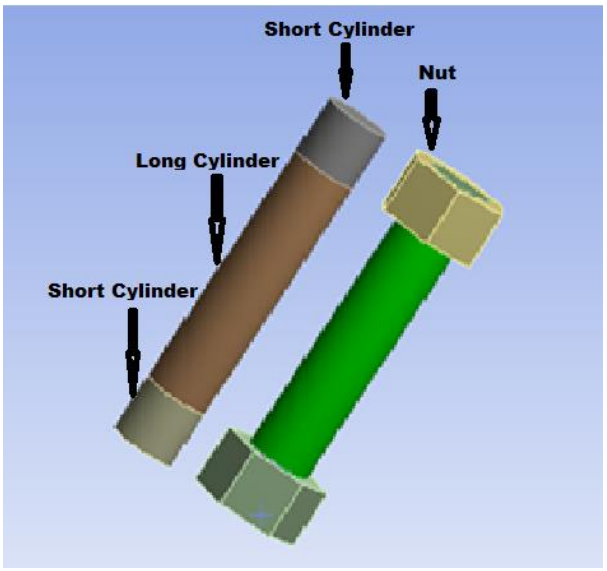

Figure 5.2: Flange Threaded Rods and Nuts

A brute force optimization methodology was performed to find out the minimum number of threaded rod necessary to hold the magnet in position while having minimum deformation. The free body diagram in Figure 5.3 shows how the magnetic forces are directed. The bottom surface of the frame is assumed to be fixed support. Disassembly facilities will be taken into consideration later in the design.

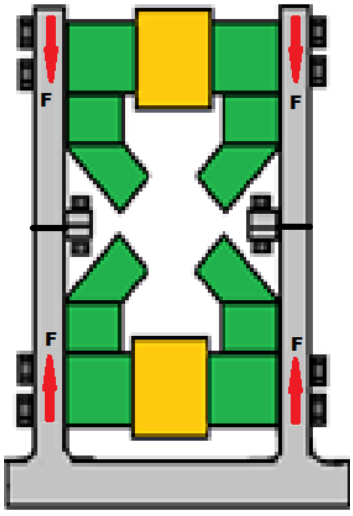

Figure 5.3: Frame FBD

There are three modes of failure by which the frame might fail: the bolts can break (shearing) (Figure 5.4), the hole may extend (bolt compresses the metal plate) (Figure 5.6) and the plate can tear (Figure 5.5) (moodlemech, 2019).

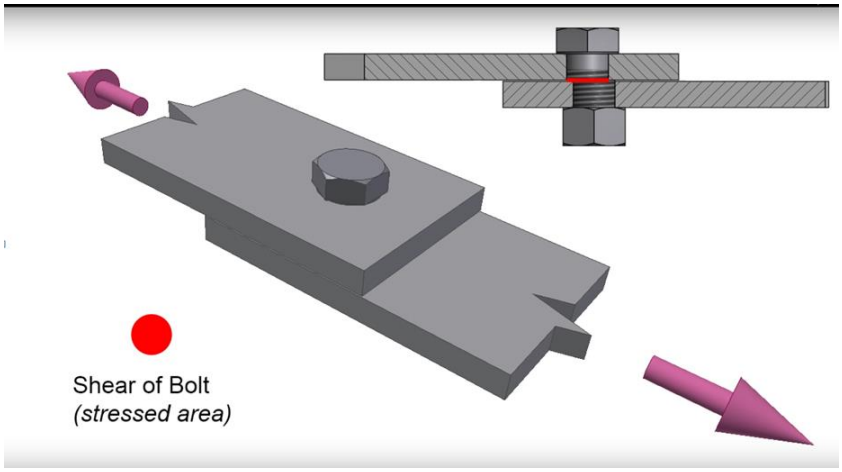

Figure 5.4: Bolt Failure (moodlemech, 2019)

Stress = Force/Area (5.1)

Area = πr^2 (5.2)

'r' is the radius of the bolt.

For the first scenario, a bolt diameter of 24 mm was selected with a factor of safety of 10 and with the assumption that the resultant force acted downwards. Plugging in the value of the resultant force from Chapter 3 in Equation 5.1:

Shear Stress = $10001/\pi \times (0.012)^2$

= 22107063.69 Pa

= 22.107 MPa

22.12 MPa is below the steel's yield shear stress of 240MPa. For comparing the stresses yield stress will be used instead of ultimate stresses because deformations in microns will be considered to be a failure.

The second way, a bolted joint can fail, is a failure by tearing the plate via tension. The area to be considered in Equation 5.1 for this failure is the area of the cross-section plate minus the hole. Drilling a hole gives rise to stresses, and, hence, this area should be considered for failure testing. A thickness of 25 mm was calculated with a factor of safety of 10 and with the assumption that the resultant force acted downwards.

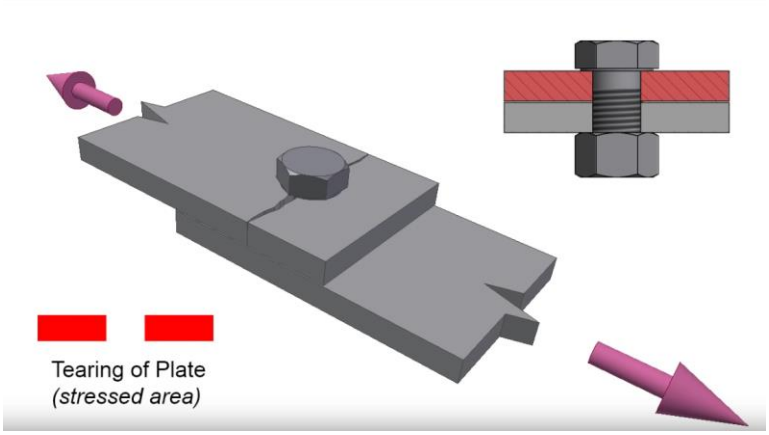

Figure 5.5: Plate Tearing (moodlemech, 2019)

This stress should be negligible as the cross-section of the plate is 240 x 25 mm^2 and the two holes are only 24 mm wide. This type of failure is common when the cross-section is small. So, this design will never fail by plate tearing.

The third mode of failure is the hole itself can fail.

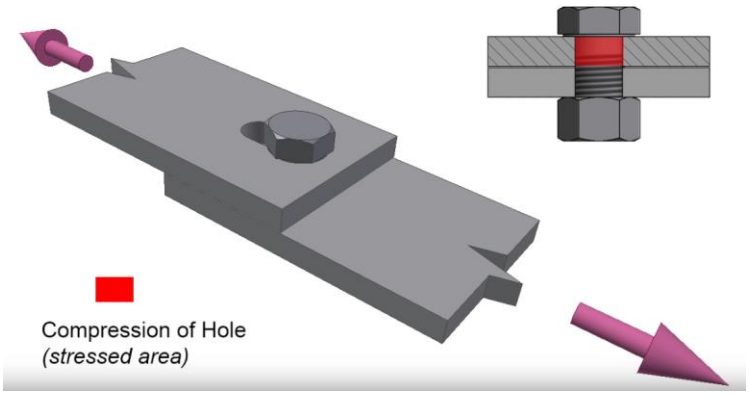

Figure 5.6: Hole Compression (moodlemech, 2019)

Area where Compressive Force is acting = d x t (5.3)

$$= 24 \times 25 \text{ mm}^2$$

$$= 600 \text{ mm}^2$$

Plugging in the value of the resultant force from Chapter 3 in Equation 5.1. In this case, however, the force will be compressive in nature:

Compressive Stress = 10001/600

= 16.67 MPa

16.67 MPa is lower than the compressive yield strength of steel which is between 140–160 MPa.

For permanent connections, the preload is calculated by (Shigley´s, 2016):

$F_i = 0.90\ F_p$ (5.4)

where F_i is the required preload and Fp is the proof load of the threaded fastener.

$F_p = A_t\ S_p$ (5.5)

where A_t is the shear area of the threaded fastener and S_p is the proof strength

F_p = 76906.19 N

F_i = 69215.57 N

Material Properties of Copper, 1010 Steel and Steel were used for the coils, magnet and the frame including the fasteners respectively. All the materials were assumed to be linear isotropic. The material properties are listed in Table 5.1.

Table 5.1: Engineering Data

Material	**Thermal Conductivity (W/mK)**	**Elastic Modulus (GPa)**	**Poisson's Ratio**	**Density (g/cm^3)**
1010 Steel	49.8	210	.27	8.96
Nonmagnetic Steel	15	193	.29	8
Copper	386	128	.36	8.96

A new coordinate system that was aligned with the RADIA coordinate system was defined. The contacts between the mating parts from the CAD geometry are defined in Table 5.2.

Table 5.2: Contacts for 25mm Plates with 2x M20

Mating Part 1	**Mating Part 2**	**Contact Type**
Rod	Frame	Frictionless (μ=0)
Magnet	Frame	Frictional (μ=0.7)
Rod	Nut	Bonded
Rod	Magnet	Frictionless
Magnet	Coil	Bonded

A hex-dominant mesh was used with body sizing of 20 mm on the plates and 10 mm on the rods. More details on mesh type and contacts are included in Chapter 6. Moreover, the analysis takes place in two time steps: first, the bolt pretension is applied and the then magnetic forces are activated. In both steps, the forces are ramped. This attempts to simulate the real-life scenario as the bolts will be tightened first and then the magnet will be energized. Further, the bottom surface is considered to be fixed support. The forces were assumed to be acting from the magnet outer surface. The bolt pretension was applied on the middle cylinder of the rod. Thermal conditions and the gravitational forces were ignored for this analysis. The analysis set up is shown in Figure 5.7.

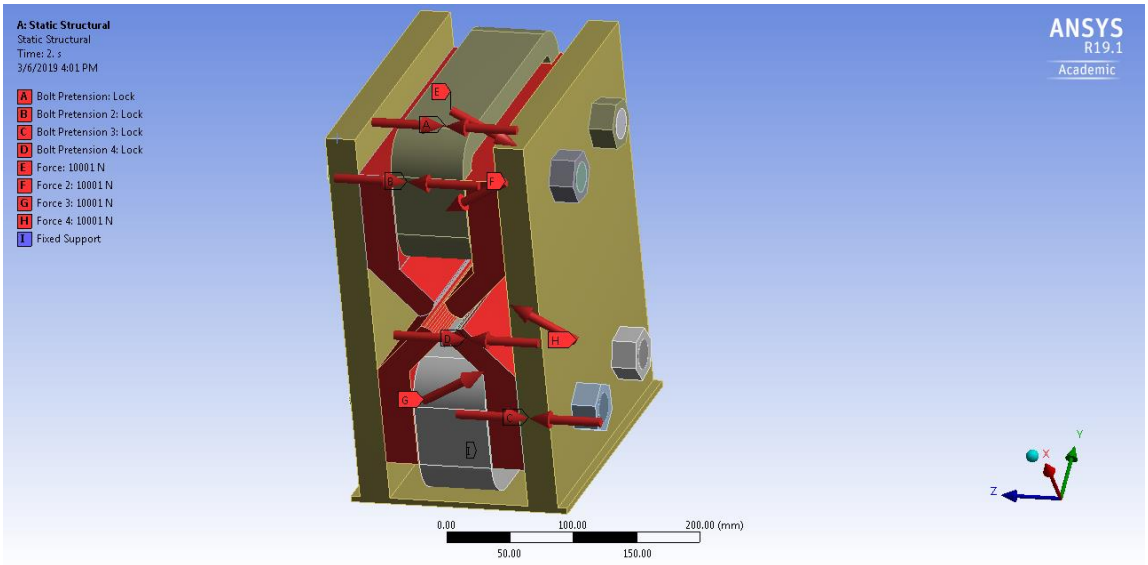

Figure 5.7: 25mm Plates with 2x M20 Analysis Setup

The pole deformation was higher than 10 microns. Hence this design can be rejected. The Total Deformation on the poles is shown in Figure 5.8.

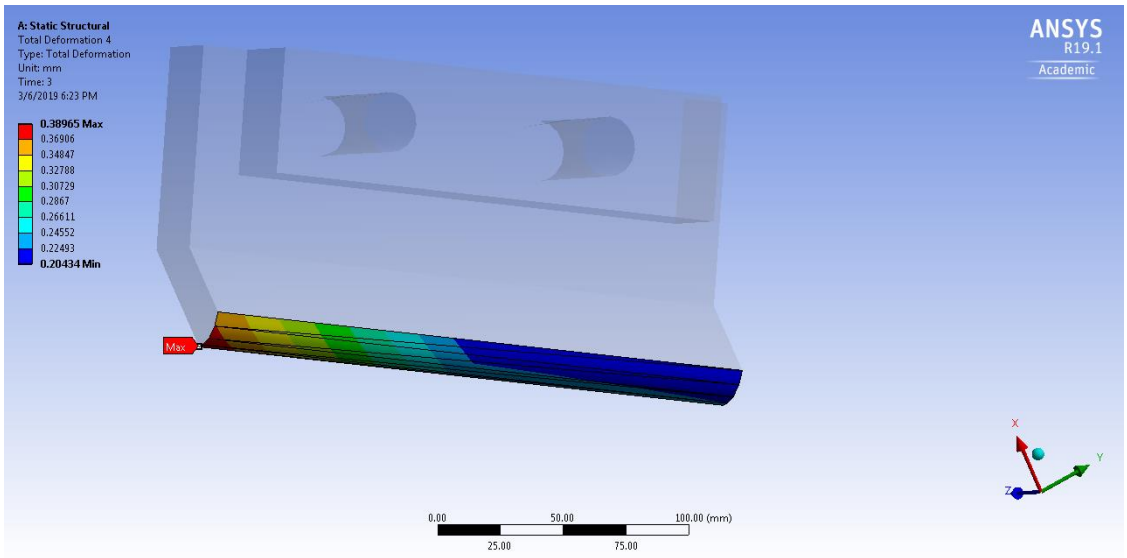

Figure 5.8: 25mm Plates with 2x M20 Pole Deformation

Using Equations 5.1 to 5.5, the failure modes and the bolt pretension was calculated for the rod diameter of 30mm and plate thickness of 36mm. Again, the pole deformation was unacceptable. The Total Deformation on the poles is shown in Figure 5.9.

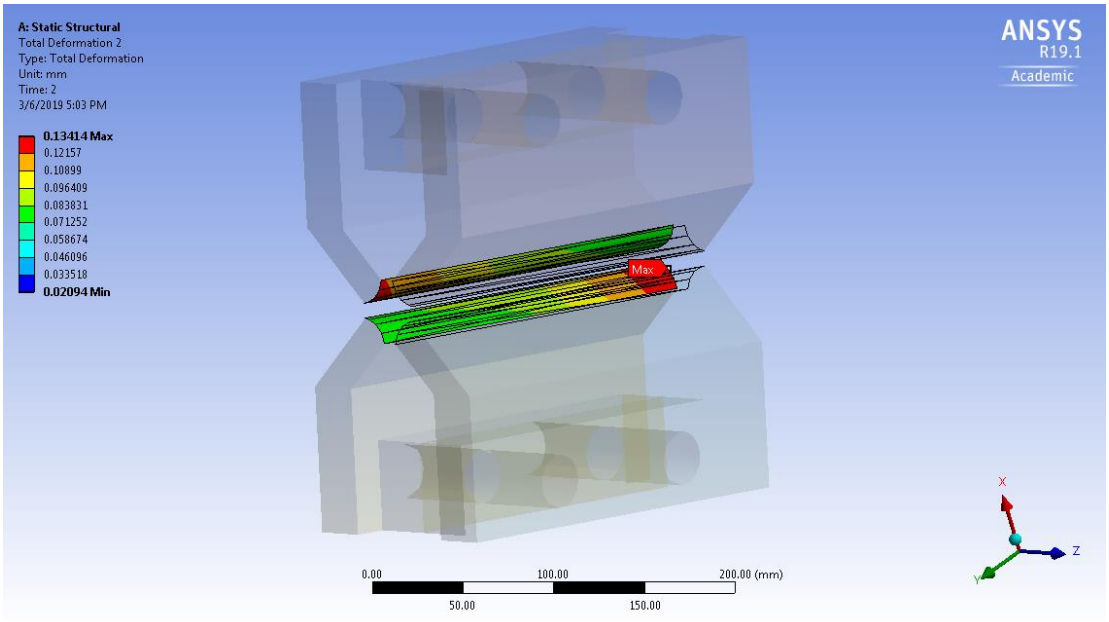

Figure 5.9: 36mm Plates with 2x M30 Pole Deformation

The stresses generated in the magnet were also unacceptable as it was beyond the yield stress of AISI 1010 Steel (305 MPa). Hence, this design was rejected. Figure 5.10 shows the Equivalent Stress results.

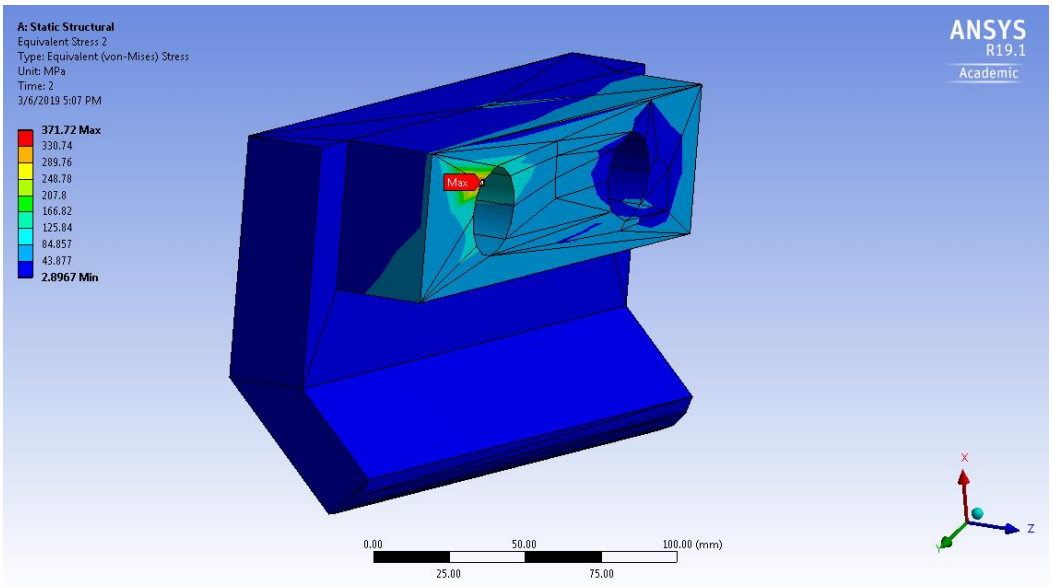

Figure 5.10: 36mm Plates with 2x M30 Magnet Stress

The next design has three bolts and has acceptable deformation and stresses. The plate thickness of 25 mm was used. The thermal conditions were taken into consideration for this analysis. Tetrahedron mesh was used for the magnet and the coils. On the other hand, a hex-dominant mesh was used for the fame and the fasteners.

As stated earlier, the initial temperature was considered to be 23^{o}C because it is the temperature of the present storage ring (Wyatt, 2018). The outlet temperature of the water going out has a maximum temperature rise of 8^{o}C (Dallin, 2001). It was assumed that the copper coils were at a temperature of 32^{o}C. Further, the bottom surface of the frame will be in contact with the girders which also can be assumed to be at the storage ring temperature of 23^{o}C. A convection boundary condition was applied on all the surfaces in contact with air. Moreover, the convection film coefficient was assumed to be a constant and equal to $5x10^{-6}$ W/mm^2.^{o}C at 21^{o}C.

The thermal load and the effect of gravity were taken as loads for the static structural analysis. Similar to the 2x M20 Analysis Setup, the forces were applied on the pole faces and the bottom plate was set as the fixed support. The bolt pretension and the failure modes were calculated from Equation 5.1 to 5.5 and the design was found safe. Contacts definition was also similar. Even

though the deformation in the Y direction was above 10 microns, the deformation of the pole was at an acceptable value (Figure 5.11).

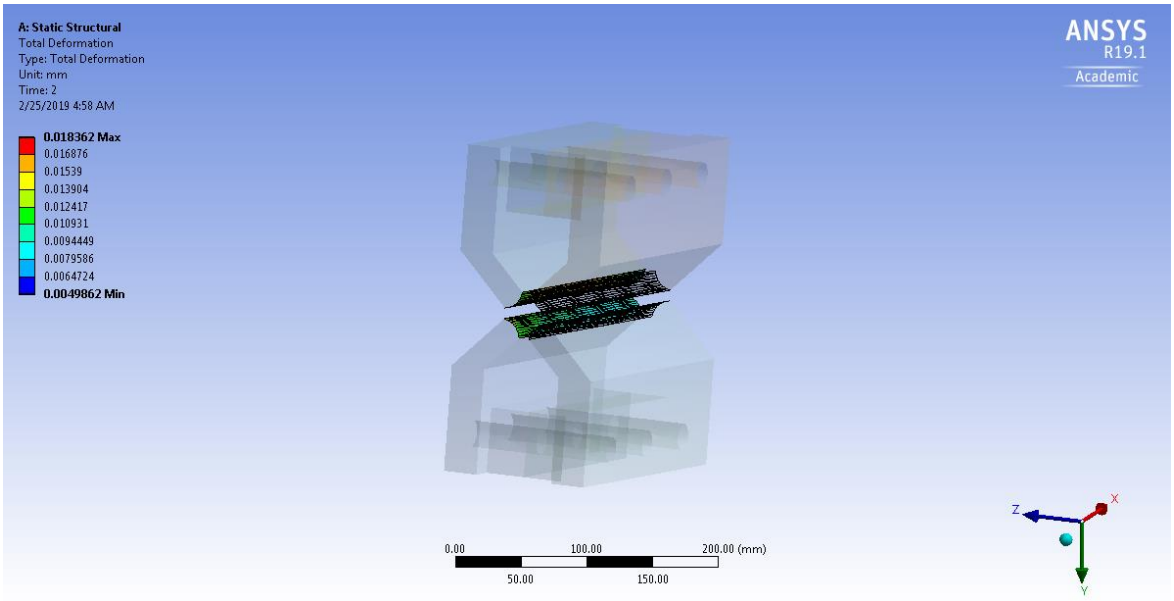

Figure 5.11: 25mm Plates with 3x M20 Pole Deformation

Hence, this basic design was selected. The bottom plate, however, was removed so the bolt pretension can effectively bear more of the magnetic force. Also, it is evident from the simulations that the bottom plate has low stresses and hence it is not an essential element of the frame. Thus, it was important to determine the number and location of the bolts before calculating the optimal thickness because the surfaces where the magnetic force acts will be more accurate. Hence, a more accurate optimal thickness can be obtained.

5.2 Correlation

Correlation is an approach that establishes any statistical relationship between two random variables. Moreover, parameter correlation makes sure that input parameters for a Goal Driven Optimization (GDO) are worth optimizing. The simulation in this project takes about an hour to solve once and, hence, there will be hundreds or thousands of FE simulation to run a Six-Sigma Analysis (SSA). So, it is impractical to use so many parameters for the analysis. The response

surface from the design of Experiments (DOE) study evolves the GDO and SSA simulation runs into function evaluations. In DOE, the number of design points increases with the number of input parameters. Parameters Correlation, thus, helps determine the most/least important input parameters for a given design and also gives a measure of the extent to which the relationship of the parameters is quadratic or linear (Workbench Documentation, 2019).

There are two basic types of correlations: Spearman correlation and Pearson correlation. Spearman correlation is used when the relationship between the two random variables are monotonic in nature. This correlation type uses the ranks of data. Spearman's Rank Correlation is deemed to be a more accurate method. On the contrary, Pearson correlation is used when the two random variables have a linear relationship. This correlation type uses actual data for correlation calculation.

The input parameters for the simulation in the present study possibly do not have a linear relationship and hence Spearman correlation was used to determine the correlation. Even if the input parameters turn out to have a linear relationship, the Spearman correlation should be good enough to calculate the correlation. The Spearman's rank correlation coefficient can be calculated by the following formula:

$$r_s = \rho_{\mathrm{rg}_X,\mathrm{rg}_Y} = \frac{\mathrm{cov}(\mathrm{rg}_X, \mathrm{rg}_Y)}{\sigma_{\mathrm{rg}_X}\sigma_{\mathrm{rg}_Y}} \tag{5.6}$$

where r_s is the Pearson correlation coefficient, cov(rg_X, rg_Y) is the rank variables covariance, σrg_x and σrg_y are the rank variables standard deviations.

5.2.1 Model Setup

For reducing the computation time only half of the frame was used to perform the correlation analysis. The acceleration due to gravity was ignored for this simulation but will be taken into consideration for the full model analysis. Furthermore, the top surface of the flange is considered to be a fixed support as this surface will be clamped to the girder. Also, the effect of bolt pretension has also been ignored. To replicate the presence of the magnets, a frictionless support was used. The frictionless support will restrict the steel plate from deforming in the (frictionless support plane) normal direction. The model setup for the correlation study is shown in Figure 5.12. Moreover, the full magnetic force was assumed to be bored by the stud holes. MultiZone meshing

was used for this simulation. A broader description of the reason behind choosing such a mesh will be described in the next chapter.

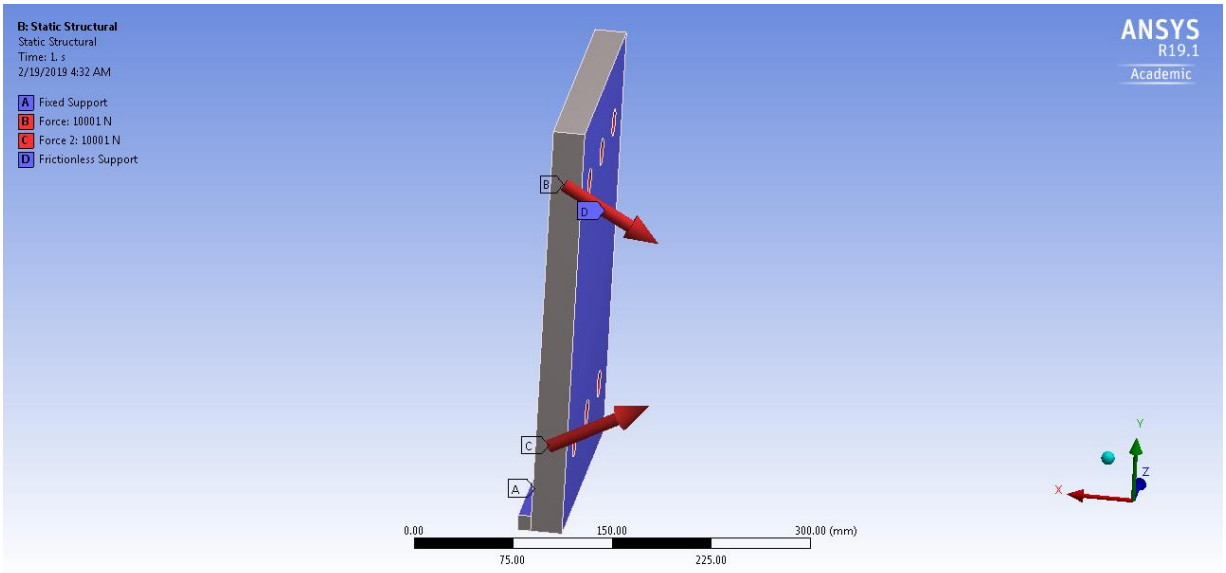

Figure 5.12: Correlation Model Setup

For the Modal analysis, the same fixed support was used. The project schematic is shown in Figure 5.13.

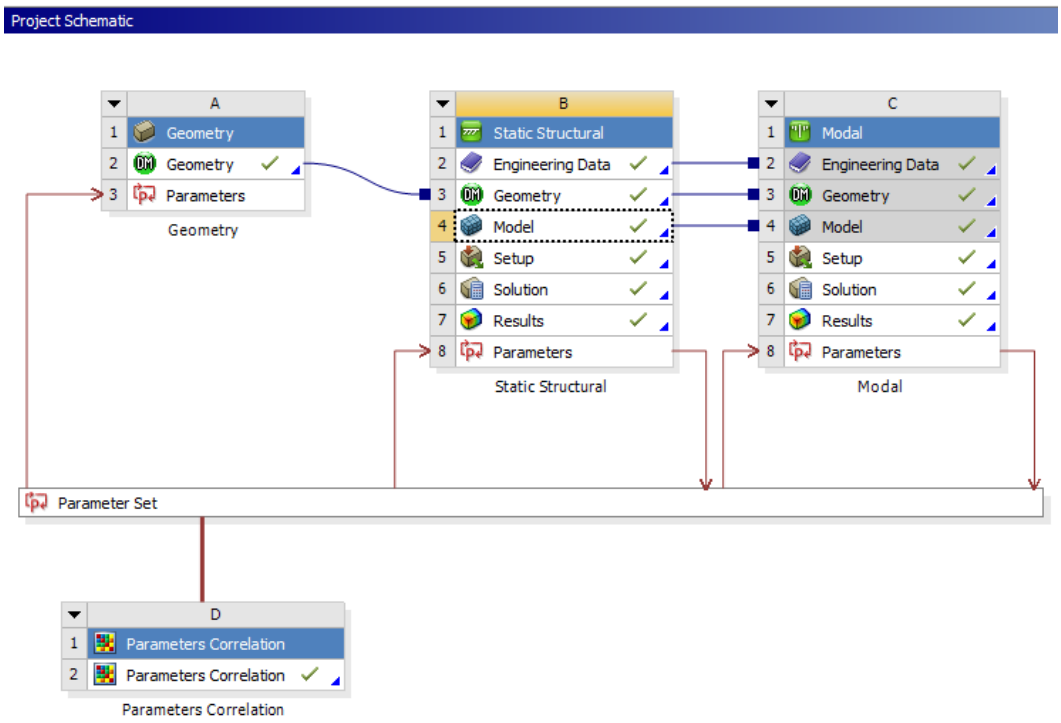

Figure 5.13: Correlation Project Schematic

Relevance threshold was set to 0.7. The frame thickness was varied from 10 to 80 mm. The Young's modulus for metals usually varies between 45 GPa to 407 GPa (amesweb.info). The Poisson's ratio for most materials varies from 0 to 0.5. Other dimensions of the frame were also included in the correlation study. This project was also intended to explore unconventional materials, hence, such a wide range of material properties was considered. The observed output parameters were: Equivalent Stress Maximum, Total Deformation Maximum and Fist Mode of Natural Frequqncy.

5.2.2 Correlation Results with Discussion

The Correlation Matrix contains the Correlation Coefficient between each element in the matrix. Further, the Correlation Coefficient is the degree to which two variables are related. When the correlation value gets closer to 1 or -1, it indicates a strong relationship. A correlation value of 1 signifies a positive correlation i.e. when the value of one variable increases the other also increases. Similarly, a correlation value of -1 implies a negative correlation i.e. when the value of one variable increases the other decreases. For Spearman correlation, the correlation value is equal to the rank values of the parameter pair linear fitting R^2. Consequently, the Correlation Matrix is the visualization of this information (Table 5.3).

Table 5.3: Correlation Matrix Chart

Table of Schematic D2: Parameters Correlation

	A	B	C	D	E	F	G	H	I
1	Name	P1 - Frame_Thickness	P2 - Baseplate_Thickness	P3 - Baseplate_Length	P12 - Young's Modulus	P13 - Poisson's Ratio	P7 - Equivalent Stress Maximum	P14 - Total Deformation Maximum	P15 - Total Deformation Reported Frequency
2	P1 - Frame_Thickness	1	-0.0065533	0.003544	-0.0022164	0.0024882	-0.81678	-0.48601	-0.058366
3	P2 - Baseplate_Thickness	-0.0065533	1	-0.00083617	-0.0057539	0.0026682	0.083182	0.046525	0.30979
4	P3 - Baseplate_Length	0.003544	-0.00083617	1	-0.0019548	-0.00036117	0.0068432	0.03894	0.12583
5	P12 - Young's Modulus	-0.0022164	-0.0057539	-0.0019548	1	-0.0063307	0.030391	-0.61878	0.81258
6	P13 - Poisson's Ratio	0.0024882	0.0026682	-0.00036117	-0.0063307	1	-0.021238	-0.026877	0.085039
7	P7 - Equivalent Stress Maximum	-0.81678	0.083182	0.0068432	0.030391	-0.021238	1	0.51762	-0.12775
8	P14 - Total Deformation Maximum	-0.48601	0.046525	0.03894	-0.61878	-0.026877	0.51762	1	-0.57691
9	P15 - Total Deformation Reported Frequency	-0.058366	0.30979	0.12583	0.81258	0.085039	-0.12775	-0.57691	1

Linear Correlation Matrix

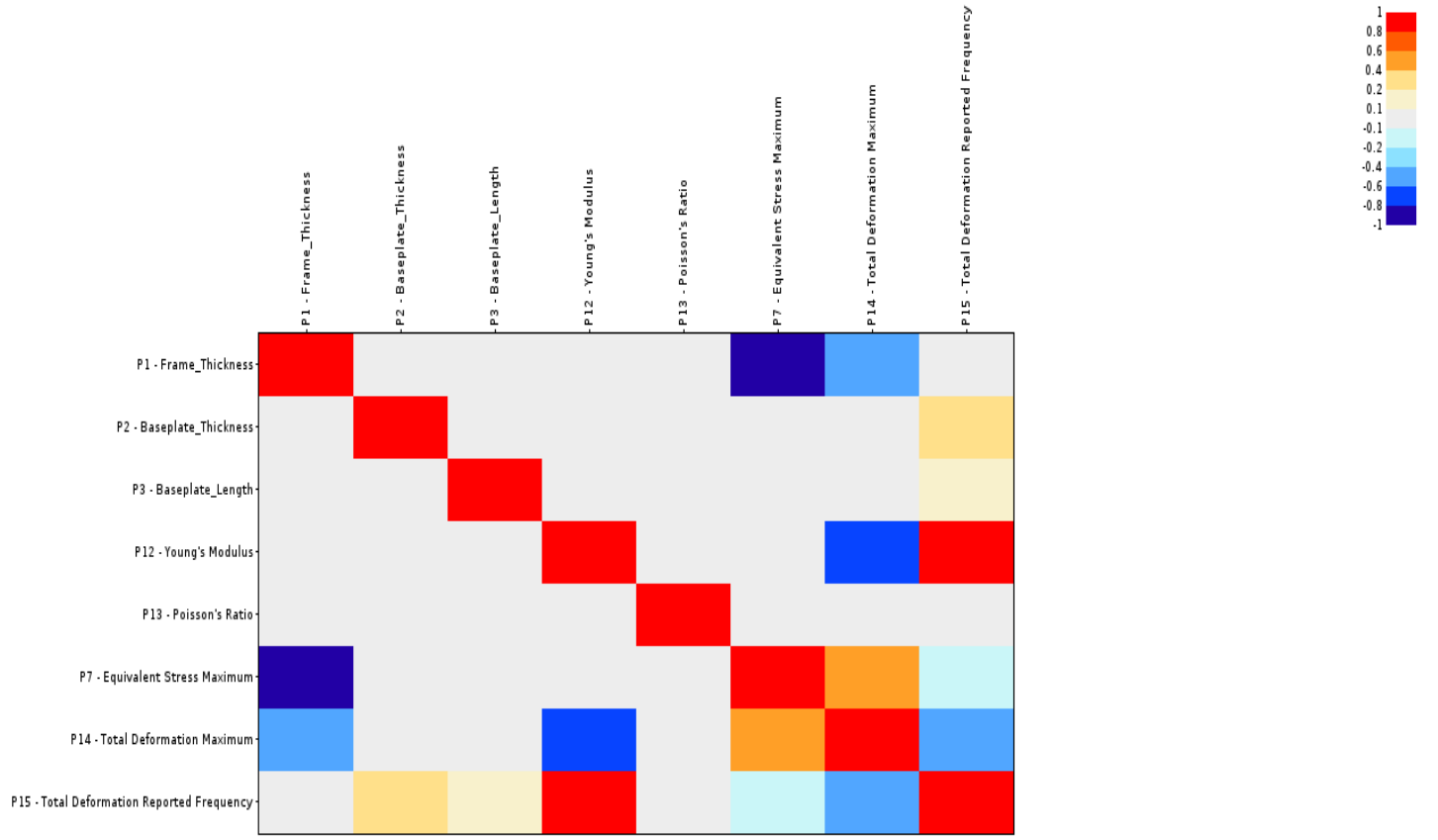

From the correlation analysis, it was concluded that the Total Deformation Maximum and the first mode of natural frequency are influenced by the Young's Modulus of the material and Equivalent Stress Maximum is dependent on the Frame Thickness. The baseplate height and the baseplate thickness did not have much effect on the output parameters. Hence, a suitable material has to be selected with a high modulus of elasticity and the Frame Thickness has to be optimized. Further, the poisson's ratio is not correlated with any other parameter as the simulation is linear.

5.3 Material Selection

A cost-effective material with the high modulus of elasticity was picked for designing the frame. The dimensions of the frame largely depends on the force that the poles exert on each other. Other magnet designs whose poles exert lower forces on each other can be explored. It is possible to build magnets that do not need frames to hold them in place. Exploring this possibility and comparative cost study while taking into consideration the magnetic field property requirements can be interesting but not in the scope of this work. As the design requires tolerances of the order of microns, a balance was struck between the effect of the tolerances and cost. The regions on the frame that experience lower stress can be removed by topology optimization to reduce cost. The modulus of elasticity of the frame material determines the structure's stiffness as well as it's resistance to deformation caused by magnetic forces. The alignment constraints also depend on the cost of the system. There is a trade-off between how much time will be spent on aligning one magnet and installing expensive alignment mechanisms. As a design constraint, the cost of the entire assembly (Frame + Magnet) can not exceed 10,000 CAD (Dallin, 2018). The material pool from which an optimal material was chosen is as follows:

- *304 Austenitic Stainless Steel* containing 18-20% chromium and 8-10.5% nickel can be used as the material for the support structure. Austenite steel has a Face Centered Cubic crystal structure which makes it nonmagnetic. It is the most common grade with 18% Cr and 8% Ni. It has an elastic modulus of 193 GPa (WorldStainless.org).
- *316 Austenitic Stainless Steel*, molybdenum-alloyed steel, has no reaction to magnetic fields. It is composed of 16-18%, chromium and 10-14% nickel, 2-3% of molybdenum and other elements in different concentrations. This grade of steel has the same elastic modulus as 304SS.

- Co-35Ni-20Mo-10Cr alloyMP35N® has an elastic modulus of 235 GPa (Lu et al., 2017). It was reported to be good for super-conducting and pulsed magnets reinforcement. This alloy is also highly corrosion resistant and has high strength. However, this material is more expensive than Stainless Steels.
- *Aluminium* has also been used in the support structure for magnets because of their manufacturing ease, its lightness and its nonmagnetic nature (Eklund et al., 2013, 2014). However, aluminium is sensitive to fatigue and it is better to use nonmagnetic steel instead.
- *Glass Fibre Reinforced Polymer* composites can also be used as support structure material. Magnetic resonance imaging equipment was supported by GFRP reinforcing bars as these machines contain sensitive magnets that can not endure steel presence (Hashmi, 2017). Further, glass fibre epoxy composite pre-compression rings have been proposed to be used in the International Thermonuclear Experimental Reactor (ITER) magnet support structure in order to reduce fatigue and coil deformation due to the strong magnetic field (compositesworld.com). GFRPs have better mechanical properties than steel and are nonmagnetic as well. Their use in synchrotron magnet support structure has not yet been explored. However, the elastic modulus of glass fibre is lower than stainless steel (Muhammad et al., 2015).

Design optimization tool was used to pick the most appropriate material for the system while considering the expenses required. Multi-Attribute Decision-Making problem is encountered when there is an alternative set with multiple characteristics from which a decision is made by analysis and evaluation. Techniques by which Multi-Attribute Decision-Making problems can be solved are Analytic Hierarchy Process (AHP), Simple Additive Weighting method (SAW) and Technique for Order Preference by Similarity to Ideal Solution (TOPSIS). In order to solve the Materials Vs Cost problem, the Analytic Hierarchy Process (AHP) developed by Prof. Thomas L. Saaty (1980) was used as it takes into account both subjective and objectives aspects of a decision.

The AHP process combines individual performance indicator to one key performance indicator by assigning each indicator different weights. AHP is a very effective decision-making tool used in the current industry. Furthermore, this method inspects the decision maker's evaluation consistency hence reducing biasness in the process. A flowchart of the AHP method is shown in Figure 5.14.

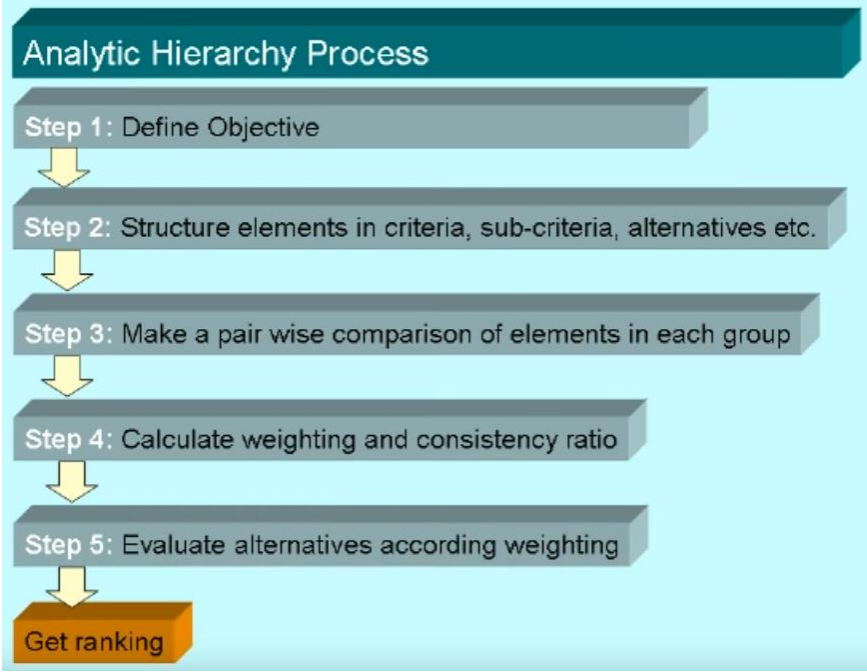

Figure 5.14: Analytic Hierarchy Process Flowchart (Goepel, 2010)

Objective: To select a material for the magnet frame

Criteria:

- Magnetic Property: Non-magnetic, Paramagnetic, Diamagnetic and Ferromagnetic
- Elastic Modulus (E): 70 GPa – 1220 GPa
- Cost: 2.07 - 1,000,000 USD/Kg

Discrete Variables: Aluminium, 304 Austenitic Stainless Steel, 316 Austenitic Stainless Steel, Glass Fibre Reinforced Composite, and Co-35Ni-20Mo-10Cr alloyMP35N®.

The sub-criteria were weighted according to the weights of the main criteria. Then, the alternatives are evaluated. Appendix G includes all the calculations used to find the AHP benefit. Table 5.4 shows the AHP benefit.

Table 5.4: AHP Benefit

Material	**Magnetic Property (77.9%)**	**Elastic Modulus (14.3%)**	**Cost/ton (7.9%)**	**Benefit**
Aluminium	13.63%	0.81%	2.69%	17.13%
304L SS	49.10%	4%	2.28%	55.54%
316 SS	49.10%	4%	1.68%	54.94%
GFRC	49.10%	0.74%	0.97%	50.81%
Co-35Ni-20Mo-10Cr alloyMP35N	12.15%	8.58%	0.28%	21.01%

Therefore, 304L Stainless Steel had the highest ranking. The use of 304L SS can also be validated as even the present CLS used this material in its magnet frames. 316 Stainless Steel was also a reasonable choice of material. India's Indus-2 uses 316 SS as material for the magnet support structure. However, 304L SS is slightly less expensive than 316 SS and has similar material properties. Hence, 304L SS is the best material for the magnet frame in the present scenario.

5.4 Frame Thickness Optimization

The frame thickness had an effect on both the static deflection of the poles from their original position and the first mode of natural frequency. Hence, an optimized thickness was chosen such that it suffices all the technical requirements.

Objective 1: Minimization of deflection

Minimize $f_1 = PL/AE$

$$= PL/btE \quad (5.7)$$

where b is the width and t is the thickness.

Objective 2: Maximization of First Mode of Natural Frequency

$$\text{Maximize } f_2 = 1/2\pi\sqrt{}\,(k/m) \quad (5.8)$$

Objective 3: Minimize Thickness (Surrogate Parameter for Cost)

The function f1 is subjected to two constraints:

Constraint 1: Maximum Stress

The maximum stress should be less than the allowable stress.

$$\sigma_{max} \leq \sigma_{allowable} \quad (5.9)$$

Constraint 2: Resultant Deflection

The final deflection and the tolerance combined should be less than 10 microns (calculated in Chapter 3). So, the deformation should be somewhere between 0 and 10 microns.

$$0 < \delta < 10\ \mu m \quad (5.10)$$

The function f2 is subjected to one constraint:

Constraint 3: Maximum Width

The aim of this project was to minimize the use of drift space (explained in Chapter 1). Thus, the final width of the frame should be less than or equal to the width of the magnet.

$$b_{frame} \leq b_{magnet}$$

Bound Constraints:

$$10 \leq t \leq 80\ mm \quad (5.11)$$

The formula for calculating stress:

$$\sigma = \text{Magnetic Force / Area} = P / bt \quad (5.12)$$

5.4.1 Multi-Objective Genetic Algorithm

The optimization method that was used in this work is the Multi-Objective Genetic Algorithm (MOGA) which is a hybrid variation of the famous NSGA-II (Konak, 2006). MOGA is also based on the controlled elitism concept. Every input parameter is supported by this algorithm. Further, a faster non-dominating sorting scheme is used to perform the Pareto ranking scheme. The non-dominance principle used while handling the constraints and the objectives is the same, hence,

Lagrange multipliers and penalty functions are unnecessary. Thus, this algorithm also ranks the practical solutions higher than the impractical ones.

The flow chart for the MOGA algorithm is shown in Figure 5.17.

.

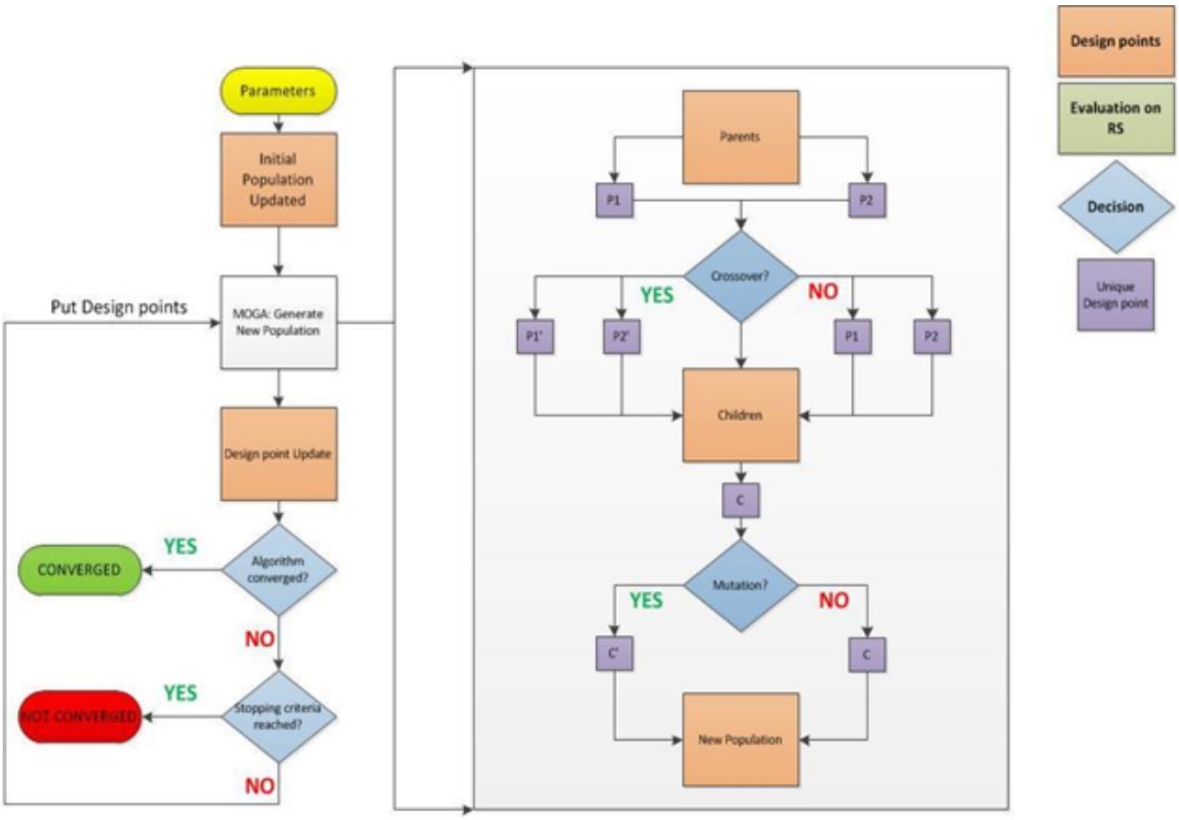

Figure 5.15: MOGA Flow (sharcnet.ca)

The following steps are involved in a MOGA technique:

1) The initial population is generated.
2) Mutation and cross-over are used to generate a new population. Since, the problem in this project deals with the thickness of 304 L stainless steel it has to be a manufacturable value. Hence, the mutation and the cross-over steps to generate a new population for discrete parameters will be used. On the contrary, the concept of cross-over is that an offspring will

have better characteristics than both the parents by combining the best attributes of the parent chromosomes. There are three different types of cross-overs present:

a) *One point:* This operator chooses a point within the chromosome randomly for cross-over and then swaps the two parent chromosomes to generate two new offspring chromosomes (Figure 5.18).

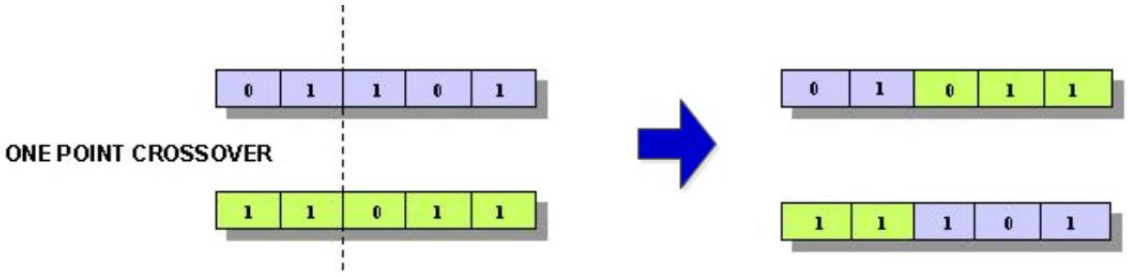

Figure 5.16: One Point Crossover (sharcnet.ca)

b) *Two-Point:* Two random points are selected by the operator for cross-over in the parent chromosomes and between these two points the exchange happens to form two new chromosomes (Figure 5.19).

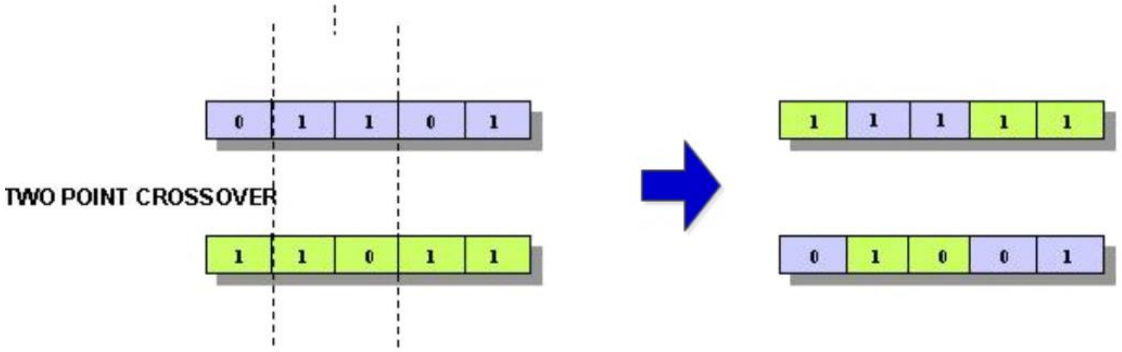

Figure 5.17: Two-Point Crossover

c) Uniform: The operator chooses a mixing ratio which is a measure of the genetic contribution of each parent chromosome in the offspring chromosome (Figure 5.20).

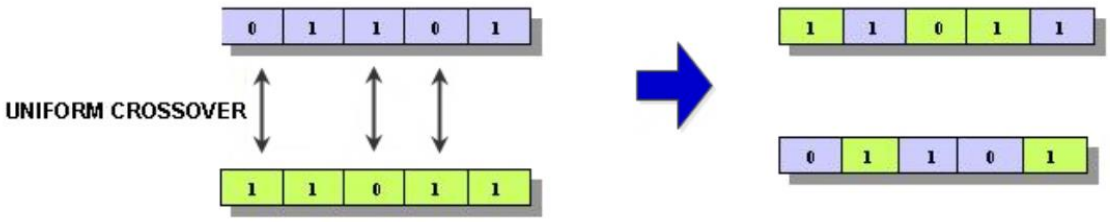

Figure 5.18: Uniform Crossover

d) The mutation changes one or more genes from the parent chromosome. It can introduce a completely new gene into the gene pool, and, hence, converge to a better solution. Moreover, a user-defined mutation probability determines the probability of mutation. In a Manufacturable Values parameter problem, the mutation operator exchanges the gene value with a 1/2 probability.

3) The update of the design points in the new population takes place.
4) The validation of the convergence for the optimization occurs:
   a) Optimization converged: Convergence Stability Percentage or Maximum Allowable Pareto Percentage is achieved.
   b) Optimization not converged: The next step continues.
5) The validation of Stopping Criteria in case the optimization did not converge:
   a) If the control meets the stopping criteria when the Maximum Number of Iterations criterion is met then the process will be stopped even when the convergence is not achieved.
   b) If the control does not meet the stopping criteria then MOGA will regenerate new population i.e. Step 2.

   Unless Stopping Criteria is met or the Optimization Converges, Steps 2 to 5 will be repeated.

5.4.2 Setting up the Optimization

The model used for optimization was the same as used in the correlation study (section 5.1.1). The only difference is that the material properties for 304L stainless steel were used. The elastic modulus of 193 GPa and a poison's ratio of 0.29 was assumed (asm.matweb.com). The project schematic is shown in Figure 5.21.

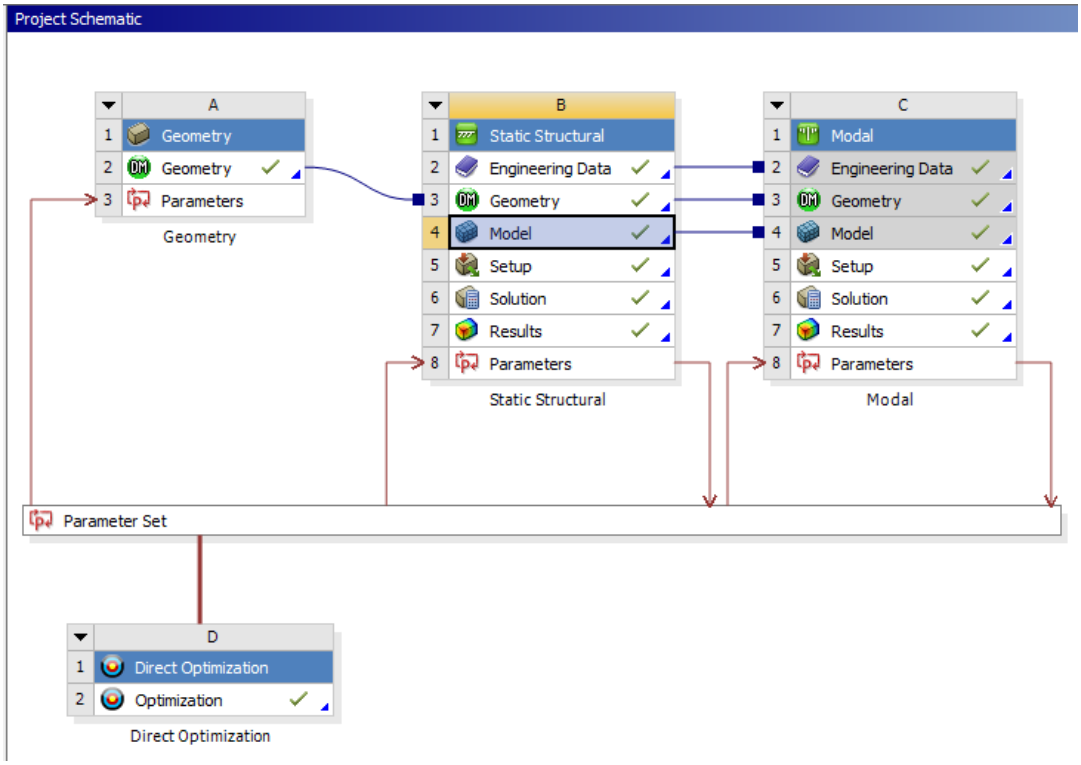

Figure 5.19: Optimization Project Schematic

From the Optimization node in the Properties view, the Method Name was set to MOGA. The number of samples to be used initially was set to 100. Number of Samples Per Iteration was set to 50 and is updated by the control every iteration. Also, the Maximum Allowable Pareto Percentage was set to 70. Maximum Allowable Pareto Percentage is the ratio of expected Pareto points to Samples Per Iteration. Thus, a Maximum Allowable Pareto Percentage of 70% and a Number of Samples Per Iteration of 50 will correspond to convergence once the MOGA optimization resulting front will have a minimum of 35 points. Further, the Maximum Allowable Pareto Percentage should be set somewhere between 55 and 75 because if it is too high the convergence will take time while if it is too low the solution will converge prematurely. On the basis of the output parameter mean and standard deviation, the population stability is checked by the Convergence Stability Percentage criterion. For the present study, the Convergence Stability Percentage was set to 2. Moreover, the convergence is observed when one population is stable with respect to the previous population. The steps involved in the criterion are as follows:

- As the first population is not produced by the MOGA, hence, it is not taken into consideration for the output range reference.
- The range reference is set to be the second population and the mean, the standard deviation, the range, the maximum and the minimum is calculated.
- Scaling the values for the fourth step onwards from a range of 0 to 100 by using the minimum and maximum values is done beginning from the third population. The mean and the standard deviation variations are compared. In case both these values are smaller than the Convergence Stability Percentage, then, the solution has converged.

Thus, convergence is achieved when:

$$\frac{|Mean_i - Mean_{i-1}|}{Max - Min} < \frac{S}{100} \tag{5.13}$$

and

$$\frac{|StdDev_i - StdDev_{i-1}|}{Max - Min} < \frac{S}{100} \tag{5.14}$$

where 'S' is the stability percentage, '$Mean_i$' is the i-th population mean, '$StdDev_i$' is the i-th population standard deviation, 'Max' is the maximum output value of the first generated MOGA population and 'Min' is the minimum output value of the first generated MOGA population.

The Maximum Number of Iterations was set to 20. This number represents the maximum number of iterations the program can possibly run. This also gives an estimate of the number of evaluations necessary for the complete cycle and hence the time needed to complete the optimization. Additionally, the Maximum Number of Candidates was set to 5. For multiple-objective algorithms, it is advisable to request several candidates as there are many potential candidates for each generated Pareto front. The next step in the optimization process is setting up the objectives and the constraints. Subsequently, the parameters identified from the correlation study, i.e. plate thickness would be the dimension to be optimized while observing the deformation, stress and first mode of natural frequency. Table 5.5 below gives a vivid description of the parameters, objectives and constraints.

Table 5.5: Optimization Setup Data

Parameter	Description	Objective	Constraint
P29	Frame Thickness	Minimize	$10 \leq t \leq 80$ mm
P7	Maximum Equivalent Stress	Minimize	≤250 MPa
P27	Maximum Total Deformation	Minimize	$0 < \delta < 10$ μm
P28	First Mode of Natural Frequency	Maximize	>50Hz

5.4.3 MOGA Results with Discussion

Once the optimization process starts with the generation of sample sets begins. All the raw data involved with this calculation is included in Appendix H. After the optimization converges, the points which best satisfy the objectives are presented as the **Candidate Points**. The results of the optimization are shown in Figure 5.22.

Optimization Method					
MOGA	The MOGA method (Multi-Objective Genetic Algorithm) is a variant of the popular NSGA-II (Non-dominated Sorted Genetic Algorithm-II) based on controlled elitism concepts. It supports multiple objectives and constraints and aims at finding the global optimum.				
Configuration	Generate 100 samples initially, 50 samples per iteration and find 5 candidates in a maximum of 20 iterations.				
Status	Converged after 36 evaluations, because all permutations have been evaluated.				
Candidate Points					
	Candidate Point 1 DP 157	Candidate Point 2	Candidate Point 3	Candidate Point 4	Candidate Point 5
P29 - Frame_Thickness (mm)	★ 32	★ 38	– 44	★★ 22	– 46
P7 - Equivalent Stress Maximum (MPa)	★★★ 4.2332	★★★ 3.6528	★★★ 3.535	★★★ 6.2202	★★★ 3.4097
P27 - Total Deformation Maximum (mm)	★★ 0.00097861	★★ 0.00084662	★★ 0.00075793	★ 0.0013656	★★ 0.0007325
P28 - Total Deformation Reported Frequency (Hz)	★★★ 177.86	★★★ 179.06	★★★ 174.56	★★ 155.88	★★★ 172.88

Figure 5.20: MOGA Results

The maximum number of Candidate points was set to 5. So, there are 5 design points that meet the design criteria. Moreover, the number of gold stars shown beside every goal-driven parameter is a measure of how well the parameter satisfied the stated objective. As a result, 22 mm was the least

thickness value but it had a lower first mode of natural frequency. When 32 mm and 38 mm were compared, they were both equally optimal but 32mm would require less material and hence less expensive to construct. Thus, 32 mm was selected as the frame thickness.

To verify the MOGA results, the Adaptive Multiple-Objective and the screening method were used to calculate three candidate points (sharcnet). 32mm, 38mm and 44mm came out to be the optimal candidate points. Hence, The MOGA results can be deemed correct.

5.5 Hole Location in the Magnet Yoke

A parametric study was undertaken to find the best location to drill holes in the magnet which corresponded to less deformation. The model was set up such that all the force in the pole was exerted by the magnet surface. The holes were considered to be fixed support. Symmetry boundary condition was also implemented to best simulate the magnet. A hex-dominant mesh was used. Further, a default mesh size was used which resulted in 11982 Nodes and 4078 Elements. The Static Structural Analysis setup is shown in Figure 5.23.

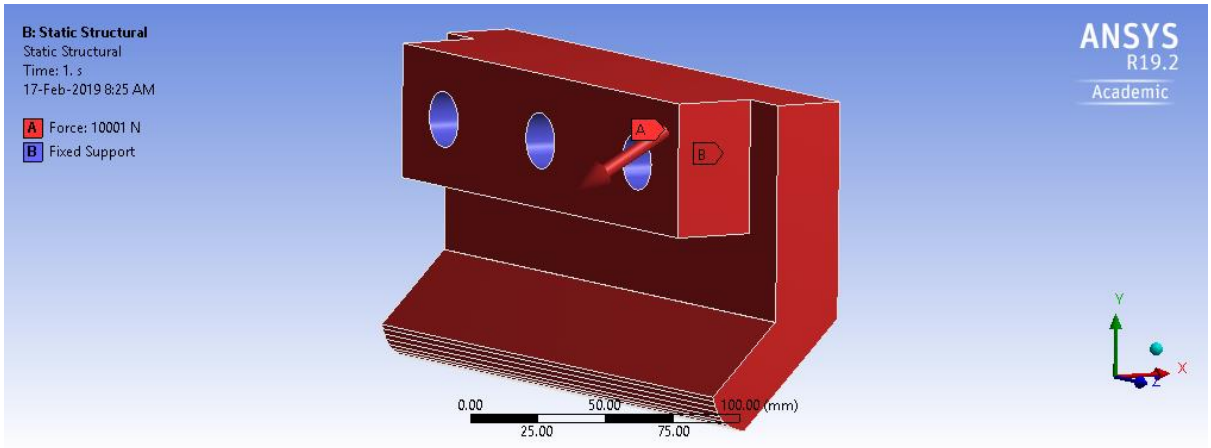

Figure 5.21: Hole Location Parametric Study Setup

The total deformation seemed to reduce as the holes came near to the coil location. The magnetic force was causing a moment in the magnet yoke which resulted in the deformation. Therefore, moving the holes near the front/back surface of the magnet was cancelling the effect if this

moment. The location of the holes and the resulting Total deformation graph in Figure 5.24 below illustrates this. The raw data from this analysis is included in Appendix I.

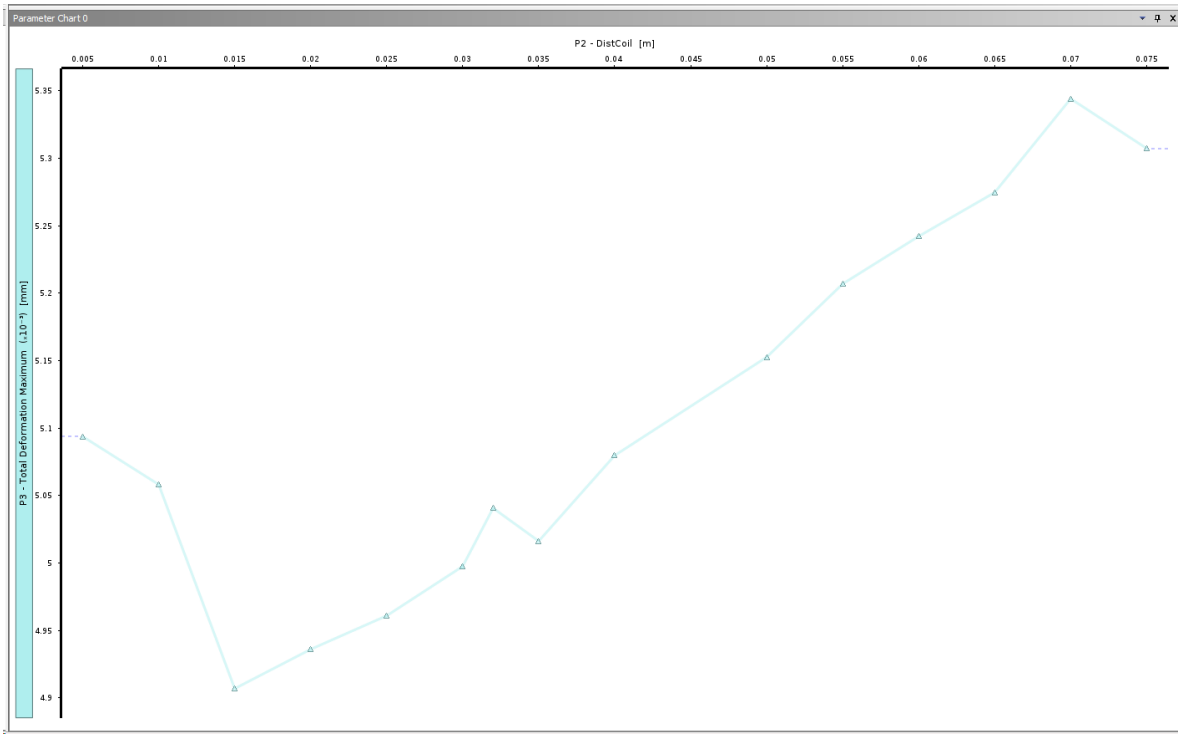

Figure 5.22: Hole Proximity to the Coils (m) VS Total Deformation Maximum (mm)

While keeping in mind that if the hole was too near to the coil there was a high possibility of failure. So, the hole was decided to be located at a distance of 30 mm from the coil on both ends.

5.6 Six Sigma Analysis

The non-technical factors such as variability in manufacturing, material quality, etc. might affect the product performance. Therefore, Six Sigma Analysis (SSA) provides a quantifiable way of ensuring the design will meet the objective(s) probabilistically while taking into consideration the input parameters uncertainty. In order to describe unknown parameters, SSA uses statistical distribution functions. SSA checks whether the design meets the Six Sigma Standard which is manufactured product failure will be encountered 3.4 times out of 1 million instances. Moreover, this standard assumes that a Gaussian distribution is followed by an output variable pertinent to

the performance and quality evaluation. To evaluate the design satisfaction, the output parameter that represents the product performance is used. This output parameter will be within the upper specification limit (USL) and the lower specification limit (LSL) as shown in Figure 5.25 below (SHARCNET):

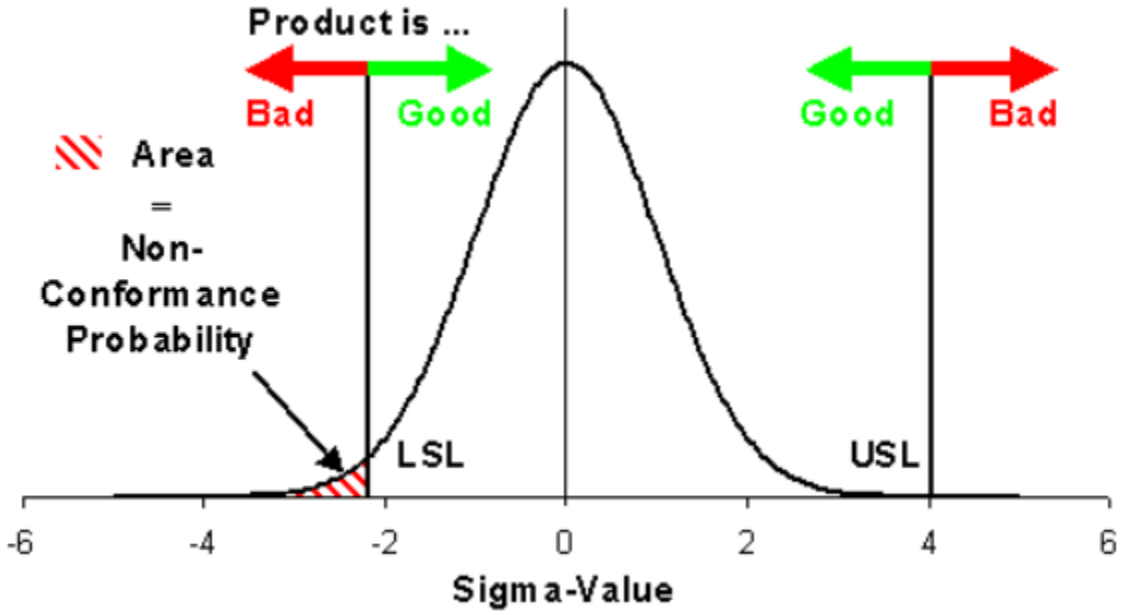

Figure 5.23: Gaussian Distribution

Latin Hypercube Sampling (LHS) technique is used to generate the samples for the six sigma analysis. Further, this process is an efficient and advanced type of Monte Carlo analysis methods. Across the design space, the design points are produced in a square grid, however, input parameters are not repeated for any two points. Compared to Direct Monte Carlo analysis technique, the Latin Hypercube Sampling technique needs 20% to 40% lesser simulations loops to obtain similar results with a similar precision.

5.6.1 Model Setup

The setup was similar to the one used in 5.2.1. However, based on decoupled integrated design, the material properties of 304L stainless steel were used for this analysis. The project schematic is shown in Figure 5.26.

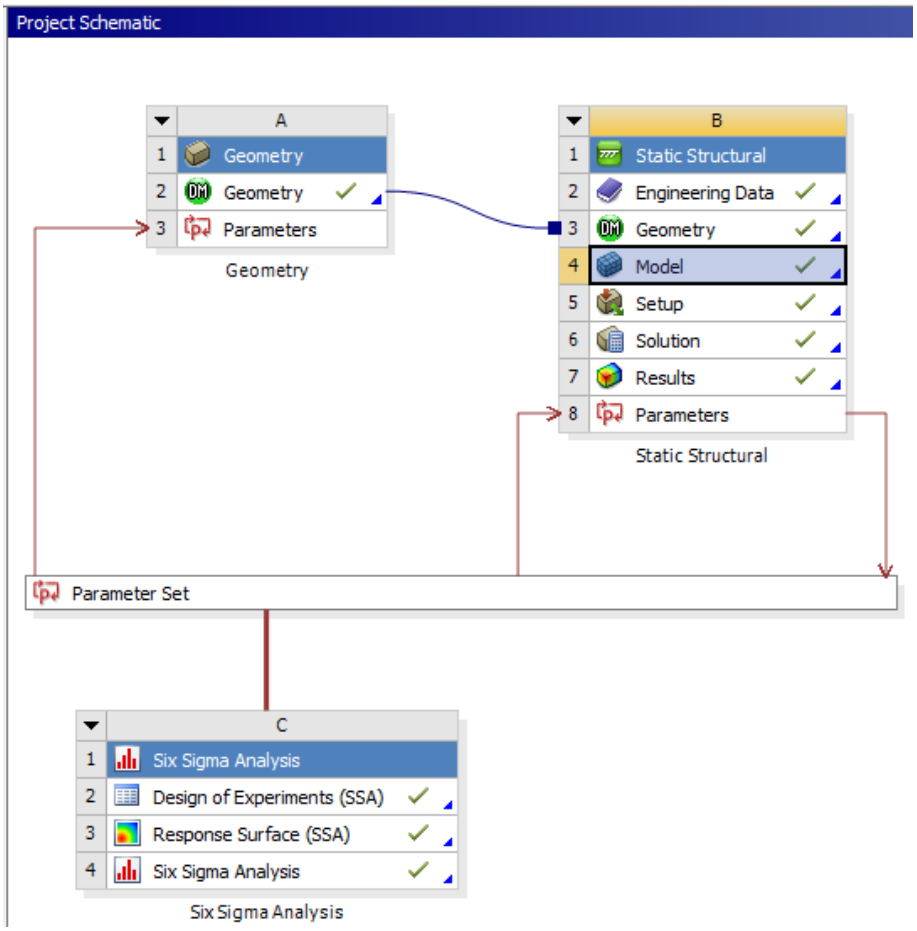

Figure 5.24: SSA Project Schematic

The Young's modulus and the Poisson's ratio were given a truncated normal distribution over the ranges 190000 MPa to 203000 MPa and 0.265 to 0.275 respectively. On the other hand, normal distribution was assigned to all the forces. The frame thickness, frame height, baseplate length and the baseplate thickness were assigned with a uniform distribution with default upper and lower limits.

5.6.2 Results with Discussion

The Equivalent Stress Maximum and the Total Deformation Maximum were the two output parameters that were monitored. The six sigma analysis results are shown in Figure 5.27 and Figure 5.28.

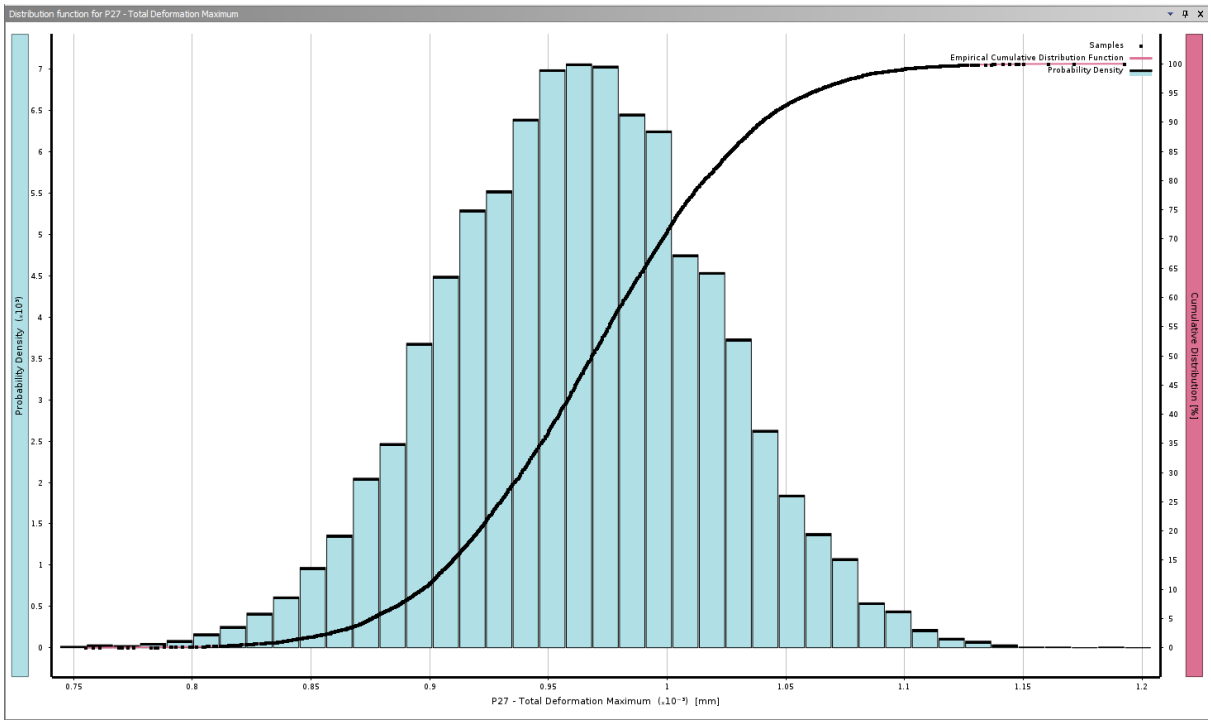

Figure 5.25: SSA for Maximum Total Deformation

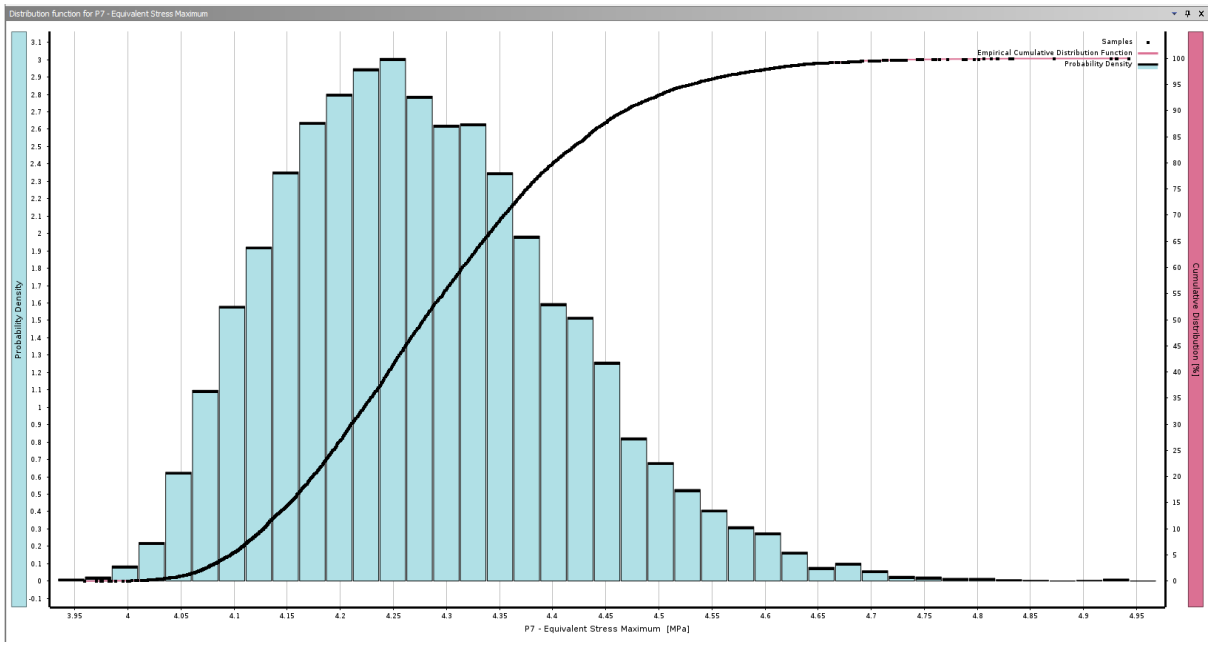

Figure 5.26: SSA for Maximum Equivalent Stress

The Maximum Total Deformation distribution function showed that under uncertainties the deformation was always under the 10 microns limit. In addition to that, the Maximum Equivalent Stress distribution function shows that the stress developed when exposed to uncertainties was always under the yield stress of 304L Stainless Steel (210MPa). In other words, the maximum total deformation and the maximum equivalent stress of 3.4 out of 1 million instances was below 1.2 microns and 4.95 MPa respectively. Hence, the design passed the six sigma criteria and was robust.

5.7 Flange Location

The next stage in the design phase was the determination of the flange location. Subsequently, two configurations were taken into consideration: placing the flanges on the inside near the magnet and placing them on the outer face. The present CLS has the flanges placed inside. Hence, this configuration was tested first. The optimized number of fasteners, material plate thickness was used in this analysis as per Decoupled Integrated Design methodology.

5.7.1 Flanges Placed-Inside Configuration

In conjunction with the contacts presented in Table 5.2 the following contact properties (Table 5.6) were also included for the present analysis:

Table 5.6: Contacts Definition for Flange Location

Mating Part 1	Mating Part 2	Contact Type
Top Frame	Bottom Frame	Frictional
Washer	Frame	Frictional
Washer	Nut	Frictional
Rod	Washer	Frictionless

A multizone mesh was assigned to the nuts, washers, rods and coils. The frame was given a fine hex-dominant mesh. The magnet had default tetrahedron mesh. Thermal conditions and static structural conditions similar to section 5.1 were used. The bolt pretension for the flange M8 fasteners was calculated using equation 5.4 and 5.5 to be 4272.6 N.

The directional deformation in the horizontal direction was unacceptable as shown in Figure 5.29.

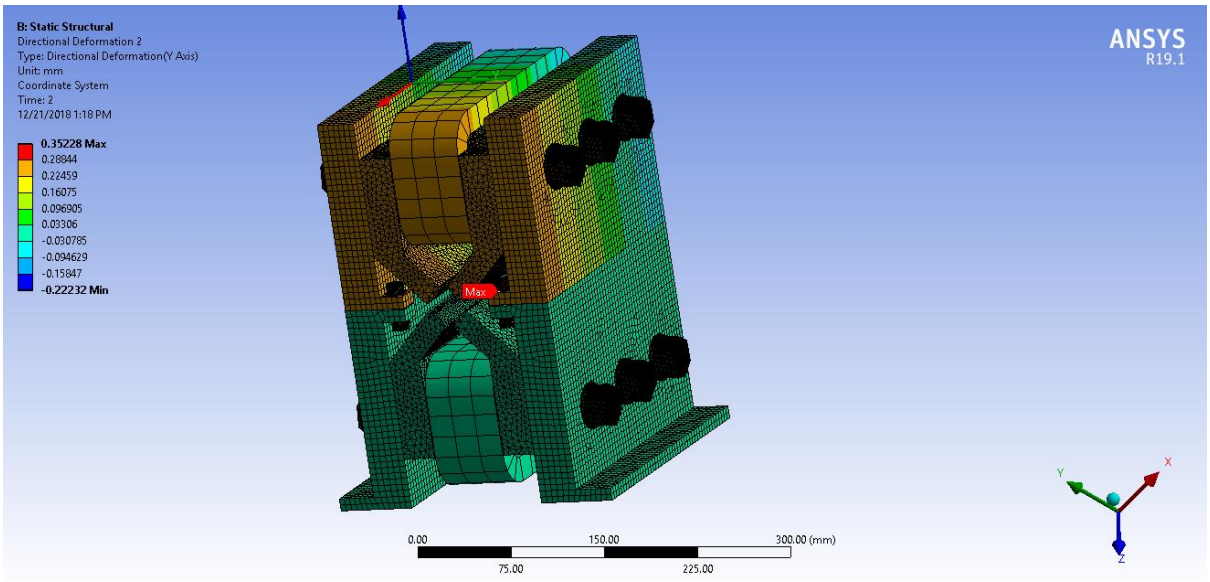

Figure 5.27: Flanges Inside-Configuration

This simulation suggested that more fasteners were required for resisting the twisting force of the magnet. However, if more fasteners were placed in the same configuration then the tightening the nuts to the rod becomes difficult. Using bolts with larger diameter had the same limitation. Hence, the flanges were considered to be placed on the outer side of the frame for more space availability.

5.7.2 Flanges Placed-Outside Configuration

Two fasteners with larger nominal diameter were used in this analysis subjected to the same thermal and static loading conditions. M12 bolts were selected for a better grip. Further, the bolt pretension using equations 5.4 and 5.5 was calculated to be 7690.6 N. Default mesh size was used. Figure 5.30 shows the Static Structural results for the directional deformation in the y-direction.

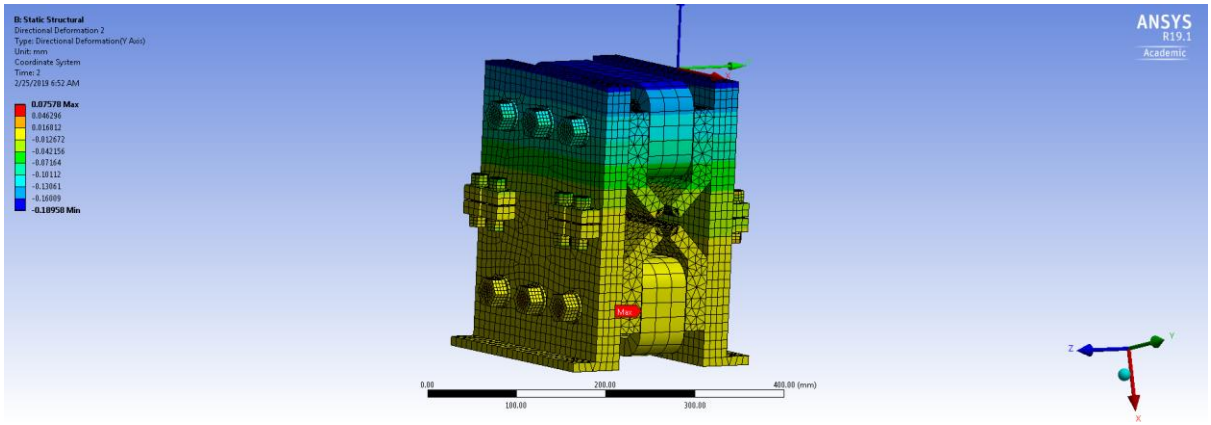

Figure 5.28: Flanges Outside-Configuration

Using this configuration an acceptable deformation was achieved. Additionally, deformation in the x and z (according to RADIA coordinate system) direction was negligible for both cases. However, high stresses that went above the yield stress were obtained near the corners of the flanges. Consequently, this suggested the use of chamfers or fillets to reduce the stress concentration. A chamfer is less expensive, less time consuming to manufacture and has a simpler tool requirement (Kupiec, 2016). It was also observed using simulations that chamfers were more effective in removing stress concentrations than fillets. Thus, chamfers were picked over fillets in this scenario.

5.8 Topology Optimization

Topology Optimization enables the computation of an optimal structural design from the input geometry while achieving certain objectives and maintaining constraints within a specified region. Moreover, the basis of this algorithm is the loads and the boundary conditions that are defined in the preceding analyses.

5.8.1 Model Setup

The model set up was similar to section 5.2 except for the definition of the frictionless support. In order to imitate the presence of the magnets in the analysis, two rectangles having similar dimensions as the magnet surface that was in contact with the frame with an infinitesimally small thickness of 0.0001mm were assumed to be the frictionless support. Consequently, this makes

more frame surface available for topology optimization. The element type was Multizone. 304L Stainless Steel was used as the material. Based on Decoupled Integrated Design, the frame thickness was taken to be 32 mm. Also, the mesh size was default. The Static Structural analysis set up is shown in Figure 5.31.

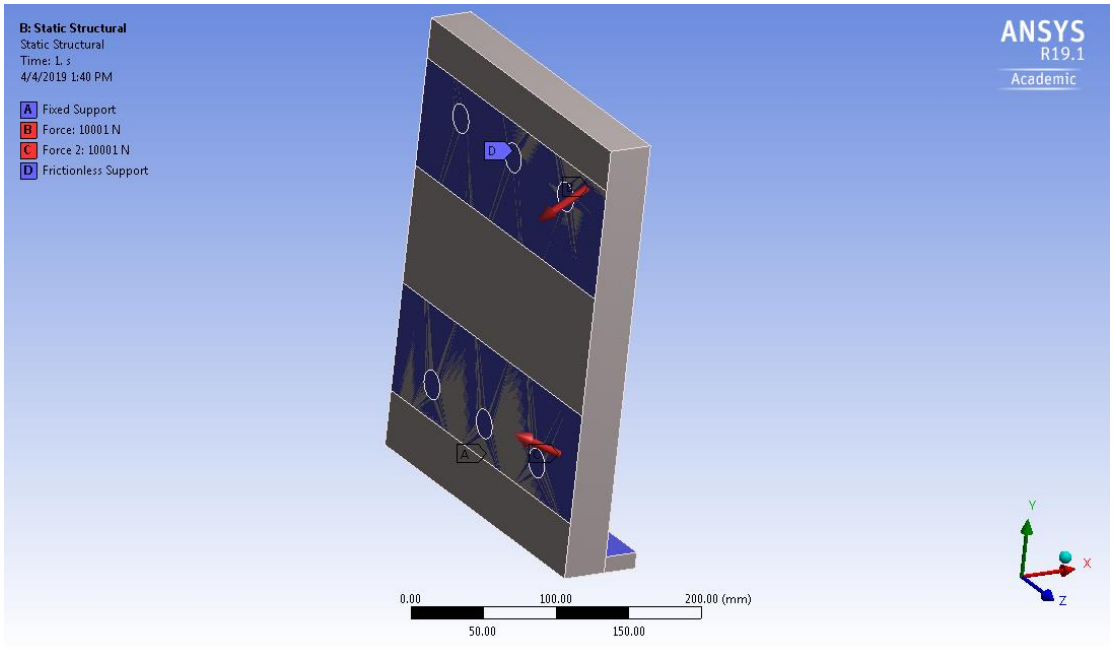

Figure 5.29: Topology Optimization Setup

The model was subjected to the same static loading conditions as the correlation analysis in section 5.2. For the modal analysis, the top surface of the baseplate was assumed to be the fixed support. Further, the analysis reported the first mode of natural frequency to be 133.01 Hz. A detailed description of the modal and the static structural analysis has been included in the following chapter. The project schematic for the topology optimization shown in Figure 5.32.

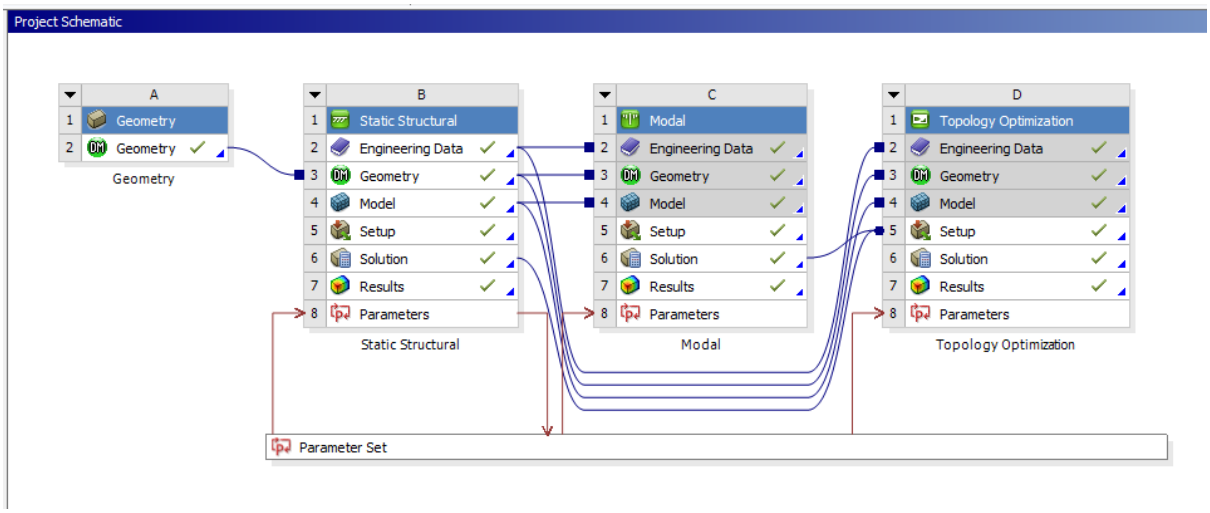

Figure 5.30: Topology Optimization Project Schematic

Default Analysis Settings properties were used. The holes and the bottom plate's top surface were defined as the exclusion region. The holes were necessary to hold the magnet in position via fasteners. Additionally, the top surface of the bottom plate is necessary to clamp the frame to the girder. The rest of the regions as the optimization region (Figure 5.33).

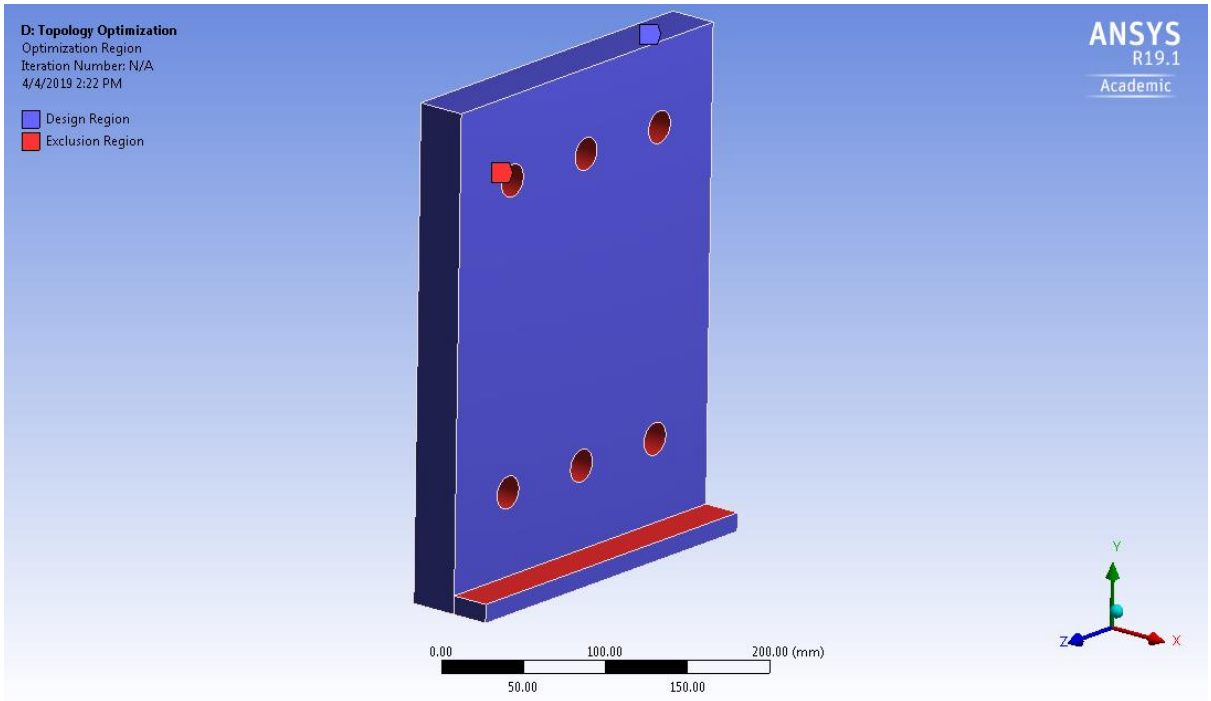

Figure 5.31: Optimization Region

The next step in the setting up the topology optimization problem was specifying the objectives. Two objectives were set: minimizing compliance and maximizing 1st mode of natural frequency (Figure 5.34).

Worksheet

Objective

Right click on the grid to add, modify and delete a row.

Enabled	Response Type	Goal	Formulation	Environment Name	Weight	Multiple Sets	Start Step	End Step	Step	Start Mode	End Mode	Mode
☑	Compliance	Minimize	Program Controlled	Static Structural	1	Enabled	1	1	1	N/A	N/A	N/A
☑	Frequency	Maximize	N/A	Modal	1	Disabled	N/A	N/A	N/A	N/A	N/A	1

Figure 5.32*: Topology Optimization Objectives*

Setting up the response constraints was the next step in the process. The 1st mode Natural Frequency Constraint was set to have a range from 50 to 100000000 Hz (L. Zhang et al., 2001). Moreover, the Displacement Constraint for all the three axes was set to 0.001mm. The Global von-Mises Stress Constraint was set to 205 MPa which is the yield stress of 304L Stainless Steel. In addition to that, an extrusion type manufacturing constraint was defined in the y-axis. This ensured that a consistent cross section was kept in the y-direction so that the design was manufacturable. The Mass Constraint to retain 90% of the mass was set. Reduction in mass will lessen the cost of the system. As the natural frequency does not always increase with the increase in mass (Z. Liu et al., 2016), the mass constraint was set to observe which sections of the frame were unnecessary.

5.8.2 Topology Optimization Solution Methodology

An evolved form of the moving asymptotes (MMA), called the Sequential Convex Programming method (SCP), which takes the derivatives of all the functions present was used to solve the topology optimization problem (Zillober, 1993). Moreover, a series of convex and separable sub-problems are solved by the MMA to approximate the topology optimization problem solution. The sub-problems special structure enables them to be solved efficiently. Therefore, SCP makes sure that the MMA achieves convergence by filtering out the steps that do not result in an optimal solution. Further, a merit function and a line search perform the acceptance test (Zillober, 2001). The merit function measures the progress and combines the constraints and the objectives in a fitting manner.

Optimizing Natural Frequencies: While optimizing the natural frequency, the final mode shape of the optimized geometry may change drastically from the initial mode. Hence, multiple eigenvalues derivatives are calculated in a unique manner. For each optimized element, an additional eigenvalue problem is solved for getting the independent mode shapes sensitivities.

Solving Global Stress Constraints: Solving for global stress constraints in a topology optimization problem requires all the elements to be within the stress upper bound. This theoretically needs the optimization problem solution with 'n' (number of optimized elements) stress constraints. Instead of using 'n' constraints, a few constraints that represent optimized elements clusters are added to reduce computational effort (Holmberg et al., 2013).

Convergence Criteria: The topology optimization solution converges when all constraints are met within 0.1% of the defined limits tolerance. If only one constraint exists, topology optimization problem optimality conditions can be given by the following equation:

$$\|\nabla L(\rho,\mu)\| = 0 \tag{5.15}$$

The Lagrange function, $L(\rho,\mu)$, can be stated by:

$$L(\rho,v) = f(\rho) - \mu\, c(\rho) \tag{5.16}$$

where 'μ' is the Lagrange multiplier, 'c' is the constraint and 'f' is the objective function. The solver stops as soon as the convergence criteria are satisfied, where: ε >0,

$$\|\nabla L(\rho,\mu)\| = \in \tag{5.17}$$

The solver terminates the iterations when three successive iterations of the following equation occur:

$$\left|\frac{f(\rho_i) - f(\rho_{i-1})}{f(\rho_i)}\right| \leq \in \tag{5.18}$$

where ρ_i is the i-th iteration pseudo densities vector.

5.8.3 Results with Discussion

The optimized geometry from the topology optimization is shown in Figure 5.35.

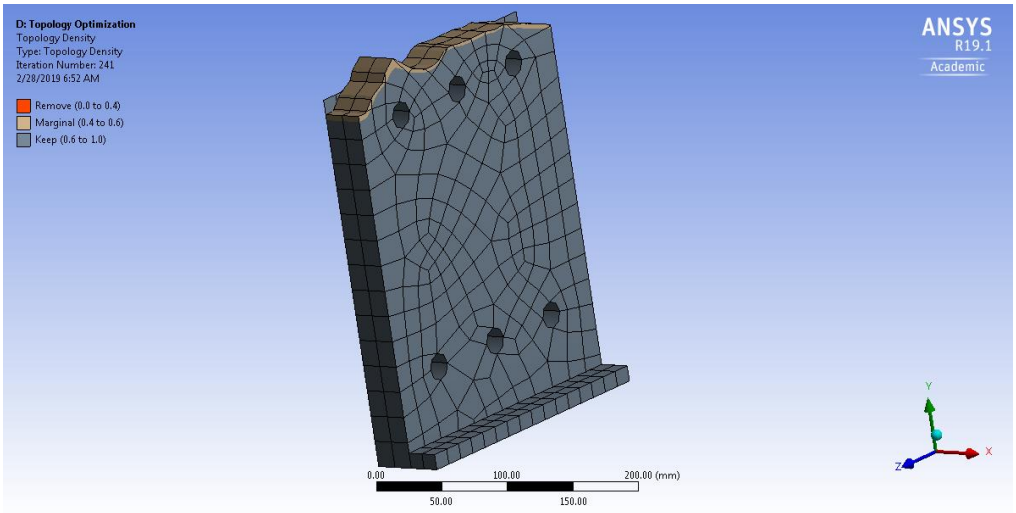

Figure 5.33*: Optimized Topology*

This geometry had a first mode of natural frequency of 151.88 Hz. Thus, an increase of natural frequency was observed from the mass reduction. From the topology optimization results, it can be concluded that a chamfer on the sided of the frame and a lower frame height will increase the natural frequency. Hence, a parametric study by changing the height and the chamfer length was done and the effect on the first mode of natural frequency was observed. Figure 5.36 shows how the natural frequency changes with the chamfer length.

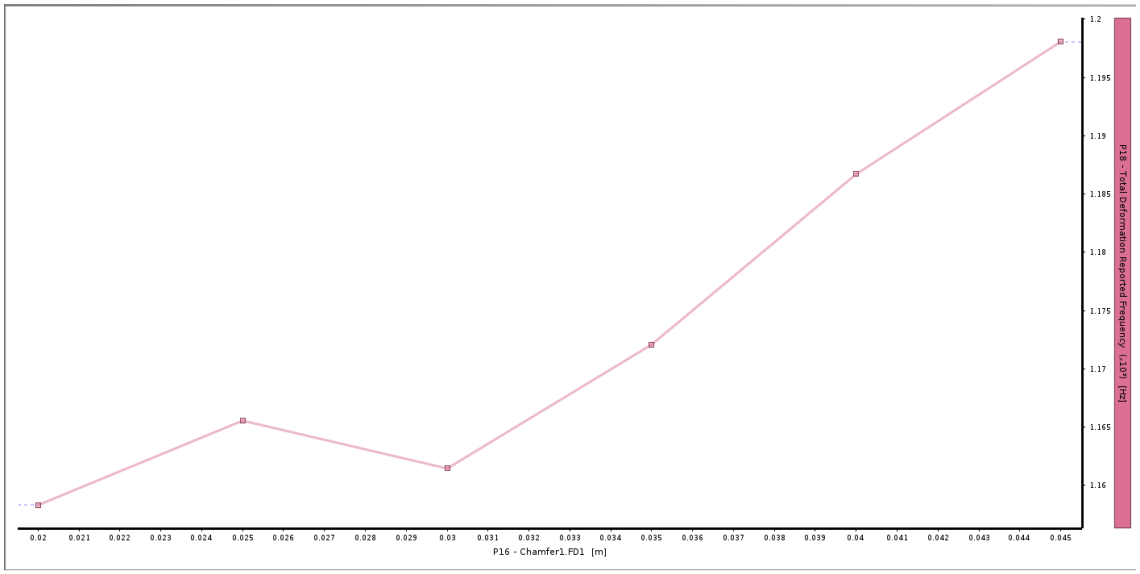

Figure 5.34: First Mode of Natural Frequency vs Chamfer Length

The natural frequency was observed to increase with the increase in the chamfer length (Figure 5.37). A chamfer length of 30 mm was chosen from the last analysis and the parametric study was performed by changing the length of the frame.

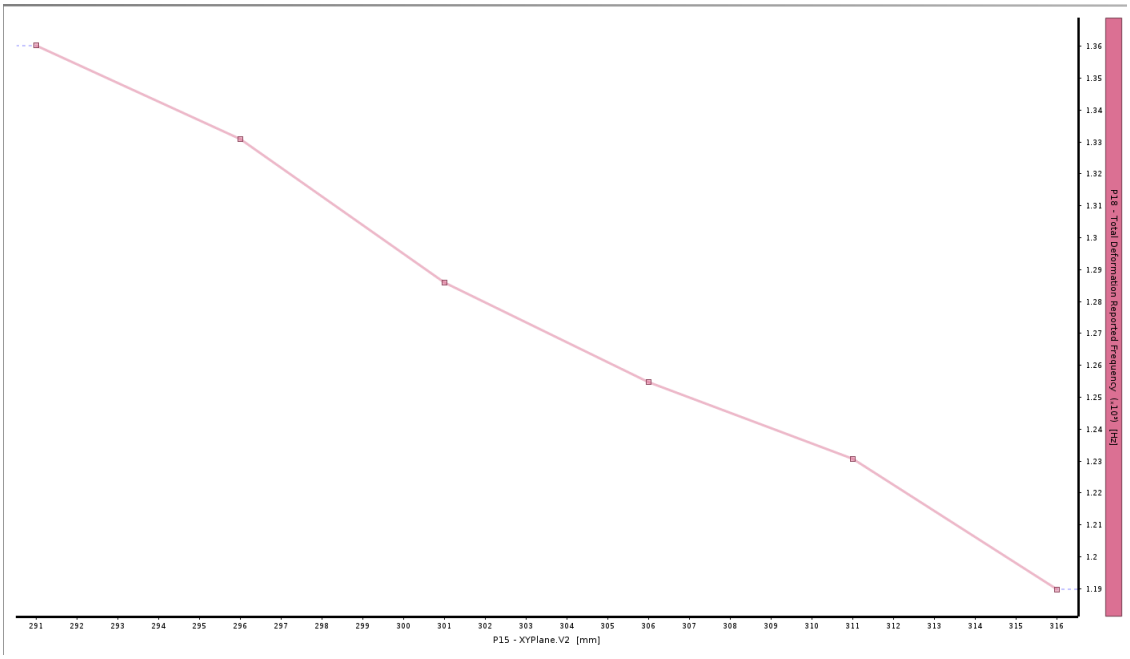

Figure 5.35: First Mode of Natural Frequency vs Frame Height

A frame height of 301 mm was chosen. The first mode of natural frequency for the frame height of 301 and a chamfer length of 30 mm was found to be 150.17 Hz which is comparable to the topology optimized geometry. Hence, the parametric study yielded satisfactory results.

5.8.4 Verification

The optimized frame shape was subjected to static loading and the total deformation was observed to be 0.00099001 mm. The Static Structural results for the Total Deformation is shown in Figure 5.38.

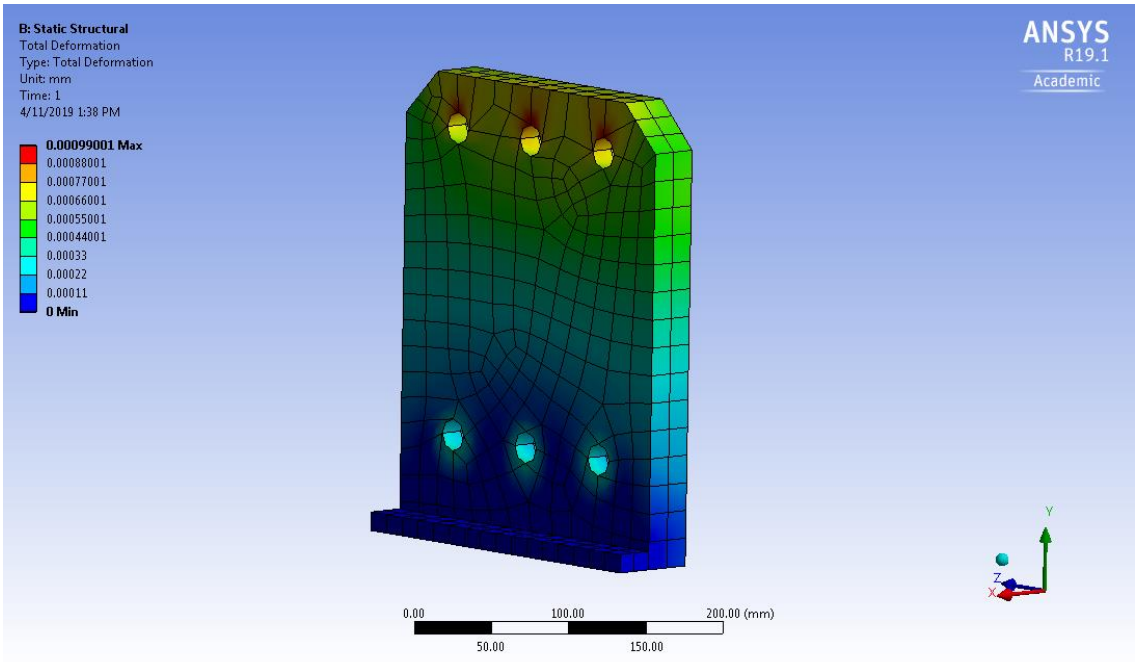

Figure 5.36: Optimized Frame Shape Total Deformation

The following (Figure 5.39) free body diagram was constructed with the available information and Hooke's law was used to determine the deformation in all the three directions:

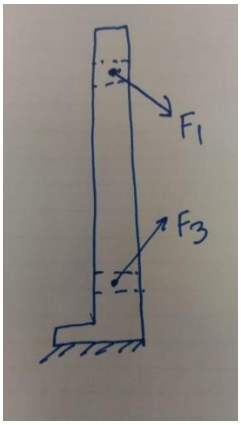

Figure 5.37: FBD Optimized Frame

$\delta = PL/AE$ (5.19)

$\delta_x = 4.28 \times 10^{-6}$ mm

$\delta_y = 2.054 \times 10^{-5}$ mm

$\delta_z = 0.00097$ mm

$\delta_{total} = 0.00099152$ mm

Error percentage is less than 1%, hence, the results can be trusted.

5.9 Final design

In the final CAD model, dowel pins were also included for alignment. However, their design is out of the scope of the present work. Increasing the chamfer length of the flanges seemed to decrease the equivalent stress. Thus, an appropriate chamfer length was chosen that corresponded to a stress below the yield stress. The length of the fasteners connecting the flanges was also adjusted accordingly. The optimized frame design is shown in Figure 5.40. Appendix J contains the general assembly (GA), part drawings and the bill of materials (BOM).

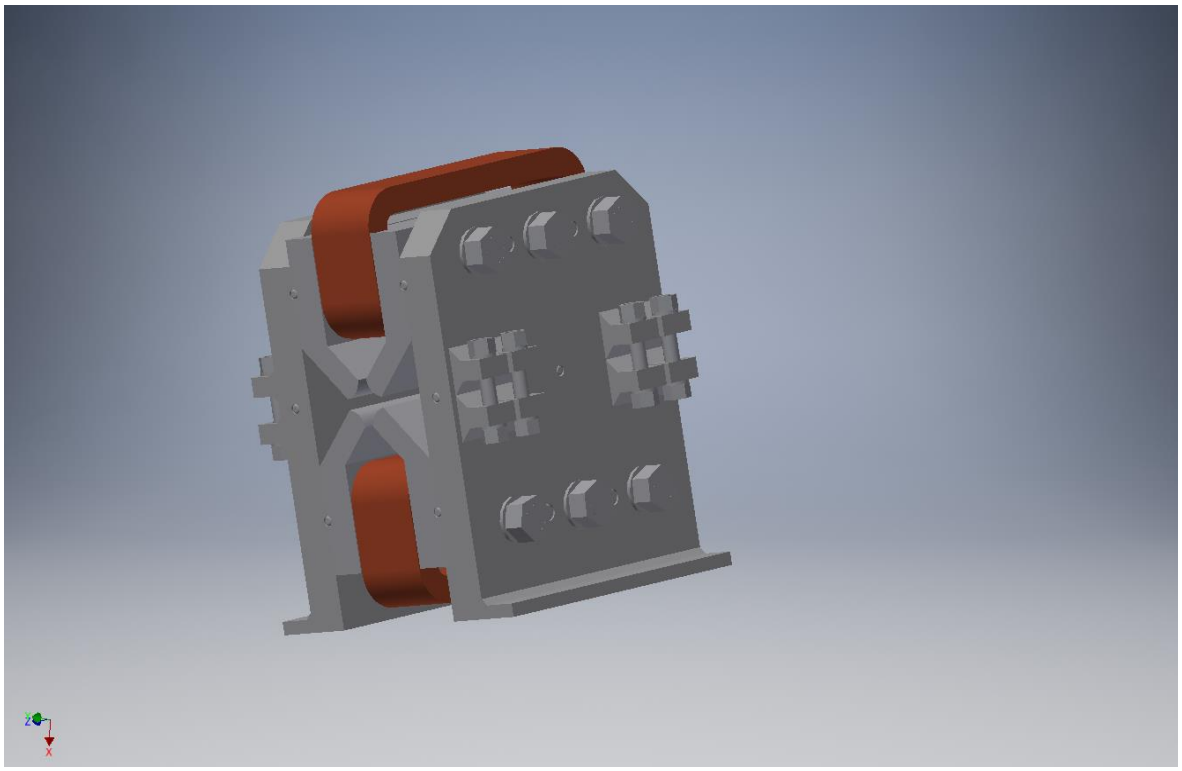

Figure 5.38: Optimized CAD Model

5.10 Conclusion

This chapter deals with the optimization of the frame. The optimization was performed by breaking down the design and optimizing one component at a time (Decoupled Integrated Design). The minimum number of fasteners necessary (three) was decided using a manual optimization technique. Then, a correlation study was performed to determine which parameters are worth optimizing in the time bound work. The material and the frame thickness came out to be the dictating factors in the design. Subsequently, 304L Stainless Steel was selected using the ADH method and a thickness of 32 mm was selected using the MOGA algorithm. After the flange location (outer surface of the frame) and the optimal frame shape (chamfering and reduced frame height) were determined, the final design was formed. Next, the final optimal design was tested in the succeeding chapter.

Chapter 6: Embodiment Design Verification and Validation

The objective of this chapter was to have a validated process in order to calculate the structural response characteristics of the magnet frame such as thermally induced distortion, static deflection, natural frequency and vibration response. The optimized frame developed in Chapter 5 needed to be checked if meet all the design constraints. A thermal load was applied on the frame in conjunction with the magnetic forces to evaluate the total deflection that the poles undergo. The overall pole deflection should be less than 10 microns which was found in Chapter 3. The thermal loading will be calculated from the ANSYS Steady state Thermal Analysis and the total pole deformation and the resulting stresses will be obtained using the Static Structural Analysis module. The dynamic behavior of the frame was also tested by exerting harmonic and random excitations. Modal Analysis was used to calculate the natural frequency and the mode shapes of the frame. The Harmonic Analysis and the Random Vibration Analysis were used to predict the dynamic behavior of the frame.

With the advancement of technology and computer power, prototyping has been reduced to a process of design verification rather than discovery. Moreover, simulations can be referred to as the virtual prototyping stage (LaCourse, 2003). The automotive industry has already adopted this technique (Birch et al., 2016). Although, the primary driving factor for using virtual prototyping in the aerospace and the automotive industry has been testing and production cost reduction, there is obviously a will to design innovative products which have higher performance levels. Therefore, this is homologous to the arena of synchrotron – to design supports for magnets which has higher mechanical stability than previous synchrotron generations. While designing components of a synchrotron, computational and analytical models have been extensively used (Preissner et al., 2016). The CAD model of the components, the material properties, the definition of the boundary conditions, thermal loading and fluid flow conditions are the governing characteristics of the thermal finite element analysis models. Subsequently, the evaluations of these finite element models have proven to be precise to the extent that they are now being used to analyze the failure mechanisms of absorbers in order to improve failure criteria. The world of synchrotron structural dynamics has never witnessed this level of before-hand computational faith. In the workflow shown in Figure 6.1, if the analysis and simulation stage is done flawlessly by identifying properties then the reliability on prototype testing is reduced drastically.

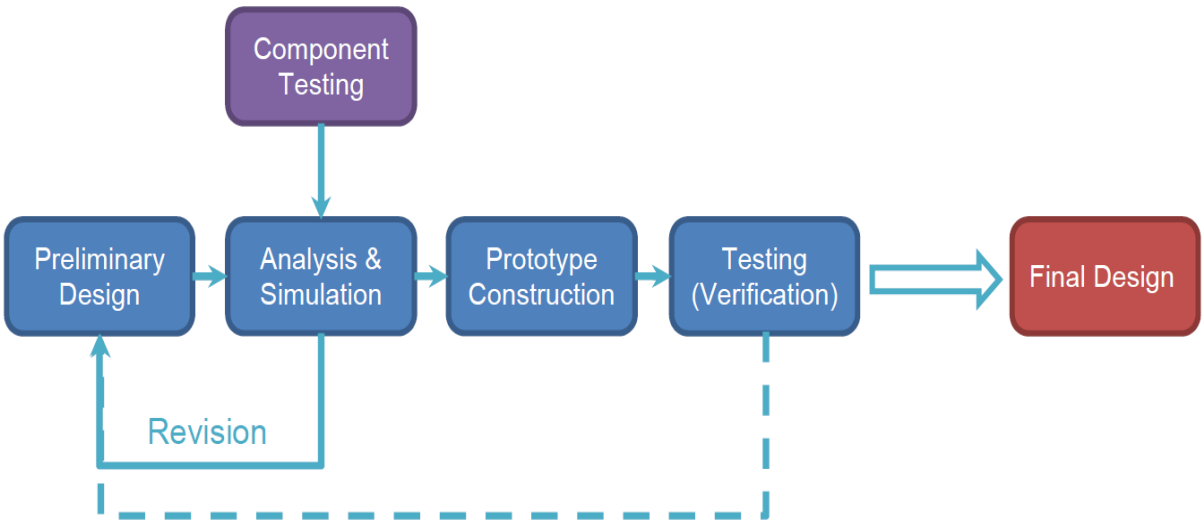

Figure 6.1: Design Workflow (Preissner et al., 2016)

The simulation for the thermal domain is different from that for the dynamic structural domain. The important part in a thermal analysis does not extend component boundaries whereas in structural analysis geometry, stiffness, mass, contact types, etc. play a major role. Moreover, the stress calculation can be done accurately using simulation software, for example, ANSYS. ANSYS takes in geometry, material properties, etc. as input and generates a mathematical model. This mathematical model is a representation of the physical problem based on physical principle and assumptions. Thus, ANSYS solves the mathematical model by producing a numerical solution and get selected variables at selected points. ANSYS 19.1 was used to perform the simulations.

This chapter aims at evaluating the support structure developed by the various stages of optimization in Chapter 5. The model was subjected to thermal and static loads, and the mode shapes were determined to find out the random and harmonic vibration response. Each of the following analysis descriptions consists of a brief introduction to the type of test, followed by the simulation setup, governing equations, results and discussion and verification of the simulation.

6.1 Thermal Load Calculation (Steady-State Thermal Analysis)

Steady-state thermal analysis was used to determine the heat load on the model. The main purpose of this analysis is to subject the frame to thermal conditions which it will experience inside the storage ring.

6.1.1 Simulation Setup

All the materials were assumed to be linear isotropic. The material properties were inputted as shown in Table 6.1.

(All the data below was retrieved from matweb.com)

Table 6.1: Engineering Data

Material	**Thermal Conductivity (W/m K)**	**Elastic Modulus (GPa)**	**Poisson's Ratio**	**Density (g/cm^3)**
1010 Steel	49.8	210	.27	8.96
304 L Stainless Steel	15	193	.29	8
Copper	386	128	.36	8.96

The final model in Chapter 5 was drafted using Autodesk Inventor Professional 2016 and this geometry was imported to perform the necessary evaluations. 1010 Steel, 304 L Stainless Steel and copper were assigned to the magnet, the support system and the coils respectively. Further, a new coordinate system was defined which was in alignment with the RADIA coordinate system. Setting up the contacts and mesh are the next steps to carry out the simulation. However, these are fairly complicated phases, and, hence, are described in detail in separate sections which are as follows:

Two surfaces are in contact when they touch each other in such a way that they become mutually tangential to each other. Bodies in contact do not penetrate each other and can transmit tangential friction forces and compressive normal forces. However, the bodies can not transfer tensile normal forces and hence they are free to separate from each other. In order to enforce contact compatibility, the program uses contact algorithms to prevent interpenetration of the contact pair. The three major types of contacts encountered in the present work are Bonded, Frictional and Frictionless. ANSYS considers frictionless and frictional contacts as non-linear contacts. Furthermore, Pure Penalty or Augmented Lagrange contact algorithms can be used to solve non-linear solid body contact of faces. Both these algorithms are penalty-based contact formulations:

$$F_{normal} = K_{normal}\, x_{penetration} \qquad (6.1)$$

where F is the contact force, K is the contact stiffness and x is the contact penetration (Figure 6.2). The contact stiffness is indirectly proportional to the penetration (Workbench Documentation, 2019).

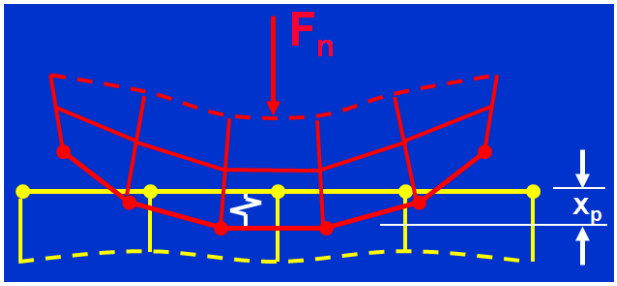

Figure 6.2: Contact Definition (Workbench Documentation, 2019)

On the contrary, Augmented Lagrange and Pure Penalty algorithms have slightly different formulations:

Pure Penalty: $F_{normal} = K_{normal}\, x_{penetration}$ (6.2)

Augmented Lagrange: $F_{normal} = K_{normal}\, x_{penetration} + \lambda$ (6.3)

where λ is the contact force (pressure). The λ term in Equation 6.3 makes the contactless sensitive to the contact stiffness. Moreover, the normal contact stiffness is dependent on the Normal Stiffness Factor which by default is set to 1. All the frictional contacts used in the simulation have the Augmented Lagrange formulations. Augmented Lagrange formulation automatically reduces the amount of penetration. Hence, it was preferred to the Pure Penalty formulation. On the other hand, the frictionless contacts have program controlled formulation i.e. Pure Penalty formulation. The bonded contacts in the simulations also used program controlled formulation which is Pure Penalty by default. In order to obtain convergence, the stiffness factor can be changed accordingly but for the present simulation, this was not necessary.

Reviewing the contact surfaces is a must. In this setup, after reviewing the contacts, many frictional contacts had open status. In other words, there were very small gaps between bodies that are supposed to be in a frictional contact. This happens due to inaccuracies in setting the CAD model and will lead to rigid body motion which is not allowed by FEM in static structural analysis. Consequently, this problem was overcome by introducing an offset to the faulty contacts using the contact treatment geometric modification. The "Adjusted to Touch" interface treatment will calculate the offset necessary to establish initial contact between the two contact regions and close the gap accordingly. The frictional surfaces involved in this simulation will be high as the surfaces will be dry. As a result, the frictional coefficient was chosen to be 0.8 (Sullivan, 1988; Encarta Encyclopedia 2004 & CRC Handbook of Physical Quantities, 1997). All the other setting was program controlled. The types of contacts designated between parts of the support system are listed in Table 6.2.

Table 6.2: Contact Designation

Mating Part 1	**Mating Part 2**	**Contact Type**
Dowel	Frame/ Magnet	Bonded
Frame	Frame	Frictional (μ=0.8)
Washer	Frame	Frictional
Rod	Frame	Frictionless (μ=0)
Magnet	Frame	Frictional
Rod	Washer	Frictionless
Rod	Nut	Bonded
Nut	Washer	Frictional
Rod	Magnet	Frictionless
Magnet	Coil	Bonded

Often tetrahedron mesh is used to mesh complicated geometry. However, using a hex mesh increases computational efficiency because it decreases the number of node and elements necessary to achieve accurate solutions (CAE Associates Inc., 2014). Moreover, not all geometry can be hex meshed as it requires a specific amount of topology cleaning and breaking down to get nearly all brick mesh. The two kinds of mesh which have been used in the present work are Hex-dominant and Multizone. The geometry could be modified to enforce sweep meshing but to avoid complications different mesh types were selected instead.

Hex Dominant: This mesh type generates hexahedral elements and also triangular or pyramidal cells. It is recommended for bodies that are not sweep-able. Further, the hex-dominant mesh is an automated and robust unstructured mesh generator can tackle grids of unlimited complexity and size. In order to generate meshes that are body-fitted, the hex-dominant mesh uses an advanced algorithm to select a suitable cell type.

Multizone: It automatically decomposes the geometry to generate a sweep mesh. Figure 6.3 shows the various steps involved in creating a Multizone mesh.

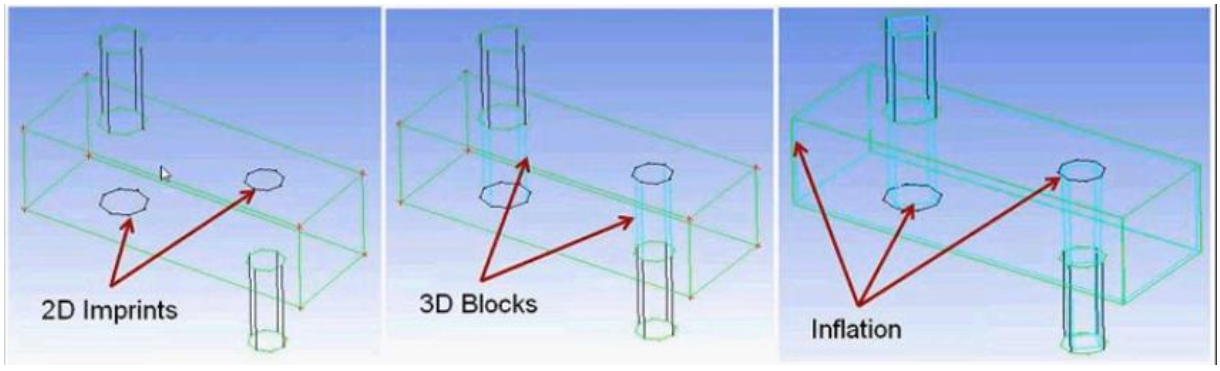

Figure 6.3: MultiZone Algorithm (CAE Associates Inc. 2014)

At first, it detects the source and the target faces and performs the imprinting on those faces. Then, the algorithm constructs the 3D blocking that is generated internally. This makes the geometry into a sweep mesh-able body and generates all brick elements.

The frame plates and the magnet yokes were assigned a hex-dominant mesh. The dowels, fasteners, washers, nuts and coils had a Multizone mesh. The next step is determining the appropriate mesh size. Therefore, a sensitivity study was performed to examine the effect of mesh size on the deformation (Smith, 2018). Since the fasteners were the most crucial part of this design, its elements were selected for the study. Table 6.3 shows how the directional deformation changed with changes in element size. Figure 6. 4 through 6.6 show a visual representation of the relations between element size and deformation.

Table 6.3: Sensitivity Study

Fastener Element Size (mm)	**Total Elements**	**Def z (mm)**	**Def y (mm)**	**Def x (mm)**
8	4480	0.059	0.232	0.047
8.5	3936	0.064	0.256	0.065
9	4058	0.065	0.236	0.054
9.5	3956	0.058	0.249	0.047
10	4184	0.048	0.237	0.047
12	3556	0.162	0.276	0.147
15	3538	0.16	0.283	0.143
20	3250	1.284	0.309	1.124

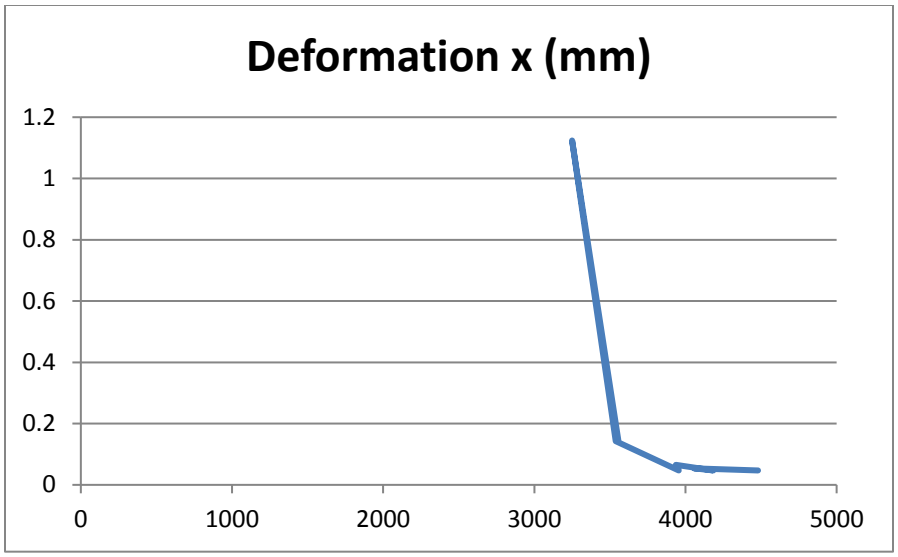

Figure 6.4: Deformation in X-direction Vs Total Elements

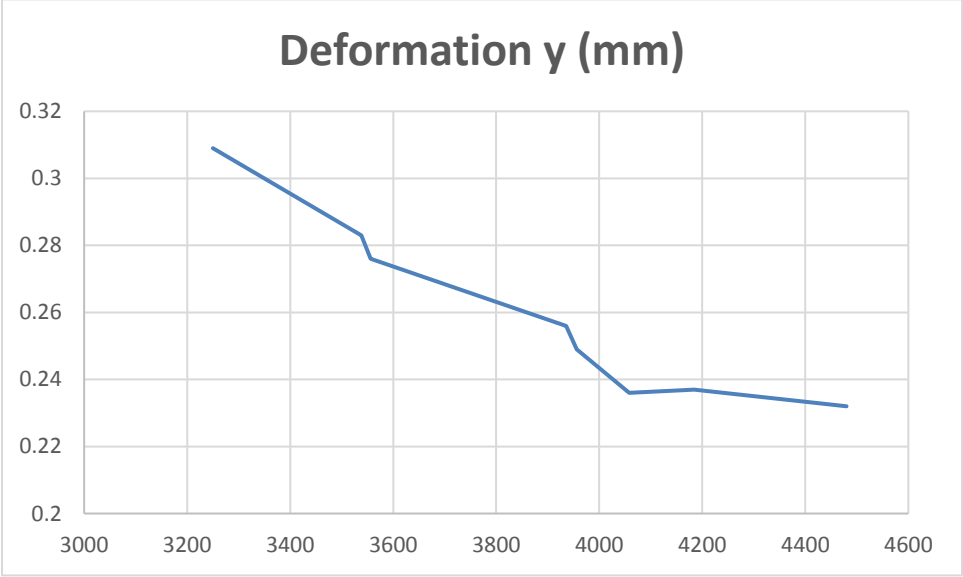

Figure 6.5: Deformation in Y-direction Vs Total Elements

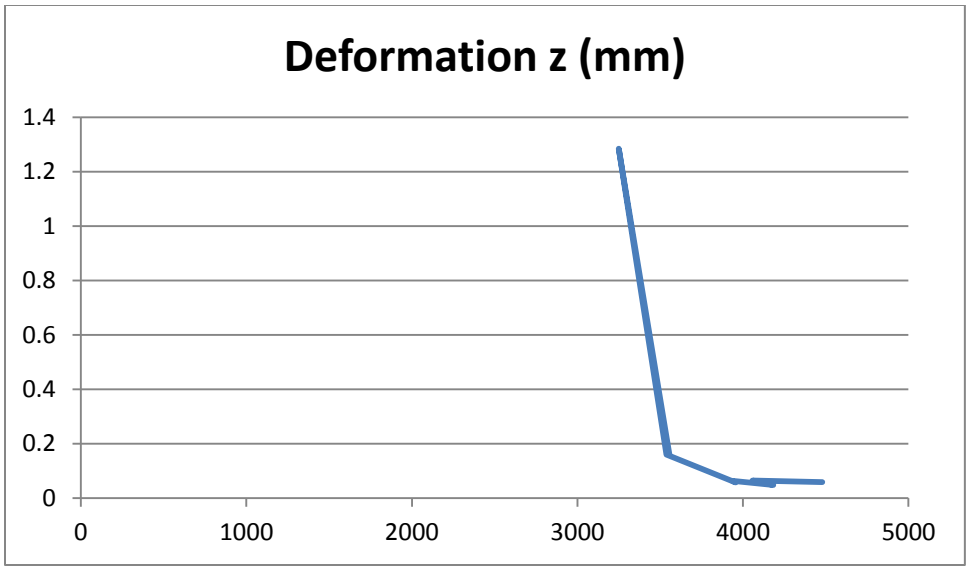

Figure 6.6: Deformation in Z-direction Vs Total Elements

From this sensitivity study, it was concluded that an element size of 8 mm or less is appropriate to capture the actual deformation of the simulation. An element size of 5 mm was chosen for all the bodies in the simulation. However, the washers showed a considerable structural error. Hence, the element size for washers was decreased to 2mm. Figure 6.7 shows the meshed geometry.

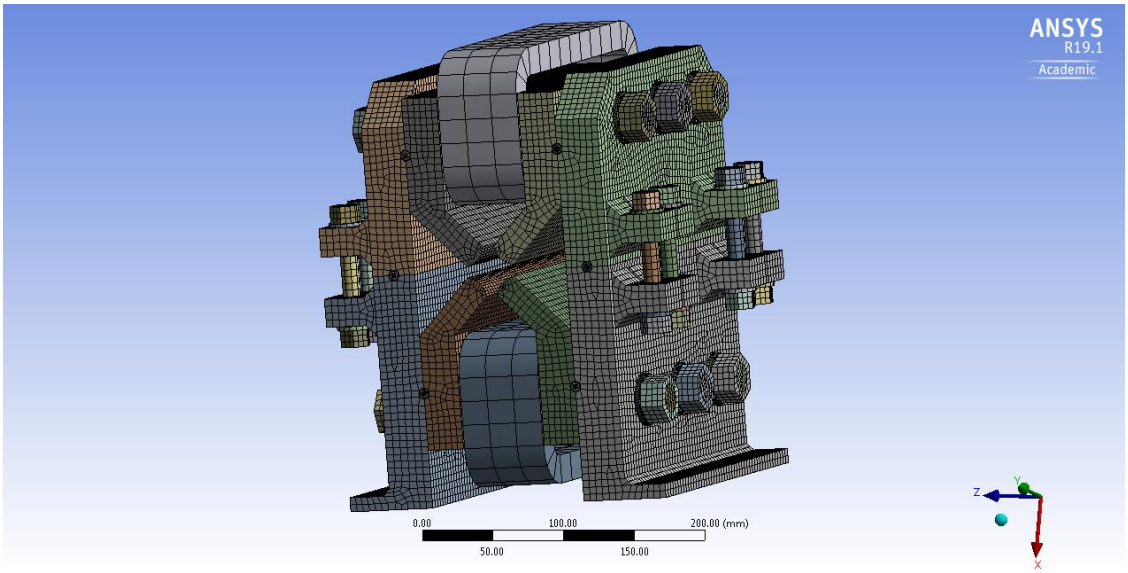

Figure 6.7: Mesh

SOLID90 Element type was used for this analysis. It consists of 20 nodes with 1 DOF, temperature, at each node. Moreover, the resulting number of nodes and elements were 562505 and 135995, respectively.

An infinitesimally small control volume, shown in Figure 6.8, with dimensions Δx, Δy and Δz was assumed to derive the governing equations (Bhaskaran, 2019):

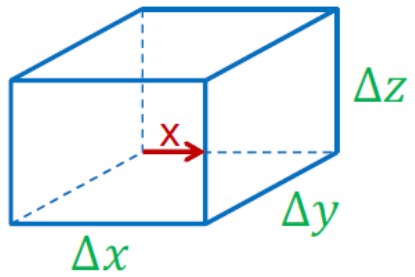

Figure 6.8: Control Volume (Bhaskaran, 2019)

If the heat flow in through the y-z plane is q_x and the heat flow out is $q_x + dq_x/dx\ \Delta x$,

Then, the net heat out can be given by $dq_x/dx\ \Delta x$.

According to Fourier's law: $q_x = -k\ dT/dx\ \Delta y \Delta z$ (6.4)

where dT/dx is the temperature gradient and k is the thermal conductivity.

Therefore, the net heat out is $-k\ d^2T/dx^2\ \Delta x \Delta y \Delta z$.

The assumptions involved in this derivation are one-dimensional heat flow, steady-state and constant thermal conductivity.

If the heat generation per unit volume, Q, is taken into consideration, then the net heat out can be given by $-k\ d^2T/dx^2\ \Delta x \Delta y \Delta z - Q\ \Delta x \Delta y \Delta z$

By conservation of energy:

$-k\, d^2T/dx^2\, \Delta x\Delta y\Delta z - Q\, \Delta x\Delta y\Delta z = 0$ (6.5)

Or, $k\, d^2T/dx^2 + Q = 0$ (6.6)

However, the system of algebraic equation in the nodal temperatures does not satisfy the above equation. So, a weighted integral form of the equation is considered to satisfy the equation.

$\int w(k\, d^2T/dx^2 + Q) = 0$ (6.7)

w(x) is an arbitrary function.

But, the equation will not satisfy for any arbitrary w within a domain but for a particular value of w.

$\int w^e(k\, d^2T/dx^2 + Q) = 0$ (6.8)

$w^e(x)$ is an arbitrary piecewise polynomial function. In other words, a value of w is assumed based on the shape of the temperature. This equation can be used to find the system of algebraic equation in the nodal temperatures. As the number of nodes increases the value of w becomes more arbitrary and it will tend to the exact solution.

By performing integration by parts of Equation 6 the weak form can be derived.

$$w^e k\frac{dT}{dx}\Big]_0^L - \int_0^L \frac{dw^e}{dx}\, k\, \frac{dT}{dx}dx + \int_0^L w^e Q\, dx = 0 \quad (6.9)$$

The above equation can be sub-dived and solved in three parts.

- The natural boundary part

$$w^e k \frac{dT}{dx}\Big]_0^L = w_L K (dT/dx)_L - w_0 K (dT/dx)_0 \quad (6.10)$$

- The stiffness matrix coefficient part

This integration will be element by element:

$$\int_0^L \frac{dw^e}{dx} k \frac{dT}{dx} dx = \{(w_2-w_1)/\Delta x\}. K \{(T_2-T_1)/\Delta x\} \int_0^L dx \quad (6.11)$$

- The source part

This integration will also be element by element:

$$\int_0^L w^e Q \, dx = w_1 (Q\Delta x/2) + w_2 (Q\Delta x/2) \quad (6.12)$$

where w_1 and w_2 , T_1 and T_2 are the weighting functions and temperature of any two consecutive elements and Δx is the distance between them.

These equations are ultimately used to solve:

$$[K] \{T\} = \{f\} \quad (6.13)$$

where K is the stiffness matrix, T is the temperature and f is the force vector.

The thermal boundary conditions in this simulation are similar to Section 5.1. Convention will take place on the surfaces that are exposed to air and is calculated from Newton's law of cooling:

$$q/A = h (t_s - t_f) \quad (6.14)$$

where q/A is heat flux, h is the film coefficient, t_s is the face temperature and t_f is the bulk fluid temperature.

6.1.2 Results and Discussions

The heat load in the simulation resulted in the following temperature distribution shown in Figure 6.9.

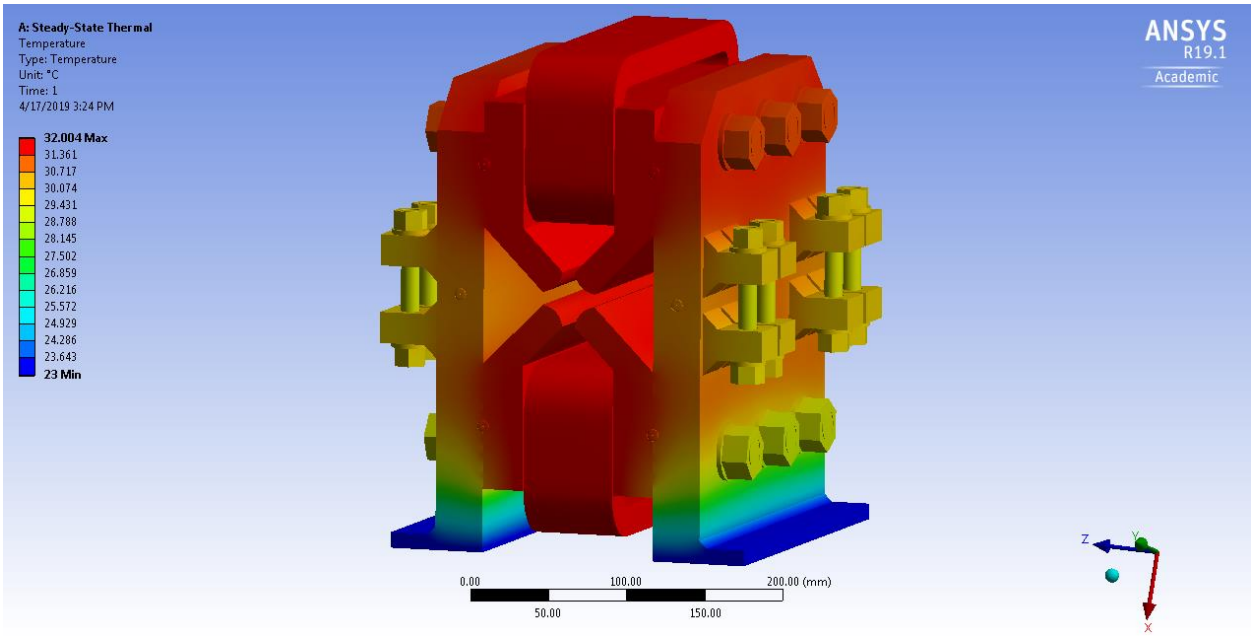

Figure 6.9: Temperature Contours

The temperature distribution seems reasonable, with more heat generation near the coils. Moreover, it can also be observed that the flanges are acting as fins as they increase the heat transfer near the region they are located. This heat load will be applied to the static-structural analysis. Also, the resulting Total Heat Flux is shown in Figure 6.10.

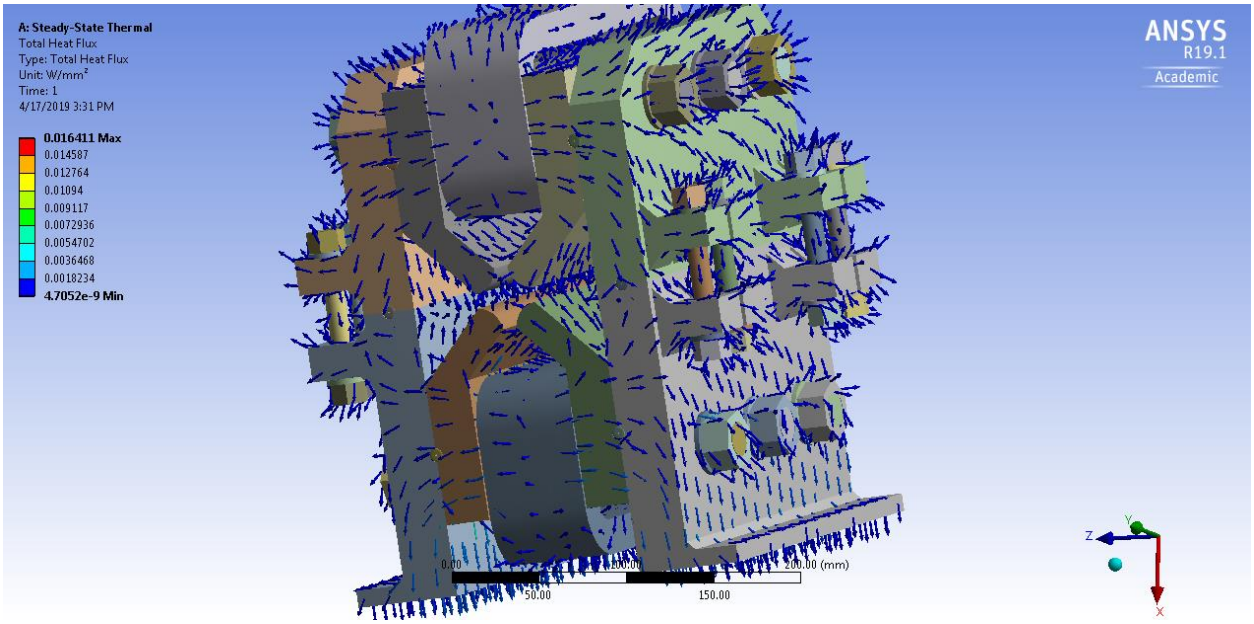

Figure 6.10: Heat Flux

Arrows are plotted at the end of each node and the direction is given by solving the components of the heat flux. The total heat flux can be expressed as:

$$\overrightarrow{q} = q_x \hat{\imath} + q_y \hat{\jmath} + q_z \hat{k} \quad (6.15)$$

where $\overrightarrow{q}$ is the total heat flux at a node and q_x, q_y and q_z are the heat flow per unit area in the x , y and z-direction respectively.

$$Q_x = -k \, \delta T / \delta x \quad (6.16)$$

where $\delta T / \delta x$ is the temperature gradient in the x-direction and k is the proportionality constant. Similarly, q_y and q_z can be defined as:

$$q_y = -k \, \delta T / \delta y \quad (6.17)$$

$$q_z = -k \, \delta T / \delta z \quad (6.18)$$

It can be observed from the heat flux results that the heat generated from the coils is getting dissipated to the environment via convection. As the bottom plates of the frame are at storage ring temperature, the heat flux is towards where the girders are supposed to be placed.

6.1.3 Verification

Verification is checking whether the mathematical model is solved correctly. The boundary conditions were checked: the temperature of the coil ranged from 31.99^{o}C to 31.968^{o}C which is very close to the assigned boundary condition (32^{o}C) and the temperature of the bottom plate was probed to be 23.0^{o}C. Also, sanity checks which are also a part of the verification process were done throughout the analysis, for instance, the direction of the heat flux seems reasonable. The exact solution of the mathematical model is as follows:

From Equation 6.14:

$q/A = h\,(t_s - t_f)$

$h = 5x10^{-6}$ W/mm^2. ^{o}C

$A = 8.1023x\ 10^{-5}$ mm^2

$t_s = 30.654^{o}$C (Average face temperature was considered)

$t_f = 23^{o}$C

$q = 31.0075$ W

The heat flow due to convection, found using ANSYS, is equal to -31.175 W

Percentage Error = (31.175-31.007)/31.175 x100% = 0.54%

The error is less than 5%. Hence, the simulation can be deemed correct.

The physical principle in the governing equation is the energy balance or energy conservation. And this can be authenticated by calculating the reactions at the essential boundary conditions.

From the simulation, it was calculated that the net heat flow at the bottom plate was -29.827 W and the direction is away from the domain hence the sign is negative. The convention boundary condition has a reaction of -31.175 W. This also has a negative sign as the heat is going out of the boundary. The reaction on the coils is 61.002 W. Therefore, by conservation of energy the summation of all the heat flows should be zero.

Or, 61.002 -31.175 -29.827 = 0

Hence, the system follows the law of energy conservation and the simulation can be considered correct.

6.2 Static Structural Analysis

To calculate stress, strains, displacements and reaction forces resulting from structures subjected to thermos/mechanical loads which do not generate notable inertia and damping effects, Static Structural Analysis can be used.

6.2.1 Simulation Setup

As the thermal load is also included for the static structural analysis, the mesh size and contacts will remain the same.

There are three major governing equations involve while solving a Static Structural Analysis: equilibrium equations, 3D-Hooke's Law and strain-displacement relations.

- Equilibrium equations: The 3D Differential Equations of Equilibrium for an infinitesimally small element (Figure 6.11) of a structure subjected to a bending load are as follows.

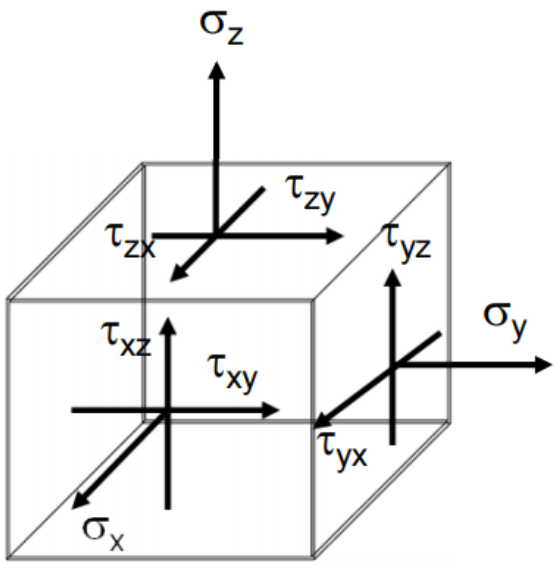

Figure 6.11: Infinitesimally Small Element (Bhaskaran, 2019)

$$\frac{\partial \sigma_x}{\partial x} + \frac{\partial \tau_{xy}}{\partial y} + \frac{\partial \tau_{xz}}{\partial z} + f_x = 0 \tag{6.19}$$

$$\frac{\partial \tau_{xy}}{\partial x} + \frac{\partial \sigma_y}{\partial y} + \frac{\partial \tau_{yz}}{\partial z} + f_y = 0 \tag{6.20}$$

$$\frac{\partial \tau_{xz}}{\partial x} + \frac{\partial \tau_{yz}}{\partial y} + \frac{\partial \sigma_z}{\partial z} + f_z = 0 \tag{6.21}$$

σ_x, σ_y and σ_z are the normal stresses and f_x, f_y and f_z are the body forces in the x, y and z-direction respectively. T_{xy}, τ_{yz} and τ_{xz} are the shear stresses in the x-y, y-z and x-z plane respectively.

- 3D-Hooke's Law: The 3D Hooke's law for the same infinitesimally small element can be given by

$$\begin{bmatrix} \sigma_x \\ \sigma_y \\ \sigma_z \\ \tau_{yz} \\ \tau_{xz} \\ \tau_{yx} \end{bmatrix} = \frac{E}{(1+\nu)(1-2\nu)} \begin{bmatrix} 1-\nu & \nu & \nu & 0 & 0 & 0 \\ \nu & 1-\nu & \nu & 0 & 0 & 0 \\ \nu & \nu & 1-\nu & 0 & 0 & 0 \\ 0 & 0 & 0 & \frac{1-2\nu}{2} & 0 & 0 \\ 0 & 0 & 0 & 0 & \frac{1-2\nu}{2} & 0 \\ 0 & 0 & 0 & 0 & 0 & \frac{1-2\nu}{2} \end{bmatrix} \begin{bmatrix} \epsilon_x \\ \epsilon_y \\ \epsilon_z \\ \gamma_{yz} \\ \gamma_{xz} \\ \gamma_{yx} \end{bmatrix} \quad (6.22)$$

ε_x, ε_y and ε_z are the strains in the x, y and z-direction respectively. N is the Poisson's ratio. Γ_{xy}, γ_{yz} and γ_{xz} are the shear strains in the x-y, y-z and x-z plane respectively.

- Strain-Displacement Relations: Strain-Displacement Relations for Normal Strain are as follows

$$\varepsilon_x = \frac{\partial u}{\partial x} \quad (6.23)$$

$$\varepsilon_y = \frac{\partial v}{\partial y} \quad (6.24)$$

$$\varepsilon_z = \frac{\partial w}{\partial z} \quad (6.25)$$

u, v and w are the displacements in the x, y and z-directions respectively.

Strain-Displacement Relations for Shear Strain is given by

$$\gamma_{xy} = \frac{\partial u}{\partial y} + \frac{\partial v}{\partial x} \quad (6.26)$$

$$\gamma_{yz} = \frac{\partial v}{\partial z} + \frac{\partial w}{\partial y} \quad (6.27)$$

$$\gamma_{zx} = \frac{\partial w}{\partial x} + \frac{\partial u}{\partial z} \tag{6.28}$$

Equations 6.19 to 6.28 are solved by the ANSYS solver to calculate the 6 stress components (σ_x, σ_y, σ_z, τ_{xy}, τ_{yz} and τ_{xz}), 6 strain components (ε_x, ε_y, ε_z, γ_{xy}, γ_{yz} and γ_{xz}) and the 3 displacement components (u, v and w). ANSYS will break the model into small elements and calculate the displacements for all the elements. Further, these equations are finally used to solve the equation below to get the nodal displacements.

$$[K]\{d\} = \{f\} \tag{6.29}$$

d is the nodal displacement. Similar to the thermal analysis, the static structural analysis also uses the special weighted integral form for the piecewise polynomial approximation for displacement. In order to obtain a converged solution, ANSYS uses the Newton-Raphson algorithm, by balancing the internal forces inside the structure with the applied external loads. As linear equations are solved, the tangent stiffness matrix gets updated until the applied loads are balanced by the internal force (Hale, 2015) (Figure 6.12).

$$[K_T]\{\Delta u\} = \{F\} - \{F^{nr}\} \tag{6.30}$$

where K_T is the tangent stiffness matrix, Δu is the displacement increment, F is the external load vector and F^{nr} is the internal load vector. The iterations continue until the difference between the external load and the internal load is within a tolerable limit.

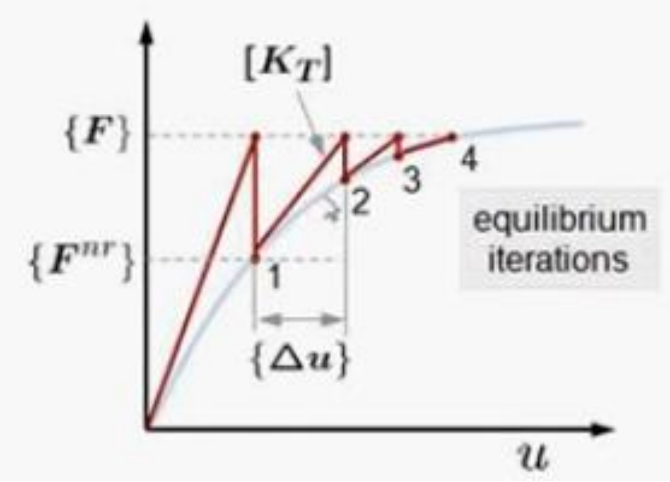

Figure 6.12: Force Vs Displacement Graph (ANSYS Convergence) (Hale, 2015)

The analysis is set to take place in two time-steps. In the first time step, all the fourteen bolt pretension was considered along with the fixed support and the acceleration due to gravity. A parametric study concluded that for the M20 fasteners 50% of the proof load (26704 N) corresponded to the lowest deformation. Similarly, for the M12 fasteners, 40% of the proof load (7690.6 N) was enough to hold the frame in position. In the second time step, the forces (Table 3.1) on the magnet yoke were enabled. Furthermore, the heat load that was determined by the steady-state thermal analysis was active for both the time steps. The bottom flanges will be clamped to the girder so a fixed support was considered on that surface. Figure 6.13 shows the simulation set up for the Static Structural Analysis.

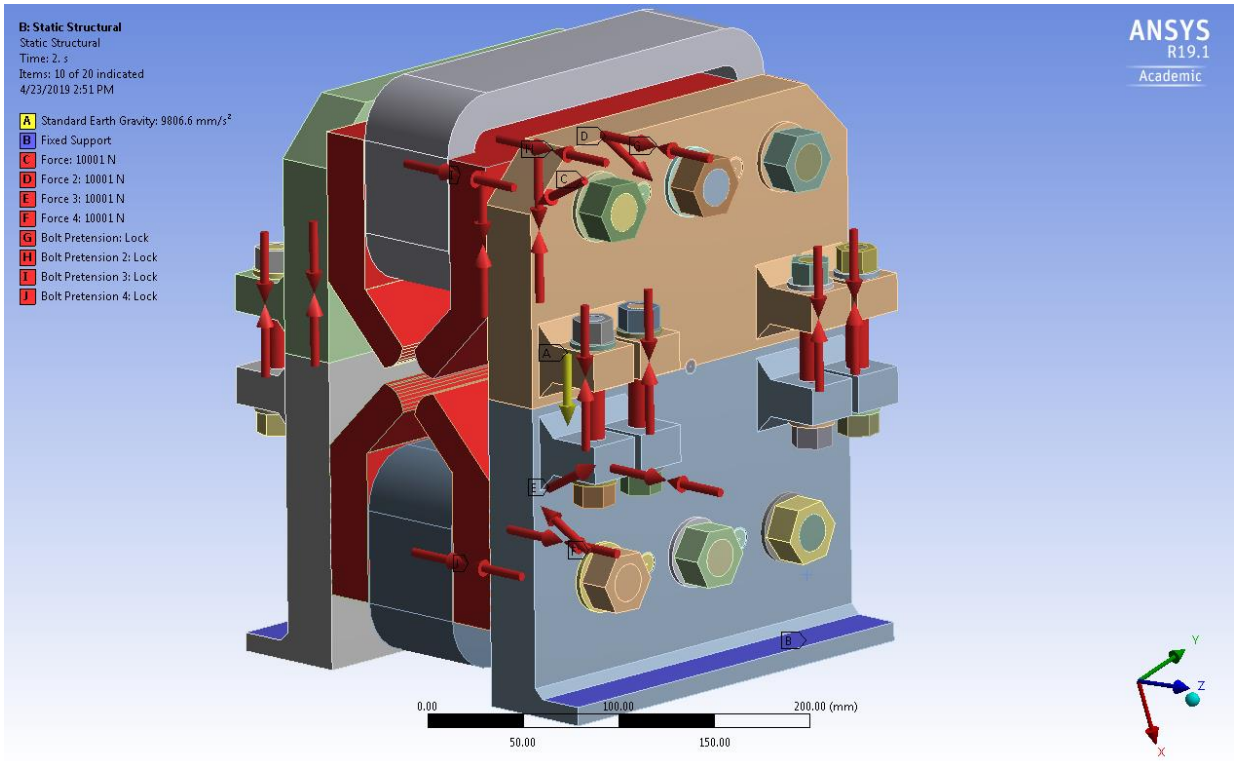

Figure 6.13: Static Structural Analysis Setup

6.2.2 Analysis Results and Discussions

The displacements at the pole were evaluated by selecting on the pole surfaces for total deformation evaluation. The results of the total deformation on the magnet poles are shown in Figure 6.14.

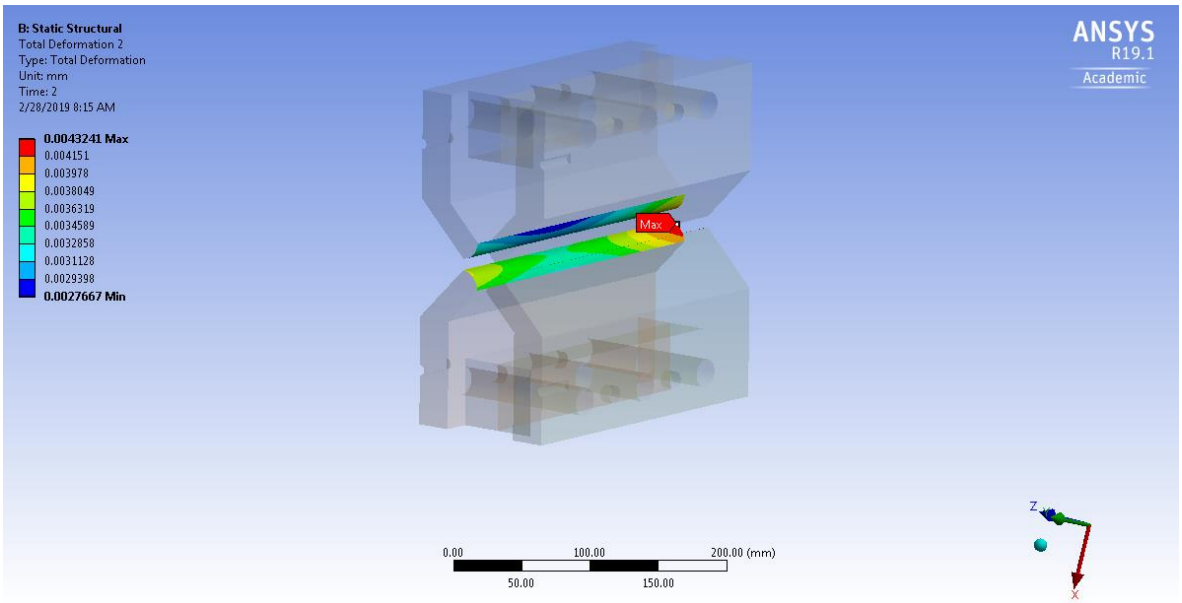

Figure 6.14: Pole Deformation

The pole deformation was acceptable. Furthermore, it can also be observed that the deformation is not symmetric. This is due to the presence of dowels only on one side of the magnet. The total deformation (Figure 6.15) and the equivalent stress (Figure 6.16) on the frame are as follows:

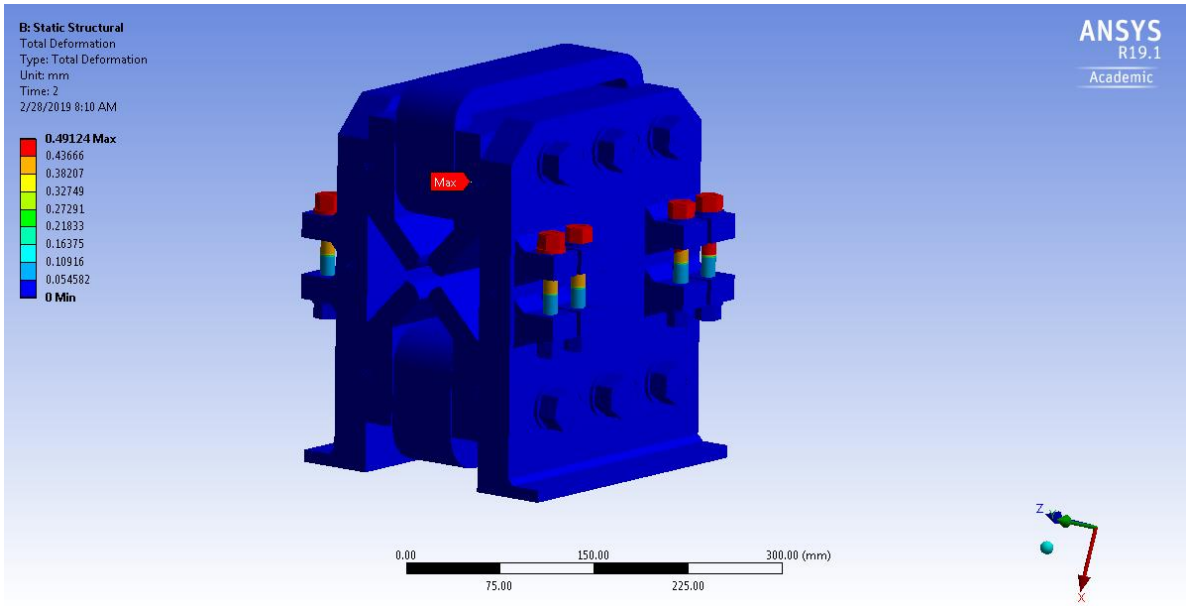

Figure 6.15: Total Deformation

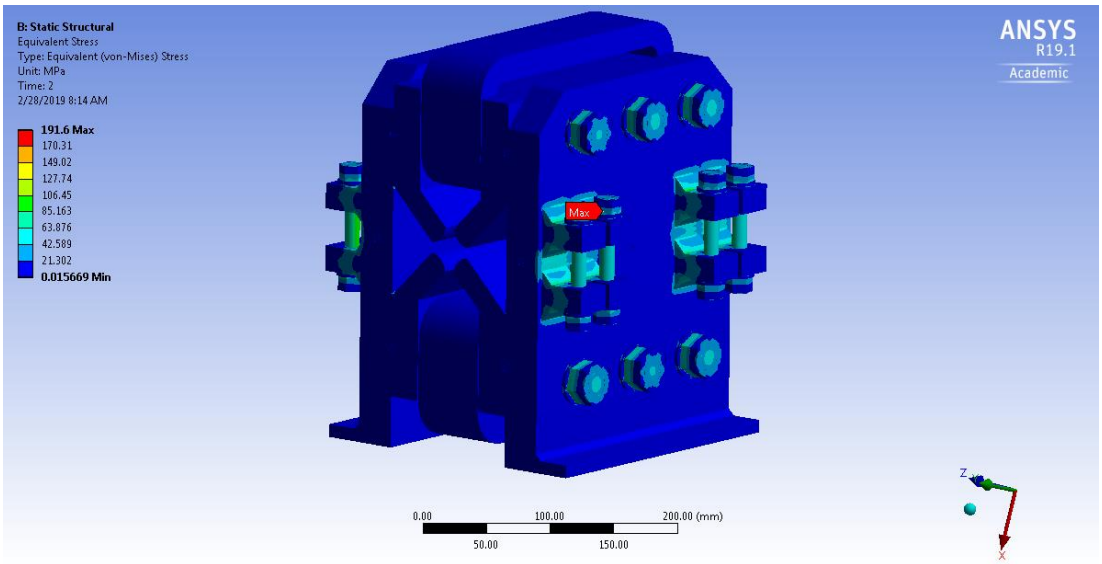

Figure 6.16: Equivalent Stress Distribution

The force convergence history plot is shown in Figure 6.17 that follows.

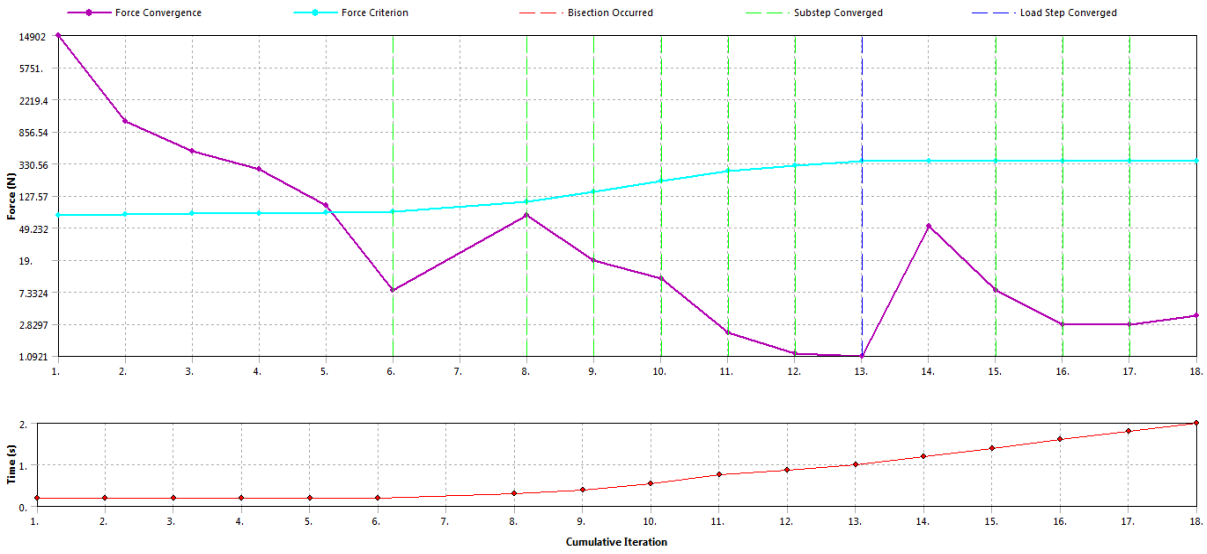

Figure 6.17: Force Convergence Graph

ANSYS breaks up the loads into smaller load steps automatically in order to obtain convergence faster. In Figure 6.17, the purple line indicates the difference between the applied force and the internal force, i.e., $\{F\} - \{F^{nr}\}$ from Equation 6.30. Once the purple line goes below the light blue line, which is the convergence tolerance number, a converged sub-step is obtained (green line). In the time step 1, the bolt pre-tension gets activated and the deep blue line indicates that this time step has converged. In time step 2, the magnetic forces along with the bolt pre-tension from the previous step are in action. When the second time step converged, the converged solution was obtained.

6.2.3 Verification

The verifications performed in the present work are adopted from the verifications done by Bhaskaran (2019) and Cornell University's online tutorials (https://confluence.cornell.edu/display/SIMULATION/ANSYS+Learning+Modules). The displacements at the bottom plates of the frame, where it is clamped to the girder, are at 0 mm. This has verified the displacement boundary condition. Theoretically, all the forces should cancel each other out. Hence, the only reaction force at the fixed support will be the weight of the magnet and its components.

The weight of the coils = 11.035 Kg

The weight of the Magnet = 31.25 Kg

The weight of the frame and its components = 45.31 Kg

Total weight = 87.595 Kg

Force exerted by the magnet and it sub-components = 874.32 N

The reaction forces calculated from ANSYS are (Figure 6.18):

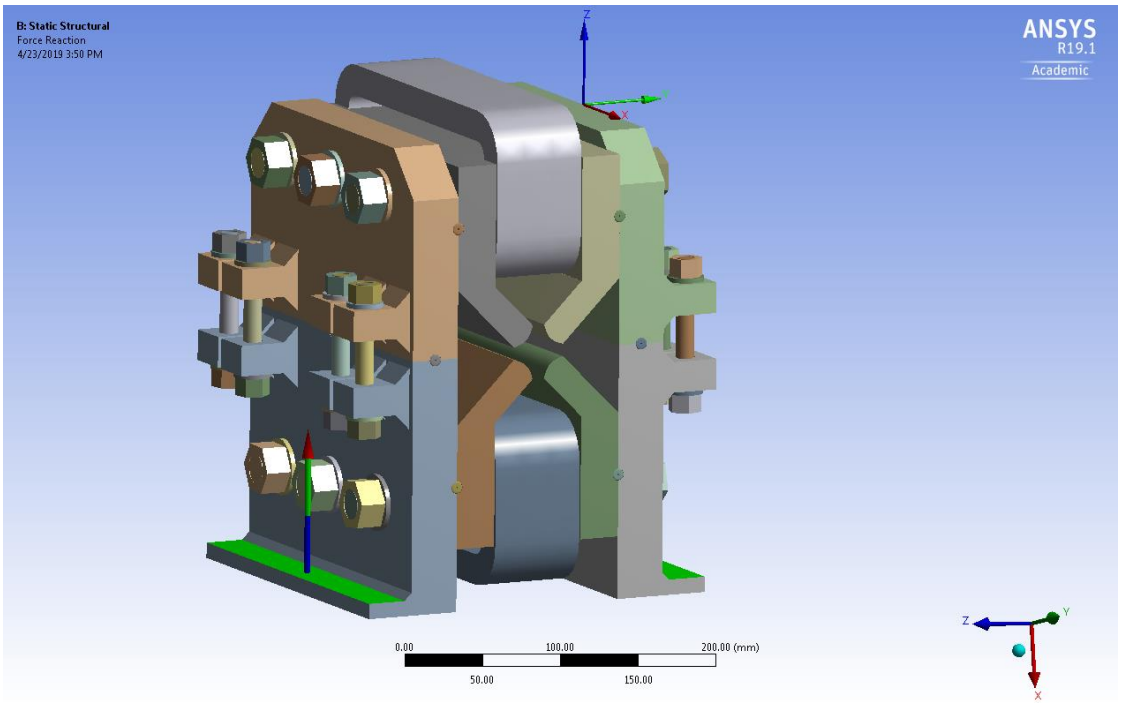

Figure 6.18: Force Reaction at Fixed Support

X-axis = 6.1765e-009 N

Y-axis = 1.4038e-004 N

Z-axis = 874.31 N

The forces in the x and y-direction are negligible and the force at the z-direction is equivalent to the weight of the magnet system. Hence, the equilibrium is satisfied.

Hand calculations have been compared with ANSYS results in Section 5.8.4.

Another type of verification for the static structural analysis is to compare the results assuming the simulation is non-linear (by turning on large deflection). This analysis was done assuming the frame will behave linearly (with a large deflection off) which considers that the displacements are small enough not to cause any change to the stiffness. When the simulation is assumed to be non-

linear (turning on large deflection settings) the stiffness changes are accounted for as well. This is elaborated below.

The material was assumed to be isotropic linear. Hence, the stress-strain relations were linear. However, for the non-linear domain, the stress-strain becomes non-linear. The strain-displacement relations only hold true for small displacements. The non-linearity can be caused by the geometry as well but the present geometry does not have any such structure. Thus, if the results with linear and non-linear domains are in agreement then the results can be trusted. The total deformation (Figure 6.19) and equivalent stress (Figure 6.20) with large deflection on are given below:

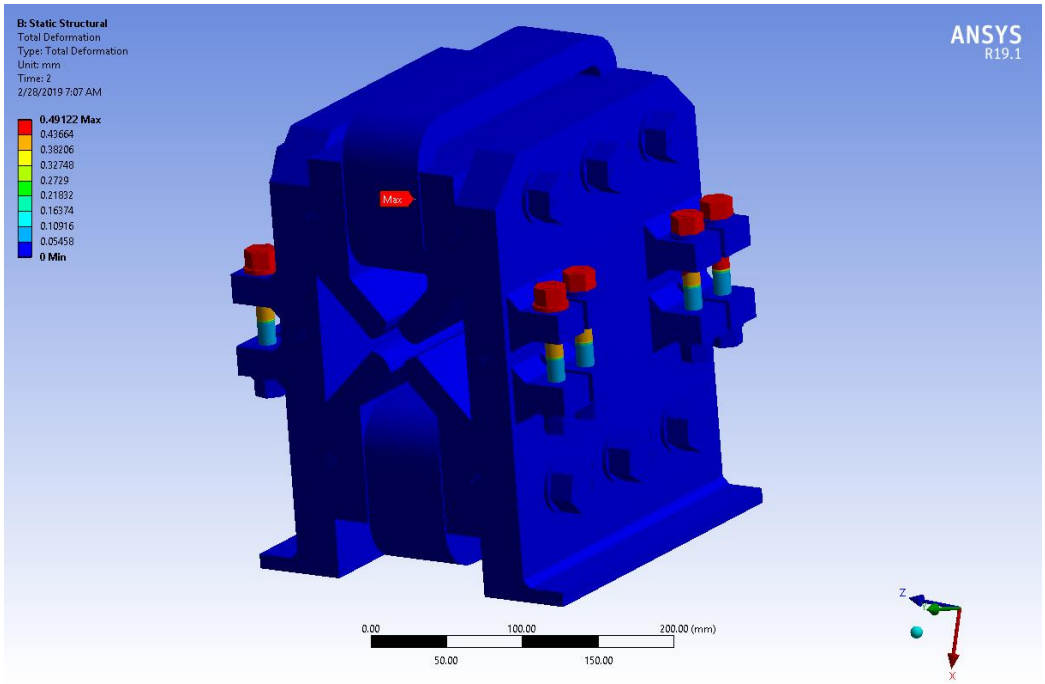

Figure 6.19: Total Deformation with Large Deflection On

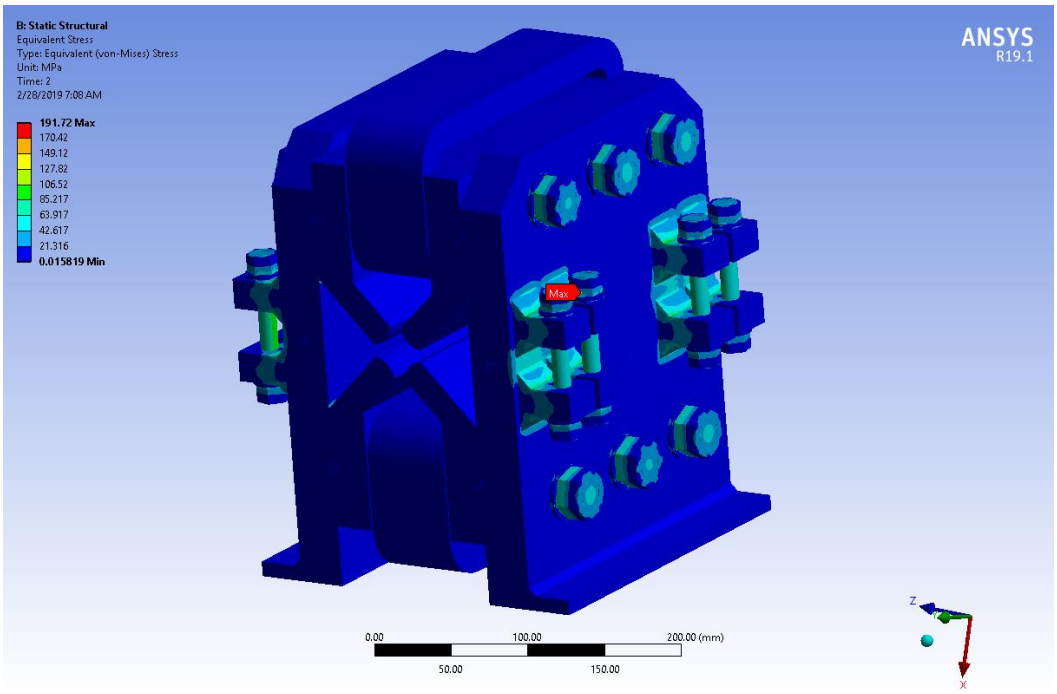

Figure 6.20: Equivalent Stress with Large Deflection On

The error percentage for Total Deformation = |0.49124 – 0.49122| / 0.49124 x 100%

$= 4.071 \times 10^{-3}$ %

The error percentage for Equivalent Stress = |191.6 – 191.72| / 191.6 x 100%

= 0.0625 %

In both cases, the error percentage is less than 1% and hence the results are verified.

The Max DOF Increment graph is shown in Figure 6.21.

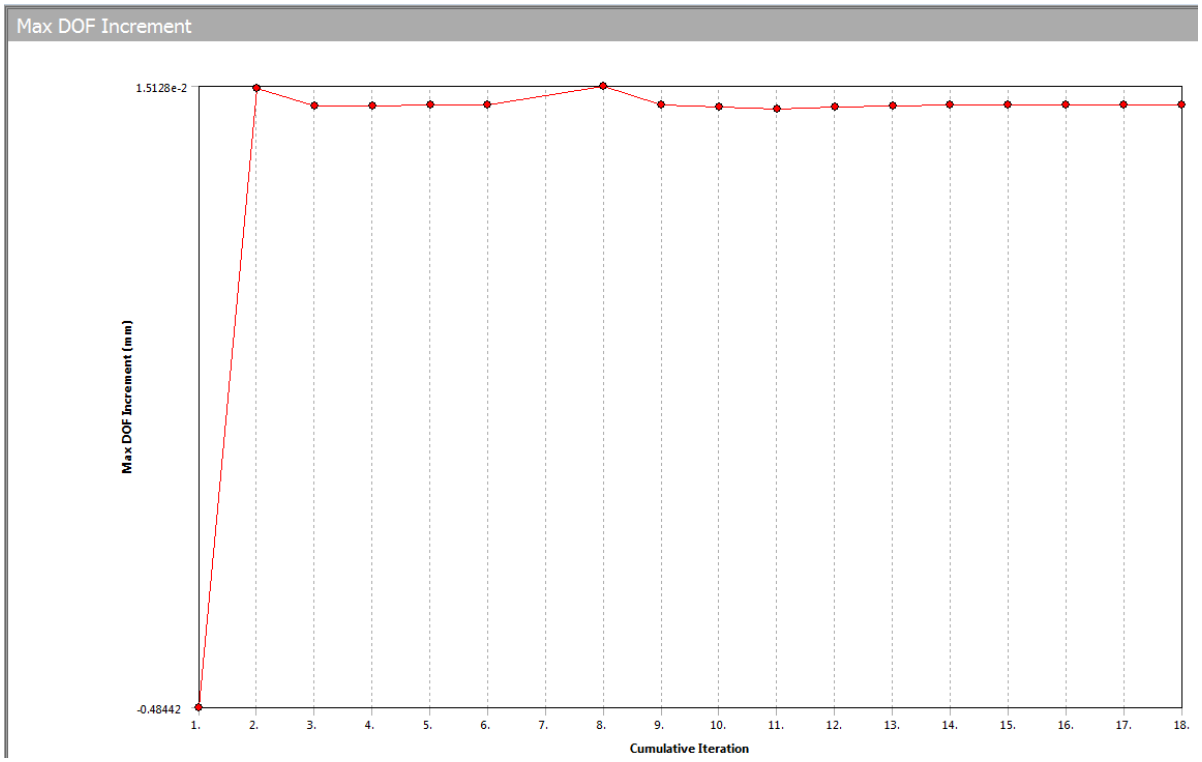

Figure 6.21: Max DOF Increment Graph

This graph indicated that the Max DOF Increment was -0.48442 mm when the solver started but soon it decreased to a negligible value. The physical interpretation of this graph is that none of the components of the magnet system experienced a very large deflection or lost contact at any point in the analysis.

To spot the regions with high error, Error (Structural) can be used. The regions with high error should be given a mesh refinement in order to obtain more accurate results. The present simulation had an error 0.6771 mJ and the fasteners, nuts and washers were identified as the regions of high error. The element sizes of these components were reduced from 5 mm to 2 mm. Then, the structural error reduced to a negligible value which is illustrated in Figure 6.22.

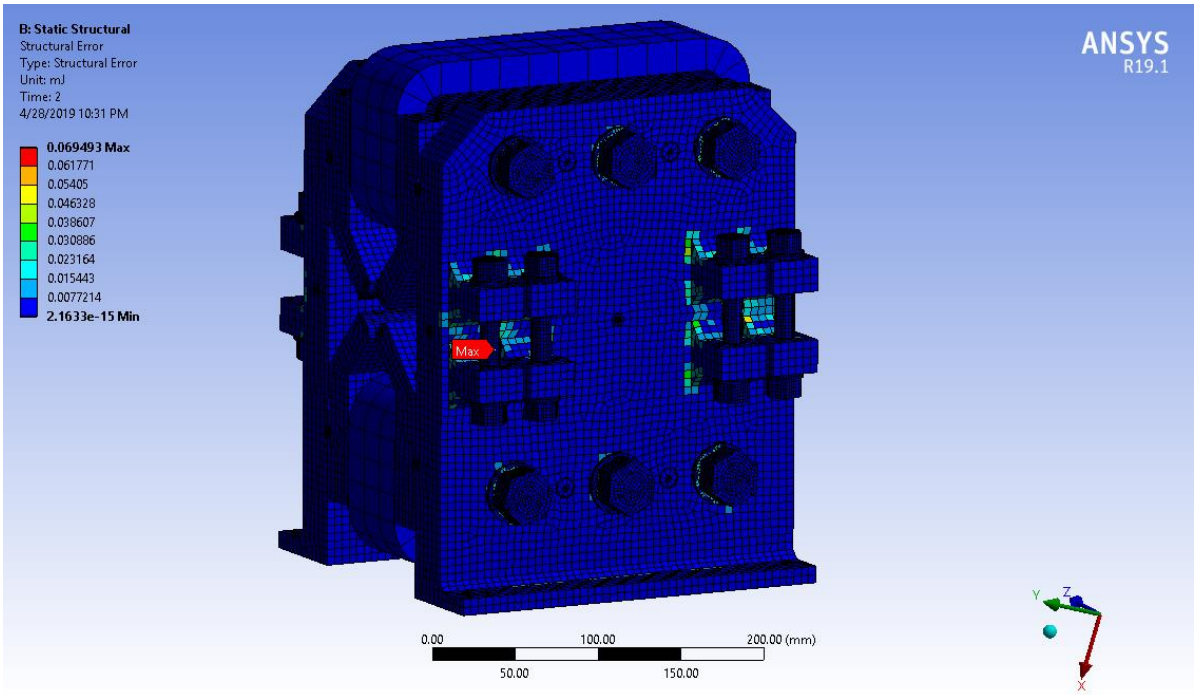

Figure 6.22: Structural Error

The resulting number of node and elements were 964371 and 218610. The maximum deformation was 0.49111 mm did not change much but the equivalent stress reduced to 183.86 Mpa. Thus, the equivalent stress is still below the yield stress of 304L Stainless Steel. The total pole deformation was 4.3242 x 10^3 mm which is also comparable to the previous results.

6.3 Natural Frequency Calculation (Modal Analysis)

The natural frequencies and mode shapes of a structure can be determined by the modal analysis.

6.3.1 Governing Equations

Based on d'Alemberts principle, the equation of motion can be written as:

$$M\cdot\ddot{u} + C\cdot\dot{u} + K\cdot u = f(t) \qquad (6.31)$$

where M is the mass matrix, C is the damping matrix, K is the stiffness matrix, f (t) is the force vector, $\ddot{u}$ is the acceleration vector, $\dot{u}$ is the velocity vector and u is the displacement vector. For modal analysis, the right-hand side of the equation of motion is considered to be zero.

$$M\cdot\ddot{u} + C\cdot\dot{u} + K\cdot u = 0 \quad (6.32)$$

The eigenvalue problem is solved to get the natural frequency and the mode shapes of a structure.

For a vibrating body with 'n' degree of freedom, modal expansion theorem states that any set of motions can be expressed as a superposition of each contributing mode (Vandiver, 2011):

$$u(t) = \{x\}^{(1)} q_1(t) + \{x\}^{(2)} q_2(t) + \ldots\ldots \{x\}^{(n)} q_n(t) \quad (6.33)$$

$\{x\}^{(i)}$ is the mode shape and q_i is the natural coordinates.

$$U = x\, q(t) \quad (6.34)$$

u is the generalized coordinates and q is the natural coordinates or modal coordinates.

$$\text{Therefore, } \dot{u} = x\dot{q} \quad (6.35)$$

$$\ddot{u} = x\ddot{q} \quad (6.36)$$

Plugging in the values of u, $\dot{u}$ and $\ddot{u}$ in the equation of motion and pre-multiplying it by x^T:

$$x^T M x\ddot{q} + x^T C\, x\dot{q} + x^T K x q = x^T f(t) \quad (6.37)$$

This equation is decoupled and describes every general 1-DOF model in the modal subspace.

$X^{(s)T} M x^I = 0$ for $r \neq s$

s is the s^{th} row of the x^T matrix and r is the r^{th} column of the $\ddot{x}$ matrix.

This implies that x^T Mx is always a diagonal matrix. Similarly, x^T Kx is also a diagonal matrix. For ideal conditions of damping, x^T Cx is also a diagonal matrix. Hence, mode shapes are orthogonal to one another.

$$[M]\ddot{q} + [C]\dot{q} + [K]q = x^T f(t) = Q(t) \quad (6.38)$$

Q(t) is the modal force.

Mode r is selected from the above equation:

$$M_r\ddot{q}_r + C_r\dot{q}_r + K_r q_r = Q_r(t) \quad (6.39)$$

This equation is similar to the generic equation of motion of a single degree of freedom oscillator. ANSYS solver calculates the mode shapes and the natural frequency using these equations.

6.3.2 Results and Discussion

The modal analysis was pre-stressed with the static structural loading conditions for vibrations tests to imitate the frame in the operational conditions. The solution to the Modal analysis is shown below in Figure 6.23.

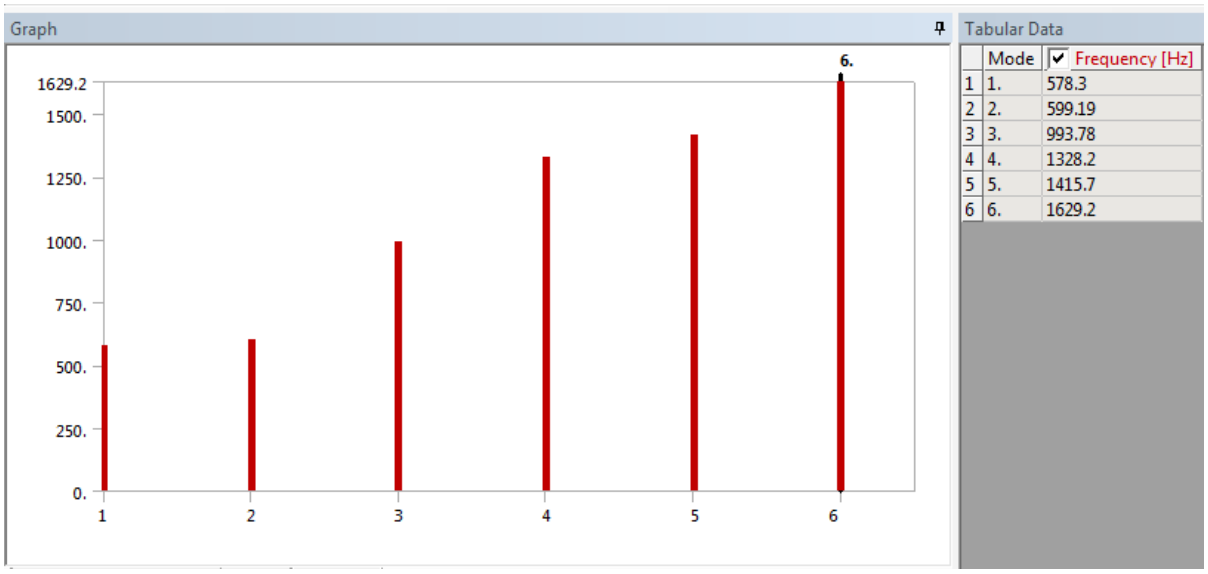

Figure 6.23: Natural Frequency

The deformation from the first through the third mode was also evaluated and illustrated in Figures 6.24 through Figure 6.26.

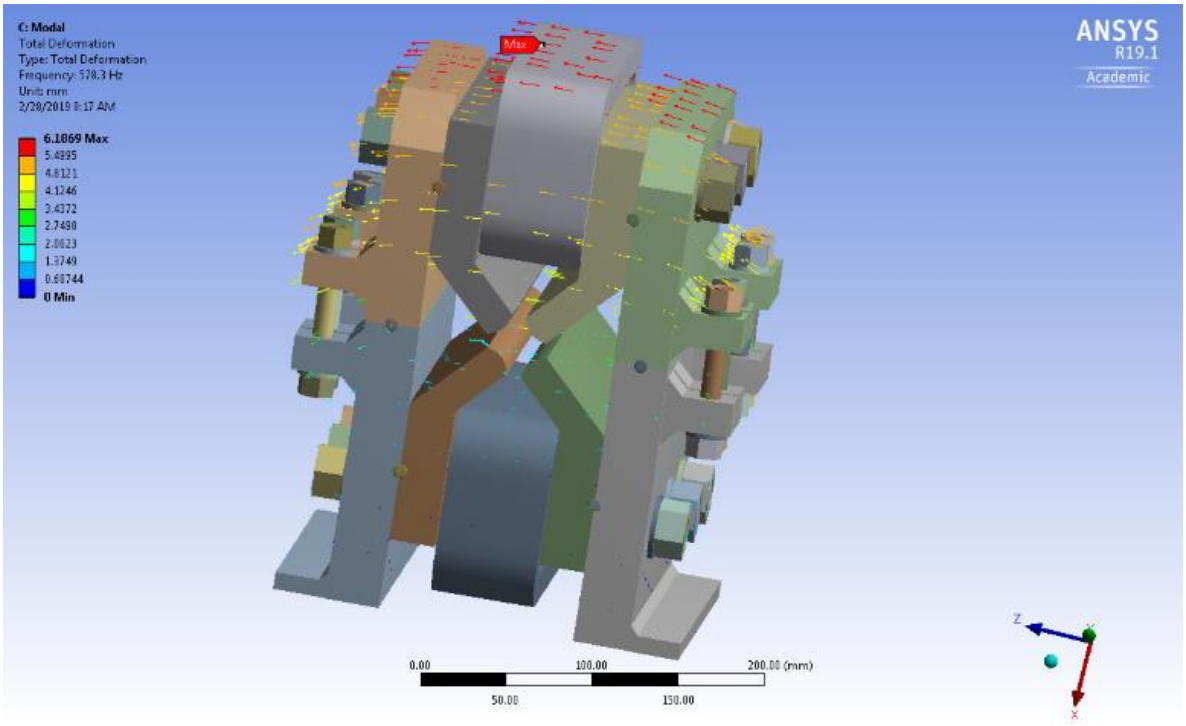

Figure 6.24: Total Deformation for Mode 1

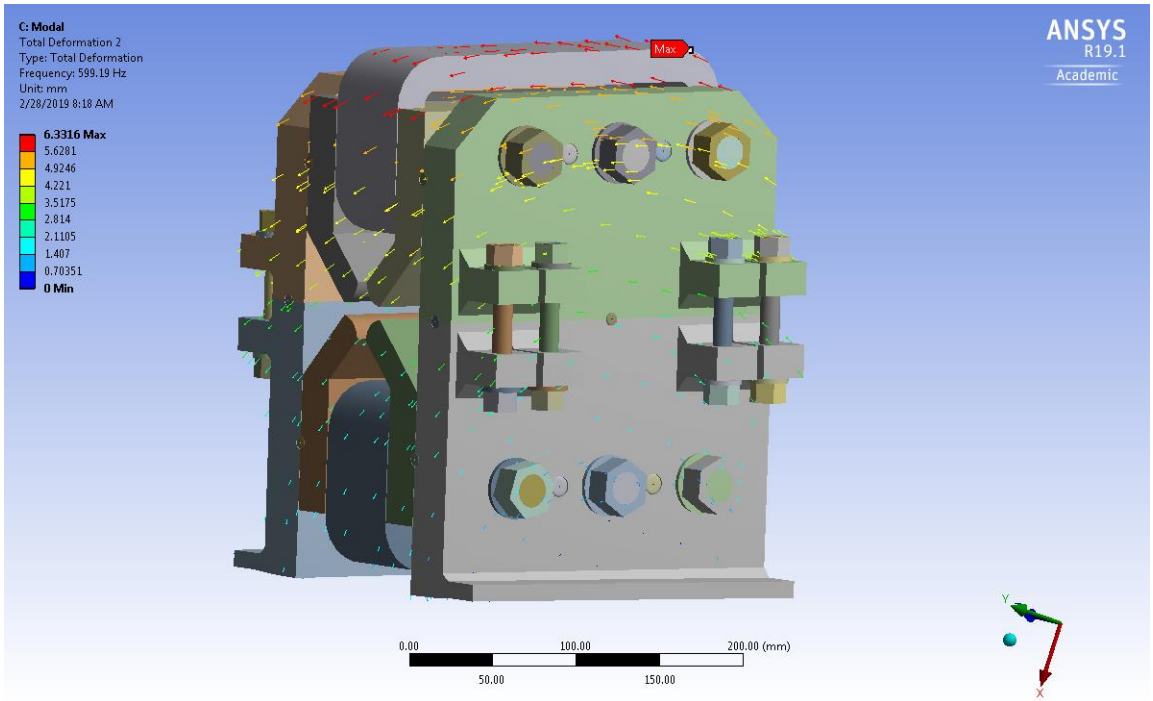

Figure 6.25: Total Deformation for Mode 2

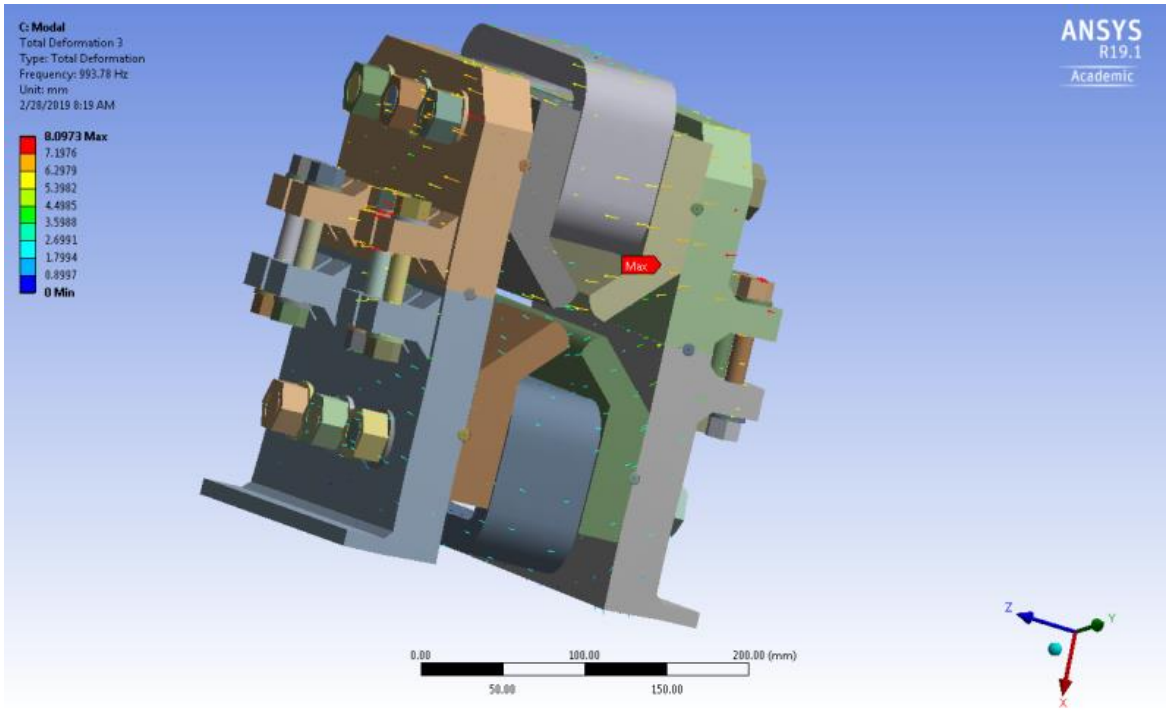

Figure 6.26: Total Deformation for Mode 3

This modal analysis was performed under the assumption that largely affected the results. The dowel pins – frame/magnet and coils-magnet were assumed to be bonded contacts and hence those locations are behaving similar to welded joints. This will increase the natural frequency calculated by ANSYS. In the real-life scenario, however, these contacts will be frictional and hence the first mode of natural frequency will change. A simulation was done by suppressing all the dowel pins and the first natural frequency reduced to 568.83 Hz. However, the mode shapes were the same.

In order to verify the modal analysis results, a mesh refinement was performed on the error-prone regions, similar to what was done in the previous section. The first, second and third mode of natural frequency was 578.46 Hz, 599.49 Hz and 994.72 Hz respectively. These results are comparable to the ones obtained before mesh refinement. Hence, the modal analysis results can be deemed correct.

6.4 Harmonic Analysis

Harmonic response analysis predicts the structure's sustained dynamic behavior. Thus, validates if the structure will be able to withstand fatigue, resonance and other forced vibrations from the environment. In this analysis, the response of the structural system under test was observed under a sinusoidal load.

6.4.1 Governing Equations

The loading which can be out-of-phase is considered for only one known frequency. The equation of motion is given by (http://www-eng.lbl.gov/~als/FEA//index_files/page0002.html):

$$[M]\{\ddot{x}\}+[C]\{\dot{x}\}+[K]\{x\}=\{F\} \tag{6.40}$$

It is assumed that the response of the linear structure will also be harmonic in nature:

$$\{F\}=\{F_{\max}e^{j\psi}\}e^{j\Omega t}$$
$$\{x\}=\{x_{\max}e^{j\phi}\}e^{j\Omega t} \tag{6.41}$$

$e^{j\psi}$ = (cos (Ψ) + j.sin(Ψ)) (6.42)

where the sinusoidal motion is given by $e^{j\psi}$ which also has a phase shift due to the presence of the imaginary term j. Ω is the frequency at which the loading takes place. F is the force and x is the response.

The harmonic response of any given structure is solved by solving the complex response for x_1 and x_2 from the equation:

$$\left(-\Omega^2[M]+j\Omega[C]+[K]\right)\{x_1+jx_2\}=\{F_1+jF_2\} \quad (6.43)$$

Further, the solver makes the following assumptions while solving the matrix equation:

- At a particular frequency, the loading and response will be cyclic or harmonic in nature.
- The material will behave linear elastically.
- There will be no non-linearity.
- '[C]' damping should not be zero as it will result in infinite resonance.
- [M], [C] and [K] are constants.

The non-linear contacts in harmonic analysis are converted to their linear counter-parts as it is assumed to be a linear analysis. The harmonic analysis in the present study was pre-stressed with the static structural environment. Moreover, the sinusoidal force was actuated on the bottom face of the magnet frame as while in operation it can only experience loads coming from the storage ring floor. This force was given as x, y and z component of 1N with zero phase angle. The Harmonic Analysis setup is shown in Figure 6.27.

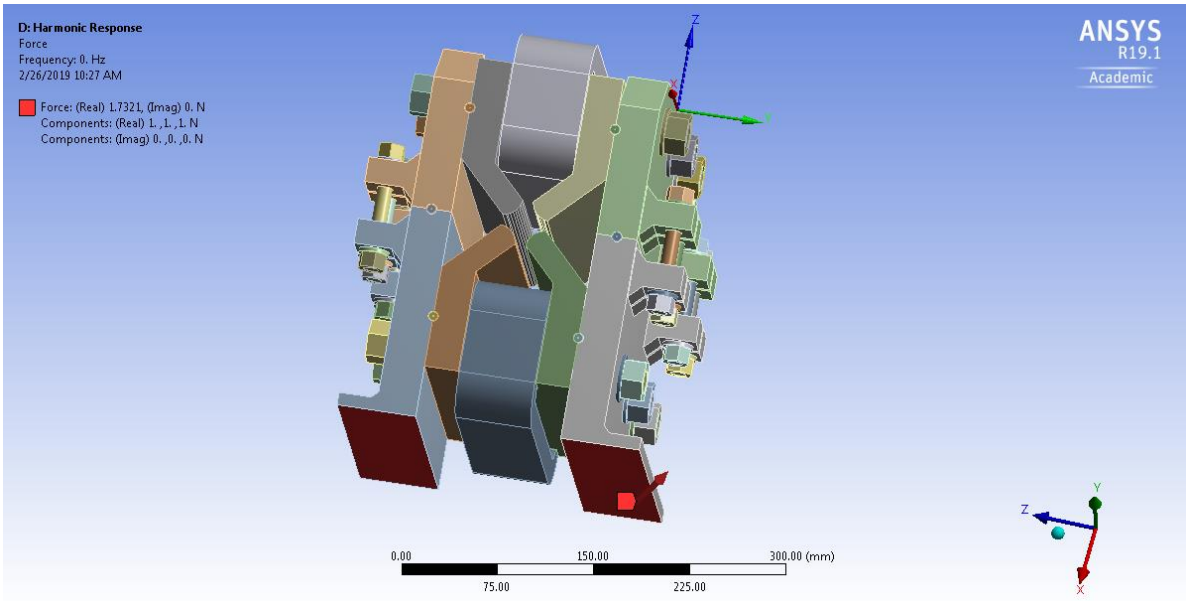

Figure 6.27: Harmonic Loading

The excitation frequency range was set from 500Hz to a maximum of 1600Hz with solution interval, n, of 100. The frequency interval will thus be given by:

$$\Delta\Omega = 2\pi \frac{f_{\max} - f_{\min}}{n} \tag{6.44}$$

The solver will solve for n frequencies beginning from $\Omega + \Delta\Omega$. In the present simulation, the superposition technique was used to solve the harmonic equation. The combination of mode shapes, Φ_i, can be used to convey the displacements, x, of a linear system:

$$\{x\} = \sum_{i=1}^{n} y_i \{\phi_i\} \tag{6.45}$$

where 'y_i' are modal coefficients.

6.4.2 Results and Discussions

As the method uses modal coordinates, modal analysis was needed to be performed before the harmonic analysis. There are two sampling methods: defining solution intervals and turning on cluster results. The following (Figure 6.28) is the frequency response of the displacement in the x-axis:

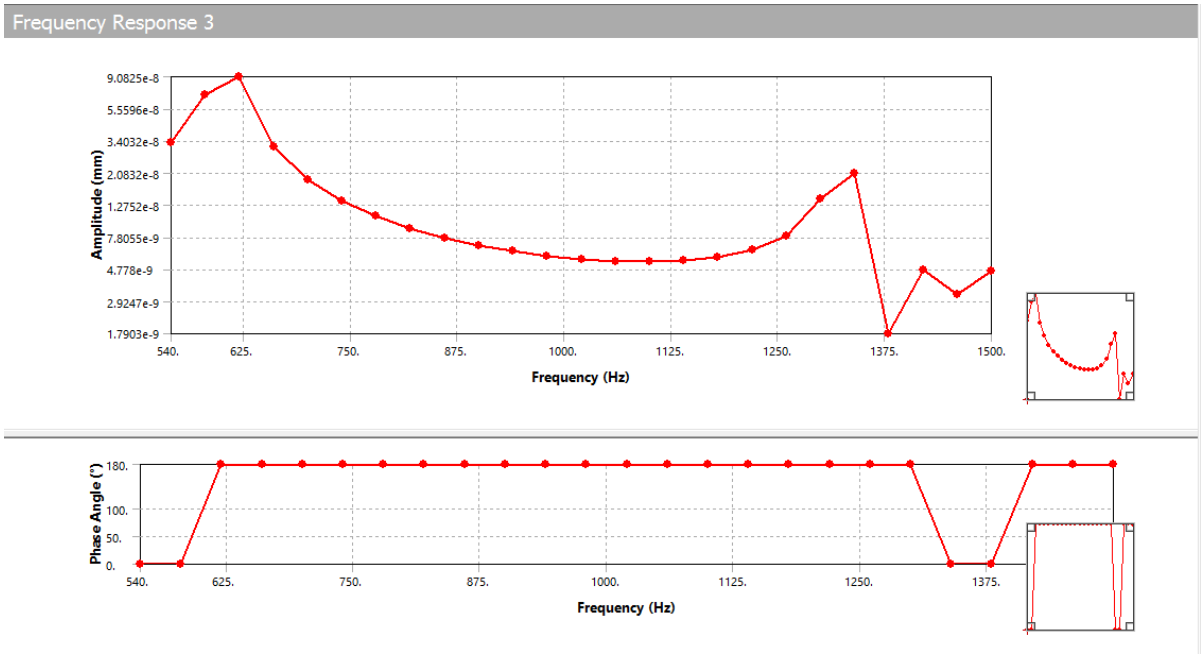

Figure 6.28: Harmonic Response When the Excitation Frequency is Evenly Spaced

Turning on cluster results corresponds to clustering results near the natural frequencies previously known from the modal analysis. The following (Figure 6.28) is the frequency response of the displacement in x-axis turning on cluster results.

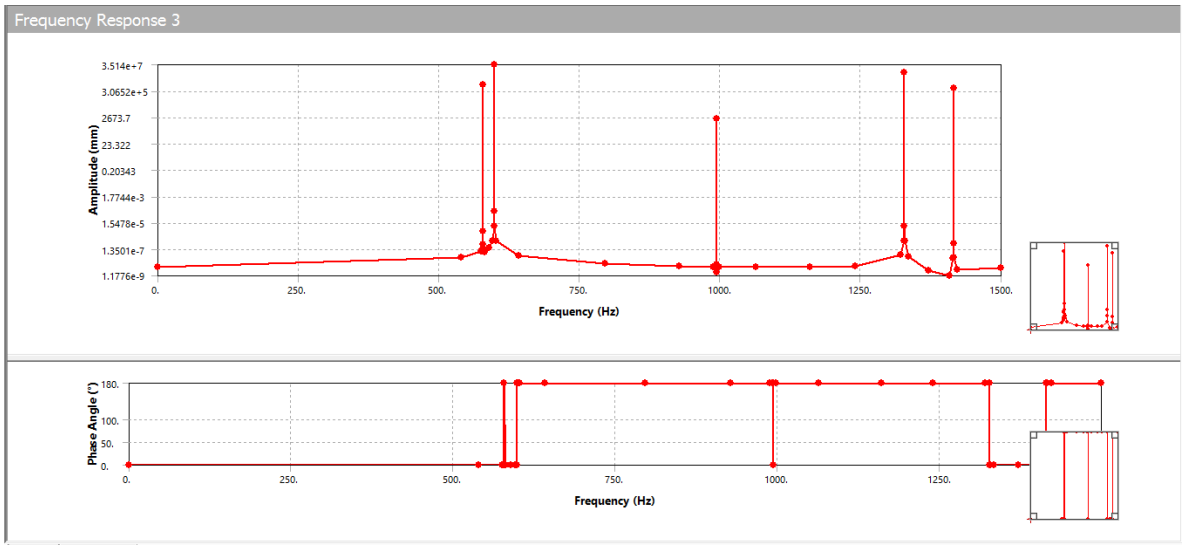

Figure 6.29: Harmonic Response with Cluster Results (x-axis)

It can be seen that the high deflections are only observed near the natural frequencies. Hence, the cluster method is more accurate. The deformation is almost negligible even past 500Hz. In a real-life scenario, a storage ring should not experience random ground vibration beyond this range. The directional displacements in the y and z-coordinate axes are shown in Figure 6.30 & Figure 6.31.

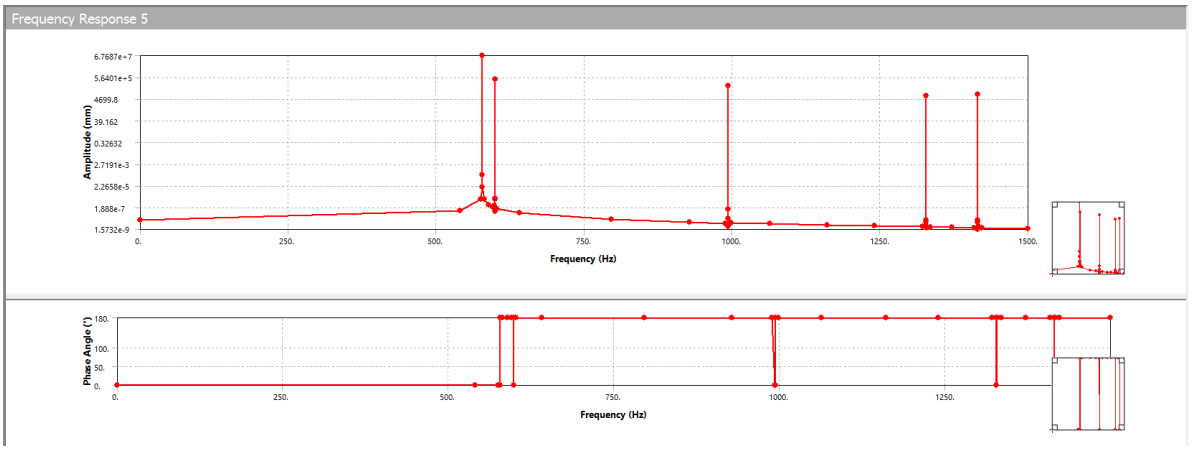

Figure 6.30: Y-Directional Deformation Harmonic Response

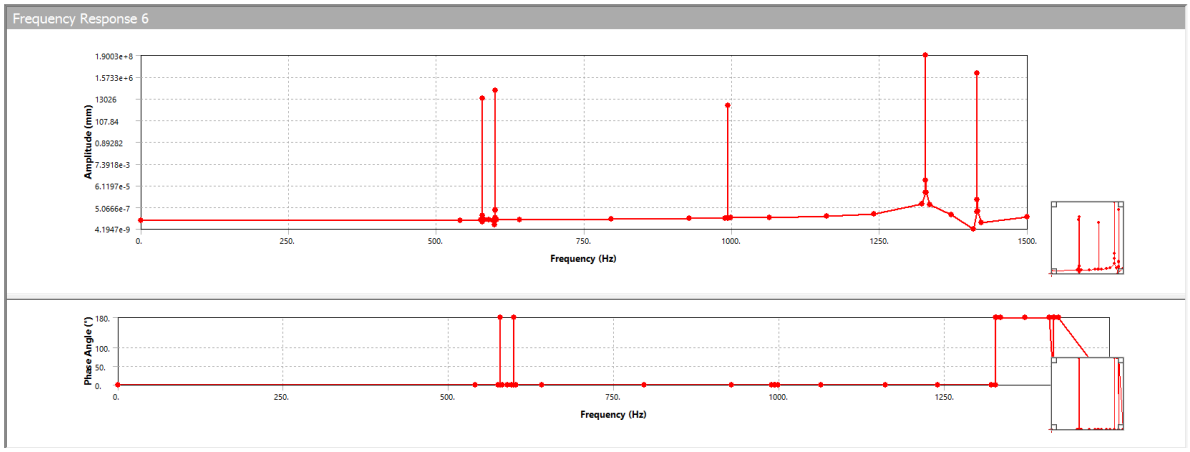

Figure 6.31: Z-Directional Deformation Harmonic Response

Therefore, it is evident from the directional deformation harmonic responses that the structure under test will not experience any high deformation under low-frequency range of 50Hz which the storage ring floor is prone to. Further, the normal stresses in the x-direction harmonic response of the magnet frame are shown in Figure 6.32.

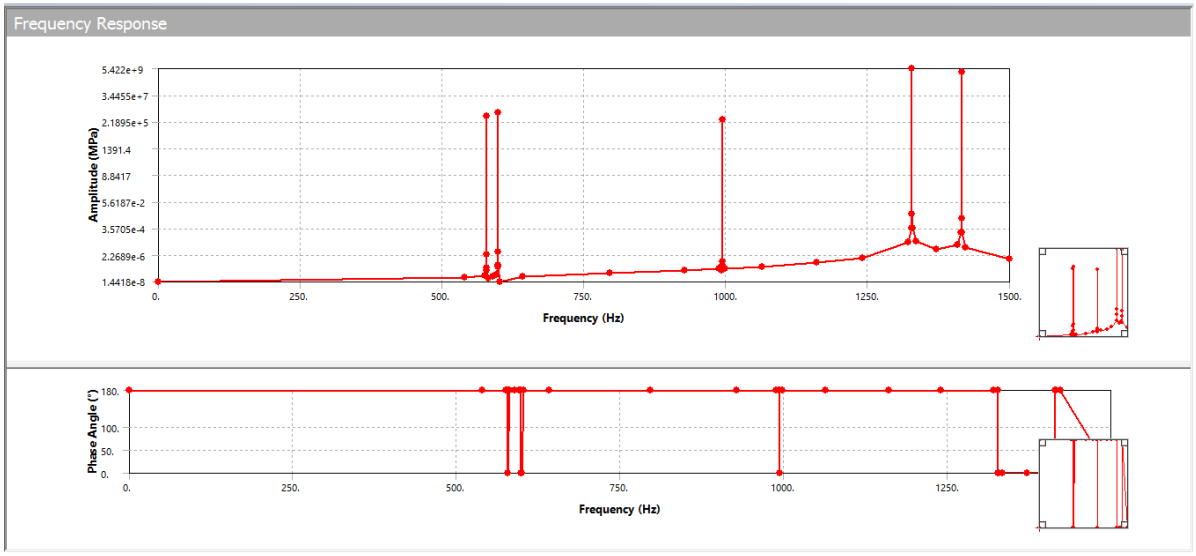

Figure 6.32: Normal Stress Harmonic Response

The stresses developed because of the harmonic force are also negligible. Moreover, the amplitude peaks correspond to the modal analysis natural frequency which indicates the analysis results are in agreement. The normal stress is below the yield stress of the materials in the structure until the resonant frequencies show up. Additionally, the shear stress in the x-y plane as a result of the cyclic load is shown in Figure 6.33.

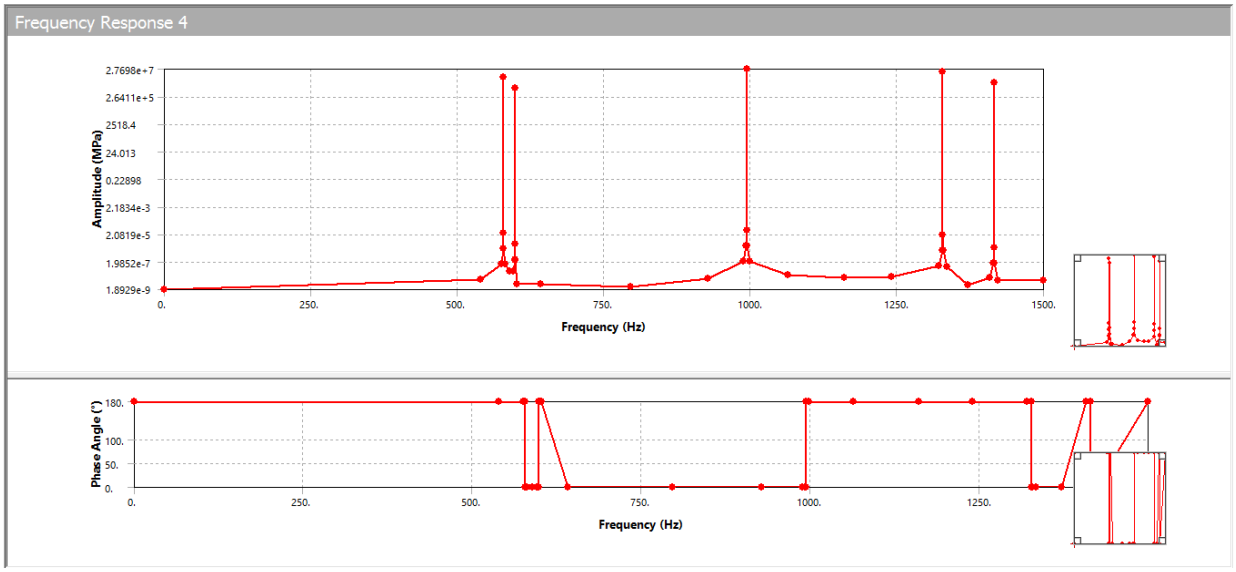

Figure 6.33: Shear Stress Harmonic Response

The shear stresses are also below the yield stress. The cyclic load does not cause any considerable deflection or stress. Thus, it can be concluded that the design is safe can withstand fatigue and forced vibrations.

6.6 Power-Spectral-Density (PSD) Response Analysis

Power-Spectral-Density (PSD) or Random Vibration Analysis determines a structure's response to nondeterministic vibration loads. Random consist of a large number of frequencies and are non-periodic in nature. Power-Spectral-Density is a function that demonstrates the variations' strength in term of a frequency function. Furthermore, the time history (Power-Spectral-Density) frequency content and the statistics are used as the random load. In Power-Spectral-Density (PSD) response analysis, a harmonic loading probabilistic spectrum is experienced by the structure under

examination from which dynamic response probabilistic distribution can be obtained. In other words, this analysis predicts the severity of random vibrations that the system is exposed (ANSYS Inc.). The PSD analysis can be used to evaluate the fatigue life of the structure undergoing random vibrations by the Three-Band Technique using Miner's Cumulative Damage Ratio (Steinberg, 2000). This analysis also helps in predicting an appropriate Factor of Safety for the system. However, fatigue life and safety factor prediction is not in the scope of the present work. PSD response analysis and harmonic response analysis can also be done to simulate the transfer function and dynamic response of the system. Moreover, the frequency response function measured from the modal analysis can be used to produce the system dynamic characteristics model. Just like the inputs of a PSD analysis, the output responses are also statistical in nature. The random vibration load is applied to the structure in the form of Power Spectral Density (PSD) which represents the mean square amplitude and the frequency of the time history of the load. The displacement response PSD (RPSD) can be given by (Grishin, 2017):

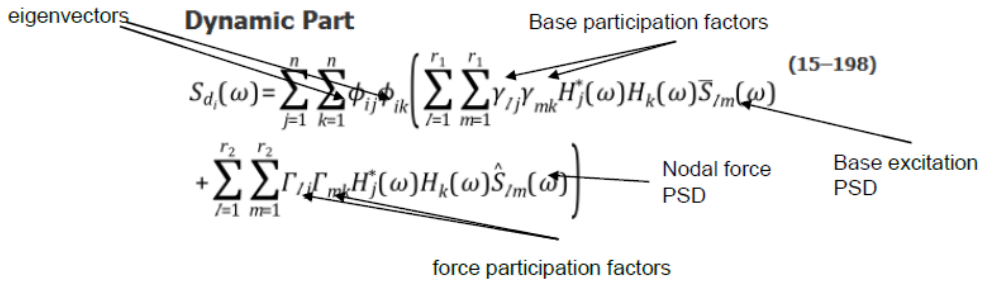

(6.46)

In the equation above, H is the transfer function:

$$H_j(\omega)=\frac{1}{\omega_j^2-\omega^2+i(2\xi_j\omega_j\omega)} \tag{6.47}$$

As the magnet frame will be experiencing random vibrations only from the base, the equation 6.46 reduces to:

$$S_{d_i}(\omega)=\sum_{j=1}^{n}\sum_{k=1}^{n}\phi_{ij}\phi_{ik}\left(\sum_{l=1}^{r_1}\sum_{m=1}^{r_1}\gamma_{lj}\gamma_{mk}H_j^*(\omega)H_k(\omega)\overline{S}_{lm}(\omega)\right) \quad \textbf{(15–198)}$$

Response PSD — Input PSD

(6.48)

The excitation root mean square (RMS) value corresponds to the square root of the area under a PSD curve. This method is based on the mode-superposition method. And, the natural frequencies and mode shapes are extracted from the modal analysis explained previously in Section 6.3.1.

6.6.1 Data Acquisition

The Displacement PSD and the corresponding frequency are the necessary inputs for the ANSYS Solver to perform the Random Vibration Analysis. Li et al (2010) performed an investigation of vibrations at the CLS Beamlines. A chiller located approximately 0.5 m away HXMA 06ID-1 endstation. A very small beam spot is necessary at the microprobe endstation, hence, it is highly sensitive to vibrations. The Vector Signal Analyzer (VSA) has two channels so the microprobe endstation was mounted with two accelerometers in order to take two-dimensional vibrations simultaneously. The displacement PSD at the microprobe endstation in the HXMA 06ID-1 in all the three directions are shown in Figures 6.34 through 6.36.

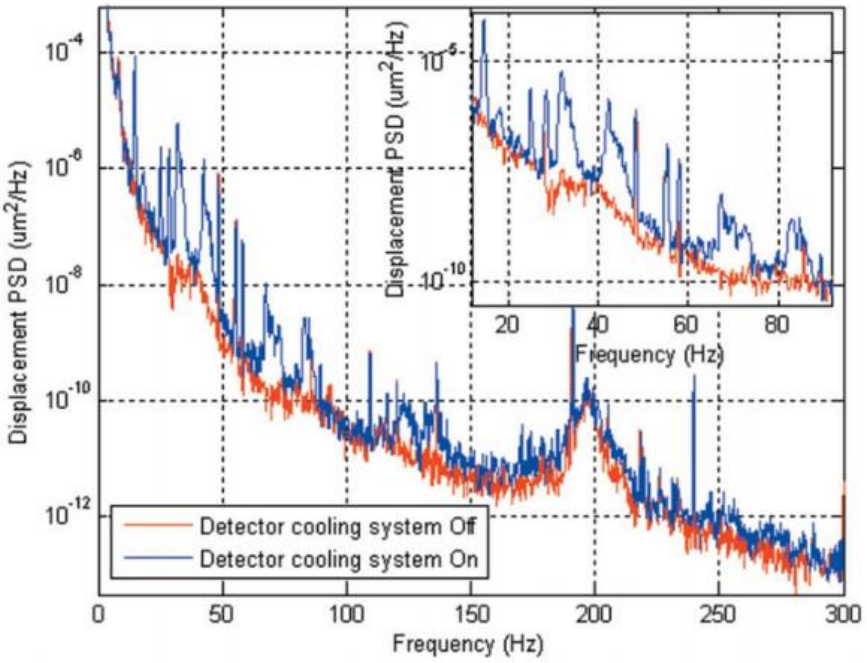

Figure 6.34: Vibrations in the x-direction (Li et al, 2010)

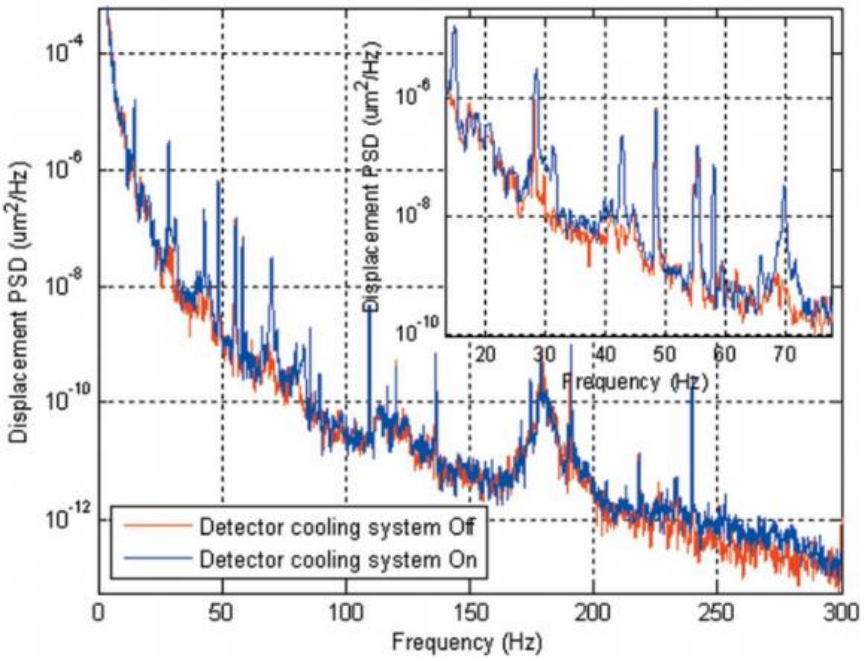

Figure 6.35: Vibrations in the y-direction (Li et al, 2010)

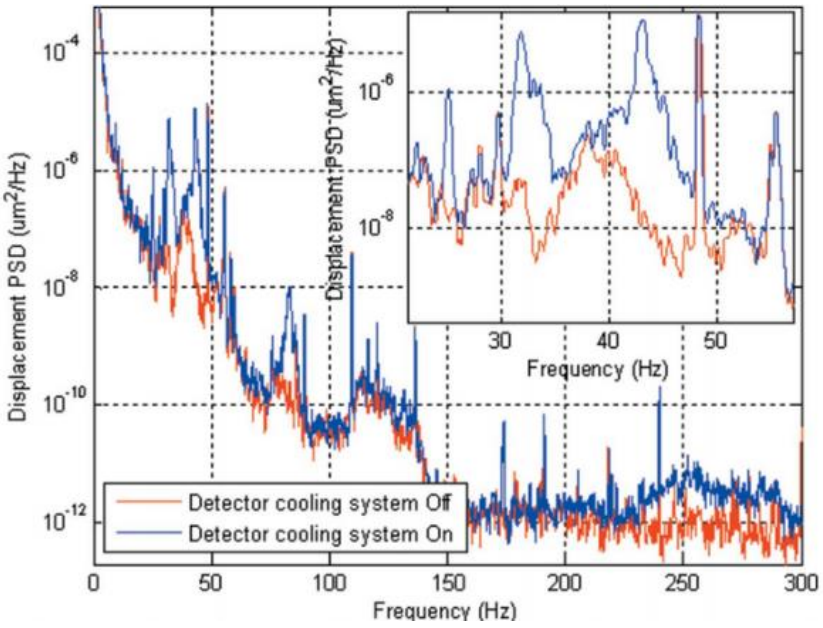

Figure 6.36: Vibrations in the z-direction (Li et al, 2010)

It was concluded that the detector's cooling system increased the microprobe endstation vibrations by 1200% in the x-direction, higher than 300% in the y-direction and almost 240% in the z-direction. This vibration produced by the cooling system was taken as the random vibration for the present magnet frame.

6.6.2 Results with Discussion

The system's response to random vibration was obtained in a 3-Sigma which accounts for 99.73% of the total response of the structure. In other words, the results below hold true for 99.73% of the cases. The directional deformations in all the three axes are shown in Figures 6.37 through Figure 6.39.

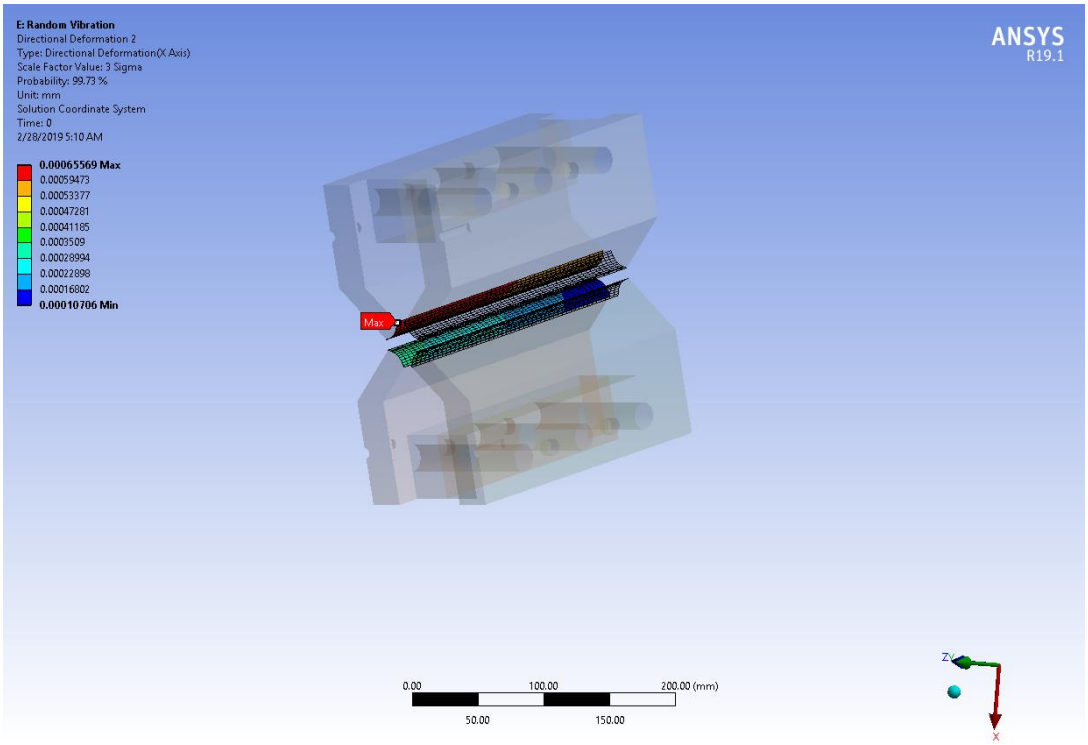

Figure 6.37: Random Vibration Induced X-Direction Deformation

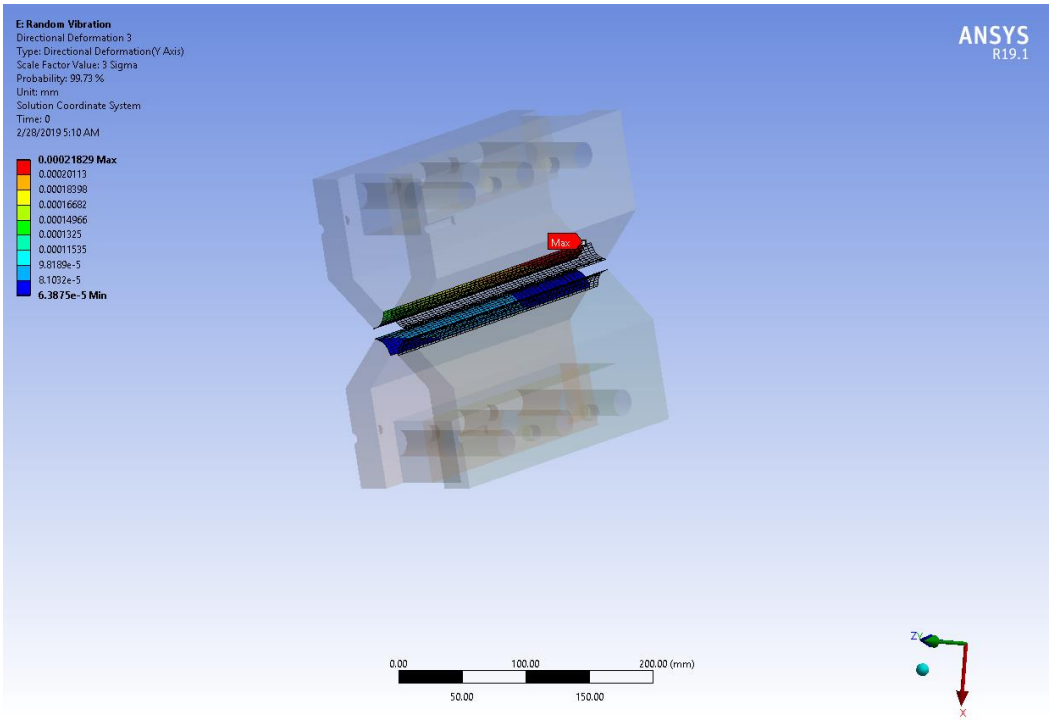

Figure 6.38: Random Vibration Induced Y-Direction Deformation

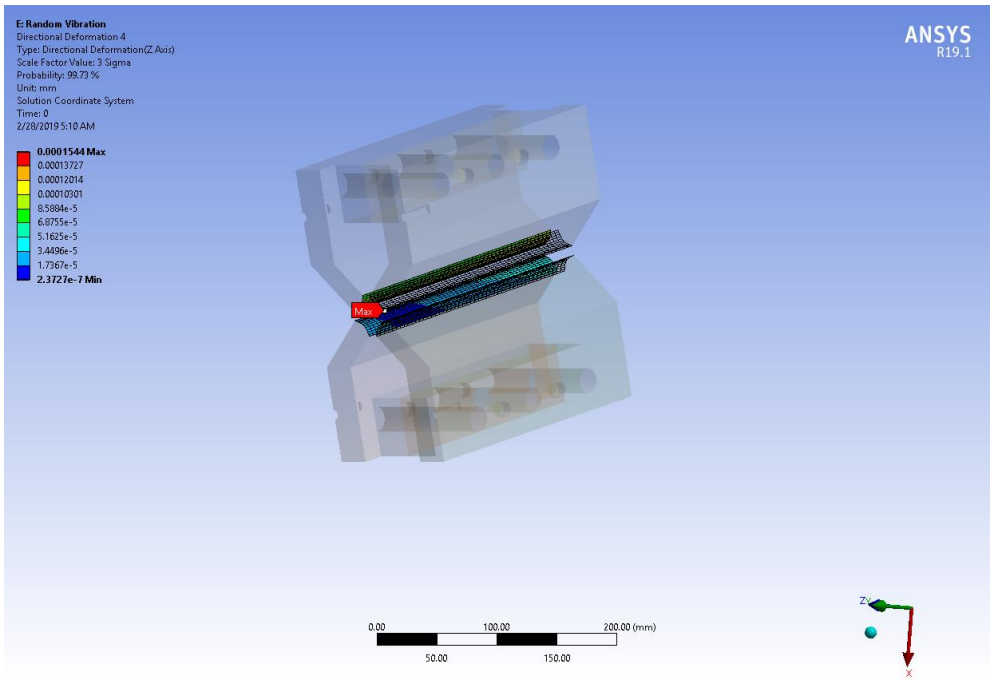

Figure 6.39: Random Vibration Induced Z-Direction Deformation

The deflection due to random vibration in all three axes is less than 10 microns. Furthermore, the equivalent stress induced in the structure due to random vibrations is shown in Figure 6.40.

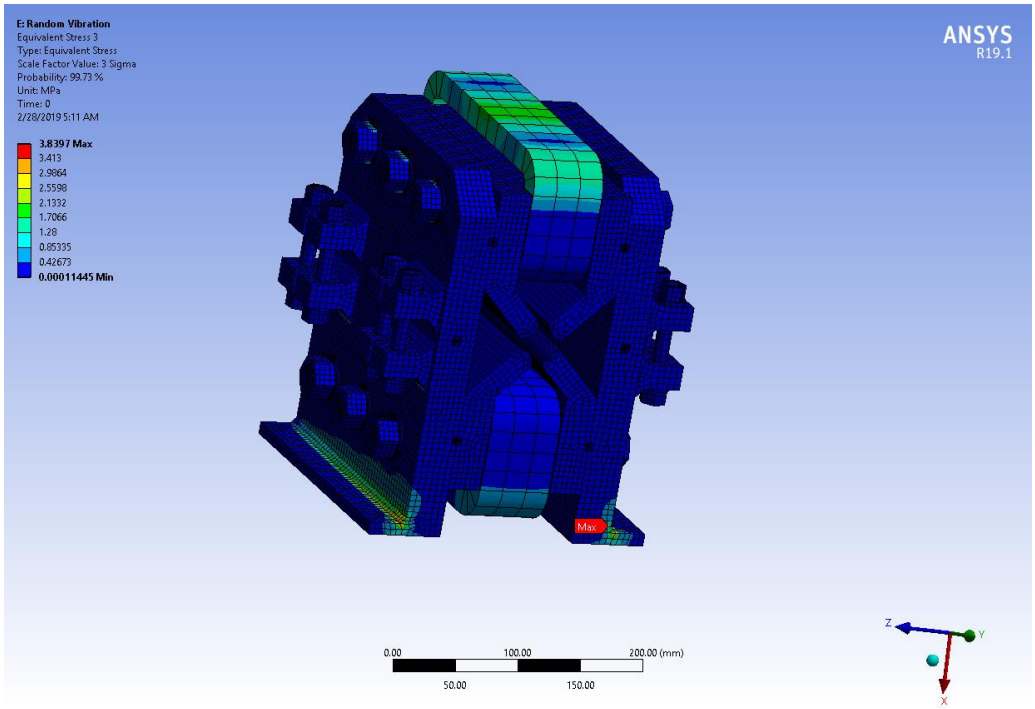

Figure 6.40: Random Vibration Induced Equivalent Stress

The Equivalent Stress is less than the yield stress of 304L stainless steel (205Mpa). Hence, it can be concluded that this frame can withstand random vibrations. However, actual vibration measurements from the storage ring will produce better confirmation of the structure's resistance to random vibrations.

The project schematic of the entire ANSYS Workbench simulation is shown in Figure 6.41.

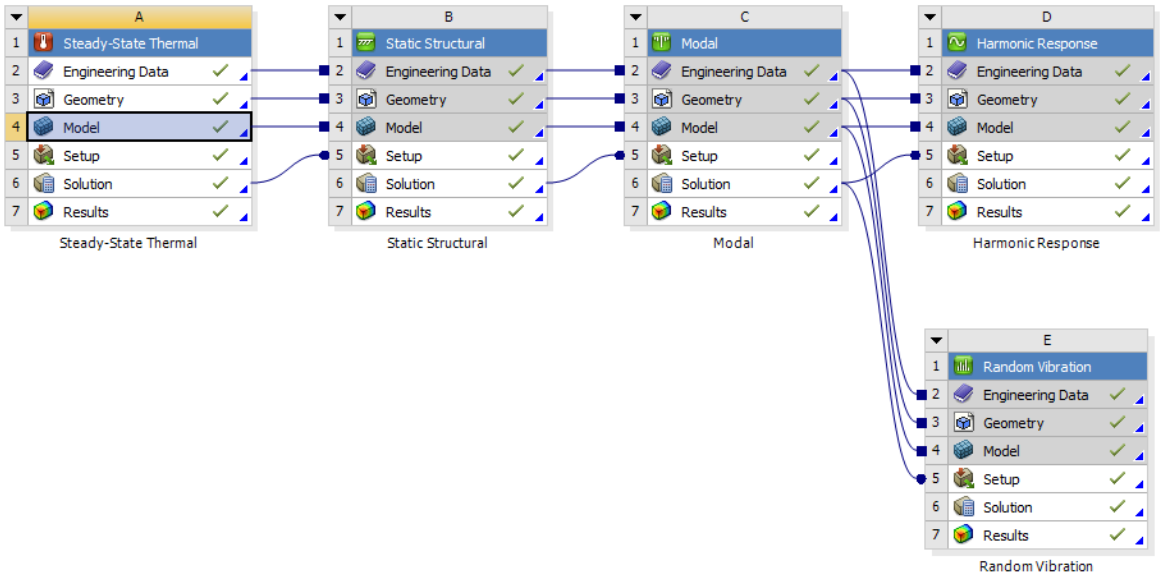

Figure 6.41: Project Schematic

6.7 Conclusion

In this chapter, the static and the dynamic behavior of the optimized model developed in Chapter 5 was examined. The optimized frame was first exposed to thermal loading and then static loading was applied on the frame to calculate the deformation at the poles and the equivalent stress. The deformation and the stress were below their allowable values. Additionally, modal analysis calculated the natural frequency and the modes of vibration. From the harmonic analysis and random vibration analysis, it was concluded that the frame was resistant to fatigue and floor vibrations. After these evaluations, it can be inferred that the frame should be able to hold the magnet in a precise position in the lattice and dampen any floor vibration from propagating into the magnet.

Chapter 7: Conclusion

The use of design optimization is a relatively new topic in the world of synchrotron component design. Topological optimization of the magnet girders is becoming popular in Mechanical Engineering Design of Synchrotron Radiation Equipment and Instrumentation (MEDSI) conferences. This work applies the optimization technique to the magnet frame design, and thus, beginning the optimization technique to an even more elemental level. Further, this project also deals with how a complicated optimization problem can be broken down into smaller optimization problems, and, thus, saving computational time. Finally, the evaluation and verification of the optimized design were performed using FEA software.

7.1 Overview of the Optimized Model

The magnet frame was optimized in the following order. First, the number of fasteners was determined using brute force optimization. Then, the material of the frame was selected using Analytic Hierarchy Process (AHP). Multi-Objective Genetic Algorithm was used to calculate an optimum thickness for the frame. Afterward, the location of the flanges was determined, and, finally, the shape was optimized using the Topology Optimization technique. To check the extent to which the objective stated in chapter one is met, it is revisited as follows:

The overall objective is designing an optimized magnet support system for the CLS 2.0 quadrupole magnet for the best performance in terms of damping and support. This overall objective is sub-divided into the following specific objectives:

Objective 1: To develop a comprehensive requirement model for the support system. The requirement needs to cover both the functional and constraint aspects.

The force exerted by one pole was found to be force -8811.72N in the horizontal direction and -4729.94N in the vertical direction (refer to Chapter 3). Based on this, the forces on all the four pole was found. The material of the frame needed to be a nonmagnetic material. The allowable deformation was decided to be kept below 10 microns to minimize machining costs.

Objective 2: To design the magnetic support to best meet the requirement.

Using Axiom Design Theory, DP1b (refer to Chapter 4) was found to be the conceptual design.

Objective 3: To conduct a simulation experiment to verify the design.

ANSYS was used to evaluate the optimized design. The static defection and equivalent stress were lower than the set limit (refer to Chapter 6). Vibration analysis showed that the structure should be resistant to fatigue and random floor vibrations.

It can be inferred that the objective has been met based on the simulation results.

7.2 Limitations

This section deals with all the limitations of this work, and they are:

- *Magnetic Force:* While evaluating the magnetic forces in Chapter 3, the mesh size can be refined and this might change the results. There is a force in the x-direction (according to RADIA coordinate system), which is small but ideally, this force should be zero. The RADIA simulations take about five hours to solve with the present mesh size and increasing the mesh density seemed impractical due to time restrictions.
- *Material Type:* Due to the unavailability of B-H curves for paramagnetic and diamagnetic materials, the effect of such type of materials being used as magnet frame material could not be studied.
- *Allowable Deformation:* The allowable deformation (Chapter 3) was only calculated for the z and y-direction (RADIA coordinate system) as POISSON is a 2D magnet code. However, as evident from the simulations, the static deflection on the in the x-direction (RADIA coordinate system) is negligible. Hence, this had no effect on the design.
- *Use of Insertion Devices:* This work assumes that the CLS 2.0 will use only closed-sided magnets as insertion devices will be used to extract the photon beam. However, in case the present design is changed, the frame design shown in Figure 4.3 I or (f) has to be adopted.
- *Divide-and-Conquer Strategy:* Concurrent design or "All-In-One (AIO)" strategy of optimization will produce the ideal optimization results. However, due to the number of variables involved it was rendered infeasible. The adopted decoupled integrated design

(DID) included many assumptions which might have resulted in slight inaccuracies in obtaining the optimal results (Chapter 4).

- *Number of Sampling Points:* A limited number of sampling points were used throughout all the optimization problems (Chapter 5). A higher number of sampling points will result in more accurate optimal solutions.
- *Topology Optimization:* ANSYS considers frictional and frictionless contacts as non-linear contacts (Chapter 5). Hence, Topology Optimization could have been performed for the whole model using better FEA software dedicated for topology optimization.
- *Mesh:* Reducing mesh size increases computational accuracy (Chapter 5 and Chapter 6). However, due to time restrictions, further mesh refinement was not performed.

- *Vibration from Water Pipes:* In case vibration result from turbulent flow inside the pipes, the frame can not damp these vibrations from reaching the magnet. This incident happened in the Australian Synchrotron where the magnet motion increased by 30% in the horizontal direction when the cooling system was completely operational (McKinlay, 2006).

7.3 Recommendations and Future Work

This section describes what could have been done differently in this work:

- *Dowel Design*: The dowel pins were not designed. Larger dowels are necessary for the front facing dowels. The contact between the dowels and frame/magnet will have a high surface finish and hence the coefficient of friction will be low (Chapter 6).
- *Bolt-Pretension:* A parametric study can be performed for all the fasteners in order to determine an appropriate pretension (Chapter 5 and 6).
- *Heat Treatment:* Machining often causes nonmagnetic steel to become magnetic. To avoid this proper heat treatment is suggested.
- *In-house Manufacturing:* Frame manufacturing is fairly easy. It can be made in-house and sent out for grinding the surfaces with high tolerances. As 304L stainless steel is used, the frame can be spray painted which will protect the frame from corrosion.
- *Magnet's Mechanical Design:* A mechanism that holds the coils to the magnet yoke has to be designed. Further, the mechanical design of the magnet yokes which will include the

dowel pins that align the yokes is yet to be done. Lastly, electrical and cooling water connections have to be designed.

- *Magnet's Physics Design:* A higher quadrupole gradient can be achieved by using the closed-sided configuration. Moreover, having a return yoke also decreases the magnetic forces on the poles. These characteristics could be demonstrated by the magnet design shown in Figure 7.1 which is similar to the MAX IV magnets but has recessed coils.

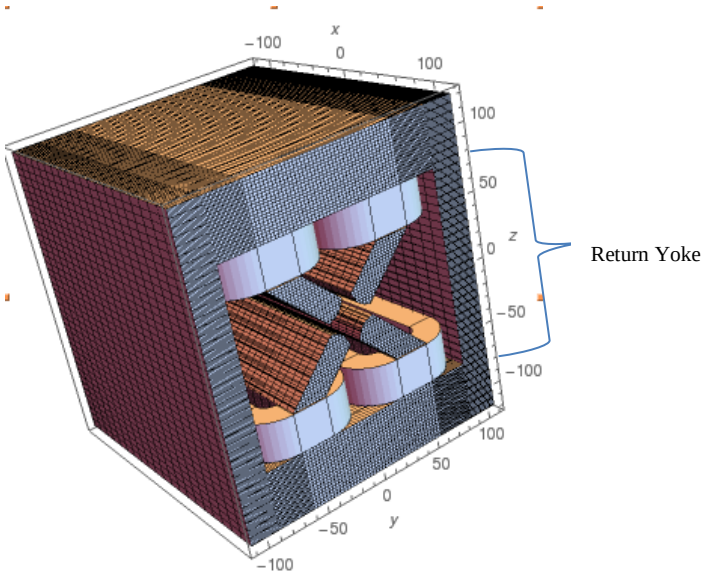

Figure 7.1: Alternate Magnet Design

In the event that an open-sided magnet is necessary for the theoretical design of the storage ring, then a hole slightly larger than the diameter of the vacuum chamber can be made in the return yoke. The return yoke can be made thicker so that it can withstand the magnetic force.

- *Higher Deformation:* If the designed magnet deforms beyond the allowable deformation (Chapter 3), then, larger holes can be drilled and larger diameter fasteners can be used.
- *Alignment:* Fiducialisation is the magnetic axis measurement (Bottura, 2006). This is done in two steps, first, a magnetic sensor detects the field null local reference system, and, then, the axis coordinates are transferred to the fiducials (Figure 7.2).

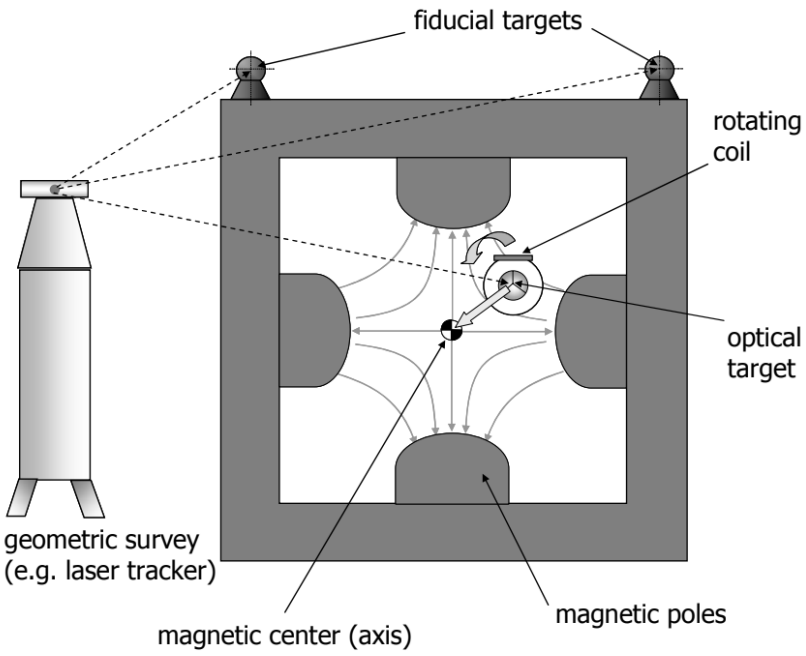

Figure 7.2: Quadrupole Fiducialisation (Bottura, 2006)

- *Fastener Thread:* For the sake of simplicity the contacts between the fasteners and the nut were assumed to be bonded. However, in real-life scenario, the fastener has to be designed and a pitch has to be selected that corresponds to the highest stiffness. A study by Zhang et al. (2016) concluded that the stiffness of a bolted joint is directly proportional to the material's elastic modulus and the engaging length. In other words, decreasing the thread pitch could increase the stiffness of the bolted joint. Hence, an appropriate thread pitch has to be determined.

7.4 Contribution

The major contributions of this thesis are that it endorses the divide-and-conquer strategy of optimization and defines a methodology for optimized synchrotron support structure design. These are discussed in detail as follows:

Designing the magnet support involved optimising a large number of design parameters. However, if the full concurrent design method was adopted then this will make the calculations more

complex and time-consuming. This work clearly exemplifies that the Decoupled Integrated Design technique of optimization can be successfully used to obtain an optimal design.

Synchrotron support structures have to be design intricately. At the same time, obtaining an optimized design can be challenging. This thesis consolidates a design process that can be used to get optimized designs for complicated synchrotron supports. For instance, the methodology developed in this project was also used to design the girders for CLS 2.0. The design goals were similar to those in the present work. The optimized girder is shown in Figure 7.3.

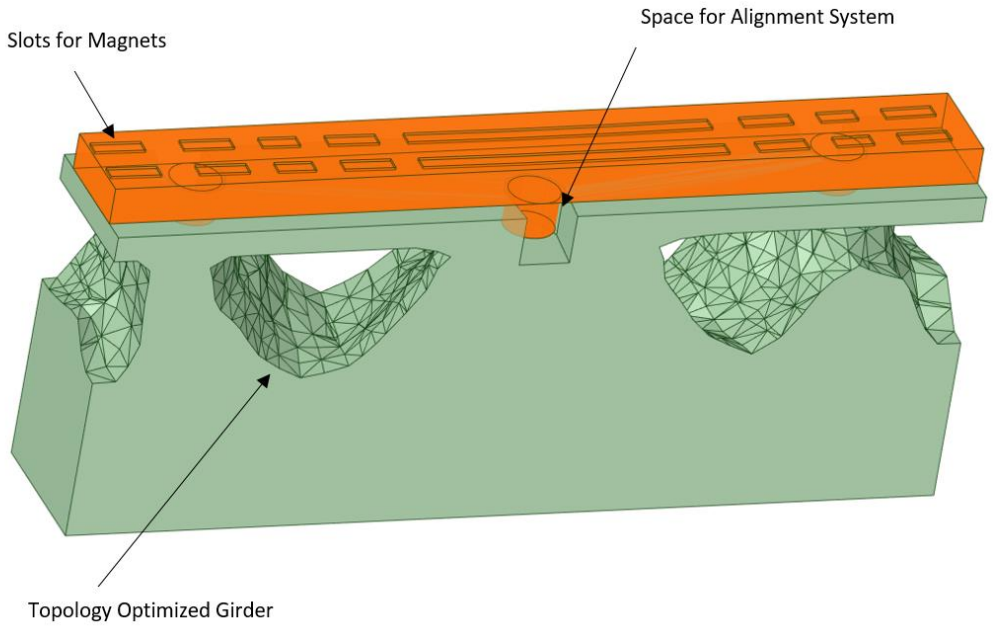

Figure 7.3: Optimized CLS 2.0 Girder (Mondol et al., 2019)

As evident from the literature review, time is an important constraint to be considered while upgrading light sources. Hence, this research is important. The girder design was completed within one month. Based on this research, frames for the dipoles, the sextupoles and other magnets can also be built. Frames form an integral part of many mechanical and biomedical devices.

7.5 Other Applications

Biomedical devices like MRI machines and surgical microscopes are also sensitive to environmental vibrations (Kellogg, 2008; Unger, 2007 & Tigli, 2014). The production process of integrated circuits, used in various medical devices, is vulnerable to mechanical vibrations as well (Department of Mechanical Engineering Eindhoven University of Technology, 2015). Devices whose performance is sensitive to vibrations can use the methodology developed by this research to maximize vibration resistance. Also, this technology can be used in damping vibrations for surgical tables where the intricate medical procedure takes place. The chassis of a vehicle must also possess vibration damping properties which can be achieved by this technology (Mohanty & Fatima, 2014). Engine vibrations are caused by the structures of the cylinder, valves, etc. These structures can be enhanced to reduce vibrations by this method.

References

Accelerator Division — Fermilab Operations Department (2013). Concepts Rookie Book.

Adam, M. (2018). Private communication.

Advanced Light Source (2019). Useful Info for FEA. Retrieved from http://www-eng.lbl.gov/~als/FEA//index_files/page0002.html

AitShalia, F, Johnson, E, Will, P, 1995. Is concurrent engineering always a sensible proposition? IEEE Trans. On Engineering Management, 42(2), 166-170.

Andresen, S. (2018). Optimizing the PETRA IV girder by using bio-inspired structures, MEDSI 2018, Paris.

ANSYS Inc. ISO 9001:2000 company.

Antokhin, E., Batrakov, A., Churkin, I., Demenev, V., Dodonov, A., Golubenko, O., Korchuganov, V., Levichev, E., Mikhailov, S., Ogurtsov, A., Philipchenko, A., Rivkin, L., Rouvinski, E., Rouvinski, S., Schreiner, K., Sernenov, E., Singatulin, S., Skorobogatov, D., Steshov, A., Sukhanov, A., Ushakov, V., Vollenweider, C. and Zichy, J. (2002). Multipoles of the SLS storage ring: manufacturing and magnetic measurements. IEEE Transactions on Appiled Superconductivity, 12(1), pp.51-54.

Ashby, M.F. and Cebon, D. (1993). Materials selection in mechanical design. Journal De Physique IV, Vol. 3, Chapter 7, pp.1–9.

ASM Material Data Sheet. (2019). Retrieved from http://asm.matweb.com/search/SpecificMaterial.asp?bassnum=mq304a

Assari, A., Mahesh, T., & Assari, E. (2012b). Role of public participation in sustainability of historical city: usage of TOPSIS method. Indian Journal of Science and Technology, 5(3), 2289-2294.

Behbahani, S. and de Silva, C. (2008). System-Based and Concurrent Design of a Smart Mechatronic System Using the Concept of Mechatronic Design Quotient (MDQ). IEEE/ASME Transactions on Mechatronics, 13(1), pp.14-21.

Behbahani, S. and de Silva, C. (2014). Niching Genetic Scheme With Bond Graphs for Topology and Parameter Optimization of a Mechatronic System. IEEE/ASME Transactions on Mechatronics, 19(1), pp.269-277.

Bendsøe, M. and Kikuchi, N. (1988). Generating optimal topologies in structural design using a homogenization method. Computer Methods in Applied Mechanics and Engineering, 71(2), pp.197-224.

Bhaskaran, R. (2019). CornellX: ENGR2000X A Hands-on Introduction to Engineering Simulations. Presentation, edx.org.

Bhaskaran, R. (2016). ANSYS Learning Modules – SimCafe – Dashboard. Retrieved from https://confluence.cornell.edu/display/SIMULATION/ANSYS+Learning+Modules#app-switcher

Birch, S., and Visnic, B. (2016). Jaguar, Exa say simulation to eliminate prototypes by 2020. Automotive Engineering, SAE International 3: 3.

Bottura, L., Buzio, M., Pauletta, S., and Smirnov, N., (2006). Measurement of magnetic axis in accelerator magnets:critical comparison of methods and instruments. In:Instrumentation and Measurement Technology Conference. IMTC 2006. Proceedings of the IEEE.pp. 765–770

Budynas, R. (2016). Shigley´s Mechanical Engineering Design. McGrae Hill Education.

CAE Associates Inc. (2014). Tips & Tricks for Hex Brick Meshing – ANSYS eLearning – CAE Associates [Video]. Retrieved from https://www.youtube.com/watch?v=EDt6mmrA66w

Callister.W.D,JR. (2007). Materials Science and Engineering: An Introduction . 7th edition. John Wiley & Sons, Inc.

Canadian Light Source Inc. (2018). Inside the synchrotron, Retrieved August 18, 2018, from http://www.lightsource.ca/inside_the_synchrotron

Collins, J., Cease, H., Izzo, S., Liu, Z., Nudell, J., and Preissner, C. (2016). Preliminary Design of the Magnet Support and Alignment Systems for the APS-U Storage Ring. 9th Edition of the Mechanical Engineering Design of Synchrotron Radiation Equipment and Instrumentation Conf. (MEDSI' 16), Barcelona, Spain, 2016, pp. 87-89.

CompositesWorld (2018). Exel Composites and CNIM Partner on Glass Fiber Components for World's Largest Fusion Facility. Available at: https://www.compositesworld.com/news/exel-composites-and-cnim-partner-on-glass-fiber-components-for-worlds-largest-fusion-facility

Conte, M., and MacKay, W. (1991). An Introduction to the Physics of Particle Accelerators, World Scientific.

CRC Handbook of Physical Quantities. (1997). Boca Raton, FL: CRC Press: 145-156.

Dai, F. (2015). On Development of a Green Web-based System for Reducing Waiting Times of Outpatients. Degree of Master of Science. University of Saskatchewan.

Dai, Z. (2018). Improvement Of General Design Theory And Methodology With Its Application To Design Of A Retractor For Ventral Hernia Repair Surgery (Master of Science). University of Saskatchewan.

Dallin, L. (2018). CLS Magnet Designs: Past and Future, AOD meeting. (Internal Document)

Dallin, L. (2018). The `Zero Drift` Quadrupole. (Internal Document).

Dallin, L. and Wurtz, W., (2016). AIP Conference Proceedings, Vol. 1741 (AIP Publishing LLC) p. 020034.

Dallin, L. (2018). Private communication.

Dallin, L. (2001). CLS design note 5.2.31.2 Rev.0, "Synchrotron Light Source Magnets". (Internal Document).

Dallin, L. (2018). Design Considerations for an ultralow emittance storage ring for the Canadian Light Source, Proc. 9th Int. Particle Accelerator Conf. (IPAC'18), Vancouver, Canada, paper TUPMF038.

Dallin, L., & Bertwistle, D. (2018). Magnet Design Considerations for An Ultralow Emittance Canadian Light Source. Retrieved from http://ipac2018.vrws.de/papers/wepmf021.pdf

Dallin, L., Lowe, D. and Swirsky, J. (n.d.). Canadian light source magnets. Proceedings of the 2003 Bipolar/BiCMOS Circuits and Technology Meeting (IEEE Cat. No.03CH37440).

Deb, K. (2009). Multi-objective optimization using evolutionary algorithms. Chichester, UK: John Wiley and Sons.

Deb, K., Zhu, L. and Kulkarni, S. (2015). Multi-scenario, multi-objective optimization using evolutionary algorithms: Initial results. 2015 IEEE Congress on Evolutionary Computation (CEC).

Department of Mechanical Engineering, Eindhoven University of Technology (2015). PhD explained; damping of mechanical vibrations. Retrieved October 31, 2018, from https://www.tue.nl/en/our-university/departments/mechanical-engineering/news/28-04-2015-phd-explained-damping-of-mechanical-vibrations/

Ding, T., Liang, L., Yang, M., and Wu, H. (2016). Multiple Attribute Decision Making Based on Cross-Evaluation with Uncertain Decision Parameters. Mathematical Problems in Engineering, vol. 2016, Article ID 4313247, 10 pages. https://doi.org/10.1155/2016/4313247.

Dweiri, F. and Al-Oqla, F.M. (2006). Material selection using analytical hierarchy process. Int. J. Computer Applications in Technology, Vol. 26, No. 4, pp.182–189.

Eiben, A., Raué, P. and Ruttkay, Z. (1994). Genetic algorithms with multi-parent recombination. Parallel Problem Solving from Nature — PPSN III, pp.78-87.

Einfeld, D., Plesko, M., and Schaper, J. (2014). First multi-bend achromat lattice consideration, Jnl of Synchrotron Radiation, 21, pp. 856-861. Doi:10.1107/S160057751401193X

Eklund, P., Sjökvist, S., Eriksson, S., Leijon, M. (2014). A complete design of a rare earth metal-free permanent magnet generator, Open Access Mach, 2, pp. 120-133.

Eklund, P. (2013). Design of a Ferrite Permanent Magnet Rotor for a Wind Power Generator, Upsalla Univeristy. Available at: http: /www. Diva-portal.org/smash/get/diva2: 632021/fulltext01.pdf.

Elettra-Sincrotrone Trieste S.C.p.A. di interesse nazionale. (2017). Elettra 2.0 Preliminary Conceptual Design Report (Mk. I). 34149 Basovizza, Trieste.

Encarta Encyclopedia 2004. Microsoft Corporation.

Erdemir, A., Guess, T., Halloran, J., Tadepalli, S. and Morrison, T. (2012). Considerations for reporting finite element analysis studies in biomechanics. Journal of Biomechanics, 45(4), pp.625-633.

European Synchrotron Radiation Facility (1997, April). Radia 2/(Version 4.1) [Computer software]. 71, avenue des Martyrs, CS 40220, 38043 Grenoble Cedex 9, France. Retrieved from http://www.esrf.eu/Accelerators/Groups/InsertionDevices/Software/Radia

Fenn, R., Slaton, T. and Woods, M. (2004). Quadrupole Vibration Measurements for QM1B and QC3 in the Final Focus Test Beam at SLAC (LCC-0036).

Goepel, K. (2010). Analytic Hierarchy Process AHP – Business Performance Management. Retrieved from https://www.youtube.com/watch?v=18GWVtVAAzs

Goswami, A., & Chakraborty, D. (2014). Mod-01 Lec-39 Multi Objective Decision Making. Retrieved from https://www.youtube.com/watch?v=9Z8NRNi2arU&t=1793s

Grishin, A. (2017). Estimating Structural Response to Random Vibration: Reaction Forces. Presentation, PADT, Tempe AZ.

Grochulski, P., Fodje, M., Labiuk, S., Wysokinski, T., Belev, G., Korbas, M., & Rosendahl, S. (2017). Review of Canadian Light Source facilities for biological applications. Nuclear Instruments And Methods In Physics Research Section B: Beam Interactions With Materials And Atoms. 411, 17-21. Doi: 10.1016/j.nimb.2017.01.065

Hale, S. (2015). Nonlinear Convergence. Presentation, CAE Associates. Retrieved from https://www.youtube.com/watch?v=njb7PWyeaH8

Hashmi, S. (2017). Comprehensive Materials Finishing, Elsevier.

Holmberg E., Torstenfelt B., and Klarbring A., (2013). Stress constrained topology optimization, Structural and Multidisciplinary Optimization, 48(1):33-47.

Holsinger, R., and Halbach, K. (2013). Poisson Superfish (Version 7.19) [Computer software]. Retrieved July 23, 2018, from http://laacg.lanl.gov/laacg/services/download_sf.phtml

Huang C-H, Galuski J, Bloebaum C.L. (2007). Multi-objective Pareto concurrent subspace optimization for multidisciplinary design. AIAA J 45:1894–1906

Jahan, A.; Ismail, M. Y.; Sapuan, S. M.; Mustaph, F. (2010). Material screening and choosing methods – a review, Materials & Design 31(2): 696–705. http://dx.doi.org/10.1016/j.matdes.2009.08.013

Johansson, M., Anderberg, B., & Lindgren, L.-J. (2014). Magnet design for a low-emittance storage ring. Journal of Synchrotron Radiation, 21(Pt 5), 884–903. http://doi.org/10.1107/S160057751401666X

Jung, J., Leitner, M., Li, N., San Mateo, E., Steier, C., Swenson, C. and Venturini, M. (2018). Design of Asymmetric Quadrupole Gradient Bending R&D Magnet For The Advanced Light Source Upgrade (ALS-U). In 9th International Particle Accelerator Conference (pp. 3667-3669). Vancouver, BC, Canada: JACoW Publishing. Doi:10.18429/JACoW-IPAC2018-THPAL020

Karantzoulis, E. (2018). Elettra 2.0 — The diffraction limited successor of Elettra. Nuclear Instruments And Methods In Physics Research Section A: Accelerators, Spectrometers, Detectors And Associated Equipment, 880, 158-165. Doi: 10.1016/j.nima.2017.09.057

Kellogg, J. (2008). Electromagnetic Interference (EMI) and Structural Vibration Effects on MRI Site Construction and Installation Requirements. Available at: https://mriquestions.com/uploads/3/4/5/7/34572113/vibration_testing.pdf

Kim Vandiver, J. (2011). Modal Analysis: Orthogonality, Mass Stiffness, Damping Matrix. Presentation, Massachusetts Institute of Technology.

Kiong, S., Lee, L., Chong, S., Azlan, M. and Muhd Nor, N. (2013). Decision Making with the Analytical Hierarchy Process (AHP) for Material Selection in Screw Manufacturing for Minimizing Environmental Impacts. Applied Mechanics and Materials, 315, pp.57-62.

Knowles, J. D. and Corne, D. (1999). The pareto archived evolution strategy: A new baseline algorithm for pareto multiobjective optimisation. In Congress on Evolutionary Computation (CEC99), Volume 1, Piscataway, NJ, pp. 98–105. IEEE Press.

Konak, A., Coit, D., & Smith, A. (2006). Multi-objective optimization using genetic algorithms: A tutorial. Reliability Engineering & System Safety, 91(9), 992-1007. Doi: 10.1016/j.ress.2005.11.018

Kupiec, H. (2016). Chamfer or Fillet: It's More Than a Coin Toss. Retrieved from https://www.engineering.com/AdvancedManufacturing/ArticleID/12682/Chamfer-or-Fillet-Its-More-Than-a-Coin-Toss.aspx

LaCourse, D. (2003). Virtual Prototyping Pays Off. Retrieved from http://www.cadalyst.com/manufacturing/virtual-prototyping-pays-9774

Lemburg, J. And Kirchner, F. (2011). Conceptual and Embodiment Design of Robotic Prototypes. International Journal of Humanoid Robotics, 08(03), pp.419-437.

Li, J. and Zhang, Y. (2008). Topological Optimization Method and Its Application Research In the Rear Platen' 3-D Structure Design. IEEE. [online] Available at: https://ieeexplore.ieee.org/iel5/4664825/4670728/04670826.pdf

Li, J., Matias, E., Chen, N., Kim, C., Wang, J., Gorin, J., He, F., Thorpe, P., Lu, Y., Chen, W., Grochulski, P., Chen, X. and Zhang, W. (2010). Investigations of mechanical vibrations for beamlines at the Canadian Light Source. Journal of Synchrotron Radiation, 18(2), pp.109-116.

Li, Q., Zhang, W. and Chen, L. (2001). Design for control-a concurrent engineering approach for mechatronic systems design. IEEE/ASME Transactions on Mechatronics, 6(2), pp.161-169.

Liu, Z., Cease, H., Collins, J., Nudell, J. and Preissner, C. (2016). Optimization for the APS-U Magnet Support Structure. Proceedings of MEDSI 2016, Barcelona, Spain.

Lu, J., Toplosky, V., Goddard, R., & Han, K. (2017). Low temperature physical properties of Co-35Ni-20Cr-10Mo alloy MP35N®. Cryogenics, 86, 106-111. Doi:10.1016/j.cryogenics.2017.07.004

Magnetic Properties of 304 & 316 Stainless Steel. (2018). Retrieved August 7, 2018, from https://greenwoodmagnetics.com/resource/what-is-the-difference-between-304-and-316-stainless-steel/

Mangra, D., Sharma, S., and Doose, C. (2000). Performance of the Vibration Damping Pads in the APS Storage Ring, MEDSI 2000, PSI, Villigen.

Marsh, E., Slocum, A. (1996). An integrated approach to structure damping, Precision Engineering, Vol.18, pp.103-109.

Masuzawa, M., Sugahara, R. & Yamaoka, H. (2006). *Proceedings of the 9th International Workshop on Accelerator Alignment*, 26–29 September 2006, Stanford Linear Accelerator Center, Stanford, CA, USA.

MAX IV (2010). MAX IV DDR, Available at: www.maxiv.lu.se/accelerators-beamlines/accelerators/accelerator-documentation/max-iv-ddr/

McKinlay, J., Barg. B., (2006). Performance of the Australian Synchrotron Storage Ring Alignment System. MEDSI, May, Himeji, Japan.

Modulus of Elasticity for Metals (2018), Retrieved from https://www.amesweb.info/Materials/Modulus-of-Elasticity-Metals.aspx

Mohanty, A., & Fatima, S. (2014). An overview of automobile noise and vibration control. Noise Notes, 13(1), 43-56. Doi: 10.1260/1475-4738.13.1.43

Mondol, S., Gilbert, J., Gorin, J., Rao, J., Boland, M. and Zhang, W. (2019). Mechanical Stability Analysis of the Topology Optimized Girder Base for a Ultralow Emittance Canadian Light Source. In: *Engineering Graduate Research Conference*. Saskatoon.

moodlemech (2019). Bolted Joints. Presentation, https://www.youtube.com/watch?v=Lq3E2OJYVzA.

Muhammad, Y., Helmi, Y., and Ahmad, S. (2015). Mechanical and Thermal Properties of Glass Fiber-Reinforced Epoxy Composite with Matrix Modification Using Liquid Epoxidized Natural Rubber. IEEE Transactions on Systems, Man and Cybernetics Part C: Applications and Reviews, Institute of Electrical and Electronics Engineers Inc., ukm.pure.elsevier.com/en/publications/mechanical-and-thermal-properties-of-glass-fiber-reinforced-epoxy.

Nashif, A. (1992). Recent application of the passive damping technology, 2nd Int. Congress on recent developments in air- and structure-borne sound and vibration, Auburn University, USA.

Nudell, J. (2016). Preliminary Design and Analysis of the FODO Module Support System for the APS-U Storage Ring -. In Proc. MEDSI'16, Barcelona, Spain,, pp. 83-85.

Park, G. (2010), Analytic Methods for Design Practice. Springer.

Penicka, J. (2018). Alignment Strategy for APS Upgrade In SLAC eConf. Retrieved from http://www.slac.stanford.edu/econf/C1610034/papers/812.pdf

Piratelli-Filho, A., & Levy-Neto, F. (2010). Behavior of granite-epoxy composite beams subjected to mechanical vibrations. Materials Research, 13(4), 497-503. Doi: 10.1590/s1516-14392010000400012

Preissner, C., Cease, H., Collins, J., Liu, Z. and Nudell, J. (2016). Nostradamus and the Synchrotron Engineer: Key Aspects of Predicting Accelerator Structural Response. Proceedings of MEDSI 2016, Barcelona, Spain.

Preissner, C. (2018). Le Guide for Support: A Cookbook for Modeling of Accelerator Structures. Presented at MEDSI, Paris, France, paper WEPH22.

Pywell, R. (2004), Canadian Light Source Inc., 5.2.31.4 RADIA Sim of CLS Storage Ring Quadrupole. (Internal Document)

Saaty, T.L. (1980). The Analytic Hierarchy Process. McGraw-Hill, New York.

Saeidi, F., Razazian, M., Rahighi, J. and Pourimani, R. (2016). Magnet design for an ultralow emittance storage ring. Physical Review Accelerators and Beams, 19(3).

Sharma, S. (2005). Design of Accelerator Girder System for Vibration Suppression, Workshop on Ambient Ground Motion and Civil Engineering for Low Emittance Electron Storage Ring, Hsinchu, China.

Sigmund, O., & Maute, K. (2013). Topology optimization approaches. Structural And Multidisciplinary Optimization, 48(6), 1031-1055. Doi: 10.1007/s00158-013-0978-6

Smith, D. (2018). MEI End of Term Presentation. (Internal Document)

Sreeramulu, K., Das, S., Ruwali, K., & Shinde, R. (2017). An Approach to the Development of Open-Type Quadrupole Magnets for Indus-2 Electron Storage Ring. International Journal Of Scientific Engineering And Technology, 6(4), 145. Doi: 10.5958/2277-1581.2017.00006.7

Steier, C., Allézy, A., Anders, A., Baptiste, K., Byrd, J., Chow, K., Cutler, G., Donahue, R., Duarte, R., Jung, J.-Y., Leemann, S., Leitner, M., Luo, T., Nishimura, H., Oliver, T., Omolayo, O., Osborn, J., Pappas, C., Persichelli, S., Placidi, M., Portmann, G., Reyes, S., Robin, D. and Sannibale, F., De Santis, S., Sun, C., Swenson, C., Venturini, M., Waldron, W., Wallén, E. and Wan, W. (2018). Status of the Conceptual Design of ALS-U. In 9th International Particle Accelerator Conference (pp. 4134-4137). Vancouver, BC, Canada: JACoW Publishing. Doi:10.18429/JACoW-IPAC2018-THPMF036

Steinberg, D.S. (2000). Vibration Analysis for Electronic Equipment, John Wiley & Sons Inc.

Streun, A., (Ed.) (2017). SLS-2 Conceptual Design Report. Paul Scherrer Institut, Villigen, Switzerland.

Suh, N. (1990). The Principles of Design, Oxford University Press.

Sullivan, J. (1988). Technical Physics. USA: Wiley: 204.

Sun, Z., Liu, X., He, D., Zhang, B. and Zhang, W. (2012). On a decoupled integrated design approach to robotic mechanisms. 2012 7th IEEE Conference on Industrial Electronics and Applications (ICIEA).

Svanberg, K. (1987). The method of moving asymptotes—a new method for structural optimization. International Journal For Numerical Methods In Engineering, 24(2), 359-373. Doi: 10.1002/nme.1620240207

Swirsky, J. (2018). Private communication.

Tanabe, J. (2005). Iron Dominated Electromagnets Design, Fabrication, Assembly and Measurements. Stanford, CA 94025: Stanford Linear Accelerator Center, Stanford Synchrotron Radiation Laboratory.

Tavares, P. F., Leemann, S. C., Sjostrom, M. & Andersson, A. (2014). J. Synchrotron Rad. 21, 862-877.

Teknomo, K. (2006). Analytical Hierarchy Process (AHP) Tutorial, Retrieved from https://people.revoledu.com/kardi/tutorial/AHP

Thakker, J., and Miller, B. (2015). Introducing Design and Robust Optimisation with ANSYS DesignXplorer. YouTube, WildeAnalysis, Available at: www.youtube.com/watch?v=fjfhcdKBnQE.

Tigli, O. (2014). Floor Vibrations on Healthcare Facilities: A Case Study on a Surgical Microscope. Dynamics Of Civil Structures, Volume 4, 91-99. Doi: 10.1007/978-3-319-04546-7_11

Tosin, G., Citadini, J., Sanchez, P., Basilio, R., Rocha, M., Siqueira, E., Potye, M., and Lin, L. (2010). Design of the magnet prototypes of the new Brazilian synchrotron light source—

Sirius. Proceedings of the 2010 International Particle Accelerator Conference, Kyoto, Japan, 3084.

Ungar, E. (2007). Vibration Criteria for Healthcare Facility Floors. Available at: http://www.sandv.com/downloads/0709unga.pdf

Vanderplaats R&D, Inc Vanderplaats R&D, Inc, Design Optimization Technologies (2018). GENESIS Structural Optimization for ANSYS Mechanical. Available at: http://www.vrand.com/GTAM.html.

Wallen, E. (2018). Think inside the box. Presentation, Berkeley, California, USA.

Wang, Y., & Kang, Z. (2017). Structural shape and topology optimization of cast parts using level set method. International Journal For Numerical Methods In Engineering, 111(13), 1252-1273. Doi: 10.1002/nme.5503

Wikimedia Commons contributors, "File:Aust.-Synchrotron,-Quadrupole-Focusing-Magnet,-14.06.2007.jpg," Wikimedia Commons, the free media repository, https://commons.wikimedia.org/w/index.php?title=File:Aust.-Synchrotron,-Quadrupole-Focusing-Magnet,-14.06.2007.jpg&oldid=198152780 (accessed May 20, 2019).

Winic, H. (1995). Synchrotron radiation sources – A Primer.

Wolski, A. (2018). Maxwell's equations for magnets, University of Liverpool, and the Cockcroft Institute, UK, Retrieved from http://pcwww.liv.ac.uk/~awolski/teaching/cas/bruges/maxwellsequations.pdf

Workbench Documentation (2019). Retrieved from https://www.sharcnet.ca/Software/Ansys/17.0/en-us/help/ai_sinfo/wb_intro.html

WorldStainless.org. (2018). Retrieved August 7, 2018, from http://www.worldstainless.org/

Wurtz, W. (2018). Shutters Open Injection Refill. Retrieved August 18, 2018, from https://gate.lightsource.ca/ CSCO 1h756767633A2F2F6A7678762E707966762E706E /wiki/Shutters_Open_Injection_Refill [Internal Document].

Wyatt, K. (2018). Private communication.

Yan, H., Yan, G., (2009). Integrated control and mechanism design for the variable input-speed servo four-bar linkages, Mechatronics, 19: 274-285.

Yin, L., & Yang, W. (2001). Optimality criteria method for topology optimization under multiple constraints. Computers & Structures, 79(20-21), 1839-1850. Doi: 10.1016/s0045-7949(01)00126-2

Zhang, D., Gao, S. and Xu, X. (2016). A new computational method for threaded connection stiffness. Advances in Mechanical Engineering, 8(12), p.168781401668265.

Zhang, L. (1996). Vibration at the ESRF, Proc. 5th European Particle Accelerator Conference, EPAC'96, June 10–14, 1996, Barcelona, Spain.

Zhang, L., Farvacque, L., Lesourd, M., Plouviez, E. (2002). Electron beam stabilization experiences at the ESRF. Proceedings of Nanobeam 2002, 26th Advanced ICFA Beam Dynamics Workshop on Nanometer Size Colliding Beams, Citeseer, Lausanne, Switzerland, doi:10.1.1.488.3193

Zhang, L., Lesourd, M., Lewis, T. (2001). Vibration damping systems for magnet girder assembly at the ESRF, Particle Accelerator Conference 2001. PAC 2001. Proceedings of the 2001, vol. 2, pp. 1465-1467 vol.2.

Zhang, W. J., Lin, Y. and Niraj, S. (2005). On the Function-Behavior-Structure Model for Design. The 2nd CDEN Conference, Alberta, 18–20 July. CD ROM, 8.

Zhang, W. (2018). Private communication.

Zhang, W. (2019). ME 886 Advanced Engineering Design Methodology. Lecture, Saskatoon, Saskatchewan.

Zhang, X., Wu, B., Ni, D., Chen, Y., Wu, W. and Ma, L. (2015). Structural analysis of superconducting dipole prototype for HIAF, Chin. Phys. C, vol. 37, no. 1.

Zickler, T. (2011). Basic design and engineering of normal-conducting, iron-dominated electromagnets, Available at: http://cds.cern.ch/record/1334336CERN-2010-004 [1103.1119]

Zillober, Ch. (1993). A globally convergent version of the method of moving asymptotes, Structural Optimization, 6(3):166-174.

Zillober, Ch. (2001). Global convergence of a nonlinear programming method using convex approximations, Numerical Algorithms, 27(3):256-289.

Zillober, Ch. (2001). A combined convex approximation { interior point approach for large scale nonlinear programming, Optimization and Engineering, 2(1):51-73.

Zillober, Ch. (2002). SCPIP {an e\u000Ecient software tool for the solution of structural optimization problems, Structural and Multidisciplinary Optimization, 24(5).

Zitzler, E., and Thiele, L. (1998). An evolutionary algorithm for multiobjective optimization: The strength pareto approach, Technical Report 43, Computer Engineering and Networks Laboratory (TIK), Swiss Federal Institute of Technology (ETH) Zurich.

Appendix A: Multi-Bend Achromat Lattice Structure

The Canadian Light Source is located on the campus of the University of Saskatchewan. It has a third generation 2.9 GeV storage ring synchrotron light source. The synchrotron radiation generated by a series of powerful magnets can be used to conduct research in a large range of fields. The repeating units that form a storage ring are called lattice. Typically, they begin and end with matching cells and have unit cells in between. The present CLS storage ring lattice is based on the Double Bend Achromat (DBA) concept with its dipoles, quadrupoles, sextupoles, and corrector magnets bending, focusing, and correcting the path of the electron beam.

The fourth generation light sources are implementing the Multi-Bend Achromat (MBA) lattice to equip beam users with high brilliance photon beams (Einfeld, 2014). Emittance can be defined by the instantaneous location of the electron beam in an area of transverse phase space region [50]. In the quest of achieving ultralow beam emittance, CLS 2.0 will incorporate the MBA lattice which will have quadrupoles and sextupoles sandwiched between nine dipoles to keep the beam highly focused. In the MBA, the electron beam is bent multiple times per unit cell (nine times in the proposed 9BA lattice) to achieve a lower emittance. Dallin (2018) designed tentative compact 9BA lattice structure shown below:

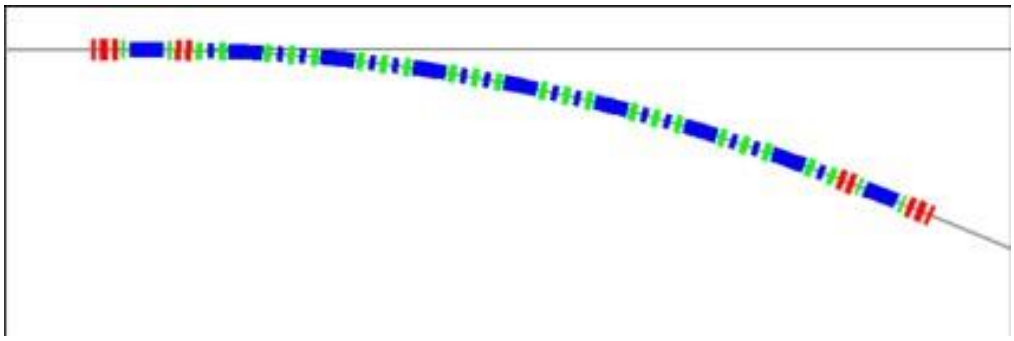

Figure A.1: MBA lattice structure 9BA. The multipoles are represented by colours (blue: dipole, red: quadrupole and green: sextupole) (Dallin, 2018)

The beam emittance of the new machine will be more than a hundred times smaller than the present CLS which increases the probability of particle interaction which corresponds to a hundred times brighter synchrotron radiation. High gradient magnets will be needed to achieve the extreme focusing of the beam. The apertures of most of the new magnets will be smaller as the vacuum chamber will also be smaller and circular in shape. In the MBA lattice, the space between the magnets is very small so the coils will need to extrude in the longitudinal direction as little as possible. All these design requirements correspond to magnets smaller in size with larger field gradients.

Appendix B: The Canadian Light Source

The FCBPSS Framework can be used to simplify the complex synchrotron system. The FCBPSS architecture distinctly comprises of function, context, behavior, principle, state, and structure (Zhang et al., 2005).

The CLS is the system. The structures that comprise the CLS are the Electron Gun, the Linear Accelerator, the Booster Ring, and the Storage Ring. The state variables, in this case, would be the injection current and wiggler and undulator gaps. The behavior of the system is the relationship between the input and the output. For the CLS, the behavior is when the electron beam is injected it produces synchrotron light. The main principles on which the CLS works are Maxwell's equations (Wolski, 2018) and Lorentz force law. The function of the CLS is to produce synchrotron radiation. As this radiation is used at the beamlines for experimentation as well as for testing the quality of beam, this function can be divided into a generic role and a specialization role according to the context. The generic role is the generation of synchrotron light while the specialization roles are for beam quality testing and beamline experimentation. Precondition for the CLS to operate would be the presence of a high potential difference in the electron gun so that it can extract electrons from the tungsten- oxide cathode, the presence of radio frequency fields to accelerate the electrons, kickers and triggers are enabled, wigglers, undulators and the LTB1 (Linac to Booster Ring) Safety Shutter are opened (Wurtz, 2018). In post-conditioning i.e. once the beam is injected into the storage ring, the kicker and triggers are turned off and the LTB Safety Shutters is closed, undulator and wiggler gaps are decreased.

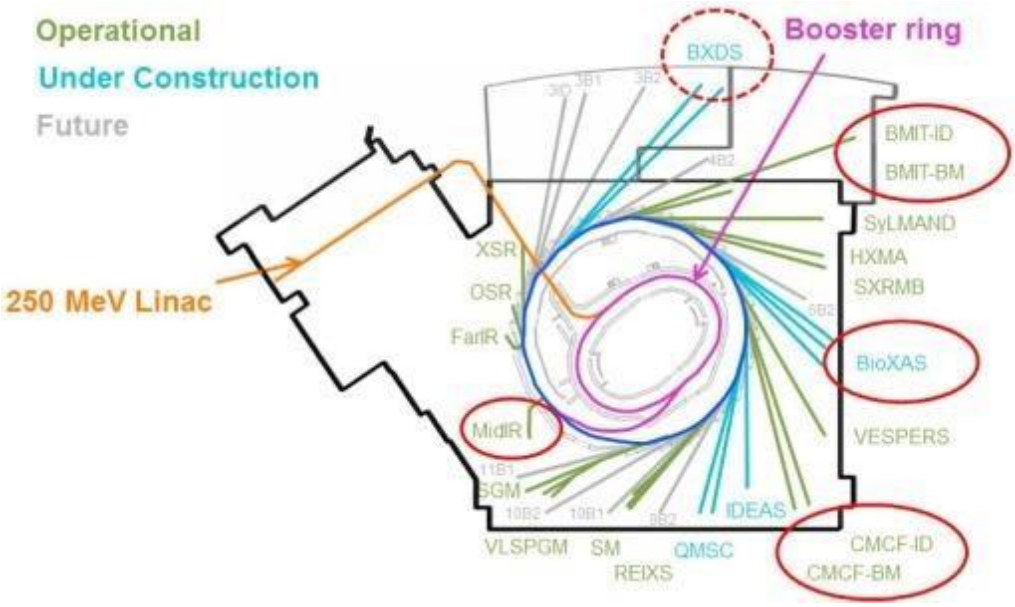

Figure B.1: CLS layout (Grochulskin et al., 2017)

The magnets are held by frames which are in turn clamped to the girders. This girder rests on concrete pedestals. Nearby vehicles and people walking around in the facility contributed to the floor vibrations. The girder has its own sources of vibration which predominantly comes from the cooling water pipes.

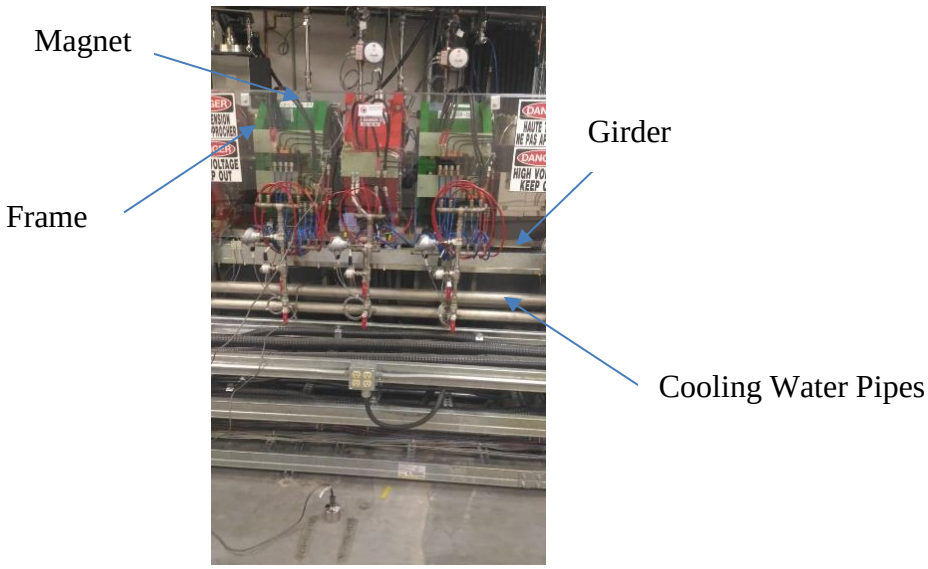

Figure B.2: CLS Storage Ring

Appendix C: CLS 2.0 Quadrupole Design

CLS 2.0 quadrupoles in some locations can be closed sided. The coils are tall, skinny and offset transversely from the pole root so it does not protrude much longitudinally when bent around the end of the yoke (Figure C.1). The aperture has been reduced from 32mm CLS design to 12mm (Dallin, 2018) to produce stronger fields.

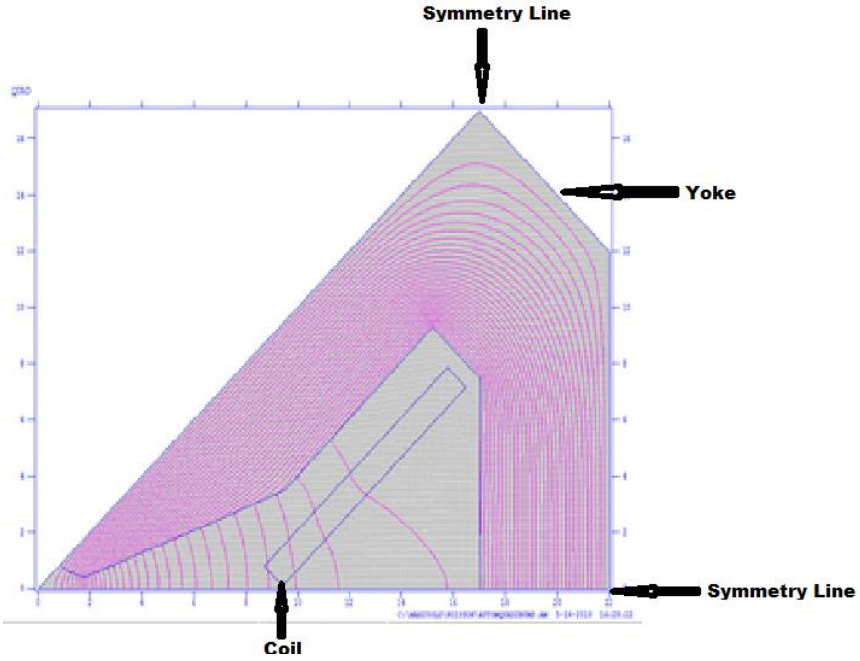

Figure C.1: CLS 2.0 Quadrupole (Closed Side) (Dallin, 2018)

When the Amp-turns are increased, the magnets begin to saturate. As there are losses due to saturation, a field of 100 T/m with 7000 Amp-turns can be reached. While designing the CLS it was thought that a field of 20 T/m was pushing the limit as larger magnets were involved with larger vacuum tubes. However, while designing for the Multi-Bend Achromat (MBA) (Appendix A), everything is miniaturized allowing fields of 100 T/m (Figure C.2). This design is not considered for recessing the coils.

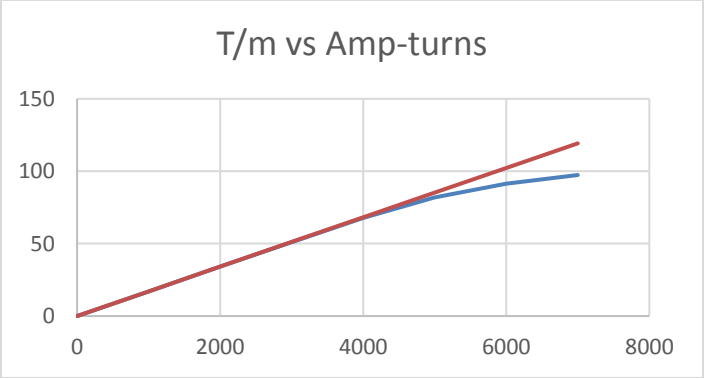

Figure C.2: Quadrupole Gradient Vs Amp-turns (Closed-Sided) (Dallin, 2018)

Another option is to design the magnet to be open-sided. POISSON (Holsinger,and Halbach, 2013) was used to study the two coil positions (top and side) with the same geometry of the yoke in term of field quality. The coils are offset transversely so that they can be wound tight to the end. The coils protrude about 20 mm at the magnet end. This magnet has the same aperture radius of 12mm as the close sided design. However, with this design, it is difficult to reach fields much above 60 T/m. Also, good field regions similar to the conventional quadrupoles will not be achievable with this design.

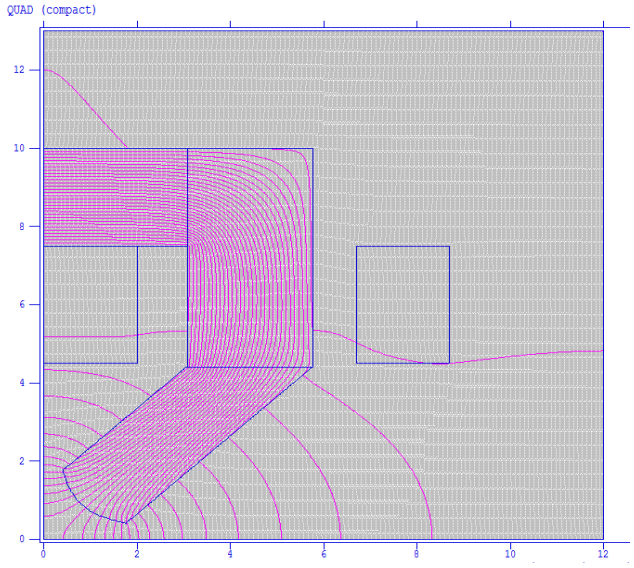

Figure C.3: Side Coil Placement (Dallin, 2018)

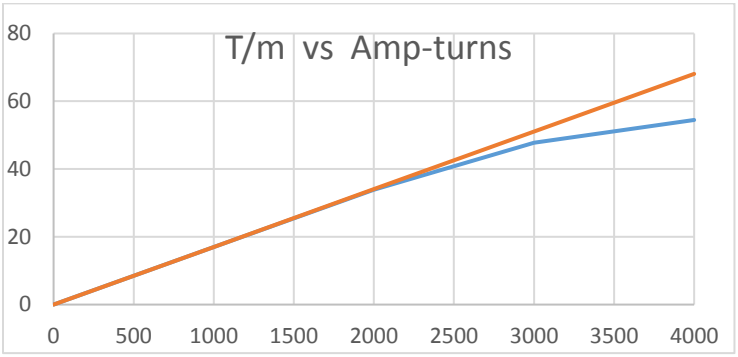

Figure C.4: Quadrupole Gradient Vs Amp-turns (Closed-Sided) (Dallin, 2018)

The coils were placed on the top (outer) yoke keeping the yoke geometry same. With 4020 Amp-turns a gradient of 54.06 T/m can be achieved. The field strength was similar to the side coil arrangement.

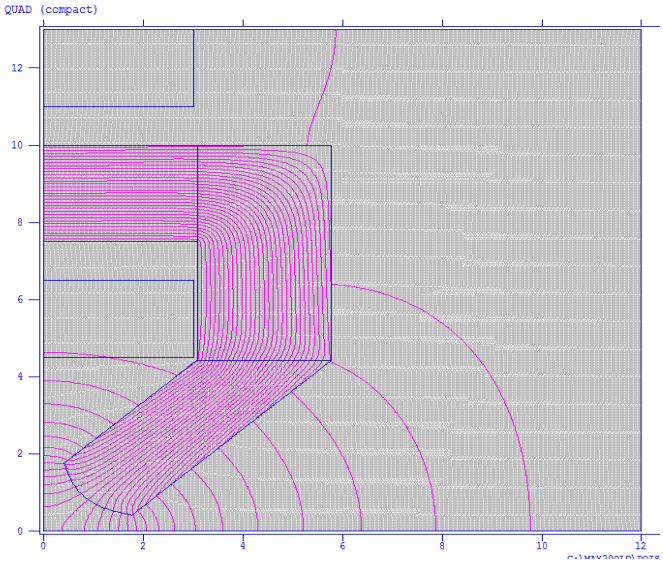

Figure C.5: Top Coil Placement (Dallin, 2018)

The study of quadrupole coil placement revealed that similar quadrupole gradients were achieved with both conventional side-coils and the new top coils. It was also observed that recessed side coils resulted in a 21% integrated field loss whereas with recessed top coils reduced the loss of in integrated field to only 2%. Thus, top coil placement was preferred to side coils in order to

compensate for the high gradient requirements. Apart from the field gradient, magnetic harmonics is another important aspect of magnet design.

The magnetic harmonic analysis is the evaluation of the presence of higher order multipoles in a magnet. The harmonic analysis of the physics design along the horizontal axis shows that the higher order harmonics do not have much effect on the magnetic field. The integrated field at an offset of 0.01m from beam axis is also almost completely retrieved (BL=0.1278 T-m) compared to the top coil without recession with thinner top yoke configuration (BL=0.1297 T-m) [‘B’ is the magnetic field and ‘L’ is the length of the magnet].

Appendix D: RADIA Code

```
<<Radia`;
Off[General::"spell1"];
```

```
Radia Version: 4.31 is loaded
Radia is copyright ESRF, France.
Portions copyright Synchrotron SOLEIL, France.
Portions copyright Wolfram Research, Inc.
```

```
yoke1 = radObjThckPgn[0, 240, { {57.6, 44.091}, {17.6, 4.091}, {15., 4.8}, {14., 5.1429}, {12., 6.}, {10., 7.2}, {8.4853, 8.4853},
    {7.2, 10.}, {6., 12.}, {5.1429, 14.}, {4.5, 16.}, {4.091, 17.6}, {30.582, 44.091}, {57.6, 44.091}}, {0, 0, 0}];
yoke1 = radObjDivMag[yoke1, {{30, 1}, {20, 1}, {20, 1}}];
yoke2 = radObjThckPgn[0, 240, {{57.6, 44.091}, {30.82, 44.091}, {30.82, 125}, {57.6, 125}, {57.6, 44.091}}, {0, 0, 0}];
yoke2 = radObjDivMag[yoke2, {{20, 1}, {20, 1}, {20, 1}}];
yoke3 = radObjThckPgn[0, 200, {{0, 125}, {30.82, 125}, {30.82, 75}, { 0, 75}, {0, 125}}, {0, 0, 0}];
yoke3 = radObjDivMag[yoke3, {{20, 1}, {20, 1}, {20, 1}}];
pole1 = radObjCnt[{yoke1, yoke2, yoke3 }];

coilh = radObjRaceTrk[{0, 100, -15}, {10, 30}, {180, 50}, 30, 10, 6.7];
radTrfOrnt[coilh, radTrfRot[ {0, 0, 0}, {1, 0, 0}, 1.5708]];
quad = radObjCnt[{pole1, coilh}];
radMatApl[pole1, RadMatSteel37[]];


RadTrfZerPara[quad, {0, 0, 0}, {0, 1, 0}];
RadTrfZerPara[quad, {0, 0, 0}, {0, 0, -1}];
Show[Graphics3D[radObjDrw[quad]], Axes → True, AxesLabel → {x, y, z}]
```

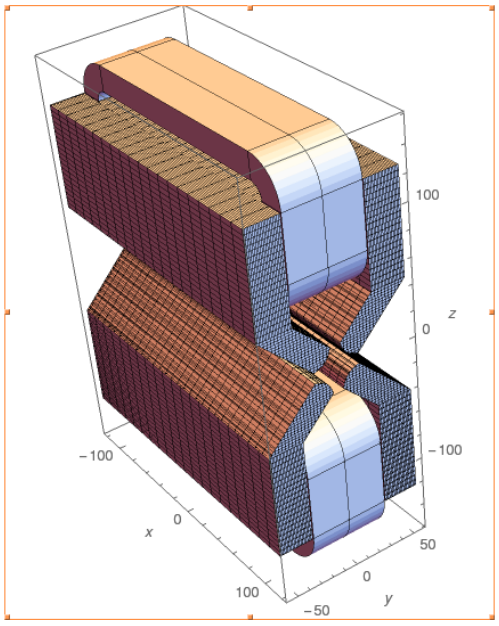

```
(*Apply Solver*)
re = RadSolve[quad, 0.001, 1000];

(*Calculate Field*)
Bfield = Table[{g, radFld[quad, "By", {0, 0, g}]}, {g, -20., 20., 1.}]
ListPlot[Bfield]
radFldInt[quad, "inf", "ibz", {-200, 10, 0}, {200, 10, 0}]
Bfield = Table[{g, radFld[quad, "By", {g, 0, 10}]}, {g, -250., 250., 10.}]
```

{{-20., -0.623147}, {-19., -0.676934}, {-18., -0.720632}, {-17., -0.744397}, {-16., -0.743748}, {-15., -0.722172}, {-14., -0.686938}, {-13., -0.644251}, {-12., -0.597851}, {-11., -0.549653}, {-10., -0.500571}, {-9., -0.451029}, {-8., -0.401222}, {-7., -0.351251}, {-6., -0.301174}, {-5., -0.25103}, {-4., -0.200847}, {-3., -0.150644}, {-2., -0.100432}, {-1., -0.0502162}, {0., -2.13227×10^{-8}}, {1., 0.0502162}, {2., 0.100432}, {3., 0.150644}, {4., 0.200847}, {5., 0.25103}, {6., 0.301173}, {7., 0.351251}, {8., 0.401222}, {9., 0.451029}, {10., 0.500571}, {11., 0.549653}, {12., 0.597851}, {13., 0.644251}, {14., 0.686938}, {15., 0.722173}, {16., 0.743748}, {17., 0.744397}, {18., 0.720632}, {19., 0.676934}, {20., 0.623147}}

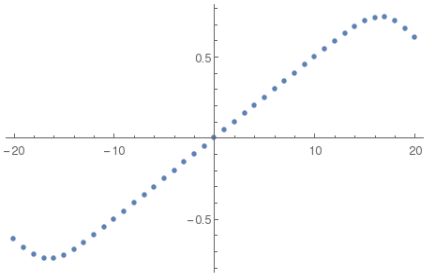

125.95

{{-250., 0.000582429}, {-240., 0.000742329}, {-230., 0.000957769}, {-220., 0.00125326}, {-210., 0.00166682}, {-200., 0.00226056}, {-190., 0.00314146}, {-180., 0.0045078}, {-170., 0.00676569}, {-160., 0.0108632}, {-150., 0.0194273}, {-140., 0.0414933}, {-130., 0.117269}, {-120., 0.384076}, {-110., 0.484901}, {-100., 0.490995}, {-90., 0.493441}, {-80., 0.495039}, {-70., 0.496725}, {-60., 0.498066}, {-50., 0.498853}, {-40., 0.499366}, {-30., 0.500017}, {-20., 0.500474}, {-10., 0.500559}, {0., 0.500571}, {10., 0.500603}, {20., 0.500467}, {30., 0.499827}, {40., 0.499051}, {50., 0.498535}, {60., 0.497727}, {70., 0.496388}, {80., 0.494699}, {90., 0.49307}, {100., 0.490583}, {110., 0.48442}, {120., 0.383815}, {130., 0.117203}, {140., 0.0414668}, {150., 0.0194076}, {160., 0.0108464}, {170., 0.00675108}, {180., 0.00449417}, {190., 0.00313539}, {200., 0.00225329}, {210., 0.00166154}, {220., 0.00124654}, {230., 0.000953802}, {240., 0.000739872}, {250., 0.000579825}}

```
ListPlot[Bfield]
```

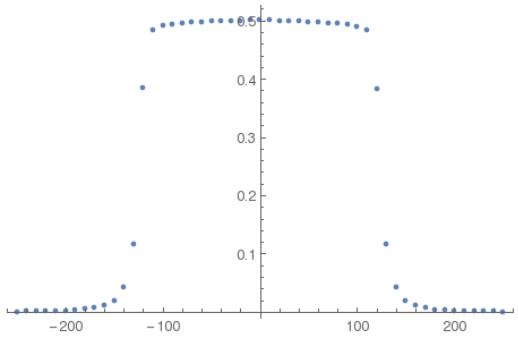


```
(*Calculate Forces*)
t1 = AbsoluteTime[];
fr1 = radFldEnrFrc[pole1, quad, ""];
t2 = AbsoluteTime[];
Print["{Pole 1 Fx, Fy, Fz} = ", N[fr1, 3], " Newton"];
Print["CPU Time for 1 pole: ", N[t2 - t1, 3], " seconds"];
```

{Pole 1 Fx, Fy, Fz} = {-32.2659, -8811.72, -4729.94} Newton

CPU Time for 1 pole: 1.21×10^{5} seconds

Table D.1: RADIA Variable Description

Variable	Description
yoke1	Holds the 2D coordinates of the points that make up the pole tip.  This polygon has its centre at 0 at the horizontal axis and an extrusion thickness of 240mm.This geometry is subdivided into 30 parts in the x-direction and 20 parts in y and z-direction.
yoke2	Holds the 2D coordinates of the rectangular yoke part.  This polygon has its centre at 0 at the horizontal axis and an extrusion thickness of 240mm. This geometry is subdivided into 20 parts in the x, y and z-direction.
yoke3	Holds the 2D coordinates of the other rectangular yoke part.  This polygon has its centre at 0 at the horizontal axis and an extrusion thickness of 200mm. This geometry is subdivided in 20 parts in the x, y and z direction.
pole1	A container that encloses yoke1, yoke2 & yoke3. It is capable of producing a magnetic field. The material `RadMatSteel37` is applied to it.
coilh	A coil carrying current for the half top pole with its centre at (0, 100, -15). The inner radius and outer radius of this coil is 10mm and 30mm respectively. 180mm and 50mm being the horizontal and longitudinal lengths of the straight section. The coil has a depth of 30mm with a current density of 6.7 A/mm^2

	and a bent segmentation of 10. This coil is rotated at an angle 90^0 about the x-axis where it intersects the point (0, 0, 0).
quad	A container that encloses pole1 and coilh. This is a quarter of the required quadrupole. Mirror symmetry was applied to this geometry about the origin in the y-direction to obtain the half quadrupole. Mirror symmetry was applied again about the origin in the negative z-direction to get the complete quadrupole geometry. The 3D graphical representation of this geometry is shown in the program.
re	The solver, RadSolve, is applied to quad with a proper absolute precision level of 0.001 and a maximum number of iterations of 1000.
Bfield (first)	Calculates the magnetic field produced by quad from a distance of +20mm to -20mm in the z-direction with a step size of 1mm and zero offset from the beam axis. This is shown in table format. A graph is also plotted using this table. From this graph, it can be concluded that the designed magnet behaves like a quadrupole.
Bfield (second)	Calculates the magnetic field produced by quad from a distance of +200mm to -200mm in the x-direction with a step size of 10mm and an offset of 10mm from the beam axis. This is shown in table format. A graph is also plotted using this table.
fr1	Stores the value of the magnetic force that quad exerts on pole1. The output is programmed to have 3 significant figures.
t1	Stores the start time for calculating the force fr1.

Appendix E: POISSON Code

QUAD (compact)

Including harmonic analysis for H type dipole magnet

Field output is requested along the X axis

[Originally appeared in 1987 Reference Manual B.2.1]


```
&reg kprob=0,          ; Declares a POISSON problem
dx=.05,                ; Mesh interval
mode=0                 ; Using internal table for material 2
IENERGY=1
conv=1.
xminf=-0,xmaxf=3.0183,       ; X range for field interpolation
yminf=0,ymaxf=0,       ; Y range (along line y = 0)



; The next 6 terms refer to the harmonic analysis:
ktype=4,               ; quad symmetry
nbslf=1.
nterm=5,               ; Number of coefficients
nptc=14,               ; Number of arc points for interpolation
rint=1.,           ; Radius of the arc
angle=90,              ; Angular extent of arc (default start = 0)
rhogam=.0005,
rnorm=1.&              ; Aperture radius
```

```
&po x=0.0,y=0.0 &
&po x=12.,y=0. &
&po x=12.,y=14. &
&po x=0.,y=14. &
&po x=0.0,y=0.0 &

&reg mat=2 &
&po x=5.76 ,y=4.4091 &
&po x=1.76,y=.4091 &
&po x=1.5,y=.48 &
&po x=1.4,y=.51429 &
&po x= 1.2,y=.6 &
&po x=1.,y=.72 &
&po x=.84853,y=.84853 &
&po y=1.,x=.72 &
&po y= 1.2,x=.6 &
&po y=1.4,x=.51429 &
&po y=1.5,x=.48 &
&po y=1.76,x=.4091 &
&po x=3.0582,y=4.4091 &
&po x=5.76 ,y=4.4091 &
&reg mat=2 &
&po x=5.76 ,y=4.4091 &
&po x=3.082 ,y=4.4091 &
&po x=3.082 ,y=10. &
&po x=5.76,y=10. &
&po x=5.76 ,y=4.4091 &
```

```
&reg mat=2 &
&po x=0 ,y=7.5 &
&po x=3.082 ,y=7.5 &
&po x=3.082 ,y=10. &
&po x=0,y=10. &
&po x=0 ,y=7.5 &

&reg cur=-2010 & ; coil
&po x=0,y=4.5 &
&po x=2.,y=4.5 &
&po x=2.,y=6.5 &
&po x=0.,y=6.5 &
&po x=0,y=4.5 &

&reg cur=2010 & ; coil
&po x=0.0,y=11.0 &
&po x=2.0,y=11.0 &
&po x=2.0,y=13.0 &
&po x=0.0,y=13.0 &
&po x=0.0,y=11.0 &
```

In order to calculate the effect of a nonmagnetic frame in Section 3.2, coordinates of a rectangle adjacent to the magnet was added to the above code.

In Section 3.3, the harmonic analysis was done by adding/subtracting 100 microns, 50 microns, and 10 microns from the above x and y coordinates.

Appendix F: Deformation induced Relative Deviation from Ideal Field

Table F.1: Relative Deviation from Ideal Field 100 micron Deformation

Offset Length (in cm)	Percentage Deviation from the Ideal Quadrupole Field
-1	6.62E-02
-0.9	3.86E-02
-0.8	2.35E-02
-0.7	1.35E-02
-0.6	7.09E-03
-0.5	3.35E-03
-0.4	1.36E-03
-0.3	4.26E-04
-0.2	8.40E-05
-0.1	5.25E-06
-1.4E-16	1.95E-65
0.1	5.25E-06
0.2	8.40E-05
0.3	4.26E-04
0.4	1.36E-03
0.5	3.35E-03
0.6	7.09E-03

0.7	1.35E-02
0.8	2.35E-02
0.9	3.86E-02
1	6.62E-02

Table F.2: Relative Deviation from Ideal Field 50 micron Deformation along the y-axis

Offset Length (in cm)	Percentage Deviation from the Ideal Quadrupole Field
-1	3.40E-02
-0.9	1.82E-02
-0.8	1.08E-02
-0.7	6.06E-03
-0.6	3.11E-03
-0.5	1.44E-03
-0.4	5.73E-04
-0.3	1.79E-04
-0.2	3.51E-05
-0.1	2.19E-06
-1.4E-16	8.14E-66
0.1	2.19E-06
0.2	3.51E-05
0.3	1.79E-04
0.4	5.73E-04
0.5	1.44E-03
0.6	3.11E-03
0.7	6.06E-03
0.8	1.08E-02
0.9	1.82E-02
1	3.40E-02

Table F.3: Relative Deviation from Ideal Field for 50 micron Deformation along the both axes

Offset Length (in cm)	Percentage Deviation from the Ideal Quadrupole Field
-1	6.19E-02
-0.9	3.67E-02
-0.8	2.24E-02
-0.7	1.29E-02
-0.6	6.77E-03
-0.5	3.20E-03
-0.4	1.30E-03
-0.3	4.08E-04
-0.2	8.04E-05
-0.1	5.02E-06
-1.4E-16	1.86E-65
0.1	5.02E-06
0.2	8.04E-05
0.3	4.08E-04
0.4	1.30E-03
0.5	3.20E-03
0.6	6.77E-03
0.7	1.29E-02
0.8	2.24E-02
0.9	3.67E-02
1	6.19E-02

Table F.4: Relative Deviation from Ideal Field for 10 micron Deformation along the y-axis

Offset Length (in cm)	Percentage Deviation from the Ideal Quadrupole Field
-1	1.86E-02
-0.9	7.95E-03
-0.8	4.07E-03
-0.7	1.93E-03
-0.6	8.27E-04
-0.5	3.25E-04
-0.4	1.15E-04
-0.3	3.36E-05
-0.2	6.42E-06
-0.1	3.98E-07
-1.4E-16	1.48E-66
0.1	3.98E-07
0.2	6.42E-06
0.3	3.36E-05
0.4	1.15E-04
0.5	3.25E-04

0.6	8.27E-04
0.7	1.93E-03
0.8	4.07E-03
0.9	7.95E-03
1	1.86E-02

Appendix G: Analytic Hierarchy Process

Figures G.1 and G.2 show how the element comparison is performed by assigning weights and the APH matrix is formed respectively. According to the first comparison, cost is five times more important than elastic modulus and so on.

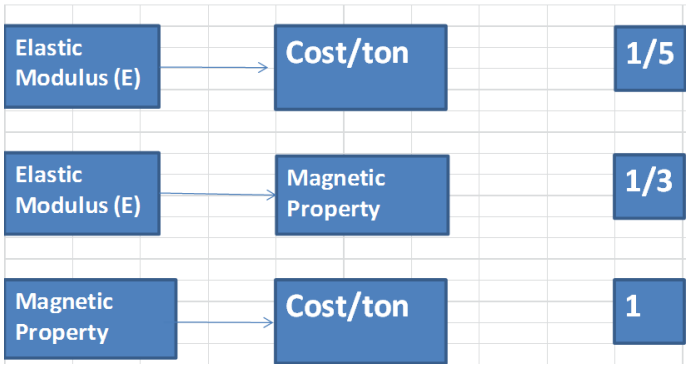

Figure G.1: Element Comparison

Figure G.2: APH Matrix

Matrix Normalized Principle Eigen Vector

	A - Importance - or B?			Equal	How much more?
1	○ Elastic Modulus	or	◉ Magnetic Property	○ 1	○ 2 ○ 3 ○ 4 ○ 5 ◉ 6 ○ 7 ○ 8 ○ 9
2	◉ Elastic Modulus	or	○ Cost	○ 1	◉ 2 ○ 3 ○ 4 ○ 5 ○ 6 ○ 7 ○ 8 ○ 9
3	◉ Magnetic Property	or	○ Cost	○ 1	○ 2 ○ 3 ○ 4 ○ 5 ○ 6 ○ 7 ○ 8 ◉ 9

CR = 1% OK

Check Consistency | Download_(.csv) ☐ dec. comma

AHP Scale: 1- Equal Importance, 3- Moderate importance, 5- Strong importance, 7- Very strong importance, 9- Extreme importance (2,4,6,8 values in-between).

Priorities

These are the resulting weights for the criteria based on your pairwise comparisons

	Category	Priority	Rank
1	Elastic Modulus	14.3%	2
2	Magnetic Property	77.9%	1
3	Cost	7.9%	3

Number of comparisons = 3
Consistency Ratio CR = 1.0%

Decision Matrix

The resulting weights are based on the principal eigenvector of the decision matrix

	1	2	3
1	1	0.17	2.00
2	6.00	1	9.00
3	0.50	0.11	1

Principal eigen value = 3.009
Eigenvector solution: 3 iterations, delta = 1.9E-9

Sample Calculation:

In the following tables, E is the elastic modulus, $ is the cost and μ is the magnetic property.

Table G.1: Sum of Columns

	E	**µ**	**$**
E	1	0.17	2
µ	6	1	9
$	0.5	0.11	1
Sum of Columns	7.5	1.28	12

Dividing every element in each column by the sum of the column.

	E	**µ**	**$**
E	1/7.5	0.17/1.28	2/12
µ	6/7.5	1/1.28	3/4
$	.5/7.5	0.11/1.28	1/12

Table G.2: Sum of Rows

	E	**µ**	**$**	**Sum of Rows**
E	0.13	0.13	0.17	0.43
µ	0.80	0.78	0.75	2.33
$	0.07	0.09	0.08	0.24

The priority vector is then calculated by diving the sum of the rows by the number of rows.

Table G.3: Priority

	E	**µ**	**$**	**Sum of Rows**	**Priority Vector**	**Priority**
E	0.13	0.13	0.17	0.43	0.143333	14.33%
µ	0.80	0.78	0.75	2.33	0.7766666	77.67%
$	0.07	0.09	0.08	0.24	0.08	8%

Priority vector for E = 0.43/3 = 0.1433

Priority for E = E Priority vector x 100% = 14.33%

The priority for µ and $ was calculated in a similar way.

Consistency Ratio: It is a measure of judgment stability and is mathematically expressed as the ratio of Consistency Index (C.I.) to Random Index (R.I.).

CI = (Maximum Eigen Value – Size) / (Size - 1) …. (F.1)

The maximum Eigen Value (λ) is calculated by the summation of the product of the reciprocal matrix sum of columns and all the Eigen value vectors (Teknomo, 2006).

λ = (7.5 x 0.14333) + (1.28 x 0.7766) + (12 x 0.08) = 1.075 + .994 + .96 = 3.029

CI = (3.029 – 3) / (3 - 1) = 0.0145

The value of RI can be found out from the study by Saaty (Winston, 1993) in the following table,

Table G.4: RI Table

n	**RI**
2	0
3	0.58
4	0.90
5	1.12
6	1.24
7	1.32
8	1.41
9	1.45
10	1.51

n will be 3 because the size of the matrix is 3 x 3. So the RI will be 0.58.

CR = 0.027

Thus, CR < 0.1, which proves that the judgment is consistent (Goswami, 2014).

Each alternative rating is then multiplied with weights of the sub-criteria.

Thus, according to the weighs assigned, the magnetic property of the material has the highest importance and the material cost has the least importance. The consistency ratio is less than 0.1 which indicates the weights designated are indeed consistent and the results can be trusted.

Similarly, the Sub-elements comparisons:

Magnetic Property

	A - Importance - or B?			Equal	How much more?
1	Non-magnetic	or	Paramagnetic	1	2 3 4 **5** 6 7 8 9
2	Non-magnetic	or	Diamagnetic	1	2 3 4 **5** 6 7 8 9
3	Non-magnetic	or	Ferromagnetic	1	2 3 4 5 6 7 8 **9**
4	Paramagnetic	or	Diamagnetic	**1**	2 3 4 5 6 7 8 9
5	Paramagnetic	or	Ferromagnetic	1	2 3 4 **5** 6 7 8 9
6	Diamagnetic	or	Ferromagnetic	1	2 3 4 5 6 **7** 8 9

CR = 7.1% OK

Check Consistency Download_(.csv) dec. comma

AHP Scale: 1- Equal Importance, 3- Moderate importance, 5- Strong importance, 7- Very strong importance, 9- Extreme importance (2,4,6,8 values in-between).

Priorities

These are the resulting weights for the criteria based on your pairwise comparisons

	Category	Priority	Rank
1	Non-magnetic	63.0%	1
2	Paramagnetic	15.6%	3
3	Diamagnetic	17.5%	2
4	Ferromagnetic	4.0%	4

Number of comparisons = 6
Consistency Ratio CR = 7.1%

Decision Matrix

The resulting weights are based on the principal eigenvector of the decision matrix

	1	2	3	4
1	1	5.00	5.00	9.00
2	0.20	1	1.00	5.00
3	0.20	1.00	1	7.00
4	0.11	0.20	0.14	1

Principal eigen value = 4.193
Eigenvector solution: 6 iterations, delta = 2.7E-9

The design constraints strictly prohibit the use of ferromagnetic material, hence, the nonmagnetic material will be given higher priority while selecting the material. Paramagnetic and diamagnetic have similar weights. A material with the least magnetic permeability will be given the highest priority.

Elastic Modulus

	A - Importance - or B?			Equal	How much more?
1	○ 193 GPa	or	◉ 235 GPa	○ 1	○ 2 ◉ 3 ○ 4 ○ 5 ○ 6 ○ 7 ○ 8 ○ 9
2	◉ 193 GPa	or	○ 69 GPa	○ 1	○ 2 ○ 3 ○ 4 ◉ 5 ○ 6 ○ 7 ○ 8 ○ 9
3	◉ 193 GPa	or	○ 40 GPa	○ 1	○ 2 ○ 3 ○ 4 ○ 5 ○ 6 ○ 7 ◉ 8 ○ 9
4	◉ 235 GPa	or	○ 69 GPa	○ 1	○ 2 ○ 3 ○ 4 ○ 5 ○ 6 ○ 7 ○ 8 ◉ 9
5	◉ 235 GPa	or	○ 40 GPa	○ 1	○ 2 ○ 3 ○ 4 ○ 5 ○ 6 ○ 7 ○ 8 ◉ 9
6	◉ 69 GPa	or	○ 40 GPa	◉ 1	○ 2 ○ 3 ○ 4 ○ 5 ○ 6 ○ 7 ○ 8 ○ 9

CR = 3.4% OK

Check Consistency Download_(.csv) ☐ dec. comma

AHP Scale: 1- Equal Importance, 3- Moderate importance, 5- Strong importance, 7- Very strong importance, 9- Extreme importance (2,4,6,8 values in-between).

Priorities

These are the resulting weights for the criteria based on your pairwise comparisons

	Category	Priority	Rank
1	193 GPa	29.1%	2
2	235 GPa	60.0%	1
3	69 GPa	5.7%	3
4	40 GPa	5.2%	4

Number of comparisons = 6
Consistency Ratio CR = 3.4%

Decision Matrix

The resulting weights are based on the principal eigenvector of the decision matrix

	1	2	3	4
1	1	0.33	5.00	8.00
2	3.00	1	9.00	9.00
3	0.20	0.11	1	1.00
4	0.12	0.11	1.00	1

Principal eigen value = 4.092
Eigenvector solution: 4 iterations, delta = 1.4E-8

The elastic modulus of a material has a direct impact on the static deformation and the first mode frequency. Hence, the materials with higher elastic modulus are ranked higher.

Cost

	A - Importance - or B?		Equal	How much more?
1	◉ 2768 USD	or ○ 3897 USD	○ 1	◉ 2 ○ 3 ○ 4 ○ 5 ○ 6 ○ 7 ○ 8 ○ 9
2	◉ 2768 USD	or ○ 2332.50 USD	◉ 1	○ 2 ○ 3 ○ 4 ○ 5 ○ 6 ○ 7 ○ 8 ○ 9
3	◉ 2768 USD	or ○ 17992 USD	○ 1	◉ 2 ○ 3 ○ 4 ○ 5 ○ 6 ○ 7 ○ 8 ○ 9
4	◉ 2768 USD	or ○ 90718.5 USD	○ 1	○ 2 ○ 3 ○ 4 ◉ 5 ○ 6 ○ 7 ○ 8 ○ 9
5	○ 3897 USD	or ◉ 2332.50 USD	○ 1	◉ 2 ○ 3 ○ 4 ○ 5 ○ 6 ○ 7 ○ 8 ○ 9
6	◉ 3897 USD	or ○ 17992 USD	○ 1	◉ 2 ○ 3 ○ 4 ○ 5 ○ 6 ○ 7 ○ 8 ○ 9
7	◉ 3897 USD	or ○ 90718.5 USD	○ 1	○ 2 ○ 3 ○ 4 ○ 5 ○ 6 ○ 7 ○ 8 ◉ 9
8	◉ 2332.50 USD	or ○ 17992 USD	○ 1	○ 2 ◉ 3 ○ 4 ○ 5 ○ 6 ○ 7 ○ 8 ○ 9
9	◉ 2332.50 USD	or ○ 90718.5 USD	○ 1	○ 2 ○ 3 ○ 4 ○ 5 ○ 6 ○ 7 ○ 8 ◉ 9
10	◉ 17992 USD	or ○ 90718.5 USD	○ 1	○ 2 ○ 3 ◉ 4 ○ 5 ○ 6 ○ 7 ○ 8 ○ 9

CR = 3.2% OK

Priorities

These are the resulting weights for the criteria based on your pairwise comparisons

	Category	Priority	Rank
1	2768 USD	28.8%	2
2	3897 USD	21.3%	3
3	2332.50 USD	34.0%	1
4	17992 USD	12.3%	4
5	90718.5 USD	3.6%	5

Number of comparisons = 10
Consistency Ratio CR = 3.2%

Decision Matrix

The resulting weights are based on the principal eigenvector of the decision matrix

	1	2	3	4	5
1	1	2.00	1.00	2.00	5.00
2	0.50	1	0.50	2.00	9.00
3	1.00	2.00	1	3.00	9.00
4	0.50	0.50	0.33	1	4.00
5	0.20	0.11	0.11	0.25	1

Principal eigen value = 5.144
Eigenvector solution: 5 iterations, delta = 3.4E-8

The materials with higher cost are not preferred and hence are ranked accordingly.

Appendix H: MOGA Raw Optimization Data

The Multi-Objective Genetic Algorithm (MOGA) design points data is shown in Table H.1

Table H.1: MOGA Raw Optimization Data

#	P29 - Frame_Thickness (mm)	P7 - Equivalent Stress Maximum (MPa)	P27 - Total Deformation Maximum (mm)	P28 - Total Deformation Reported Frequency (Hz)
Name	P29	P7	P27	P28
1	10	16.13597	0.002823	83.4312
2	12	13.68679	0.002394	98.51071
3	14	11.78855	0.002085	112.7178
4	16	10.29529	0.00185	125.818
5	18	9.102213	0.001665	137.6011
6	20	8.134823	0.001515	147.8872
7	22	6.220225	0.001366	155.8802

8	24	5.67878	0.001262	162.9909
9	26	5.219863	0.001175	168.6385
10	28	4.82757	0.0011	172.8728
11	30	4.48929	0.001035	175.8917
12	32	4.233168	0.000979	177.86
13	34	4.018277	0.000929	178.9436
14	36	3.825922	0.000885	179.2982
15	38	3.652833	0.000847	179.0641
16	40	3.496224	0.000812	178.3626
17	42	3.670447	0.000786	176.0388
18	44	3.534995	0.000758	174.5613
19	46	3.409719	0.000732	172.8775
20	48	3.293292	0.000709	171.0446
21	50	3.184593	0.000688	169.1084
22	52	3.08268	0.000668	167.1048

23	54	2.986753	0.00065	165.0618
24	56	2.896139	0.000633	163.0011
25	58	2.810239	0.000616	137.6701
26	60	2.72863	0.000601	136.0715
27	62	2.786259	0.000587	131.1059
28	64	2.711001	0.000574	129.5063
29	66	2.638869	0.000561	127.9472

Appendix I: Hole Location in the Magnet Yoke Raw Data

Table I.1: Hole Location in the Magnet Yoke Raw Data

#	P1 - Distance_Coil [mm]	P2 - DistCoil [mm]	P3 - Total Deformation Maximum [mm]	P4 - Equivalent Stress Maximum [MPa]
#				
# The following header line defines the name of the columns by reference to the parameters.				
Name	P1	P2	P3	P4
DP 0	30	30	0.004998	7.898187
DP 1	50	50	0.005153	7.895515
DP 2	40	40	0.00508	7.147796
DP 3	55	55	0.005207	7.536383
DP 4	25	25	0.004961	8.224596
DP 5	35	35	0.005016	8.050931

DP 6	20	20	0.004936	7.158451
DP 7	15	15	0.004907	8.101801
DP 8	10	10	0.005058	7.621538
DP 9	5	5	0.005094	8.066945
DP 10	60	60	0.005242	8.687726
DP 11	65	65	0.005275	7.355989
DP 12	70	70	0.005344	7.96701
DP 13	75	75	0.005307	8.228703
DP 14	32	32	0.005041	8.254316
DP 15	30	30	0.004998	7.898187

Appendix J: Magnet Frame General Assembly and Part Drawings

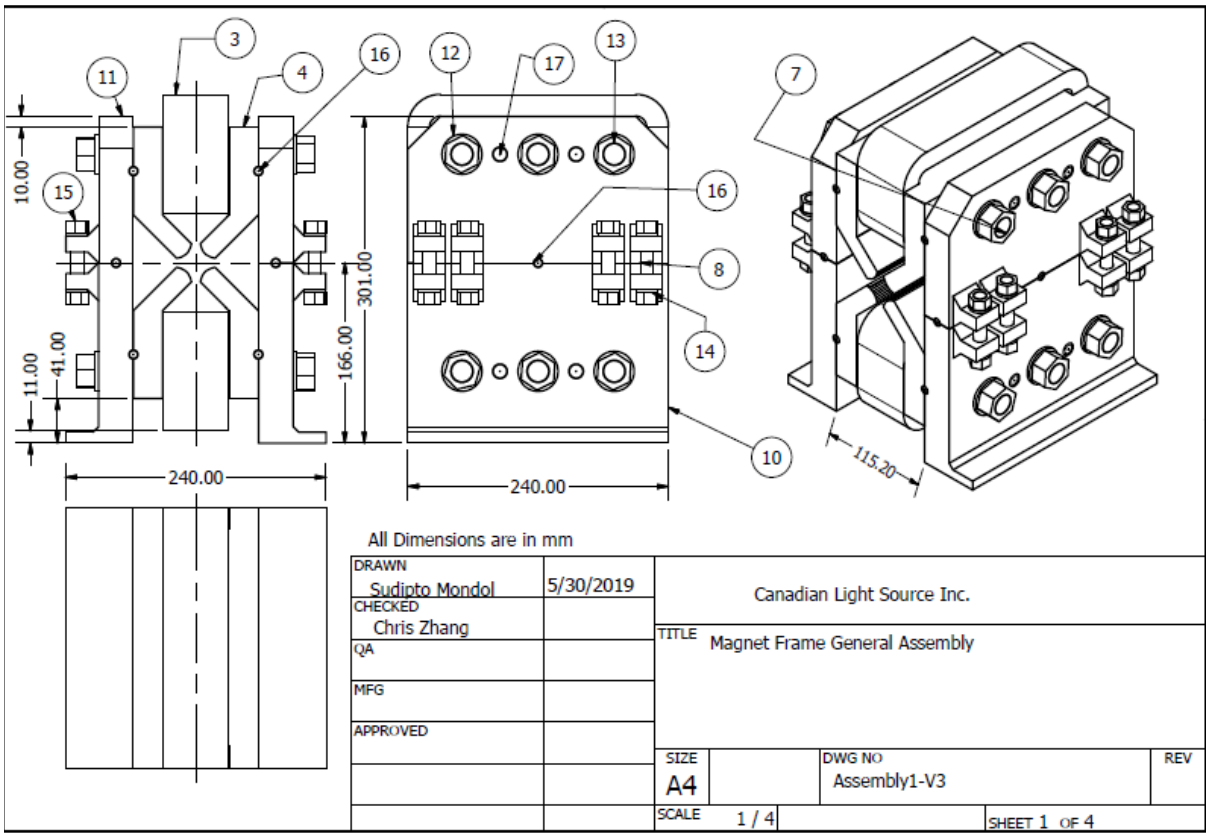

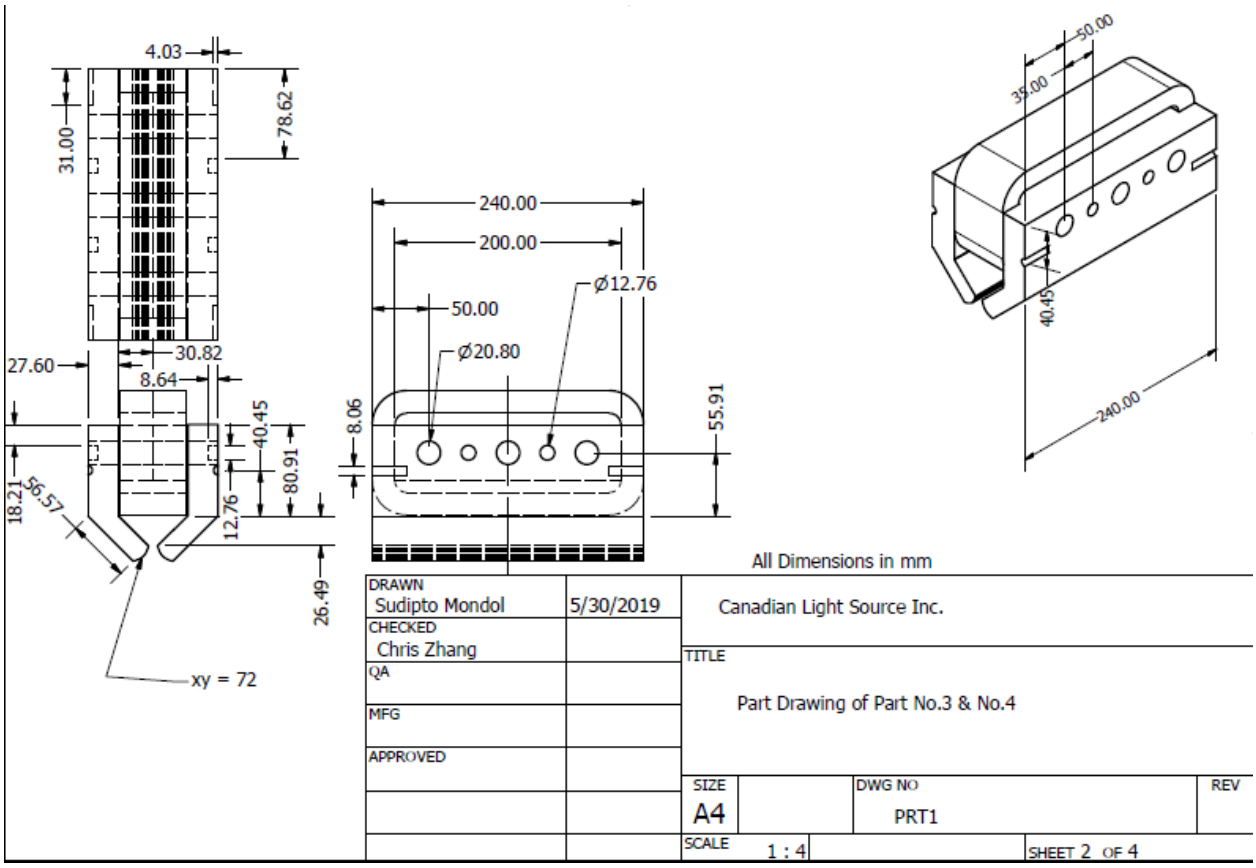
4.03
78.62
31.00
240.00
200.00
Ø12.76
50.00
Ø20.80
27.60
30.82
8.64
40.45
80.91
8.06
55.91
18.21
56.57
12.76
26.49
xy = 72
50.00
35.00
40.45
240.00
All Dimensions in mm
DRAWN
Sudipto Mondol
5/30/2019
CHECKED
Chris Zhang
QA
MFG
APPROVED
Canadian Light Source Inc.
TITLE
Part Drawing of Part No.3 & No.4
SIZE
A4
DWG NO
PRT1
REV
SCALE
1 : 4
SHEET 2 OF 4

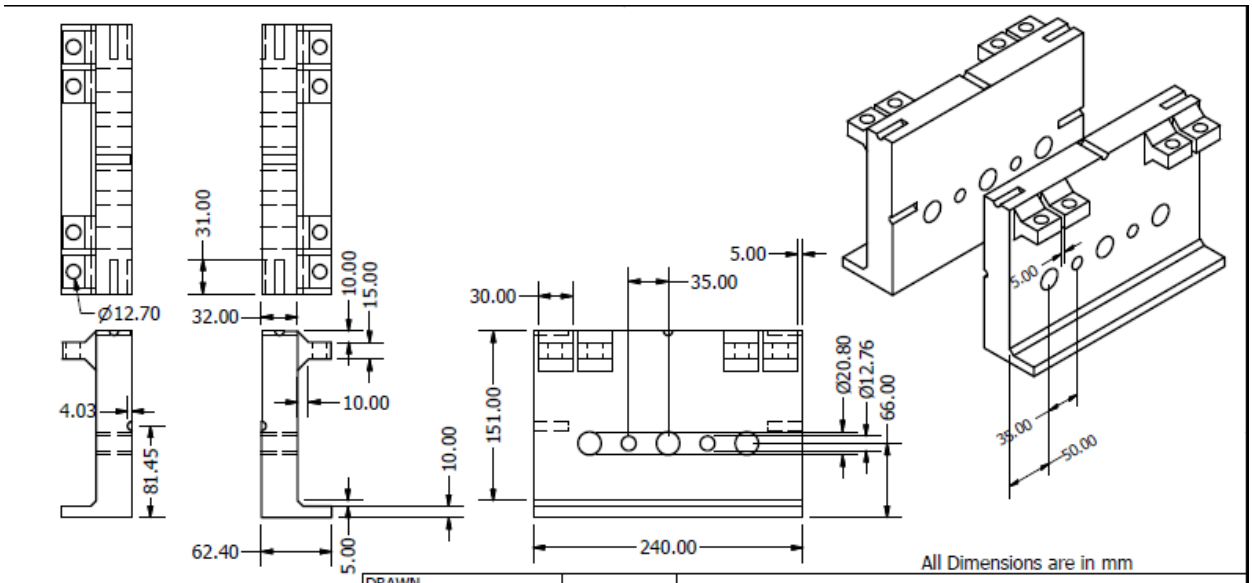

All Dimensions are in mm

DRAWN Sudipto Mondol	5/30/2019	Canadian Light Source Inc.
CHECKED Chris Zhang		TITLE Part No. 10
QA		
MFG		
APPROVED		
		SIZE A4 / DWG NO PRT2B / REV
		SCALE 1 / 4 / SHEET 3 OF 4

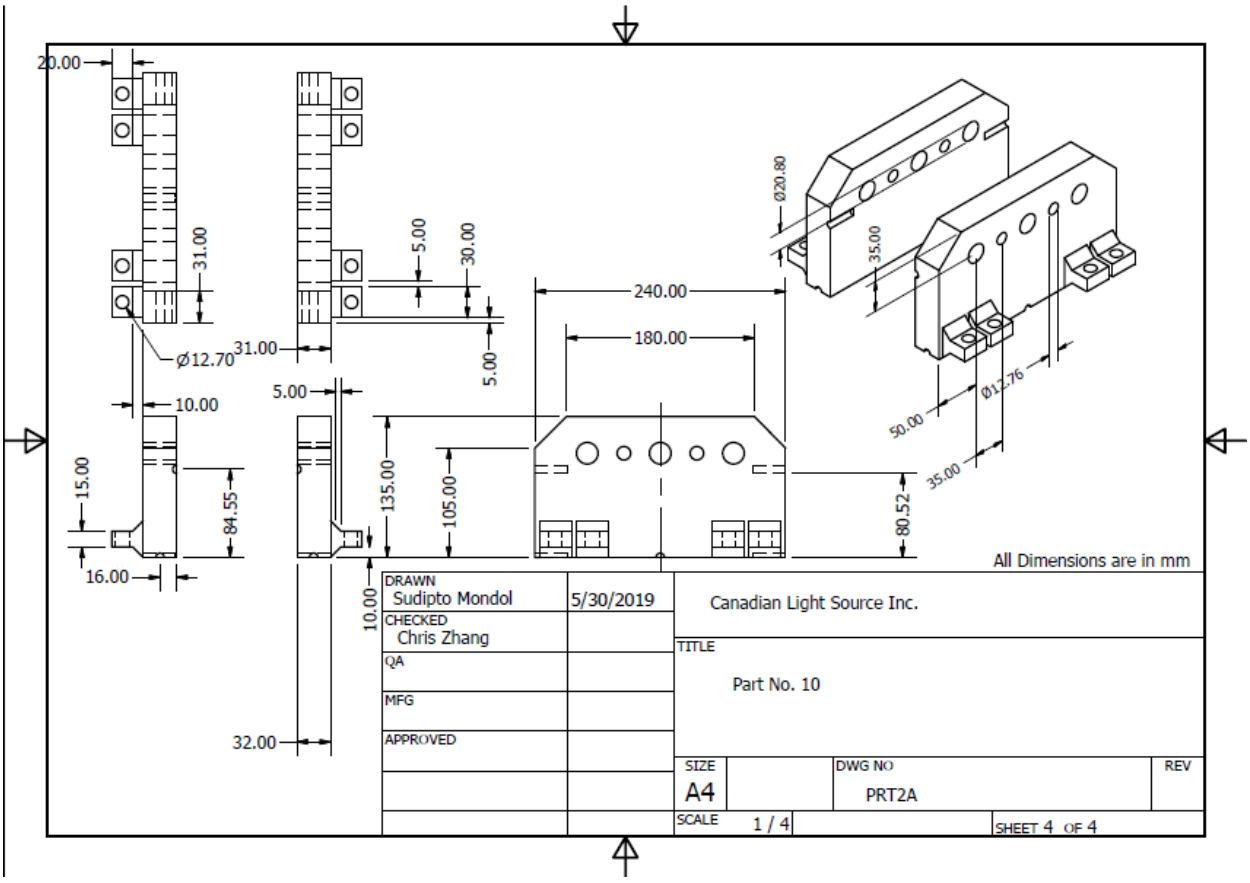
20.00
31.00
Ø12.70
10.00
15.00
84.55
16.00
31.00
5.00
30.00
5.00
5.00
135.00
105.00
10.00
32.00
240.00
180.00
Ø20.80
35.00
50.00
Ø12.76
35.00
80.52
All Dimensions are in mm
DRAWN
Sudipto Mondol
5/30/2019
CHECKED
Chris Zhang
QA
MFG
APPROVED
Canadian Light Source Inc.
TITLE
Part No. 10
SIZE
A4
DWG NO
PRT2A
REV
SCALE
1 / 4
SHEET 4 OF 4

Table J.1: Bill of materials

Item No.	Item	Quantity	Material
17	Dowels 12.6mm x 40mm	8	304L Stainless Steel
16	Dowels 8mm x 30mm	8	304L Stainless Steel
15	M12 Nut	16	304L Stainless Steel
14	M12 Washer	16	304L Stainless Steel
8	M12 Threaded Rod	8	304L Stainless Steel
12	M20 Washer	12	304L Stainless Steel
13	M20 Nut	12	304L Stainless Steel
7	M20 Threaded Rod	6	304L Stainless Steel
10	Bottom Frame	2	304L Stainless Steel
11	Top Frame	2	304L Stainless Steel
3	Coil	2	Copper
4	Magnet Yoke	4	AISI 1010 Steel

Bill of Materials